



**HAL**  
open science

# Vibration Analysis and Reduction of Cable-Driven Parallel Robots

Sana Baklouti

► **To cite this version:**

Sana Baklouti. Vibration Analysis and Reduction of Cable-Driven Parallel Robots. Mechanical engineering [physics.class-ph]. INSA de Rennes, 2018. English. NNT : 2018ISAR0034 . tel-02163227

**HAL Id: tel-02163227**

**<https://theses.hal.science/tel-02163227>**

Submitted on 24 Jun 2019

**HAL** is a multi-disciplinary open access archive for the deposit and dissemination of scientific research documents, whether they are published or not. The documents may come from teaching and research institutions in France or abroad, or from public or private research centers.

L'archive ouverte pluridisciplinaire **HAL**, est destinée au dépôt et à la diffusion de documents scientifiques de niveau recherche, publiés ou non, émanant des établissements d'enseignement et de recherche français ou étrangers, des laboratoires publics ou privés.

# THESE DE DOCTORAT DE

L'INSA RENNES

COMUE UNIVERSITE BRETAGNE LOIRE

ECOLE DOCTORALE N°602

Sciences pour l'Ingénieur

Spécialité : « Génie Mécanique »

Par

« **Sana BAKLOUTI** »

« **Vibration Analysis and Reduction of Cable-Driven Parallel Robots** »

Thèse présentée et soutenue à « Rennes », le « 11/12/2018 »

Unité de recherche : LGCGM - EA 3913

Thèse N° : 18ISAR 35 / D18 - 35

## Rapporteurs avant soutenance :

**Edouard LAROCHE**

Professeur des Universités, iCube - Université de Strasbourg

**Marc GOUTTEFARDE**

Directeur de Recherche CNRS, LIRMM, Montpellier

## Composition du Jury :

**Jean-Pierre MERLET**

Directeur de Recherche, INRIA Sophia Antipolis / Président

**Edouard LAROCHE**

Professeur des Universités, iCube - Université de Strasbourg /  
Rapporteur

**Marc GOUTTEFARDE**

Directeur de Recherche CNRS, LIRMM, Montpellier / Rapporteur

**Hélène PIET-LAHANIER**

Chercheur Adjointe Scientifique HDR, ONERA DTIS, Palaiseau /  
Examinatrice

Directeur de thèse

**Éric RAGNEAU**

Professeur des Universités, INSA Rennes

Co-encadrants de thèse

**Éric COURTEILLE**

Maître de Conférences HDR, INSA Rennes

**Stéphane CARO**

Directeur de recherche CNRS, LS2N, Nantes



Intitulé de la thèse :

## Vibration Analysis and Reduction of Cable-Driven Parallel Robots

**Sana BAKLOUTI**

En partenariat avec :





# Acknowledgments

During the preparation of my PhD thesis, I had to take the help and guidance of some respected persons, who deserve my deepest gratitude. I would like to thank my thesis director, Mr. **Eric RAGNEAU**, for having me in his team.

To achieve the target of a thesis work, to put it into shape and to publish, requires regular supervision. Advice, ideas, long discussions and experienced feedback are necessary to progress. I would like to show my sincere gratitude to my supervisors, Mr. **Eric COURTEILLE** and Mr. **Stéphane CARO**, for their guidance and effort they have given me throughout my thesis. Your precious ideas guided me in my hesitation, and your scientific rigor allowed to carry out this work. I have great pleasure working with you, and wish you a lot of success in your future research! A big thank you for these three years very rich in lessons. I hope to have the chance to continue working with you in the future.

I extend a big thank you to Mr. **Philippe LEMOINE**, the LS2N engineer, who helped me in my experimentations. I really enjoyed our many exchanges!

I would like to thank my reporters, Mr. **Edouard LAROCHE** and Mr. **Marc GOUTTEFARDE**, who took the time to evaluate my work carefully. I also thank my examiners, Mrs. **Hélène PIET-LAHANIER** and Mr. **Jean-Pierre MERLET**, for their attention to my work. I enjoyed our discussions and your constructive comments.

Furthermore, I would also like to thank **my parents** for their endless love and support. You are proud to have a doctor daughter and I am proud to have you parents. I love you!

My gratitude goes to **my fiancé** who never stopped encouraging me and helping me enrich my technical background. I know I could always count on you... Thank you!

I would like to expand my gratitude to all those who have directly and indirectly supported me.



# Abstract

This thesis aims at improving the static positioning and trajectory tracking accuracy of Cable-Driven Parallel Robots (CDPRs) while considering their overall elasticity. Accordingly, two complementary control strategies that are valid for any CDPR configuration are proposed.

First, a robustness analysis is performed to lead to a robust model-based control of CDPRs. As a result, an appropriate CDPR model is defined as a function of the targeted application and the main sources of CDPR moving-platforms pose errors are identified.

A first control method is determined based on the results of the robustness analysis. This first method lies in the coupling of a model-based feed-forward control scheme for CDPR with a PID feedback controller. An elasto-dynamic model of the CDPR is expressed in order to compensate the oscillatory motions of its moving-platform due to cable elongations and its dynamic behavior. The second control method uses input-shaping filters into the proposed model-based feed-forward control in order to cancel the oscillatory motions the moving-platform. Thus, the input signal is modified to make the CDPR self-cancel residual vibrations.

Experimental validations are performed while using a suspended and non-redundant CDPR prototype. The proposed feed-forward model-based control schemes are implemented and their effectiveness is discussed. Results show the relevance of the proposed control strategies in terms of trajectory tracking accuracy improvement and vibration reduction.



# Résumé

Cette thèse vise à améliorer le positionnement statique et la précision de suivi de trajectoire des Robots Parallèles à Câbles (RPC) tout en prenant en compte leur élasticité globale. A cet effet, deux stratégies de commandes complémentaires valables pour toute configuration de RPC sont proposées.

Tout d'abord, une analyse de robustesse est réalisée pour aboutir à une commande robuste des RPC référencée modèle. Un modèle de RPC approprié est défini en fonction de l'application visée et les principales sources d'erreurs de pose de la plate-forme mobile sont identifiées.

Une première méthode de commande est proposée sur la base des résultats de l'analyse de robustesse. Cette première méthode réside dans le couplage d'une commande référencée modèle avec un contrôleur PID. Dans le cadre de cette thèse, un modèle élasto-dynamique de RPC est exprimé afin de compenser le comportement oscillatoire de sa plate-forme mobile dû à l'élongation des câbles et de son comportement dynamique. La deuxième méthode de commande utilise des filtres "input-shaping" dans la commande référencée modèle proposée afin d'annuler les mouvements oscillatoires de la plate-forme mobile. Ainsi, le signal d'entrée est modifié pour que le RPC annule automatiquement les vibrations résiduelles.

Les résultats théoriques obtenus sont validés expérimentalement à l'aide d'un prototype de RPC non redondant en actionnement et en configuration suspendue. Les résultats expérimentaux montrent la pertinence des stratégies de commande proposées en termes d'amélioration de la précision de suivi de trajectoire et de réduction des vibrations.



# Table of contents

<b>I Cable-Driven Parallel Robots</b>	<b>29</b>
I.1 Cable-Driven Parallel Robots	29
I.1.1 Redundant and non-redundant CDPRs	32
I.1.1.1 Non-redundant CDPR	32
I.1.1.2 Redundant CDPR	33
I.1.2 Suspended and fully-constrained CDPRs	34
I.1.2.1 Fully-constrained configuration	34
I.1.2.2 Suspended configuration	34
I.1.3 Applications	35
I.1.3.1 Production engineering	35
I.1.3.2 Logistics	35
I.1.3.3 Rescue and Rehabilitation	36
I.1.3.4 Acquisition	37
I.1.3.5 Construction	38
I.1.3.6 Entertainment	38
I.2 Pose accuracy	39
I.2.1 Modeling	39

---

I.2.2	Error sources affecting accuracy ·····	40
I.2.3	Control for accuracy improvement ·····	43
I.3	Objectives and contributions ·····	46
I.3.1	Contribution on CDPR modeling ·····	47
I.3.2	Static and dynamic robustness analysis ·····	47
I.3.3	Control for CDPR accuracy improvement ·····	49
<b>II</b>	<b>CDPR models and properties</b>	<b>51</b>
II.1	Introduction ·····	51
II.2	Rigid dynamic model ·····	52
II.2.1	Dynamics of actuators ·····	55
II.2.2	Complete dynamic model ·····	56
II.2.3	Determination of the cable tensions ·····	57
II.3	Dynamic modeling considering cable stiffness : Elasto-static model ·····	59
II.3.1	Cable stiffness modeling ·····	60
II.3.1.1	Sag-introduced stiffness ·····	60
II.3.1.2	Axial stiffness ·····	62
II.3.2	Linear and non-linear cable tension models ·····	62
II.3.2.1	Non-linear tension of cables with linear damper ·····	64
II.4	Elasto-dynamic modeling ·····	66
II.5	Summary of the chapter ·····	68
<b>III</b>	<b>Robustness analysis of CDPR</b>	<b>71</b>
III.1	Introduction ·····	71
III.2	Error sources affecting CDPR accuracy ·····	72
III.2.1	Modeling ·····	72
III.2.2	Parameters ·····	72
III.2.2.1	Geometrical parameters ·····	72
III.2.2.1.1	Base frame geometrical errors ·····	73
III.2.2.1.2	Moving-platform geometrical errors ·····	73
III.2.2.2	Mechanical parameters ·····	74
III.2.2.2.1	End-effector mass ·····	74
III.2.2.2.2	Cables parameters ·····	74
III.2.2.2.2.1	Linear mass ·····	74
III.2.2.2.2.2	Modulus of elasticity ·····	74

---

III.2.2.2.3 Tension distribution ·····	76
III.3 Sensitivity analysis of CDPR accuracy to modeling ·····	77
III.3.1 Linear and non-linear cable tension models ·····	77
III.3.1.1 Illustrative example ·····	78
III.3.1.2 Semi-industrial examples ·····	82
III.3.2 Sensitivity of CDPR dynamic behavior to the modeling type ·····	85
III.4 Uncertainty analysis of CDPR to parameters ·····	89
III.4.1 Dynamic uncertainty analysis ·····	89
III.4.1.1 Dynamic stiffening ·····	89
III.4.1.2 Axial cable damping ·····	93
III.4.2 Static uncertainty analysis ·····	95
III.4.2.1 Static deflection ·····	96
III.4.2.2 Uncertainty range of parameters ·····	97
III.4.2.3 Uncertainty analysis with unknown tension set-point ·····	99
III.4.2.3.1 Analysis of the elasticity modulus over the workspace ·····	101
III.4.2.4 Uncertainty analysis with known tension set-point ·····	102
III.4.2.4.1 Analysis of the natural frequency over the workspace ·····	104
III.5 Summary of the chapter ·····	105
<b>IV CDPR control for accuracy improvement</b>	<b>107</b>
IV.1 Introduction ·····	107
IV.2 Feed-forward model-based control ·····	108
IV.2.1 Discrete-time control of CDPR ·····	110
IV.2.1.1 Actuation system ·····	110
IV.2.1.2 Feedback control loop ·····	111
IV.2.1.3 Feed-forward control loop ·····	111
IV.2.2 Pre-compensation ·····	112
IV.2.2.1 Rigid pre-compensation ·····	113
IV.2.2.2 Elasto-static pre-compensation ·····	114
IV.2.2.3 Elasto-dynamic pre-compensation ·····	114
IV.2.3 Controller tuning ·····	115
IV.2.4 Numerical results ·····	116
IV.2.4.1 Trajectory generation ·····	118

---

IV.2.4.2	Trajectory tracking	118
IV.2.4.2.1	Transitional phase	120
IV.2.4.2.2	Steady-state phase	121
IV.2.5	Experimental results	124
IV.2.5.1	Test bench	125
IV.2.5.2	Experimental setup	130
IV.2.5.3	Static analysis	131
IV.2.5.4	Trajectory tracking	132
IV.2.5.4.1	Transitional phase	134
IV.2.5.4.2	Steady-state phase	136
IV.3	Input-shaping for feed-forward control	<b>139</b>
IV.3.1	Single mode Input-shaping control	142
IV.3.1.1	Zero-Vibration input-shaper	143
IV.3.1.2	Zero-Vibration-Derivative input-shaper	143
IV.3.1.3	Robustness to modeling errors	143
IV.3.2	Multi-mode input-shaping control	145
IV.3.3	Experimental results	145
IV.3.3.1	Trajectory generation	145
IV.3.3.2	Input-shaping	146
IV.4	Summary of the chapter	<b>150</b>
<b>V</b>	<b>Conclusions and Future Work</b>	<b>153</b>
V.1	Conclusions	<b>153</b>
V.1.1	Contribution on CDPR dynamic modeling	154
V.1.2	Robustness analysis	155
V.1.3	Control for CDPR accuracy improvement	156
V.2	Future Work	<b>156</b>
<b>A</b>	<b>Cable identification : Modulus of elasticity</b>	<b>161</b>
A.1	Steel Cable	<b>161</b>
A.1.1	Modulus of elasticity	161
A.1.2	Dynamic modulus of elasticity	164
A.2	Polyethylene Cable	<b>167</b>

---

<b>B Example prototypes</b>	<b>169</b>
B.1 CAROCA	169
B.1.1 Redundant configuration	169
B.1.2 Non-redundant configuration	169
B.2 FAST	170
B.3 CREATOR prototype	171
<b>C Complement for modeling</b>	<b>175</b>
C.1 Euler angles convention	175
C.1.1 Angular velocity	176
C.2 Elasto-dynamic model resolution	177
<b>Bibliography</b>	<b>179</b>



## List of figures

I.1 (a) SurgiScope in action at the Surgical Robotics Lab, Humboldt-University at Berlin (b) Demaurex’s Line-Placer installation for the packaging of pretzels in an industrial bakery . . . . .	<b>30</b>
I.2 CDPR composition : CREATOR prototype (Courtesy of LS2N, Nantes, France)	<b>30</b>
I.3 Schematics of (a) Redundant, (b) Non-redundant CDPR . . . . .	<b>32</b>
I.4 Schematics of (a) Suspended, (b) Fully-constrained CDPR . . . . .	<b>34</b>
I.5 Cable robot IPAnema 2 : (a) Vision of assembly of parabolic reflector panels [PMV10] (b) Large-scale handling of collector modules shown at Automatica 2010 trade fair, Munich, Germany [Pot18a] . . . . .	<b>36</b>
I.6 The cable robots of the Marionet family : Courtesy of INRIA Sophia-Antipolis, France . . . . .	<b>37</b>
I.7 The cable robot String-Man : Courtesy of Fraunhofer IPK, Berlin . . . . .	<b>37</b>
I.8 Cogiro, Pylos and the high print being processed [IDH <sup>+</sup> 18] . . . . .	<b>38</b>
I.9 (a) Concept for a thrill ride with winches moving along a track (b) Two large-scale cable robots are core elements of the show at the German pavilion on the Expo 2015 fair in Milan, 2015 [TSPE15, Pot18b]. . . . .	<b>39</b>
I.10 General control scheme for CDPR . . . . .	<b>43</b>

I.11	The input shaping process	46
I.12	CAROCA prototype : a reconfigurable CDPR (Courtesy of IRT Jules Verne, Nantes)	48
II.1	The $i$ th closed-loop of a CDPR	52
II.2	Graphical representation of sign versus hyperbolic tangent	57
II.3	Schematic of the CDPR rigid model : Planar example	59
II.4	Schematic of the CDPR elasto-geometric model with straight cables : Planar example	60
II.5	Schematic of elasto-sagging cable	61
II.6	Hysteresis loops for a 4 mm steel wire cable preloaded at 1500 N with force controlled sine waves applied at 0.1, 1, 2, 5, 10, and 20 Hz	65
II.7	Schematic of the CDPR elasto-dynamic model : Planar example	66
II.8	Cable parametrization while considering dead length	68
III.1	Error sources affecting CDPR accuracy	73
III.2	Load-elongation diagram of a steel wire cable measured in steady state conditions at the rate of 0.05 mm/s	75
III.3	Circular helical trajectory : (a) Trajectory and (b) velocities of the end-effector	79
III.4	Cable linear velocity profiles	79
III.5	Comparison between linear and non-linear tension formulations : Tension, elongation and strain for three cables. Time history of (a) $\tau_1$ , (b) $\delta l_1$ , (c) $s_1$ , (d) $\tau_2$ , (e) $\delta l_2$ , (f) $s_2$ , (g) $\tau_3$ , (h) $\delta l_3$ , and (i) $s_3$	81
III.6	Comparison between linear and non-linear tension formulations : Positioning error of the end-effector along (a) $x$ -axis, (b) $y$ -axis and (c) $z$ -axis	82
III.7	Schematics of the (a) CAROCA and (b) FAST CDPR	83
III.8	Comparison between linear and non-linear tension formulations with respect to CDPR overall size. Time history of (a) $\tau_2$ : CAROCA, (b) $\delta l_2$ : CAROCA, (c) $s_2$ : CAROCA (d) $\tau_2$ : FAST, (e) $\delta l_2$ : FAST and (f) $s_2$ : FAST	83
III.9	Positioning errors of the CDPR end-effector calculated with a linear and a non-linear cable tension model, respectively : (a) CAROCA (b) FAST	84
III.10	(a) Desired position (b) velocity and (c) acceleration of the moving-platform	86
III.11	Comparison between the cable responses while using different CDPR models : Time history of (a) $\tau_1$ , (b) $\tau_3$ , (c) $\delta l_1$ and (d) $\delta l_3$	87
III.12	Comparison between the different dynamic CDPR models : Time history of (a) the deviation $\delta z$ of the end-effector position along $z$ -axis and (f) Zoom in $\delta z$	88

III.13	Trapezoidal-velocity trajectory : (a) Trapezoidal actuation velocities (b) Trajectory of the end-effector	89
III.14	Comparison between cables responses while using static or dynamic modulus : Time history of (a) $\tau_1$ , (b) $\delta l_1$ , (c) $s_1$ , (d) $\tau_2$ , (e) $\delta l_2$ , (f) $s_2$ , (g) $\tau_3$ , (h) $\delta l_3$ and (j) $s_3$	91
III.15	Comparison between the CDPR responses while using static or dynamic modulus : Time history of positioning error along (a) $x$ -axis, (b) $y$ -axis and (c) $z$ -axis	92
III.16	Comparison between the CDPR natural frequencies while using static or dynamic modulus (2 Hz) : Time history of natural frequencies (a) $f_1$ , (b) $f_2$ and (c) $f_3$	93
III.17	Comparison between dynamic responses of the CAROCA while using quasi-static or dynamic modulus (10 Hz) : Time history of (a) $\tau_2$ , (b) $\delta l_2$ , (c) $s_2$ , Positioning error (d) along $x$ -axis, (e) along $y$ -axis, (f) along $z$ -axis, natural frequencies (g) $f_1$ , (h) $f_2$ and (i) $f_3$	94
III.18	Comparison between cables responses with and without damping : Time history of (a) $\tau_1$ , (b) $\delta l_1$ , (c) $s_1$ , (d) $\tau_2$ , (e) $\delta l_2$ , (f) $s_2$ , (g) $\tau_3$ , (h) $\delta l_3$ and (j) $s_3$	95
III.19	Comparison the CDPR responses while using tension model with or without damping : Time history of positioning error along (a) $x$ -axis, (b) $y$ -axis and (c) $z$ -axis	96
III.20	(a) Distribution of the RMS of the moving-platform static deflection, Evolution of the RMS under a simultaneous variations of (b) $E$ and $\rho$ (c) $m$ and $\rho$	100
III.21	Variation of the static deflection norm considering uncertainty on the modulus of elasticity over the sub-workspace ( $-1.5 < x < 1.5$ m, $-1.5 < y < 1.5$ m and $z = 1$ m)	101
III.22	(a) Distribution of the RMS of the moving-platform static deflection (b) Effect of uncertainties in $\mathbf{a}_i$ (c) Effect of uncertainties in $\mathbf{b}_i$	103
III.23	Variation in the end-effector natural frequencies $f_1$ , $f_2$ and $f_3$ over a sub-workspace ( $-1.5 < x < 1.5$ m, $-1.5 < y < 1.5$ m and $z = 1$ m)	104
III.24	Increasing priority of identification of uncertain parameters	106
IV.1	Feed-forward model-based PID control	109
IV.2	Equivalent control scheme : Discrete-time control	111
IV.3	Model-based pre-compensation	112
IV.4	Pre-compensation : illustrative example	113
IV.5	(a) CREATOR prototype CAD diagram (b) End-effector desired path in $\mathcal{F}_b$	117
IV.6	Desired (a) Position (b) Velocity and (c) Acceleration profiles of the end-effector	119

---

IV.7 (a) Position error of the end-effector along the $z$ -axis (b) 2-norm of the end-effector Cartesian trajectory tracking error vector	120
IV.8 Position error norm during the transitional phase	121
IV.9 Illustrative example : Peak-to-Peak amplitudes	122
IV.10 Position error norm during the steady-state phase	122
IV.11 Histogram of the first and fifth Peak-to-Peak amplitude of $\ \delta\mathbf{p}\ $ during the steady-state phase	123
IV.12 Histogram of Decrement of the Peak-to-Peak amplitudes of $\ \delta\mathbf{p}\ $ during the steady-state phase	124
IV.13 Equivalent architecture of the CREATOR prototype	126
IV.14 Determination of the static friction	126
IV.15 3D-printed pulleys used for the CREATOR prototype	127
IV.16 End-effector and laser tracker target	128
IV.17 CAD modeling and manufacturing drawings of the end-effector	128
IV.18 Base frame $\mathcal{F}_b$ of the CREATOR prototype	129
IV.19 Experimental setup : (a) Non-suspended, (b) Suspended initial pose of the end-effector	130
IV.20 Experimental results : Current set-points (a) $i_m^1$ , (b) $i_m^2$ and (c) $i_m^3$	133
IV.21 Experimental results : (a) Position error along $z$ -axis of the end-effector (b) Position error norm	134
IV.22 Experimental results : Trajectory tracking error norm during the transitional phase	135
IV.23 Experimental results : Positioning improvement with respect to rigid control at time $t = 3$ s.	135
IV.24 Experimental results : Position error norm during the steady-state phase	136
IV.25 Experimental results : Histogram of the first and fifth Peak-to-Peak amplitudes of $\ \delta\mathbf{p}\ $ during the steady-state phase	136
IV.26 First Peak-to-Peak amplitudes of $\ \delta\mathbf{p}\ $ : Comparison of numerical and experimental results	137
IV.27 Experimental results : Decrement of the Peak-to-Peak amplitudes of $\ \delta\mathbf{p}\ $ during the steady-state phase	138
IV.28 Vibration improvement of the elasto-dynamic control with respect to rigid control during the steady-state phase	139
IV.29 Block diagram for closed-loop input-shaping control scheme	140
IV.30 Sensitivity curves of ZV and ZVD input-shapers	144

---

IV.31	Nominal (a) position (b) velocity (c) acceleration profiles of the moving-platform	<b>147</b>
IV.32	Determinant of the global stiffness matrix along the nominal trajectory of the moving-platform	<b>148</b>
IV.33	(a) Moving-platform Velocity error with and without input-shaping (b) Zoom on the moving-platform velocity error with and without input-shaping	<b>149</b>
IV.34	Bar chart of the first period Peak-to-Peak amplitude of $\delta\dot{z}$	<b>150</b>
A.1	Tema Concept cyclic loading test bench	<b>162</b>
A.2	Cross section of a rotation-resistant steel wire cable; Carl Stahl Technocables Ref 1692	<b>162</b>
A.3	Load-elongation diagram of a steel wire cable measured in steady state conditions at the rate of 0.05 mm/s	<b>163</b>
A.4	Hysteresis loops for a 4 mm steel wire cable preloaded at 1500 N with force controlled sine waves applied at 0.1, 1, 2, 5, 10, and 20 Hz	<b>165</b>
A.5	Polyethylene Cable used for the CREATOR prototype	<b>167</b>
A.6	Elongation-load diagram of a polyethylene cable	<b>168</b>
B.1	CAROCA prototype, Courtesy of IRT Jules Verne, Nantes	<b>170</b>
B.2	CAROCA schematic (a) in a symmetric position (b) in a non-symmetric position	<b>171</b>
B.3	CREATOR prototype : Courtesy of LS2N, Nantes, France	<b>172</b>
B.4	RADIAN Laser tracker	<b>173</b>
C.1	Representation of the successive rotations of the Euler X-Y-Z convention	<b>176</b>
C.2	Elasto-dynamic model resolution method	<b>177</b>



# List of tables

1 Abbreviations	15
2 Notations	15
3 Notations	16
III.1 Modulus of elasticity while loading or unloading phase	75
III.2 Nominal values, uncertainty ranges and discretization step of uncertain parameters	98
IV.1 Characteristics of the CREATOR actuators	117
IV.2 $K_p$ , $K_d$ and $K_i$ gains of the PID controller	117
IV.3 Experimental data : Static deflection of the end-effector before compensation	132
A.1 Frequency dependency of the modulus of elasticity of the steel wire cable at loading frequencies between 0.1 and 20 Hz	166
B.1 Redundant CAROCA prototype : Cartesian coordinates of anchor points $A_i$ (exit points $B_i$ , resp.) expressed in $\mathcal{F}_p$ (in $\mathcal{F}_b$ , resp.)	170
B.2 Non-redundant CAROCA : Cartesian coordinates of anchor points $A_i$ (exit points $B_i$ , resp.) expressed in $\mathcal{F}_p$ (in $\mathcal{F}_b$ , resp.)	171

B.3 Non-redundant FAST : Cartesian coordinates of anchor points $A_i$ (exit points $B_i$ , resp.) expressed in $\mathcal{F}_p$ (in $\mathcal{F}_b$ , resp.)	171
B.4 Characteristics of CAROCA and FAST CDPRs	172
B.5 Measured Cartesian coordinates of exit points $B_i$ in $\mathcal{F}_b$	173

# Notations

Table 1 – Abbreviations

Abbreviation	Signification
CDPR	Cable-Driven Parallel Robot
PM	Parallel Manipulator
EE	End-effector
DOF	Degree-Of-Freedom
DOR	Degree-Of-Redundancy
DGM	Direct geometric model
IGM	Inverse geometric model
DKM	Direct kinematic model
IKM	Inverse kinematic model
DESM	Direct elasto-static model
IESM	Inverse elasto-static model

Table 2 – Notations

Symbol	Use
$\mathcal{F}_b$	The base frame
$\mathcal{F}_p$	The end-effector frame
$\mathcal{F}_i$	The $i$ th cable frame
$A_i$	$i$ th anchor point
$B_i$	$i$ th exit point
$\mathbf{a}_i$	Cartesian coordinate vector of $A_i$
$\mathbf{b}_i$	Cartesian coordinate vector of $B_i$
$\mathbf{x}$	Vector defining the pose of the end-effector
$\mathbf{p}$	Vector defining the position of the end-effector
$\mathbf{o}$	Vector defining the orientation of the end-effector
$\mathbf{q}$	Vector defining the articular variables
$\dot{\mathbf{x}}$	Vector defining the twist of the end-effector
$\mathbf{dp}$	Vector defining the static deflection of the end-effector
$\chi$	Vector defining the winch winding ratios
$\mathbf{w}$	Vector defining the wrench applied to the end-effector
${}^b\mathbf{R}_p$	Rotation matrix of the end-effector
$\mathbf{M}$	Mass matrix of the end-effector
$\mathbf{C}$	Centrifugal matrix
$\mathbf{W}$	Wrench matrix

Table 3 – Notations

Symbol	Use
$m$	Total DOF of the end-effector
$n$	Number of cables
$u$	Number of translational degrees-of-freedom
$v$	Number of rotational degrees-of-freedom
$m_{ee}$	Mass of the end-effector
$g$	acceleration due to gravity
$S$	Cable cross sectional area
$E$	Cable modulus of elasticit
$l_i$	Length of the $i$ th cable
$\delta l_i$	Elongation of the $i$ th cable
$\rho_i$	Linear mass of the $i$ th cable
$\tau_i$	Tension on the $i$ th cable
$\zeta_i$	Torque on the $i$ th motor
$t$	Time
$f$	Temporal frequency
$I_{motor}$	Inertia of the motor with brakes in its entry
$I_{reducer}$	Inertia of the reducer
$r$	Transmission ratio of the reducer
$I_m$	Total inertia of the motor brought to its exit
$\varpi$	Resistance of the motor armature
$k_e$	Motor counter-electromotive force coefficient
$k_t$	Electromagnetic torque coefficient of the motor

# General introduction

Cable-Driven Parallel Robots (CDPRs) are part of the large group of multi-body systems. They are a special kind of parallel robots, where rigid links are replaced by cables. A CDPR is decomposed into a moving-platform connected to a fixed base frame through cables. The variation of cable lengths is provided by fixed motors and winches, leading to the end-effector motion. In contrast to rigid links, cable lengths can vary in a wide range, which increases the CDPR workspace. Thus, CDPRs may be used in some application fields where industrial robots cannot be used due to limitation of their workspace, payload and the required cycle time. In the past few decades, these specifications have attracted the interest of many researchers [[ABAV11](#), [DGA<sup>+</sup>12](#), [Mer14](#), [NGP<sup>+</sup>14](#), [MLB<sup>+</sup>16](#), [YCGH17](#), [Mer18](#), [IDH<sup>+</sup>18](#)].

Thanks to their low inertia, CDPRs can reach high velocities and accelerations in large workspaces [[LGCH13](#)]. However, vibrations may occur and pose stabilization and/or trajectory tracking of the end-effector can be degraded due to cable elasticity. Considering the physical cable characteristics, the cable elasticity has mainly two origins. The first one is the axial stiffness of the cables, which is associated with the elastic material modulus and the cable structure. The second is the sag-introduced flexibility, which comes from the effect of cable weight onto the static cable profile. The sag-introduced flexibility corresponds to the gravitational potential energy stored in the cable. The improvement of the robot performances can be done through the modification of the robot structure either by optimizing the design [[ADG<sup>+</sup>09](#), [XCCJ10](#), [GCG<sup>+</sup>14](#), [YTWH10](#)] or by adding other components to the robot structure as in [[VP15](#), [WCG14](#)]. Improving accuracy is still possible once the robot is in operation through a suitable control scheme.

Several controllers have been proposed in the literature to improve CDPR accuracy locally or on trajectory tracking [[JFGK15](#), [FFT<sup>+</sup>04](#), [ZDDB08](#), [dRRK18](#)].

The dynamic control for CDPRs depends on the stiffness consideration. Some research works deal with CDPR control while considering cable elongations and their effect onto the CDPR dynamic behavior [KT11, KT14, KT16]. However, those approaches require cable length measurement and the knowledge of the moving-platform pose in real-time through exteroceptive measurements for instance.

Other works [CLP18, BLS<sup>+</sup>13] propose model-based feed-forward control for CDPRs. Despite cable stiffness is considered in these control schemes, a limitation lies in the cable interactions with the overall system that are not considered. Besides, cable elongations are estimated while isolating cables from the end-effector. This control type named *elasto-static control* in this thesis manuscript. Note that the latter does not pre-compensate the oscillatory motions of the CDPR moving-platform. In real applications of CDPRs, cable elongations and their interaction with the environment are not independent. This fact can result in unwanted oscillations of the end-effector, which are not predicted through the elasto-static model. Therefore, an **elasto-dynamic model** is proposed to deal with the prediction of the dynamic behavior of the CDPR while taking into account the oscillatory and dynamic behavior of the end-effector due to cable elongations. Here, cables are no-longer isolated and are affected by the end-effector dynamic behavior.

As a consequence, a contribution of this thesis deals with a *first control method*, which lies in the coupling of a **model-based feed-forward control** scheme for CDPR with a PID feedback controller. Here, the elasto-dynamic model of the CDPR is used in order to compensate the oscillatory motions of its moving-platform due to cable elongations and its dynamic behavior. The integration of cable tension calculation or tension distribution algorithms [GG11, Pot14, GLRB15, YCD16, RLMGC18b] is proposed to be part of this control strategy to deal with the different configurations of CDPRs and to guarantee positive cable tensions along the trajectory.

A second contribution of this thesis deals with a *second control method*, which uses **input-shaping** filters into the proposed model-based feed-forward control in order to cancel the oscillatory motions the moving-platform. Thus, the input signal is modified for the CDPR to self-cancel residual vibrations. The amplitudes and time locations of the impulses are based on the robot natural frequen-

cies and damping ratios. The shaped command resulting from the convolution is used to drive the robot and it will stimulate less residual vibrations than the unshaped one. Previous works integrated this method for under-constrained robots [HBY<sup>+</sup>16, BFV16, LL16, MV17, PKP13]. Despite the fact that the research work in [YHB<sup>+</sup>16] deals with over-constrained CDPRs, this control does not allow to manage the actuation redundancy and positive cable tensions are not guaranteed. Accordingly, Section IV.3 proposes input-shaping for model-based feed-forward control to increase the CDPR performance by vanishing residual vibrations of the manipulator. The novelty of this control scheme lies in the integration of input-shaping filters to the closed-loop model-based control scheme, where the presence of tension distribution makes it valid for any CDPR configuration.

The parameters used in the proposed CDPR control models are subjected to uncertainties. The mathematical models do not perfectly reflect the robot behavior because of uncertainties such as the assembly and manufacturing inaccuracies of geometrical components like pulleys [MP10, Pot12]. Moreover, these models are influenced by non-geometrical origin uncertainties. These latter are attributed to the quality of mechanical components of the robot manipulator, such as cables and their interactions with the complete system.

A **robustness analysis** is performed through sensitivity and uncertainty analysis to lead to a robust model-based control of CDPRs. As a result, an appropriate CDPR model is defined as a function of the targeted application and the main sources of CDPR moving-platform pose errors are identified.

This manuscript is organized into five chapters :

In **Chapter I**, the state-of-art in CDPRs is studied. After emphasizing the configurations, applications and importance of CDPRs, the problematic and current research works on the CDPR static and dynamic accuracy are discussed.

In **Chapter II**, the dynamic modeling of CDPRs is introduced. Different dynamic models of CDPRs used for feed-forward control are reviewed and the **elasto-dynamic model** is presented. As the choice of cable models is a primary task for CDPR modeling, the different levels of cable stiffness used for dynamic modeling

are also discussed in Section II.3. Usually, the dynamic stiffness analysis of CDPRs is made under the assumption that dynamic loads induce only small elongations of the cables. The cable tension is usually considered proportional to the variations in the cable length for a constant stiffness coefficient. Therefore, such a model is not valid when cables are subjected to high strains due to large dynamic oscillations or quick cable-length variations. As a consequence, a new **non-linear cable tension model** is proposed in Section II.3.2 to express the dynamic and oscillatory motions of CDPRs with cables subjected to fast varying lengths. This formulation reveals a softening behavior when strains become large.

**Chapter III** lists the different mechanical and geometrical error sources and investigates their effects onto the trajectory tracking accuracy. **Sensitivity analysis** is made through a comparison between the conventional dynamic models and the proposed elasto-dynamic model of CDPR. A weakness of the conventional models used for model-based control is that they neglect the dynamic effects due to cable interactions with the whole system. The elasto-dynamic model tries to remedy this weakness by anticipating the oscillatory behavior of CDPR while the moving-platform tracks a trajectory. Such a model is useful for control purposes as it predicts not only the cable elongations but also their dynamic interaction with the moving-platform.

In addition, an **uncertainty analysis** is performed to test the robustness of CDPR model to variations in parameters into a known range. It is useful for the reduction of uncertainty, through the identification of model inputs that cause significant uncertainty and should therefore be the focus of attention. It appears from this analysis that the effect of the modulus of elasticity of cables is the highest onto the dynamic and oscillatory motions of the moving-platform. For this purpose, the experimental method named **Dynamic Mechanical Analysis** (DMA) is proposed to identify carefully the dynamic elastic and damping moduli of some cables to better compensate the stiffness effects leading to pose errors and trajectory tracking degradation.

**Chapter IV** deals with the implementation of two complementary feed-forward model-based control strategies, which aim to improve the end-effector trajectory tracking and reduce vibrations due to overall elasticity.

Section IV.2 deals with the introduction of the proposed **elasto-dynamic feed-forward control** and the establishment of the corresponding control laws. To check the effectiveness of this control, a numerical comparison of the end-effector trajectory tracking with respect to the classical feed-forward control schemes is made. Moreover, experimentations are performed on the CREATOR prototype located at LS2N, Nantes, France ; a CDPR with three cables and three Degree-Of-Freedom. The experimental tests confirm the numerical results.

In addition, Section IV.3 deals with the integration of **input-shaping** filters into the proposed model-based feed-forward control. These filters are integrated upstream of the pre-compensation block in order to increase the CDPR performances by the improvement of residual vibrations attenuation. Experimental tests are made on the CREATOR prototype to verify the ability of the control scheme to vanish residual vibrations of the manipulator.

A general conclusion is written in **Chapter V** on the research work carried out in the framework of this doctorate thesis. Additionally, an overview of topics for future research works is given to enhance CDPRs controllability and accuracy.



# Introduction générale

Les Robots Parallèles à Câbles (RPC) constituent un type particulier de robots parallèles, dans lesquels les segments rigides sont remplacés par des câbles. Un RPC est décomposé en une plate-forme mobile reliée à un bâti fixe par des câbles. La variation de la longueur des câbles est assurée par des moteurs fixes et des treuils, entraînant le mouvement de l'effecteur final. Contrairement aux segments rigides, les longueurs de câble peuvent varier dans une large plage, ce qui augmente l'espace de travail de RPC. Ainsi, les RPCs peuvent être utilisés dans certains domaines d'application où les robots industriels ne peuvent pas être utilisés en raison de la limitation de leur espace de travail, de leur charge utile et du temps de cycle requis. Au cours des dernières décennies, ces spécifications ont suscité l'intérêt de nombreux chercheurs [[ABAV11](#), [DGA<sup>+</sup>12](#), [Mer14](#), [NGP<sup>+</sup>14](#), [MLB<sup>+</sup>16](#), [YCGH17](#), [Mer18](#), [IDH<sup>+</sup>18](#)].

Grâce à leur faible inertie, les RPCs peuvent atteindre des vitesses et des accélérations élevées dans les grands espaces de travail [[LGCH13](#)]. Cependant, des vibrations peuvent se produire et la stabilisation de la pose et / ou le suivi de trajectoire de l'effecteur peuvent être dégradés à cause de l'élasticité du câble. Compte tenu des caractéristiques physiques du câble, son élasticité a principalement deux origines. Le premier est la rigidité axiale des câbles, qui est associée au module élastique de matériau et à la structure du câble. La seconde est la flexibilité introduite par l'affaissement, qui provient de l'effet du poids du câble sur le profil du câble statique. La flexibilité introduite par l'affaissement correspond à l'énergie potentielle gravitationnelle stockée dans le câble. L'amélioration des performances du robot peut être réalisée par la modification de la structure du robot, soit en optimisant la conception [[ADG<sup>+</sup>09](#), [XCCJ10](#), [GCG<sup>+</sup>14](#), [YTWH10](#)], soit en ajoutant d'autres composants à la structure du robot [[VP15](#), [WCG14](#)]. Il est encore possible d'améliorer la précision tant que le RPC est opérationnel par une commande ap-

propriée.

Plusieurs contrôleurs ont été proposés dans la littérature pour améliorer la précision des RPCs localement ou sur le suivi de trajectoire [JFGK15, FFT<sup>+</sup>04, ZDDB08, dRRK18]. La commande dynamique des RPCs dépend de la rigidité à prendre en compte. Certaines recherches traitent la commande de RPC en tenant compte de l'élongation des câbles et de leurs effets sur le comportement dynamique du robot [KT11, KT14, KT16]. Cependant, ces approches nécessitent une mesure de la longueur de câble et la connaissance de la plate-forme mobile en temps réel à travers des mesures extéroceptives.

D'autres travaux [CLP18, BLS<sup>+</sup>13] proposent une commande référencée modèle pour les RPCs. Bien que la rigidité des câbles soit prise en compte dans ces schémas de commande, une limitation réside dans les interactions des câbles avec le système global qui ne sont pas prises en compte. En outre, les allongements de câble sont estimés tout en isolant les câbles de la plate-forme mobile. Ce type de commande est nommé commande *élasto-statique* dans ce manuscrit de thèse. Notez que ce dernier ne pré-compense pas le comportement oscillatoire de la plate-forme mobile de RPC. Dans les applications réelles des RPCs, les élongations de câbles et leurs interactions avec l'environnement ne sont pas indépendantes. Cela peut entraîner des oscillations non souhaitées de la plate-forme mobile, qui ne sont pas prédites par le modèle élasto-statique. Par conséquent, un **modèle elasto-dynamic** est proposé pour traiter la prédiction du comportement dynamique du RPC tout en tenant compte du comportement oscillatoire et dynamique de l'effecteur final dû aux allongements de câble. Ici, les câbles ne sont plus isolés et sont affectés par le comportement dynamique de l'effecteur.

En conséquence, une contribution de cette thèse concerne une *première méthode de commande*, qui consiste à coupler un schéma de **commande référencée modèle** pour RPC avec un contrôleur PID. Ici, le modèle élasto-dynamique du RPC est utilisé afin de compenser les effets oscillatoires de sa plate-forme mobile en dûs aux allongements de câble et de son comportement dynamique. L'intégration d'algorithmes de distribution de tension de câble [Pot14, GLRB15, YCD16, RLMGC18b] est proposée dans le cadre de cette stratégie de commande pour traiter les différentes configurations de RPC et garantir des tensions positives dans les câble le

---

long du parcours.

Une deuxième contribution de cette thèse concerne une *deuxième méthode de commande*, qui utilise des filtres "input-shaping" dans la commande référencée modèle proposée afin d'annuler les mouvements oscillatoires de la plate-forme mobile. Ainsi, le signal d'entrée est modifié pour que le RPC annule automatiquement les vibrations résiduelles. Les amplitudes et les emplacements temporels des impulsions sont basés sur les fréquences propres et les coefficients d'amortissement du robot. Le signal de commande résultant de la convolution est utilisée pour entraîner le robot et stimule moins de vibrations résiduelles que celle non modifiée. Des travaux antérieurs intégraient cette méthode pour les RPCs sous-contraints [HBY<sup>+</sup>16, BFV16, LL16, MV17, PKP13]. Bien que les travaux de recherche dans [YHB<sup>+</sup>16] portent sur des RPCs sur-contraints, cette commande ne permet pas de gérer la redondance des actionnements et les tensions positives des câbles ne sont pas garanties. En conséquence, la Section IV.3 propose de mettre en forme les entrées pour une commande référencée modèle afin d'améliorer les performances du RPC en supprimant les vibrations résiduelles du manipulateur. La nouveauté de ce schéma de commande réside dans l'intégration de filtres "input-shaping" au schéma de commande référencée modèle en boucle fermée, où la présence d'une distribution de tension le rend valide pour toute configuration de RPC.

Les paramètres utilisés dans les modèles de commande de RPC proposés sont soumis à des incertitudes. Les modèles mathématiques ne reflètent pas parfaitement le comportement du robot en raison d'incertitudes telles que l'assemblage et l'imprécision de composants géométriques tels que les poulies [MP10, Pot12]. De plus, ces modèles sont influencés par des incertitudes d'origine non géométriques. Ces derniers sont attribués à la qualité des composants mécaniques du robot, tels que les câbles et leurs interactions avec le système complet.

Une **analyse de robustesse** est réalisée au moyen d'une analyse de sensibilité et d'incertitude afin de permettre une commande référencée modèle robuste des RPC. En conséquence, un modèle de RPC approprié est défini en fonction de l'application visée et les principales sources d'erreurs de pose de la plate-forme mobile sont identifiées.

Ce manuscrit est organisé en cinq chapitres :

Dans **Chapitre I**, l'état de l'art des RPC est étudié. Après avoir mis l'accent sur les configurations, les applications et l'importance des RPC, les travaux de recherche en cours sur la précision statique et dynamique du RPC sont abordés.

Dans **Chapitre II**, la modélisation dynamique des RPC est introduite. Différents modèles dynamiques de RPC utilisés pour la commande référencée modèle sont revus et le **modèle élasto-dynamique** est présenté. Le choix des modèles de câbles étant une tâche primordiale pour la modélisation RPC, les différents niveaux de rigidité de câble utilisés pour la modélisation dynamique sont également abordés à la Section II.3. Habituellement, l'analyse de la rigidité dynamique des RPC est faite en supposant que les charges dynamiques n'induisent que de faibles allongements des câbles. La tension du câble est généralement considérée comme proportionnelle aux variations de la longueur du câble avec un coefficient de rigidité constant. Par conséquent, un tel modèle n'est pas valable lorsque les câbles sont soumis à des contraintes élevées dues à des oscillations dynamiques importantes ou à des variations rapides de la longueur des câbles. En conséquence, un nouveau **modèle de tension de câble non linéaire** est proposé dans la Section II.3.2 pour exprimer les mouvements dynamiques et oscillatoires des RPC avec des câbles soumis à des longueurs variables rapidement. Cette formulation révèle une rigidification lorsque les contraintes deviennent grandes.

**Chapitre III** liste les différentes sources d'erreur mécaniques et géométriques et étudie leurs effets sur la précision du suivi de trajectoire. **L'analyse de sensibilité** est réalisée par comparaison entre les modèles dynamiques conventionnels et le modèle élasto-dynamique proposé. Une faiblesse des modèles conventionnels utilisés pour la commande référencée modèle est qu'ils négligent les effets dynamiques dus aux interactions des câbles avec l'ensemble du système. Le modèle élasto-dynamique tente de remédier à cette faiblesse en anticipant le comportement oscillatoire du RPC lorsque la plate-forme suit une trajectoire. Un tel modèle est utile à des fins de commande car il prédit non seulement les allongements de câbles, mais également leur interaction dynamique avec la plate-forme mobile.

En outre, une **analyse d'incertitude** est réalisée pour tester la robustesse du modèle de RPC aux variations de paramètres. Il est utile pour réduire l'incertitude

---

en identifiant les entrées de modèle qui entraînent une incertitude significative et devrait donc être au centre de l'attention. Il ressort de cette analyse que l'effet du module d'élasticité des câbles est le plus élevé sur les mouvements dynamiques et oscillatoires de la plate-forme mobile. À cette fin, la méthode expérimentale nommée **Analyse Mécanique Dynamique** (AMD) est proposée pour identifier avec soin les modules d'élasticité et d'amortissement dynamiques de certains câbles afin de mieux compenser les effets de rigidité conduisant à des erreurs de pose et à la dégradation du suivi de trajectoire.

**Chapitre IV** traite deux stratégies de commandes complémentaires valables pour toute configuration de RPC sont proposées. Ils visent à améliorer le positionnement statique et la précision de suivi de trajectoire des Robots Parallèles à Câbles (RPC) tout en prenant en compte leur élasticité globale.

La Section IV.2 traite l'introduction de la **commande élasto-dynamique** et de l'établissement des lois de commande correspondantes. Pour vérifier l'efficacité de cette commande, on effectue une comparaison numérique du suivi de la trajectoire de l'effecteur par rapport aux schémas de commande référencée modèle classiques. De plus, des expérimentations sont effectuées sur le prototype CREATOR situé à LS2N, Nantes, France ; un RPC avec trois câbles et trois degrés de liberté. Les tests expérimentaux confirment les résultats numériques.

De plus, la Section IV.3 traite l'intégration des filtres **input-shaping** dans la commande référencée modèle proposé. Ces filtres sont intégrés en amont du bloc de pré-compensation afin d'augmenter les performances du RPC par l'amélioration de l'atténuation des vibrations résiduelles. Des tests expérimentaux sont effectués sur le prototype CREATOR pour vérifier la capacité du schéma de commande à éliminer les vibrations résiduelles du manipulateur.

Une conclusion générale est écrite dans **Chapitre V** sur les travaux de recherche menés dans le cadre de cette thèse de doctorat. De plus, un aperçu des futurs sujets des travaux de recherche est donné pour améliorer la contrôlabilité et la précision des RPC.



# I

## Cable-Driven Parallel Robots

### Contents

---

I.1 Cable-Driven Parallel Robots ·····	29
I.2 Pose accuracy ·····	39
I.3 Objectives and contributions ·····	46

---

### I.1 Cable-Driven Parallel Robots

Robots are classified into serial and parallel manipulators based on their topology. Serial robots are opened kinematic chains with joints and bodies mounted in series. Parallel robots are defined by Merlet [Mer06] as follows :

*"A generalized parallel manipulator is a closed-loop kinematic chain mechanism whose end-effector is linked to the base by several independent kinematic chains".*

Parallel Manipulators (PMs) have attracted the attention of academic and industrial communities. As compared with serial manipulators, properly designed PMs have higher stiffness and higher accuracy, although their workspace is smaller. Since the design of the Delta robot [PRF90], lower-mobility PMs have replaced their six Degree-Of-Freedom (DOF) counterparts in some particular applications such as surgery or industrial applications such as packaging. Later on, Cable-Driven Parallel Robots (CDPRs) appeared. They are a particular class of parallel robots, where the rigid links are replaced by cables.

A CDPR consists of a moving-platform<sup>1</sup> connected to a base<sup>2</sup> through cables<sup>3</sup>. The size and shape of the moving-platform of the CDPR depend on the target

---

1. The moving-platform can be also called end-effector or mobile platform.  
2. The base can be also called fixed machine frame, fixed platform or simply fixed frame.  
3. The cables can be also called wires, ropes, tendons.

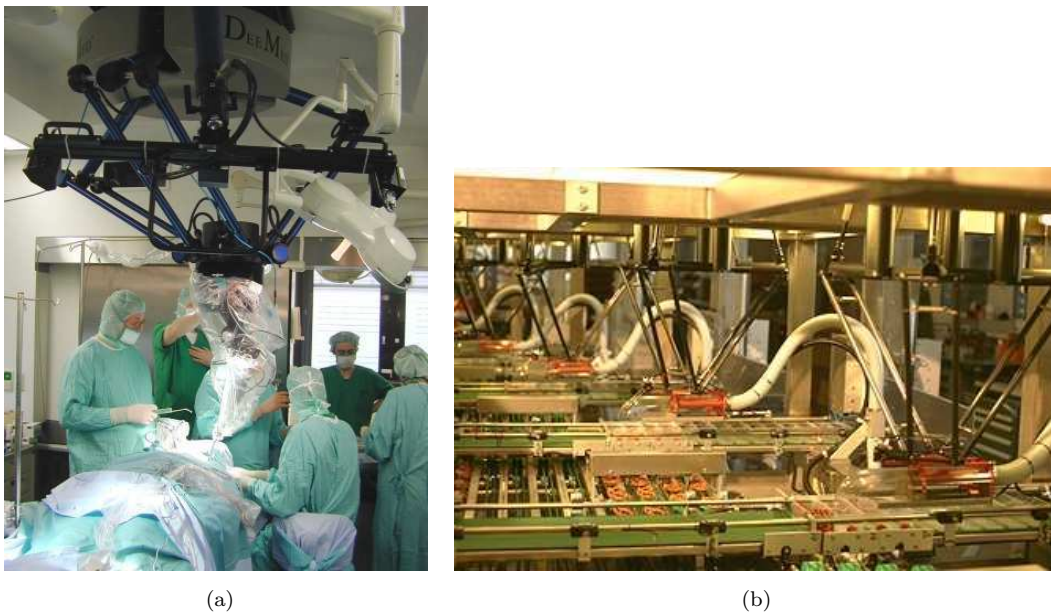


Figure 1.1 – (a) SurgiScope in action at the Surgical Robotics Lab, Humboldt-University at Berlin (b) Demareux's Line-Placer installation for the packaging of pretzels in an industrial bakery



Figure 1.2 – CDRP composition : CREATOR prototype (Courtesy of LS2N, Nantes, France)

application. Some CDRPs present light-weight end-effectors and others carried out large and heavy platforms like the Arecibo telescope [Alt02] whose end-effector weighs 900 tons. The moving-platform is characterized by the anchor points location with respect to its gravity center. The fixed-platform is a mechanical structure that sustains the winches or the exit points. Regarding the cables, different materials can be used. The cables are usually made up of steel and synthetic fibers. The

cable lengths are controlled thanks to actuation systems usually composed of a motor, a gear-head and a winch. Usually, the cable length variations are measured through proprioceptive sensors such as motor encoders.

The main advantages of CDPRs are the following :

- **Large workspace** : Thanks to the high cable lengths, the end-effector of CDPRs can reach larger range of motions comparing to parallel robot with rigid links.
- **High dynamics** : CDPRs are able to generate trajectories with high velocities and high accelerations, thanks to the low mass in motion. For example, the FALCON manipulator [K<sup>+</sup>95] attains a peak speed of about 13 m/s, and a peak acceleration of 43G.
- **Large payload capacity** : CDPRs are able to carry heavy payloads. As shown by the CoGiRo prototype [LG13], the payload capability of the cable robot can reach up to 500 kg, while the total mass of the moving components of the prototype is about 100 kg .
- **High energy efficiency** : CDPRs have higher energy efficiency than serial and conventional parallel robots.

For serial robots, an actuator bears the weight of the ulterior links and actuators in addition to the payload. These facts result in high energy consumption. For conventional parallel robots, the fact that the actuator payloads can be shared by links makes their energy efficiency higher than serial robots [LB01]. The energy consumption of CDPRs is concentrated on the motion of the moving-platform and the payload. It is shared by the number of the lightweight cables, leading to very low energy consumption and high payload-to-weight ratio

- **Low cost** : A CDPR has usually a simple architecture, mainly composed of cheap and simple mechanical components. These components are usually standard, having a low production cost. Let's take the example of the low cost FASTKIT<sup>4</sup> prototype, which manifests in a mobile CDPR providing fast picking and kitting operations [RLMGC18a].
- **Simple structure** : CDPRs are known by their simple structure. The assembly and disassembly of these manipulators are easy. Moreover, some CDPRs are reconfigurable, so that they can easily modify the position of the attach-

---

4. [www.fastkit-project.eu](http://www.fastkit-project.eu)

ment points. Reconfiguration planning is proposed to provide the reconfiguration of some cable manipulators, e.g. the CAROCA prototype [GCGG15].

- **Good safety** : Safety fulfillments are taken into consideration for most of CDPR applications, so that these manipulators can be used in delicate fields. For example, the robot String-Man was used at Fraunhofer IPK (Berlin, Germany) for gait-rehabilitation with focus on safety considerations [SB04]. The robot family Marionet, at INRIA in France, is used for rescue and person assistance [Mer08]. In addition, CDPRs are used for some entertainments while integrating safety mechanisms [CN12, TSPE15].

Nevertheless, existing CDPRs have some drawbacks such as low static accuracy due to static deflection and bad dynamic accuracy due to trajectory tracking errors, settling time and vibrations.

### 1.1.1 Redundant and non-redundant CDPRs

According to [Pot18b], CDPRs can be classified with respect to the number of cables  $n$  and the controllable DOF of the end-effector  $m$ . This classification is based on the Degree-Of-Redundancy (DOR)  $r = n - m$ , allowing to distinguish between redundant and non-redundant cable robots.

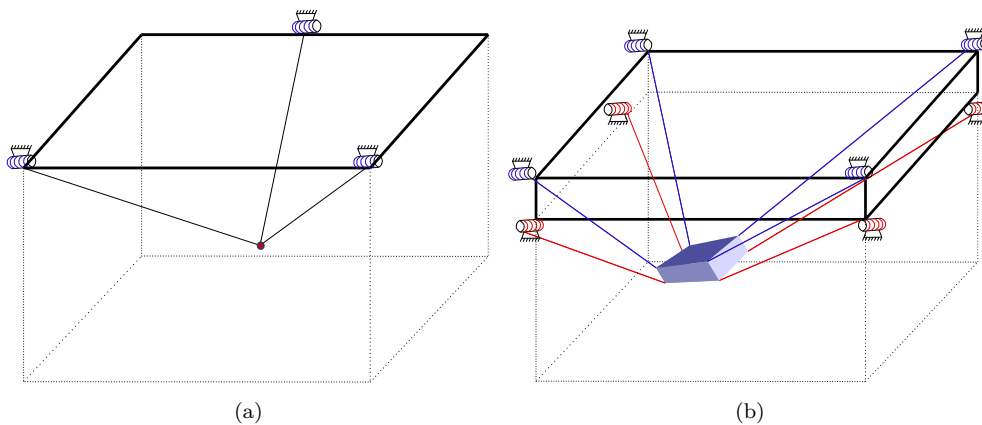


Figure 1.3 – Schematics of (a) Redundant, (b) Non-redundant CDPR

#### 1.1.1.1 Non-redundant CDPR

A CDPR is non-redundant when its DOR  $r = 0$ . Here, the number of cables is equal to the number of the controlled DOF, leading to a square wrench ma-

trix<sup>5</sup>. As a result, the cable tension vector is obtained as a function of the external wrench exerted on the moving-platform as long as the wrench matrix is not singular. Figure I.3(a) presents an example of a 3-DOF CDPR with 3 cables, where the end-effector is considered as a point-mass. It is a non-redundant CDPR. Different applications are proposed based on non-redundant configurations of CDPRs. For instance, the first RoboCrane demonstrator Nist [BAD<sup>+</sup>94], which is a non-redundant CDPR with 6 cables. In [XCCJ10], a 6-DOF CDPR with 6 cables was also discussed.

### I.1.1.2 Redundant CDPR

A CDPR is redundant when  $n > m$ , *i.e.*  $r > 0$ . The redundancy, or the use of more actuated cables than DOF, presents many interests for CDPRs. It makes it possible to increase the ratio between the CDPR workspace and the total structure volume [Mer12, VvdWH12]. The use of a number of cables higher than the minimum one makes it possible to customize the shape and the size of the workspace. This permits the robot acquire more robustness against failure in single drive-trains, which is highly required for applications with high demands of safety such as rescue operations [Pot18b]. Also, the use of more cables than DOF increases the capability of the CDPR to carry heavier payloads.

Figure I.3(b) presents an example of a 6-DOF CDPR with 8 cables. It is a redundant CDPR with 2-DOR. Numerous redundant CDPRs are discussed in literature such as the 1-DOR CDPR with 7 cables Segesta-7 [HFM<sup>+</sup>05]. The Falcon was proposed by Kawamura [K<sup>+</sup>95]. It is a redundant CDPR with 7 cables and 6 DOF, dedicated to pick-and-place applications. It should be noted that the wrench matrix of a redundantly actuated CDPR is not square and, as a consequence, cannot be inverted. Therefore, some tension distribution algorithms have been proposed in the literature in order to determine the cable tension vector for a given moving-platform pose as a function of the external wrench applied to the latter [FFT<sup>+</sup>04, PBM09, Pot14, GG11, BJS<sup>+</sup>09, YCD16].

<sup>5</sup>. The wrench matrix is a function of the end-effector pose and maps the cable tension vector into the wrench applied by the cables to moving-platform.

## 1.1.2 Suspended and fully-constrained CDPRs

CDPRs can be also classified according to the cable arrangement and spatial layout into fully-constrained and suspended robots.

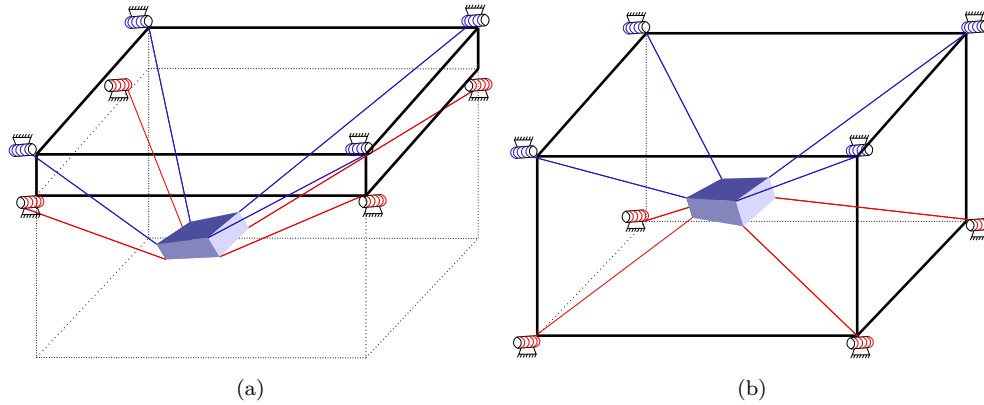


Figure I.4 – Schematics of (a) Suspended, (b) Fully-constrained CDPR

### 1.1.2.1 Fully-constrained configuration

According to the arrangement of the cables, a necessary condition for a CDPR to be in a fully-constrained configuration is when at least one driven cable is below the end-effector. For horizontally planar applications, the CDPR is considered fully-constrained as the gravity has no effect on the end-effector. Here, the support of the plane balances the weight of the end-effector. Fully-constrained CDPRs were discussed several times in literature [BKT15, Dia15]. We have the example of the Falcon [K<sup>+</sup>95], the IPAnema [PMV10], the Segesta [HFM<sup>+</sup>05, FFT<sup>+</sup>04], etc.

### 1.1.2.2 Suspended configuration

The driving cables of a suspended CDPR are all present above the moving-platform. In this configuration, the gravity is considered as a virtual cable to maintain the equilibrium. This configuration was discussed in different research works [AC15, AA02, XCCJ10]. Some famous applications adopt the suspended configuration such as the CoGiRo [LG13], the FAST [DQZZ09, Hui15], the CableV [HW06], etc. The arrangement of cables of a suspended CDPR leads to less risks of interference of the cables with each other or with the environment than for the fully-constrained configuration. Moreover, as the cables are above the end-effector, the payload is shared by each cable. This allows the suspended CDPR to have

a better payload capacity. A weakness of suspended CDPRs is that they present weak stiffness along horizontal directions. This may lead to instability and vibrations under the effect of external disturbances, especially while using a light-weight end-effector.

### I.1.3 Applications

CDPRs are used in different fields of applications. They can be appropriate to tasks where traditional robots are not able to provide because of their low ability to carry loads and the limitation of their workspace. Some relevant fields of applications for CDPRs are presented thereafter.

#### I.1.3.1 Production engineering

CDPRs succeeded in the field of production especially for painting, sand blasting [GCGG16] and assembly operations. Some production processes require the positioning of specific equipments through a large workspace or products like buildings, ships or airplanes. Therefore, the use of CDPRs for painting aircrafts was suggested by the research project CableBOT [cab]. The assembly of collectors in solar-thermal power plants was provided by the IPAnema CDPR (Fig. I.5(a)). This was studied and evaluated in [PMV10] based on the international standard ISO-9283. This project was shown at Automatica 2010 trade fair, Munich, Germany (Fig. I.5(b)). In [ABVA09], the large cable delta robot (LCDR) is introduced. It manifests in a CDPR dedicated to automated machining of large workpieces and material handling.

#### I.1.3.2 Logistics

The advantage of having a large workspace and high dynamics makes the CDPRs suitable for handling, sorting, and palletizing. The idea of building ultra-high speed pick-and-place CDPRs was addressed by Kawamura in 90s through the FALCON robot [K+95]. Besides, a cable robot system was addressed in [COR14] for the transport of persons across a river. The CoGiRo prototype [LG13] ensures handling of boxes in automatic operations. It can carry up to 500 kg. Besides, the FASTKIT project [RLMGC18b] dealt with a low cost and versatile robotic solution for logistics using a unique combination of mobile robots and CDPR. This

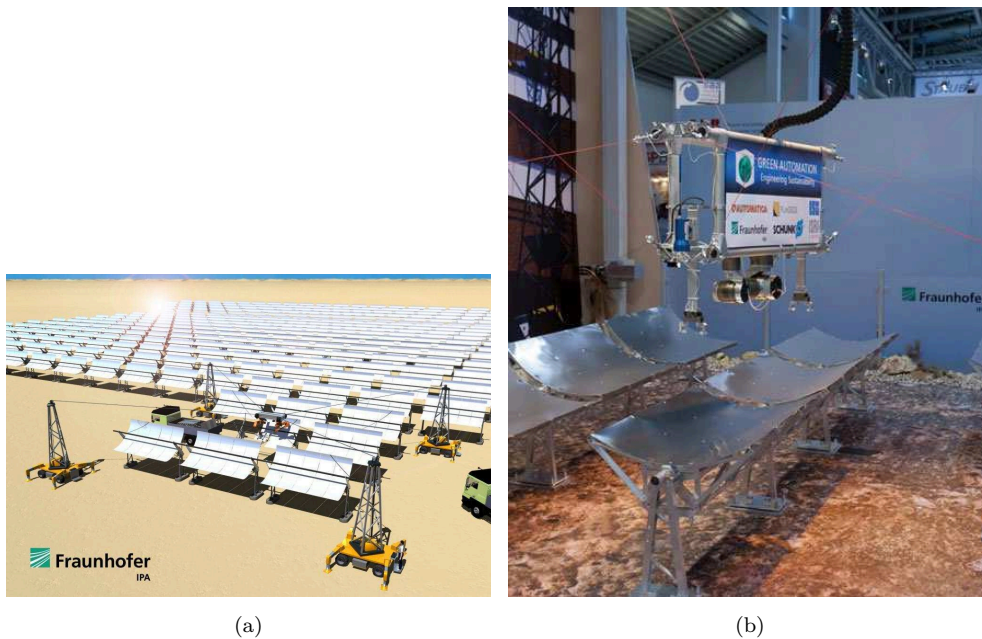


Figure 1.5 – Cable robot IPAnema 2 : (a) Vision of assembly of parabolic reflector panels [PMV10] (b) Large-scale handling of collector modules shown at Automatica 2010 trade fair, Munich, Germany [Pot18a]

prototype addresses an industrial need for fast picking and kitting operations in existing storage facilities.

### 1.1.3.3 Rescue and Rehabilitation

Thanks to cable flexibility and their low mass on motion, CDPRs are suitable for some rescue tasks. In [TVHT99], a CDPR dedicated to rescue operations after natural disasters as earthquakes was proposed. Later on, the robot family Marionet, at INRIA in France, is proposed for rescue and person assistance requirements [MD10, Mer08]. Practical tests were performed with these manipulators for lifting elderly and disabled humans in an ambient assisted living environment.

CDPRs are also used for rehabilitation [RABG07]. The force control of these manipulators allows to reduce the effective mass and then to comfort the patient from the weight of some parts of his body during the exercise. A gait-rehabilitation CDPR, implemented at Fraunhofer IPK (Berlin, Germany), was proposed in [SB04]. CDPRs are also used for arms [ADG<sup>+</sup>09, RGM07, GCRS15] and legs [MD10, HFN02, GCRS15] rehabilitation.



Figure I.6 – The cable robots of the Marionet family : Courtesy of INRIA Sophia-Antipolis, France



Figure I.7 – The cable robot String-Man : Courtesy of Fraunhofer IPK, Berlin

#### I.1.3.4 Acquisition

Numerous CDPRs, whose end-effector is dedicated for measurements by equipping it with camera or any other sensor, are proposed. In [JKKS98, JKK99], a CDPR is proposed for measuring the end-effector pose along a trajectory. Some projects such as FAST [DQZZ09, Hui15] and Carlina [LCDA<sup>+</sup>04] use CDPRs to guide huge telescopes. Some CDPRs are employed as aerial cameras at sport or entertainment events like Skycam [Con85] and CableCam [RB93], whose end-effectors are cameras. Thanks to their large workspace, these robots are usually used in stadiums or for movie shooting.

### 1.1.3.5 Construction

The flexibility of cables allows CDPRs to be used in building construction through suitable geometrical configurations. The project MEDIA-TIC [Bes16] was proposed to establish an intelligent building. For this purpose, a CDPR whose end-effector is equipped with atmospheric sensors is integrated in the building facades [IGB<sup>+</sup>13]. In [IDH<sup>+</sup>18], a CDPR dedicated to construction by means of additive manufacturing is discussed. This manifests in the mount of the extruder of the Pylos project [Pyl] on the Cogiro robot [GCRB15] to obtain a large scale 3D printing machine for construction tasks.



Figure 1.8 – Cogiro, Pylos and the high print being processed [IDH<sup>+</sup>18]

### 1.1.3.6 Entertainment

CDPRs are also used for entertainment. They can be implemented in amusement parks such as Disney [CN12], which has thrill rides based on suspended CDPRs. The principle of these attractions is the following : People sit inside a vehicle, which presents the CDPR moving-platform. This latter is connected to the base through moving winches along roller coaster rails (Fig. I.9(a)). At the German Pavilion, at the EXPO 2015 in Milan, two large-scale CDPRs [TSPE15] were installed whose end-effectors were flying above the heads of the visitors (Fig. I.9(b)). Each robot consists of a mobile platform suspended by eight cables and following a prescribed trajectory. In all those activities, safety requirements are guaranteed.

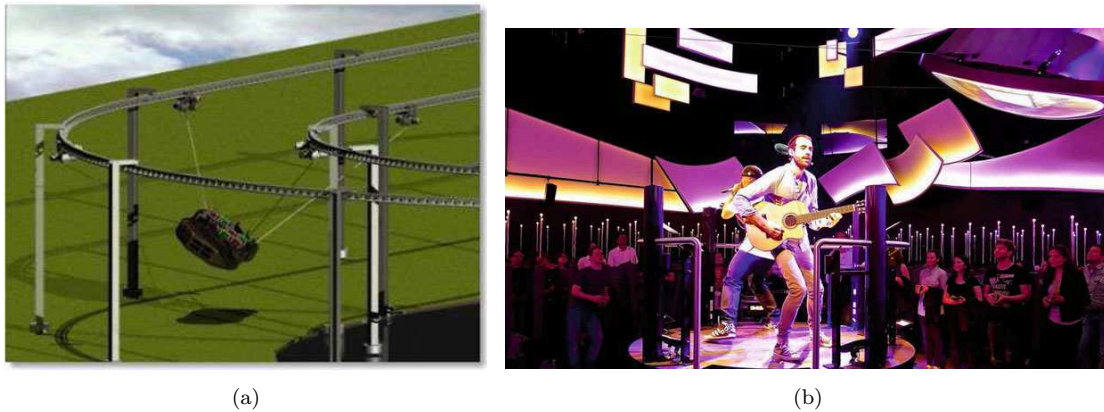


Figure I.9 – (a) Concept for a thrill ride with winches moving along a track (b) Two large-scale cable robots are core elements of the show at the German pavilion on the Expo 2015 fair in Milan, 2015 [TSPE15, Pot18b].

## I.2 Pose accuracy

The improvement of the robot performances can be done through the modification of the robot structure either by optimizing the design [ADG<sup>+</sup>09, XCCJ10, GCG<sup>+</sup>14, YTWH10] or by adding other components to the robot structure as in [VP15, WCG14]. Improving accuracy is still possible once the robot is operational through a suitable control scheme. Numerous control schemes were proposed to enhance the CDPRs precision on static tasks or on a trajectory tracking [JFGK15, FFT<sup>+</sup>04, ZDDB08, dRRK18]. See that the response of a cable robot depends strongly on its overall stiffness, including the stiffness of its cables. The effectiveness of a control strategy depends strongly on the choice of the robot model, including the modeling of cables stiffness.

### I.2.1 Modeling

The development and the design of controllers for CDPRs require the establishment of accurate models of the cable manipulators. This depends on the considered properties of the robot cables with respect to the overall CDPR size. CDPRs models can be classified based on the considered cables stiffness. Two classes of cables stiffness are defined : (i) The axial stiffness of the cables associated with the elastic material modulus and the cable structure; and (ii) the sag-introduced flexibility coming from the effect of cable weight onto the static cable profile.

In case the cable mass is important with respect to the overall size of the CDPR,

the consideration of the sag-introduced stiffness is important. In statics, numerous works describe the sag effect through the catenary model of cables [Irv92, YLZ13]. The modeling of CDPRs with long cables whose stiffness depends on the sagging effect and on cable tension is treated in [Li15]. More recently, [Ars13a] and [YCD15] studied the effect of the elasto-sagging of cables on the CDPR stiffness. A good correlation between experimental results and theoretical ones was highlighted in [YCD15], validating the elasto-sagging model for static stiffness modeling. CDPR modeling can be also provided by finite-element models. An accurate representation of the oscillatory behavior of the CDPR was shown in [DDB13] through finite-element analysis. The limitation of this method is that repeated mesh generations and calculations for numerous payload directions are time-consuming, which is not convenient for dynamic tasks.

The lumped-mass model can also be used as a method of modeling flexible CDPRs. A spatial CDPR with sagging cables was modeled in [LNC07]. As an alternative, a similar lumped-mass model, considering the actuator dynamics and the wrap around the winch, is proposed in [CF14, CFM15]. However, these models are valid only when working in a reduced workspace, in which there is no contact between lumped masses and the winches. Besides, to accurately achieve the true cable natural frequencies, many lumped masses are needed.

The Rayleigh-Ritz method can also be used to develop an accurate model of cable manipulator. The work of [GCF18] uses this method to describe the longitudinal vibrations of cables, a way to make this model useful for controller design. It highlights the importance of using this method rather than the lumped-mass methods.

A simpler way to model CDPRs is to consider cables as linear springs, whose stiffness is inversely proportional to the cable lengths [KT14, WCG15]. When the moving-platform of a CDPR with a relatively small overall size is suspended by tensed cables and balanced by the gravity, the full stiffness of the cables may be generalized to only axial flexibility [BCCD17]. This latter manifests in cable elongations.

## 1.2.2 Error sources affecting accuracy

All models are approximations and the parameters used into a CDPR given model are subjected to uncertainties. The mathematical models do not perfectly

reflect the robot behavior because of uncertainties such as the assembly and manufacturing inaccuracies of geometrical components like pulleys [MP10, Pot12]. Also, these models are influenced by non-geometrical origin uncertainties. These latter are attributed to the quality of mechanical components of the robot manipulator as the deformation of mechanical components due to efforts, their interactions, etc.

Some models propose and investigate the influence of temperature variation into the CDPR accuracy. The work of [Sch17] mentions that an increase of temperature from 23° to 70° generates a variation of cables stiffness from 113500 kN/mm to 90119 kN/mm, representing a decay of 20.6 % for the 2.5 mm Dyneema cable used in the IPAnema robots. Such a variation may strongly affect the moving-platform positioning accuracy. Generally, the thermal expansion is considered to have negligible effects on components, like the end-effector, frame and links as CDPRs are mostly operated at ambient temperature.

Cables themselves are physical components whose behavior affects the CDPR response. The CDPR mechanical behavior depends on cable properties such as the cable mass [KZW06, RGPB10, OC10] and elongation [SP17]. In the simplest form, such a stress-strain relationship is translated by the Young's modulus of the material. Large range of materials are used to make CDPR cables. Besides, the properties of a given material can vary a lot. It was shown that some ropes used in robots have a considerable hysteresis in elongation under force. For example, the cable robot IPAnema at Fraunhofer IPA uses Dyneema cables instead of conventional steel cables, which brings the advantage of the lower weight. At the same time, this cable introduces a more complex elastic behavior in the most relevant force transition element of the cable robot. It showed that the Dyneema polyethylene cables have a changing elastic behavior over time, are subject to settling effects, are sensitive to overload, and show hysteresis effects [MKLP15].

The cable material is not the only factor having a significant effect on the CDPR mechanical behavior. Other research works are looking into the properties affecting the CDPR accuracy such as the abrasive wear [dSF02] or cable fretting [ZGQ03], which depend on the UV rays and temperature.

Other production parameters are also relevant like coating materials and the meshing of individual strands [SP18]. Additional sources of error affecting by the cable manipulator include bending cycles and forces applied to the cables. This

leads to abrasion in the cable when individual strands are rubbing against each other to cause friction.

It is clear that the lifetime depends greatly on the cable tension, whether it is continuous or not, depending of the bending diameters and on the cable velocity [VW04]. The cable force is highly dependent on the cable properties. An efficient force distribution method taking into account the effect of cable sag is presented in [YCD16]. An example of a 6-DOF CDPR with 8 cables was analyzed. This mentions that the relative difference of cable force between the ideal model and the non-ideal sagging model becomes larger as the level of cable sag increases. Here, the force error is as small as 0.35 % when the weight/length ratio is 0.3 N/m. However, this force error can even reach 10.5 % when the weight/length ratio is 2.4 N/m. Furthermore, the cable force is highly dependent of the moving-platform pose and cannot be maintained in the same manner. If we consider the movement of the end-effector along a trajectory, the cables density of different driving cables are usually not the same, and the cable weight of a certain driving cable is also changing with the pose of the end-effector along the trajectory. In [YCD16], an original method is proposed to determine pose-dependent force boundary used as constraint in the force distribution for better accuracy.

Some errors in the control signals lead to undesired wrench exerted on and twist of the moving-platform. The effect of variations in parameters and data on the actuator torque vector of CDPRs is examined utilizing interval arithmetics in [Not15].

Because of manufacturing and assembling errors, the variations in material properties and the uncertainty in actuator inputs and operating conditions make the robot data and exact parameters unknown. Using nominal values, the cable-actuated system characteristics may differ from the real performance. Calibration enhances their operation to a certain extent, but does not result in the exact parameters values [Not16]. As a result, their action may be degraded due to calculations made with inaccurate parameters, which make them unsuitable. According to the CDPR operation, the variance in its parameters can be permitted within a defined variation range. It may be preferred to study the performance of CDPRs for a range of parameter values, to identify all designs that meet the requirements, and to choose the suitable designs for a given application of the studied CDPR [Mer09]. One must be careful to neglect uncertainty in some factors having negligible effects on the CDPR mechanical behavior in order to obtain reliable control. The uncertainty

analysis of the CDPR allows us to identify the uncertainties in parameters that mainly affect the moving-platform pose.

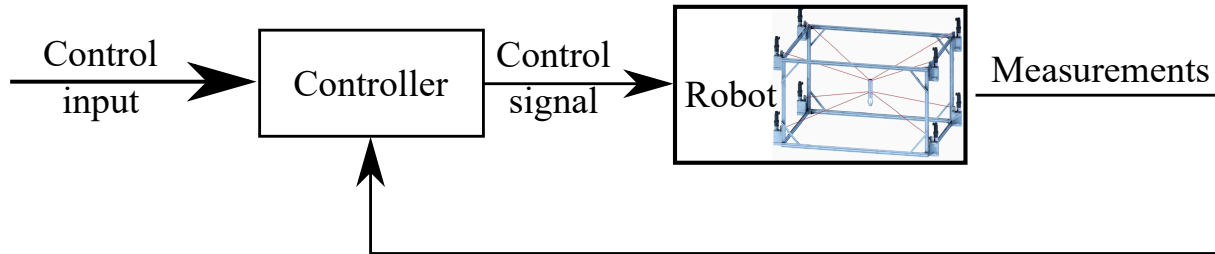


Figure I.10 – General control scheme for CDPR

### 1.2.3 Control for accuracy improvement

Two main issues related to CDPRs are discussed : pose stabilization and trajectory tracking. While the pose stabilization aims to stabilize the robot in a reference pose, the trajectory tracking aims to have the moving-platform following a reference trajectory.

Several controllers have been proposed in the literature to improve CDPR accuracy locally or on trajectory tracking. They can be divided into two main categories : The first one is based on iterative algorithms, so that efficient constrained optimization methods can be used such as Linear Programming Methods (LPMs) [OA05, YLK09]. For example, in [JFGK15], an adaptive controller is presented based on the linear techniques of pole placement control (PPC) and also linear quadratic regulation (LQR) method. It aims to minimize the CDPR vibrations through maximizing its stiffness in the presence of end-effector mass and inertia uncertainties.

Other optimization methods are Non-Linear Programming Methods (NLPMs) in the particular case of Quadratic Programming Methods (QPMs) [OA05, VAT10], and the general NLPM with the gradient descent method to resolve the problem in a quadratic formulation. In [JKFK18], LPV -  $H_\infty$  control strategy is proposed to suppress the unwanted effect of external disturbances. This method is based on modeling the vibration dynamics as an linear parametric variable (LPV) system, while decoupling the unwanted vibrations from motion equations. A non-iterative algorithm with a non-evolutionary criterion, inspired from [Laf04], is proposed in [CCL15] for the control of a 6-DOF INCA Robot [CLCG13].

A control strategy of a fully-constrained CDPR is proposed in [AY17]. It consists in determining the motor torque allowing to minimize the errors between the measured cable tensions and the desired ones. The latter are defined by the outer-loop controller, which manifests in an adaptive robust feedback controller with bounded feed-forward compensation terms. Bounded positive cable tensions are generated by the outer-loop controller, utilizing the integral of the sign of the error (RISE) approach.

In [CLP18], the control of CDPR in the operational space is presented, where the CDPR model is derived using Lagrange equations of motion for constrained systems, while considering non elastic but sagging cables through the Assumed Mode Method.

A discrete-time control strategy is proposed in [Mer17] to estimate the positioning accuracy of the end-effector by taking into account the actuator model, the kinematics and static behavior of the CDPR, but dynamic effects are neglected.

Multiple papers have dealt with the CDPR control while considering cable elongations and their effect on the dynamic behavior. In [KTH17], an approach of wave based control (WBC) is proposed for large scale robots whose cables sagging effect cannot be neglected. It combines the position control and the active vibration damping simultaneously. This control strategy assumes actuator motion as launching a mechanical wave into the flexible system, which is absorbed on its return to the actuator. The assumption of modeling cables as elastic straight massless links is valid for robots with relatively small size [BCCD17]. Here, the cable mass is ignored with respect to the end-effector mass [DM09, KMP13]. On these grounds, a robust  $H_\infty$  control scheme for CDPR is described in [LCCG13] while considering the cable elongations into the dynamic model of the end-effector and cable tension limits. Besides,  $H_\infty$  control scheme for position control of 6-DOF CDPRs is proposed in [CLC14]. Compared to [LCCG13] position control scheme is done in the operational space and the tension management is made separately in a more efficient way. Assuming flexibility in the longitudinal direction of cable, a control strategy is proposed for CDPRs in [KT14], [KT16], [KT11]. It consists in adding an elongation compensation term to the control law of a CDPR with rigid cables, using singular perturbation theory to prevent undesirable vibrations. Here, cables are modeled by linear axial springs but with constant stiffness. This control method is improved in [KT15] by integrating variable stiffness for cable. In

this context, authors of [BKT15] have also proposed a robust adaptive controller to attenuate vibrations in presence of kinematic and dynamic uncertainties. This method of control requires the measurement of cables length and the knowledge of the real-time end-effector pose through exteroceptive measurements. However, the external-measurement-based control methods add complexity to the cable-driven manipulators and restrict the application conditions due to the need of additional devices [CCYJ13].

The importance of the feed-forward effect on non-linear systems control is highlighted in [SL<sup>+</sup>91]. It leads to stable systems with enhanced trajectory tracking performances. Feed-forward model-based controllers are used to fulfill accuracy improvement by using a CDPR reference model [ZSC17]. This latter predicts the mechanical behavior of the robot ; and then generates an adequate reference signal to be followed by the CDPR. This type of control provides the compensation of the desirable effects without exteroceptive measurements. A model-based control scheme for CDPR used as a high rack storage is presented in [BLS<sup>+</sup>13]. This research work takes into account the mechanical properties of cables, namely their elasticity. This strategy, integrating the mechanical behavior of cables in the reference signal, enhances the CDPR performances.

To improve the robot accuracy, a frequency dependent control method was proposed for different types of robotic manipulators. This method is named as input-shaping. Input-shaping filters consist in convolving the desired command signal with a sequence of impulses. The result of the convolution is then used as the new reference control signal for the controlled robot. Input-shaping is used for manipulators with flexible joints to remedy the resulting oscillations. It was used for serial robots [PCPL06, AYTK10, ZCTT16] such as the industrial SCARA manipulator [HK15]. Oscillation control by shaping the input signal was also applied for conventional parallel robots [KEUS04, LZM<sup>+</sup>09, ÖKO16]. The non-rigid behavior of humanoid robots causes unwanted vibrations. To deal with this issue, input-shaping was used for the control of such robotic systems [KSHA16, YZXW16, RHK15].

This control strategy has already been implemented in some CDPRs. For instance, it was implemented for under-constrained CDPRs, which suffer from control problems as their end-effector pose is partially mastered and negative cable tension

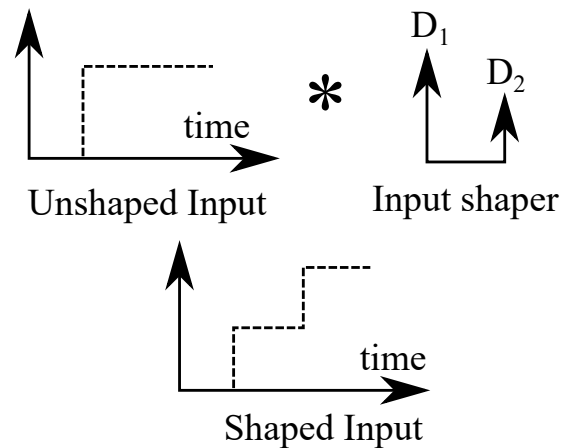


Figure I.11 – The input shaping process

may occur whatever is the operating conditions of the robot [HBY<sup>+</sup>16, BFV16, LL16, MV17, PKP13]. As conventional control methods are limited and not all DOF of the moving-platform can be controlled, such filters could be used to exhibit significant reduction in oscillations of the payload. In [YHB<sup>+</sup>16], input-shaping was proposed for redundantly actuated CDPRs. However, for the control of non-linear systems, the corrector deals with the compensation of the internal and external efforts of the manipulator, which are considered as perturbations. In this case, the control signal is subjected to strong variations in amplitudes and tries to make some cables pull the end-effector. It was verified that when the robot natural frequency is well known, the implementation of input-shaping control could effectively improve the performances of the robot.

### I.3 Objectives and contributions

The main objective of this thesis is the improvement of CDPRs accuracy and the reduction of their vibrations. Feed-forward model-based control taking advantage of an elasto-dynamic model of CDPRs is proposed. In addition, a closed-loop input-shaping control strategy is proposed for CDPRs in order to attenuate the maximum of residual vibrations. These two methods aim to improve the static positioning accuracy and trajectory tracking of CDPRs dedicated to high dynamic applications. To achieve this objective, this thesis was decomposed into the following three tasks.

### **I.3.1 Contribution on CDPR modeling**

As the choice of cable models is a primary task for CDPR modeling, the different levels of cable stiffness are reviewed in Section II.3. In Section II.3.2, a new non-linear cable tension model, valid when cables are subjected to large strains, is proposed to better describe CDPRs with fast varying cable lengths. As the identification of cable parameters is useful for the improvement of CDPR modeling, the experimental method named Dynamic Mechanical Analysis (DMA) is presented in Section A. It enables to identify carefully the dynamic elastic and damping moduli of some cables to better compensate the stiffness effects. Different dynamic models of CDPRs used for feed-forward control are reviewed. CDPR control based on these conventional dynamic models pre-compensate the unwanted effects due to cable elasticity by compensating only for the end-effector positioning errors due to its rigid body behavior. In other words, the compensation does not take into account the interaction between cables and the whole system. Then, an elastodynamic model for CDPRs is proposed in Section II.4 to predict the full dynamic and oscillatory behavior of the CDPR. This model is proposed to generate the adequate reference signal for the control loop, pre-compensating the unwanted effects due to the overall stiffness.

### **I.3.2 Static and dynamic robustness analysis**

The robustness analysis in this thesis deals with both sensitivity and uncertainty analysis. A sensitivity analysis is made in Section III.3 to study how the robot response is sensitive to modeling and make decisions on the choice of CDPR model with respect to the target application. In order to overcome the effects of uncertainties, uncertainty analysis is performed to deal with CDPR design such that the CDPR is robust to variations in parameters and disturbances while performing a prescribed task. An uncertainty analysis is made in Section III.4 to analyze the influence of uncertain parameters on the dynamic behavior of CDPRs. For this study, the CAROCA prototype (at the courtesy of IRT Jules Verne, Nantes, France) is used as a case of study. The uncertain model of CDPR used for the static uncertainty analysis treats not only the axial compliance of cables but also the sag-introduced compliance. As static deflection is a projection of the static compliant displacement and as it evaluates the static stiffness performance, it is

used as an index to analyze the effect of uncertainties on different mechanical and geometrical parameters.



Figure I.12 – CAROCA prototype : a reconfigurable CDPR (Courtesy of IRT Jules Verne, Nantes)

A dynamic analysis is made in Section III.4.1. It aims to analyze the dynamic and oscillatory motions of CDPRs with different levels of cables modeling. This study is based on experimental data of the dynamic modulus of cables obtained through Dynamic Mechanical Analysis. It depicts the effect of cable stiffening and damping onto the dynamic behavior of the moving-platform. It supports the idea to adjust each cable model and parameters to the appropriate CDPR natural frequency for a good trajectory tracking. Another uncertainty analysis is made to check the effect of the CDPR model choice onto its dynamic and oscillatory response. This is done through comparing the open-loop conventional rigid, elasto-static models [BLS<sup>+</sup>13] of CDPR with the proposed elasto-dynamic model [BCC19]. It should be noted that uncertainties do not affect all CDPRs the same way. However, conclusions are valid for every CDPR whatever its size.

### I.3.3 Control for CDPR accuracy improvement

Another contribution of this thesis deals with the synthesis of two control strategies for CDPRs. **The first control strategy**, presented in Section IV.2, consists in a closed-loop feed-forward model-based control. It deals with the coupling of a model-based feed-forward torque control scheme for CDPRs with a PID feedback controller. This control type pre-compensates much as possible the cable elasticity while isolating them. Knowing the cable tensions and adopting a tension model, the cable elongations are determined. In this thesis, the elasto-dynamic model of the CDPR is used as a feed-forward unit to pre-compensate not only cable elongations but also the effect of their interaction with the complete robotic system.

Closed-loop control methods are not allowing all DOF of the moving-platform of an under-constrained CDPR ( $n < m$ ) to be controlled. The extra DOFs in motion of the moving-platform makes it easy to sway [YYM01]. This leads to low operational efficiency and then the lost of controllability. Input-shaping method for under-constrained CDPRs was proposed as an alternative to attenuate residual vibrations [HBY<sup>+</sup>16, BFV16, LL16, MV17, PKP13]. Despite the fact that the research work in [YHB<sup>+</sup>16] deals with over-constrained CDPRs, this control does not allow to manage the actuation redundancy and positive cable tensions are not guaranteed. Accordingly, a **second control method** is proposed in Section IV.3 to increase the CDPR performances by vanishing residual vibrations of the manipulator. The novelty of this control scheme lies in the integration of input-shaping filters to the closed-loop model-based control scheme. Cable tension distribution is considered in addition to the input-shaping filter to satisfy positive tensions along the prescribed trajectory of the moving-platform. As a result, this control method uses an input-shaping filter in conjunction with a feedback control for disturbance rejection.

Experimental tests are made on the CREATOR prototype (See Fig. I.2) located at LS2N, Nantes, France, in order to validate the theoretical results.



# II

---

## CDPR models and properties

### Contents

---

II.1 Introduction ·····	51
II.2 Rigid dynamic model ·····	52
II.3 Dynamic modeling considering cable stiffness : Elasto-static model ·····	59
II.4 Elasto-dynamic modeling ·····	66
II.5 Summary of the chapter ·····	68

---

### II.1 Introduction

The positioning accuracy of CDPRs can be significantly degraded because of cable elasticity. The stiffness analysis thus becomes a vital concern to improve the static and dynamic behavior of CDPRs. Section II.2 presents the dynamic model of CDPRs where cables are supposed to be straight. As cables are flexible, their elongation should be considered in CDPR modeling. Section II.3.1 presents the different levels of cable stiffness for CDPR modeling. Section II.3.2 discusses the cables tension models for the control of CDPRs. The contributions of this chapter are the following :

- A new non-linear cable tension model [BCCD17] relevant for cables subjected to fast length variations is introduced and studied.
- Elasto-dynamic modeling of CDPRs allowing to simulate their dynamic behavior while considering the cable elongations and their interaction with the whole system.

## II.2 Rigid dynamic model

Dynamic modeling consists in establishing the relationship between the actuators efforts and the moving-platform velocity and acceleration. In this manuscript, the CDPR is supposed to be torque controlled. This method allows to satisfy the redundancy by applying a set of torques leading to positive cable tensions. The inverse dynamic model of CDPRs expresses the motor torques as a function of the moving-platform velocity and acceleration in a given pose.

The input joint coordinate vector is denoted as  $\mathbf{q} = [q_1, \dots, q_n]^T \in \mathbb{R}^n$ ,  $n$  being the number of cables. As shown in Fig. II.1, the Cartesian coordinate vectors of

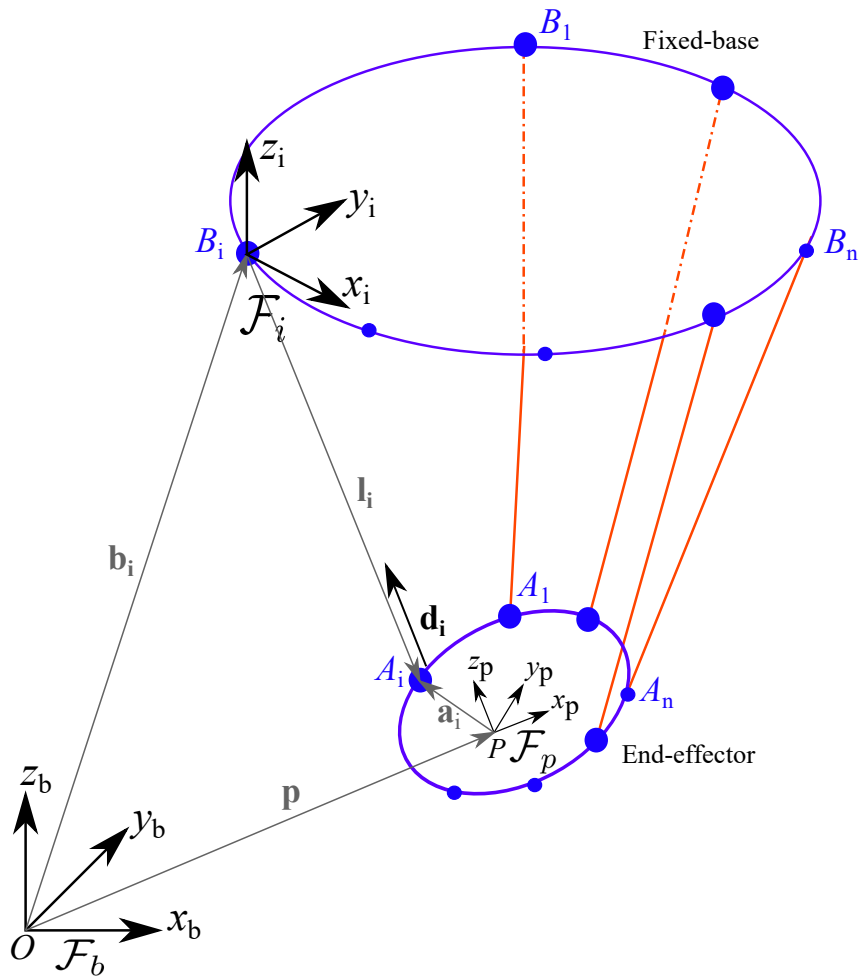


Figure II.1 – The  $i$ th closed-loop of a CDPR

anchor points  $A_i$  and exit points  $B_i$ ,  $i = [1..n]$ , are denoted  $\mathbf{a}_i$  and  $\mathbf{b}_i$ . These vectors are expressed in the moving-platform frame  $\mathcal{F}_p = \{P, x_p, y_p, z_p\}$  and in the base

frame  $\mathcal{F}_b = \{O, x_b, y_b, z_b\}$ , respectively.  $\mathcal{F}_i = \{B_i, x_i, y_i, z_i\}$  is the  $i$ th cable frame, where axes  $z_i$  and  $z_b$  are parallel.

The pose  $\mathbf{x} = [\mathbf{p}^T \ \mathbf{o}^T]^T \in \mathbb{R}^m$  of the moving-platform center  $P$  in the base frame  $\mathcal{F}_b$  is described by the position vector  $\mathbf{p} = [x, y, z]^T \in \mathbb{R}^u$  and the orientation vector  $\mathbf{o} = [\phi, \theta, \psi]^T \in \mathbb{R}^v$ . The orientation of the moving-platform is parameterized by Euler angles  $\phi, \theta$  and  $\psi$ .  $u$  being the number of translational Degree-Of-Freedom (DOFs),  $v$  being the number of rotational DOF and  $m$  being the total DOF of the end-effector. The  $i$ th cable connecting exit point  $B_i$  and anchor point  $A_i, i = [1..n]$ , exerts a force from  $A_i$  to  $B_i$  of magnitude  $\tau_i, \tau_i$  being positive. The unit vector  $\mathbf{d}_i \in \mathbb{R}^u$  of this force is denoted as :

$$\mathbf{d}_i = \frac{\mathbf{b}_i - \mathbf{p} - {}^b\mathbf{R}_p \mathbf{a}_i}{\|\mathbf{b}_i - \mathbf{p} - {}^b\mathbf{R}_p \mathbf{a}_i\|}. \quad (\text{II.1})$$

The wrench matrix  $\mathbf{W} \in \mathbb{R}^{m \times n}$  generated on the moving-platform center for a given pose is expressed as follows :

$$\mathbf{W} = \begin{bmatrix} \mathbf{d}_1 & \dots & \mathbf{d}_n \\ {}^b\mathbf{R}_p \mathbf{a}_1 \times \mathbf{d}_1 & \dots & {}^b\mathbf{R}_p \mathbf{a}_n \times \mathbf{d}_n \end{bmatrix}. \quad (\text{II.2})$$

According to Euler formalism (See App. C), the orientation of the mobile frame  $\mathcal{F}_p$  with respect to the fixed frame  $\mathcal{F}_b$  is defined by the rotation matrix  ${}^b\mathbf{R}_p$  as follows :

$${}^b\mathbf{R}_p(\phi, \theta, \psi) = \begin{bmatrix} c_\theta c_\psi & -c_\theta s_\psi & s_\theta \\ c_\phi s_\psi + s_\phi s_\theta c_\psi & c_\phi c_\psi - s_\phi s_\theta c_\psi & -s_\phi c_\theta \\ s_\phi s_\psi - c_\phi s_\theta c_\psi & s_\phi c_\psi + c_\phi s_\theta c_\psi & c_\phi c_\theta \end{bmatrix} \quad (\text{II.3})$$

where  $c_\theta = \cos(\theta), c_\phi = \cos(\phi), c_\psi = \cos(\psi), s_\theta = \sin(\theta), s_\phi = \sin(\phi)$  and  $s_\psi = \sin(\psi)$ . More details about the Euler angles convention are presented in Appendix C.

Knowing the position  $\mathbf{p}$  and the orientation  $\mathbf{o}$  of the moving-platform, the geometric closed-loop equation of the  $i$ th cable is expressed in  $\mathcal{F}_b$  as follows :

$$\mathbf{l}_i = \mathbf{p} - \mathbf{b}_i + {}^b\mathbf{R}_p \mathbf{a}_i, \quad (\text{II.4})$$

where  $\mathbf{l}_i$  is the  $i$ th cable length vector connecting point  $B_i$  to point  $A_i$  along the  $i$ th cable. The Euclidean norm of Eq. (II.4) leads to the simplest geometric model, so that the  $i$ th cable length is expressed as :

$$l_i = \|\mathbf{p} - \mathbf{b}_i + {}^b\mathbf{R}_p \mathbf{a}_i\|_2. \quad (\text{II.5})$$

The relationship between the cable length vector  $\mathbf{l} = [l_1, \dots, l_n]^T \in \mathbb{R}^n$  and the motor angular displacement vector  $\mathbf{q}$  is supposed to be linear :

$$\mathbf{l} = \boldsymbol{\chi} \mathbf{q}, \quad (\text{II.6})$$

where  $\boldsymbol{\chi} = \text{diag}[\chi_1, \dots, \chi_n] \in \mathbb{R}^{n \times n}$  is a diagonal matrix presenting the winches winding ratio. From Eq. (II.5) and Eq. (II.6), the articular coordinate  $q_i$  of the  $i$ th joint is expressed as a function of the moving-platform pose  $\mathbf{x}$  as follows :

$$q_i = \frac{1}{\chi_i} \|\mathbf{p} - \mathbf{b}_i + {}^b\mathbf{R}_p \mathbf{a}_i\|. \quad (\text{II.7})$$

The kinematics of a CDPR is presented by the relationships between the moving-platform twist vector  $\dot{\mathbf{x}} = [\dot{\mathbf{p}}^T \boldsymbol{\omega}^T]^T \in \mathbb{R}^m$  and the input velocity vector  $\dot{\mathbf{q}} \in \mathbb{R}^n$ . The vector  $\dot{\mathbf{p}}$  is the linear velocity vector of the moving-platform.  $\boldsymbol{\omega} = [\omega_1 \ \omega_2 \ \omega_3]^T$  is its angular velocity vector, which is expressed in  $\mathcal{F}_b$  as :

$$\boldsymbol{\omega} = \begin{bmatrix} \omega_1 \\ \omega_2 \\ \omega_3 \end{bmatrix} = \mathbf{U} \dot{\boldsymbol{\theta}}, \quad (\text{II.8})$$

where

$$\mathbf{U} = \begin{bmatrix} 1 & 0 & s_\theta \\ 0 & c_\phi & -c_\theta s_\phi \\ 0 & s_\phi & c_\theta c_\phi \end{bmatrix}, \quad \dot{\boldsymbol{\theta}} = \begin{bmatrix} \dot{\phi} \\ \dot{\theta} \\ \dot{\psi} \end{bmatrix}. \quad (\text{II.9})$$

The end-effector velocities are mapped to the cable velocities by the Jacobian matrix  $\mathbf{J}$  as follows :

$$\dot{\mathbf{l}} = \mathbf{J} \dot{\mathbf{x}}, \quad (\text{II.10})$$

where  $\mathbf{W} = -\mathbf{J}^T$  [K+95] and  $\dot{\mathbf{l}} \in \mathbb{R}^n$  is the cable velocity vector. This latter is obtained upon time differentiation of Eq. (II.6) :

$$\dot{\mathbf{l}} = \boldsymbol{\chi} \dot{\mathbf{q}}. \quad (\text{II.11})$$

Inversing Eq. (II.11) and substituting Eq. (II.10), the relationship between the moving-platform velocity and the input velocity is written as follows :

$$\dot{\mathbf{q}} = \boldsymbol{\chi}^{-1} \mathbf{J} \dot{\mathbf{x}}, \quad (\text{II.12})$$

The equations of motions are derived from the equations of Newton-Euler while considering the center of mass of the moving-platform coincident with its geometric

center. The Newton-Euler equations are expressed in matrix form as follows :

$$\mathbf{M}(\mathbf{x}) \ddot{\mathbf{x}} + \mathbf{C}(\mathbf{x}, \dot{\mathbf{x}}) \dot{\mathbf{x}} = \mathbf{W}\boldsymbol{\tau} + \mathbf{w}_{ex}, \quad (\text{II.13})$$

with

$$\mathbf{M}(\mathbf{x}) = \begin{bmatrix} m_{ee}\mathbb{I}_u & \mathbf{0}_{u \times v} \\ \mathbf{0}_{v \times u} & \mathbf{S} \end{bmatrix}, \quad \mathbf{C}(\mathbf{x}, \dot{\mathbf{x}}) = \begin{bmatrix} \mathbf{0}_{u \times u} & \mathbf{0}_{u \times v} \\ \mathbf{0}_{v \times u} & \dot{\mathbf{S}} \end{bmatrix}, \quad (\text{II.14a})$$

$$\mathbf{w}_{ex} = \mathbf{w}_g + \mathbf{w}_e. \quad (\text{II.14b})$$

where :

- $\mathbf{M} \in \mathbb{R}^{m \times m}$  is the mass matrix of the moving platform.
- $m_{ee}$  is the mass of the moving-platform.
- $\mathbf{C} \in \mathbb{R}^{m \times m}$  is the matrix of Coriolis and centrifugal forces.
- $\ddot{\mathbf{x}} \in \mathbb{R}^m$  is the acceleration vector of the moving-platform.
- $\mathbf{S} = {}^b\mathbf{R}_p \mathbf{I}_c {}^b\mathbf{R}_p^T$  is the inertia matrix of the moving-platform expressed in  $\mathcal{F}_b$ .
- $\mathbf{I}_c$  is the inertia tensor of the moving-platform relative to point  $P$  expressed in  $\mathcal{F}_p$ .
- $\mathbf{w}_{ex} \in \mathbb{R}^m$  is the external wrench applied on the moving-platform.
- $\mathbf{w}_g \in \mathbb{R}^m$  is the wrench due to gravity acceleration.
- $\mathbf{w}_e \in \mathbb{R}^m$  is any other wrench, except  $\mathbf{w}_g$ , applied to the mobile platform.

According to [SSVO09], the product  $\mathbf{C}(\mathbf{x}, \dot{\mathbf{x}}) \dot{\mathbf{x}}$  can be simplified to  $\mathbf{c} \in \mathbb{R}^m$  :

$$\mathbf{c} = \mathbf{C}(\mathbf{x}, \dot{\mathbf{x}}) \dot{\mathbf{x}} = \begin{bmatrix} \mathbf{0}_{u \times 1} \\ \boldsymbol{\omega} \times \mathbf{S}\boldsymbol{\omega} \end{bmatrix} \quad (\text{II.15})$$

## II.2.1 Dynamics of actuators

The dynamics of actuators links the vector of motor torques  $\boldsymbol{\zeta}_m$  to the vector of actuator accelerations  $\ddot{\mathbf{q}}$ . In this manuscript, it is assumed that all components (motor, reducer and winch) of an actuator are coaxial. Classically, the actuators dynamics can be expressed in the following form :

$$\boldsymbol{\zeta}_m = \mathbf{I}_m \ddot{\mathbf{q}} + \boldsymbol{\zeta}_f(\dot{\mathbf{q}}) + \boldsymbol{\zeta}_{rg}, \quad (\text{II.16})$$

where

- $\zeta_m \in \mathbb{R}^n$  is the motor torque vector.
- $\mathbf{I}_m \in \mathbb{R}^{n \times n}$  is a diagonal matrix containing the winch moment of inertia.
- $\ddot{\mathbf{q}} \in \mathbb{R}^n$  is the angular acceleration vector.
- $\zeta_{rg} = \chi \tau \in \mathbb{R}^n$  is the torque vector induced by the cable tensions onto the drums.
- $\zeta_f \in \mathbb{R}^n$  is the friction torque vector.

According to the static model of friction [KD04], the vector of friction torques can be expressed as follows :

$$\zeta_f(\dot{\mathbf{q}}) = \zeta_d \operatorname{sgn}(\dot{\mathbf{q}}) + \zeta_v \dot{\mathbf{q}}, \quad (\text{II.17})$$

where

- $\zeta_d \in \mathbb{R}^{n \times n}$  : a diagonal matrix containing the dry friction coefficients.
- $\zeta_v \in \mathbb{R}^{n \times n}$  : a diagonal matrix containing the viscous friction coefficients.

Since Eq. (II.17) contains the sign function, its integration in direct application of CDPR control laws may result in amplified vibrations caused by the signal discontinuity. To overcome this problem, the friction torque expression is modified to get a soft variation when the sign function is zero thanks to the hyperbolic tangent function as illustrated in Eq. (II.18) and Fig. II.2.

$$\zeta_f(\dot{\mathbf{q}}) = \zeta_d \tanh(c \dot{\mathbf{q}}) + \zeta_v \dot{\mathbf{q}}, \quad (\text{II.18})$$

$c$  being the slope of the *tanh* function.

Therefore, the extended dynamics of actuators is described by the following matrix expression :

$$\zeta_m = \mathbf{I}_m \ddot{\mathbf{q}} + \zeta_d \tanh(c \dot{\mathbf{q}}) + \zeta_v \dot{\mathbf{q}} + \chi \tau. \quad (\text{II.19})$$

## II.2.2 Complete dynamic model

From Eq. (II.19) and Eq. (II.13), the equation of motion of the moving-platform takes the form :

$$\mathbf{M}(\mathbf{x}) \ddot{\mathbf{x}} + \mathbf{C}(\mathbf{x}, \dot{\mathbf{x}}) \dot{\mathbf{x}} = \mathbf{W} \chi^{-1} (\zeta_m - \mathbf{I}_m \ddot{\mathbf{q}} - \zeta_f(\dot{\mathbf{q}})) + \mathbf{w}_{ex}, \quad (\text{II.20})$$

$\ddot{\mathbf{q}}$  is obtained upon time differentiation of Eq. (II.12) :

$$\ddot{\mathbf{q}} = \chi^{-1} (\mathbf{J} \ddot{\mathbf{x}} + \dot{\mathbf{J}} \dot{\mathbf{x}}) \quad (\text{II.21})$$

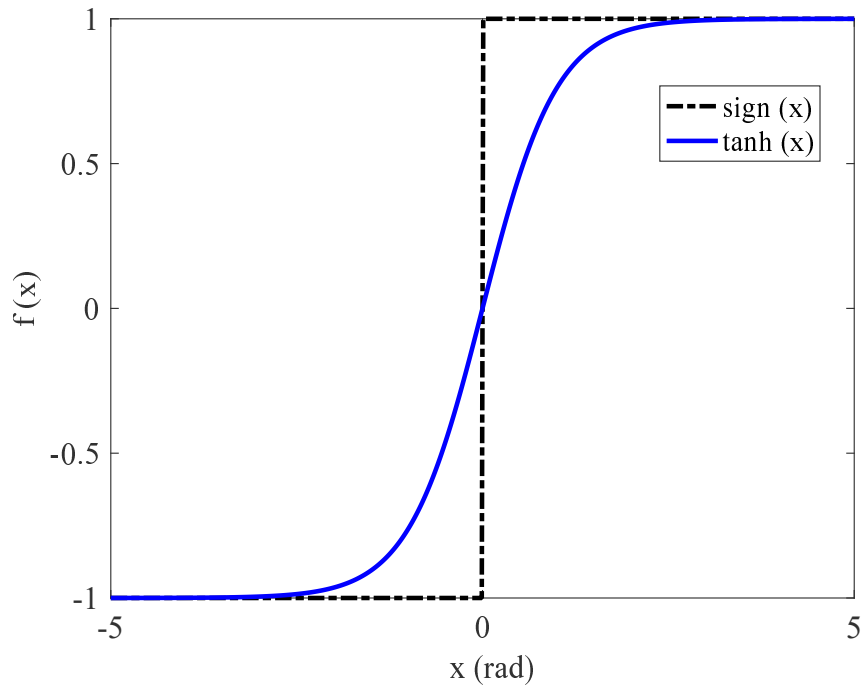


Figure II.2 – Graphical representation of sign versus hyperbolic tangent

Substituting Eq. (II.12) and Eq. (II.21) in Eq. (II.20), the dynamic constraints become :

$$\mathbf{M}^* \ddot{\mathbf{x}} + \mathbf{C}^* \dot{\mathbf{x}} + \mathbf{W}\boldsymbol{\chi}^{-1}\boldsymbol{\zeta}_f(\dot{\mathbf{q}}) = \mathbf{W}\boldsymbol{\chi}^{-1}\boldsymbol{\zeta}_m + \mathbf{w}_{ex}, \quad (\text{II.22})$$

where  $\mathbf{M}^* \in \mathbb{R}^{m \times m}$  and  $\mathbf{C}^* \in \mathbb{R}^{m \times m}$  are the equivalent mass and Coriolis matrices respectively and they are expressed as follows :

$$\mathbf{M}^* = \mathbf{M} + \mathbf{W}\boldsymbol{\chi}^{-1}\mathbf{I}_m\boldsymbol{\chi}^{-1}\mathbf{J}, \quad (\text{II.23a})$$

$$\mathbf{C}^* = \mathbf{C} + \mathbf{W}\boldsymbol{\chi}^{-1}\mathbf{I}_m\dot{\boldsymbol{\chi}}^{-1}\mathbf{J}. \quad (\text{II.23b})$$

### II.2.3 Determination of the cable tensions

The determination of the cable tension vector  $\boldsymbol{\tau} \in \mathbb{R}^n$  is a function of the moving-platform pose and the wrench that the latter should support. It is about solving an equilibrium for a given pose  $\mathbf{x}$  of the end-effector. This equilibrium can be described in a matrix form as follows :

$$\mathbf{W}\boldsymbol{\tau} + \mathbf{w}_{ex} = \mathbf{0}. \quad (\text{II.24})$$

Two cases are discussed to solve Eq. (II.24). The first case is when the external wrench  $\mathbf{w}_{ex}$  gathers only the wrench due to gravity  $\mathbf{w}_g$  and to other wrench  $\mathbf{w}_e$  applied on the moving-platform. The second case is when the inertial effects due to the twist  $\dot{\mathbf{x}}$  and acceleration  $\ddot{\mathbf{x}}$  of the moving-platform are considered into the external wrench  $\mathbf{w}_{ex}$ . In this case, the system of equations to solve comes from the re-organization of Eq. (II.13) :

$$\mathbf{W}\boldsymbol{\tau} + \mathbf{w}_{ex} = \mathbf{0}, \quad (\text{II.25a})$$

$$\mathbf{w}_{ex} = \mathbf{w}_g + \mathbf{w}_e - \mathbf{M}^* \ddot{\mathbf{x}} - \mathbf{C}^* \dot{\mathbf{x}}. \quad (\text{II.25b})$$

The cables can only pull and not push the moving-platform. If the number of cables  $n$  is equal to the DOF  $m$ , the inversion of Eq. (II.24) is possible, as long as the wrench matrix  $\mathbf{W}$  is not singular, and the cable tension vector can be calculated as :

$$\boldsymbol{\tau} = -\mathbf{W}^{-1}\mathbf{w}_{ex}. \quad (\text{II.26})$$

In this case, the determination of cable tensions leads to only one solution. However, this tension set can present negative values. That means that one or more cable(s) may push the moving-platform, which is unfeasible.

When  $m < n$ , Eq. (II.24) may have an infinite number of solutions. Therefore, the redundancy allows to select a solution amongst the infinite set cable tension vectors satisfying some criteria. The problem of force distribution presents one important design issue for redundant actuated CDPRs, which is the determination of feasible cable force distribution<sup>1</sup>. The problem in the calculation of force distribution has been addressed in many scientific papers [PBM09, Pot14, GG11, BJS<sup>+</sup>09, MBHS08]. Optimization methods with user-defined cost function are usually employed to obtain a unique solution.

When the cables tension vector is equal to the calculated  $\boldsymbol{\tau}$ , the moving-platform of the CDPR is supposed to follow exactly the desired trajectory  $\mathbf{x}_{rg}$ . The cable length vector  $\mathbf{l}_{rg}$  corresponds to the unstrained cable length vector coming from the closed-loop constraints with respect to Eq. (II.4). No deviations or cable elongations

---

1. A cable force distribution is said to be feasible in a particular configuration and for a specified set of wrenches, if the tension forces in the cables can counteract any external wrench of the specified set applied to the end-effector [EUV04].

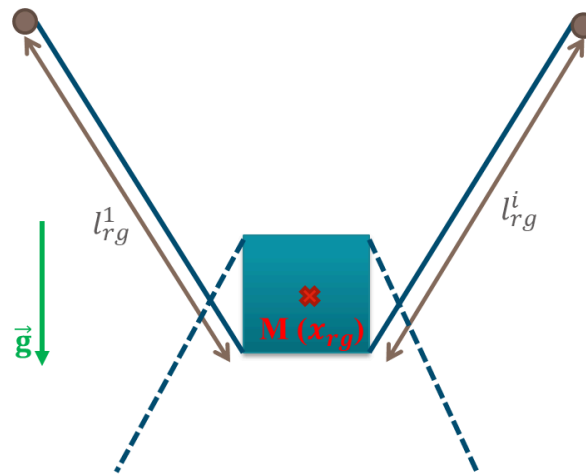


Figure II.3 – Schematic of the CDPDR rigid model : Planar example

are depicted. Some previous studies model the cables as massless rigid bodies. This assumption is usually valid for robots of reasonable size carrying light payloads. However, this assumption may not be valid for big cable-driven robots or for heavy payloads [RGK<sup>+</sup>09].

## II.3 Dynamic modeling considering cable stiffness : Elasto-static model

Section II.2 dealt with a dynamic model where no elongation of cables was considered. For that model, when the cables tension vector is equal to the calculated  $\boldsymbol{\tau}$ , the moving-platform of the CDPDR presents no deviation with respect to the desired pose  $\mathbf{x}_{rg}$ . However, as cables are a flexible, cable elongations occur once an external wrench is exerted onto the moving platform. The cable elongation is a function of its stiffness and the cable tension. As a consequence, some cable stiffness modeling are reviewed in Section II.3.1. A new non linear cable tension model is proposed in Section II.3.2. Indeed, Sec. II.3.2, deals with a dynamic model of CDPDR where cable elongations are taken into consideration. The corresponding model is named **elasto-static model**. Once the cables are isolated, their elongation is determined to come up with this elasto-static model. Knowing the effort applied on each cable, we can estimate its elongation based on the chosen cable tension model. When the elongation  $\delta \mathbf{l}_{es}$  is determined, the deviation of the moving platform  $\delta \mathbf{x}_{es}$  with respect to the desired pose  $\mathbf{x}_{rg}$  can be calculated through the geometrical model expressed by Eq. (II.4).

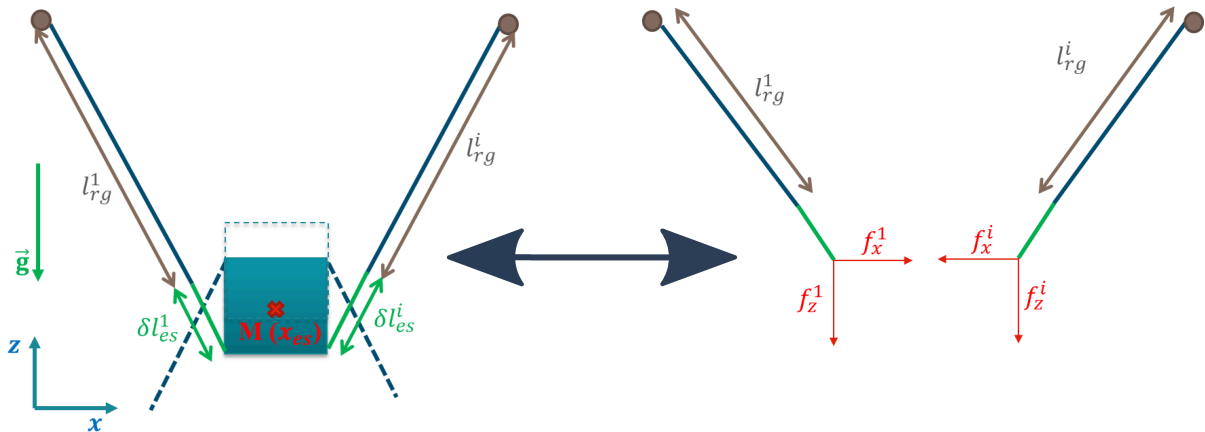


Figure II.4 – Schematic of the CDPR elasto-geometric model with straight cables : Planar example

### II.3.1 Cable stiffness modeling

Considering the physical cable characteristics, the compliance of cables has mainly two origins. The first one is the axial stiffness of the cables, which is associated with the elastic material modulus and the cable structure. The other one is the sag-introduced flexibility, which comes from the effect of cable weight onto the static cable profile. The sag-introduced flexibility corresponds to the gravitational potential energy stored in the cable.

#### II.3.1.1 Sag-introduced stiffness

Both axial and sag-introduced stiffness are discussed in the static and dynamic modeling of CDPRs. The elasto-sagging cable model resulting from the cable model [Irv92] takes into consideration both sag-introduced and axial stiffness of cables. It has been considered in several previous studies on large-dimension CDPRs [KZW06, DQZZ09, ZDDB08, DBDC10]. For instance, such a cable model was used for a 6-DOF cable-suspended parallel manipulator, while considering the dynamic stiffness of elastic sagging cables and experimental validations were performed in [YCD15, YCD14]. The elasto-sagging cable model describes the relationships between the force  ${}^i\tau_i = [{}^i\tau_{xi}, 0, {}^i\tau_{zi}]$  applied at the anchor point  $A_i$  of the  $i$ th

cable and the coordinates vector  ${}^i\mathbf{a}_i = [{}^ix_i, 0, {}^iz_i]$  of the same point resulting from the elasto-sagging cable model [Irv92] in  $\mathcal{F}_i$  as follows :

$${}^ix_i = \frac{{}^i\tau_{xi}l_{usi}}{ES} + \frac{|{}^i\tau_{xi}|}{\rho g} \left[ \sinh^{-1} \left( \frac{{}^i\tau_{zi}}{{}^i\tau_{xi}} \right) - \sinh^{-1} \left( \frac{{}^i\tau_{zi} - \rho gl_{usi}}{{}^i\tau_{xi}} \right) \right], \quad (\text{II.27a})$$

$${}^iz_i = \frac{{}^i\tau_{xi}l_{usi}}{ES} - \frac{\rho gl_{usi}^2}{2ES} + \frac{1}{\rho g} \left[ \sqrt{{}^i\tau_{xi}^2 + {}^i\tau_{zi}^2} - \sqrt{{}^i\tau_{xi}^2 + ({}^i\tau_{zi} - \rho gl_{usi})^2} \right], \quad (\text{II.27b})$$

where  $l_{usi}$  is the unstrained length of  $i$ th cable,  $g$  is the acceleration due to gravity,  $S$  is the cable cross sectional area,  $\rho$  denotes the cable linear mass and  $E$  the cable modulus of elasticity.

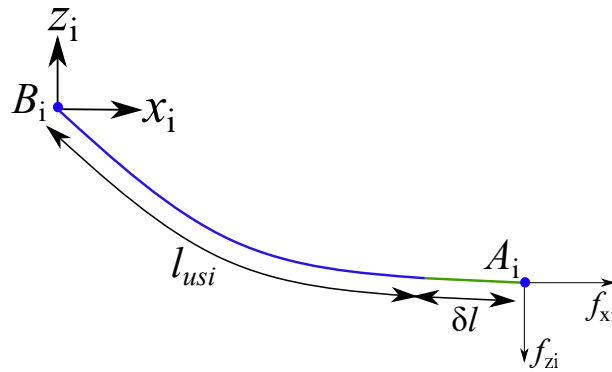


Figure II.5 – Schematic of elasto-sagging cable

As discussed in [KZW06], a CDPR can be described through the elasto-geometric model, which is based on geometric loop closure equations (Eq. (II.4)), cable sagging relationships (Eq. (II.27)) and static equilibrium equations (Eq. (II.24)). This leads to a system of non-linear equations. The Inverse Elasto-Geometric Modeling (IESM) of a CDPR aims at calculating the unstrained cable length for a given pose of its moving-platform. If both cable mass and elasticity are considered, the inverse kinematics of the CDPR and its static equilibrium equations will be solved simultaneously.

The Direct Elasto-Static Model (DESM) aims to determine the pose of the mobile platform for a given set of unstrained cable lengths. The constraints of the DESM are the same as those used to solve the IESM, *i.e.*, Eq. (II.4), Eq. (II.24) and Eq. (II.27). If the effect of cable weight on the static cable profile is non-negligible, the direct geometric model of CDPRs will be coupled with the static equilibrium of the moving-platform. For a  $m$  DOF CDPR with  $n$  driving cables, there are  $2n + m$

equations and  $2n + m$  unknowns. In this manuscript, the non-linear MATLAB<sup>®</sup> function *lsqnonlin* is used to solve the DESM.

Other works in the literature consider inextensible cables with non-negligible mass [KZW06, Ars13b, RGK<sup>+</sup>09] based on the well-known catenary cable model established by Irvine [Irv92], but neglecting the cables elasticity [GCRB12].

### II.3.1.2 Axial stiffness

For the dynamic and workspace analysis of CDPRs, the cables are often considered either rigid or elastic, namely, with an axial stiffness [KT15]. Simplified cable models are usually used because they lead to lower computing-time [BG05]. However, those simplified models may lead to modeling errors. These errors should be analyzed and corrected to satisfy the positioning accuracy of the robot. To better understand the dynamic behavior of CDPRs with long cables, a dynamic model where each cable is considered with distributed mass and time-varying length is addressed in [DA15]. The dynamic equations are derived using Hamilton principle. The resulting infinite dimensional problem is transformed into a finite dimensional one using the assumed-mode method. Vibration analysis in both directions were made and it turns out that the transversal vibrations remain negligible with respect to the axial vibrations for several configurations [DM09].

There are few studies in the literature about the dynamic analysis of CDPRs with long sagging cables, and to the best of our knowledge only cable linear axial stiffness formulation is considered. The dynamic stiffness analysis of CDPRs is made under the assumption that dynamic loads induce only small elongations of the cables. The cable tension is usually considered proportional to the variations in the cable length for a constant stiffness coefficient. Therefore, such a model is not valid when cables are subjected to high strains due to large dynamic oscillations or quick cable-length variations. As a consequence, Section II.3.2 aims at expressing a non-linear cable tension model [BJLP16] to be used for dynamic and oscillatory motions of CDPRs with cables subjected to fast varying lengths. This cable tension model reveals a softening behavior when strains become large.

## II.3.2 Linear and non-linear cable tension models

It is obvious that the consideration of sag has an important impact on the CDPR modeling. However, the assumption of a negligible sag is validated along

the trajectory mapped by the moving-platform, either when the sag to span ratio of the cable remains lower than  $1/20$  [Sta91], or by a simple performance criterion ensuring that the effect of gravity on a cable can be neglected [OPND<sup>+</sup>09]. Under these assumptions, the CDPR cables are assumed to keep linear shape along a trajectory and their stiffness is equivalent to stiffness related to the elasticity effects.

Classically, when the cables of a CDPR are tensed along a prescribed trajectory and their tension remains in an elastic range, the total time-depending tension in a cable is expressed as follows :

$$\tau(t) = k(t) \delta l_i(t) + \tau_0, \quad (\text{II.28})$$

where :

- $\tau(t)$  is the cable tension,
- $\delta l_i(t)$  is its elongation,
- $k(t)$  is its stiffness,
- $E$  is its modulus of elasticity,
- $S$  is its cross sectional area,
- $l(t)$  is its length,
- $\tau_0$  is its tension at the initial time ( $t = 0$  s).

Here, the length  $l_i$  of the  $i$ th cable at each time  $t$  can be expressed as follows :

$$l_i(t) = l_{i,0} + \delta l_i(t) - \int_0^t V_i(t) dt, \quad i = 1, \dots, n \quad (\text{II.29})$$

where  $V_i$  is the linear velocity at the entrance of the  $i$ th pulley,  $l_{i,0}$  is the  $i$ th cable length at time  $t = 0$  s under the effect of the initial tension  $\tau_{i,0}$  defined with respect to the static equilibrium and  $\delta l_i$  is the elongation of the  $i$ th cable.

This linear formulation of the cable tension is commonly used and it shows a behavior similar to a linear spring with constant stiffness  $k$ . The classical linear tension formulation expressed in Eq. (II.28) can not satisfy non-linear cable elasticity or viscosity resulting from dynamic phenomena with high cable-length variations. As a result, it cannot be used for the dynamic modeling of CDPR achieving high velocities and accelerations. Therefore, a non-linear tension formulation is required in such a case. The work presented in [BJLP16] is adopted regarding that it provides a total non-linear tension formulation valid for high dynamic applications. Accordingly, this paper aims to integrate this new tension formulation in CDPR

dynamic modeling and to analyze its effect on the dynamic responses of the CDPR end-effector.

According to [BJLP16], the non-linear formulation for cable tension is defined as follows. Applying the general Hooke's law  $\sigma(t) = E\varepsilon(t)$ , where  $d\varepsilon(t) = \frac{dl(t)}{l(t)}$ , and assuming that cable tension, with constant cross sectional area  $S$ , can be written as  $\tau(t) = S\sigma(t)$ , the time derivative of the cable tension can be expressed as :

$$\dot{\tau}(t) = \frac{ES}{l(t)}\dot{l}(t). \quad (\text{II.30})$$

Equation (II.30) shows that the time derivative of cable tension depends on the cable instantaneous length. The non-linear tension formulation of the cable tension is obtained by integrating Eq. (II.30) :

$$\tau(t) = ES \ln\left(\frac{l(t)}{l_0}\right) + \tau_0. \quad (\text{II.31})$$

This non-linear tension expression is valid for high dynamic systems and does not restrict the applications with small strains. As the cable is considered without inertia, the longitudinal wave propagation is possible and a non-linear cable behavior exists. This non-linear tension formulation is valid when the rate of strain is much smaller than the longitudinal wave velocity into the cable, which is usually true for flexible wires used in high dynamic cable systems such as high-speed CDPRs.

### II.3.2.1 Non-linear tension of cables with linear damper

Cables used in CDPR have a frequency-dependent dynamic modulus of elasticity as shown in Fig. II.6, which plots the Hysteresis loops for a 4 mm steel wire cable preloaded at 1500 N with force controlled sine waves applied at 0.1, 1, 2, 5, 10, and 20 Hz. More details in the determination of cable dynamic modulus of elasticity and damping parameters are presented in Appendix A.1.2.

To better predict the dynamic behavior of cables and the CDPR response, we can account for the Maxwell model to integrate a viscous damper to the elastic cable model [RR06]. For an elastic cable with a linear viscous damper, the cable stress is written as follows :

$$\sigma(t) = E' \varepsilon(t) + c\dot{\varepsilon}(t), \quad (\text{II.32})$$

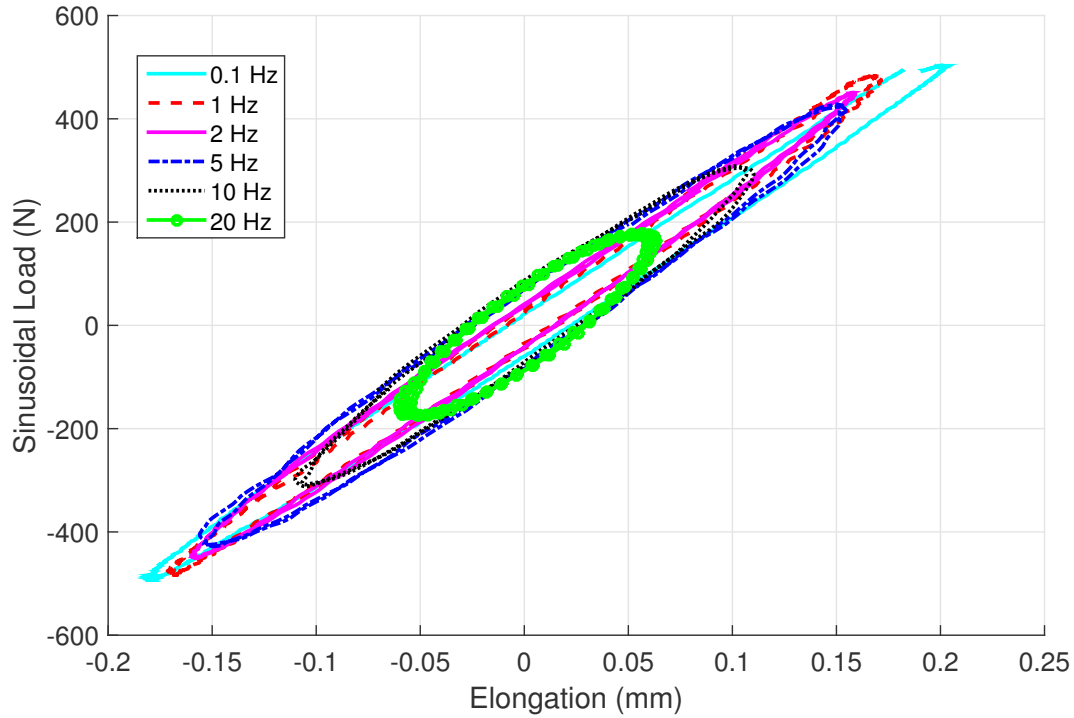


Figure II.6 – Hysteresis loops for a 4 mm steel wire cable preloaded at 1500 N with force controlled sine waves applied at 0.1, 1, 2, 5, 10, and 20 Hz

where  $E'$  is the real part of the dynamic modulus of elasticity and  $c$  is the corresponding damping coefficient.

As  $\tau(t) = S\sigma(t)$  for a constant cross sectional area cable and as the differentiation of deformation  $\dot{\epsilon}(t)$  is expressed as  $\frac{\dot{l}(t)}{l(t)}$ , we can write :

$$\dot{\tau}(t) = \frac{E'S}{l(t)}\dot{l}(t) + \frac{cS}{l(t)} \left( \ddot{l}(t) - \frac{\dot{l}^2(t)}{l(t)} \right) . \quad (\text{II.33})$$

By integrating Eq. (II.33), the new tension formulation considering the cable damping is defined as follows :

$$\tau(t) = E'S \ln \left( \frac{l(t)}{l_0} \right) + cS \frac{\dot{l}(t)}{l(t)} + \tau_0 . \quad (\text{II.34})$$

This formulation considers the non-linear elastic behavior of the cable and its damping. It will be valid even if the system presents high dynamics and large strains in the cables.

The cable tension vector is determined as explained in Section II.2.3 basing on the rigid model. When the cable is supposed to keep linear shape along the

prescribed trajectory, either the linear or the non-linear cable tension model should be taken to determine the cable elongations depending on the CDPR application.

Note that the choice of the suitable model with regard to the targeted application and CDPR configuration is discussed in Chapter III. Despite that cable elongations are considered in this section, a limitation of this modeling is that the interaction of cables with the complete system is not considered and then no oscillation is considered.

## II.4 Elasto-dynamic modeling

In real applications of CDPRs, the elongation of cables and their interaction with the environment do not occur separately. This fact can result in unwanted oscillations of the end-effector, which are not predicted through the elasto-static model. The proposed elasto-dynamic model aims to predict the dynamic behavior of the CDPR, while being open-loop torque controlled.

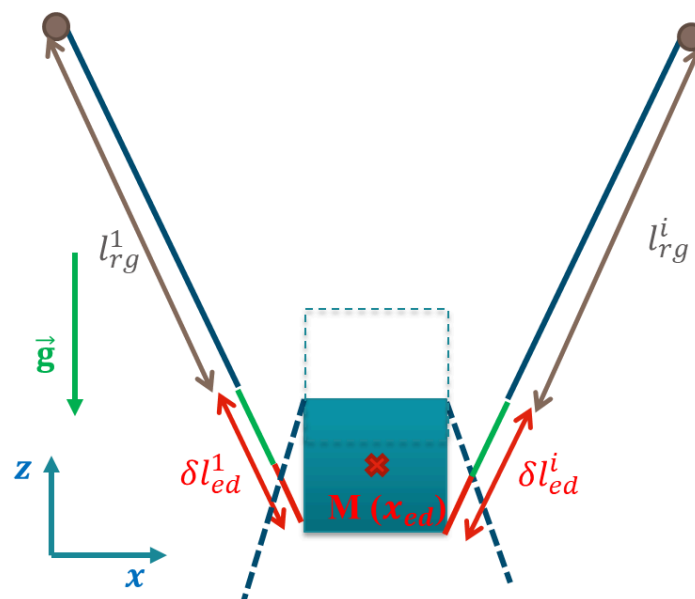


Figure II.7 – Schematic of the CDPR elasto-dynamic model : Planar example

The CDPR elasto-dynamic model takes into account the oscillatory and dynamic behavior of the end-effector due to cable elongations. Here, the cables are no-longer isolated and are affected by the end-effector dynamic behavior. As illustrated in Fig. II.7, the cables of the elasto-static model of CDPRs present a deviation with respect to the rigid model as cable elasticity is considered. In addition to this deviation, the elasto-dynamic model presents another part (red part) of deviation

which corresponds to the dynamic effects. The length of the  $i$ th cable in the elasto-dynamic model can be expressed as follows :

$$l_{ed}^i = l_{rg}^i + \delta l_{ed}^i, \quad (\text{II.35a})$$

$$\delta l_{ed}^i = \delta l_{es}^i + \delta l_{vib}^i. \quad (\text{II.35b})$$

$\delta l_{ed}^i$  being the  $i$ th cable elongation assessed by considering cable elasticity and oscillations,  $\delta l_{vib}^i$  being the cable elongation due to the vibratory effects only.

Cable elongations make the end-effector deviate from its desired pose  $\mathbf{x}_{rg}$ . As a result, the real end-effector pose is expressed as :

$$\mathbf{x}_{ed} = \mathbf{x}_{rg} + \delta \mathbf{x}_{ed}. \quad (\text{II.36})$$

The end-effector displacement leads to some variations in both cable lengths and cable tensions. Indeed, the  $i$ th cable tension  $\tau_{ed}^i$  obtained from the elasto-dynamic model differs from  $\tau^i$ , namely :

$$\tau_{ed}^i = \tau^i + \delta \tau_{ed}^i. \quad (\text{II.37})$$

The expression of  $\tau_{ed}^i$  as a function of the  $i$ th cable stiffness and depends on the chosen cable tension model. For example, when the linear cable tension is considered, the elasto-dynamic tension of the  $i$ th cable is expressed as :

$$\tau_{ed}^i = \tau^i + \delta \tau_{ed}^i = ES \frac{\delta l_{ed}^i}{\delta l_{ed}^i + l_{rg}^i}. \quad (\text{II.38})$$

When the winches are fixed below the pulleys, cable length is divided into two parts as shows Fig. II.8. The first length  $l_{ed}^i$  is variable and corresponds to the distance between  $A_i$  and  $B_i$ . It is influenced by cable elongations. The second is not variable and is called a dead length linking between the  $i$ th drum and  $B_i$ . In this case, the linear stiffness of a cable becomes :

$$k_i(t) = \frac{ES}{l_{ed}^i + l_{dead}^i}, \quad (\text{II.39})$$

where  $l_{dead}^i$  is the dead length of  $i$ th cable. In this case, the cable tension expression becomes :

$$\tau_{ed}^i = ES \frac{\delta l_{ed}^i}{l_{ed}^i + l_{dead}^i} = ES \frac{\delta l_{ed}^i}{\delta l_{ed}^i + l_{rg}^i + l_{dead}^i}. \quad (\text{II.40})$$

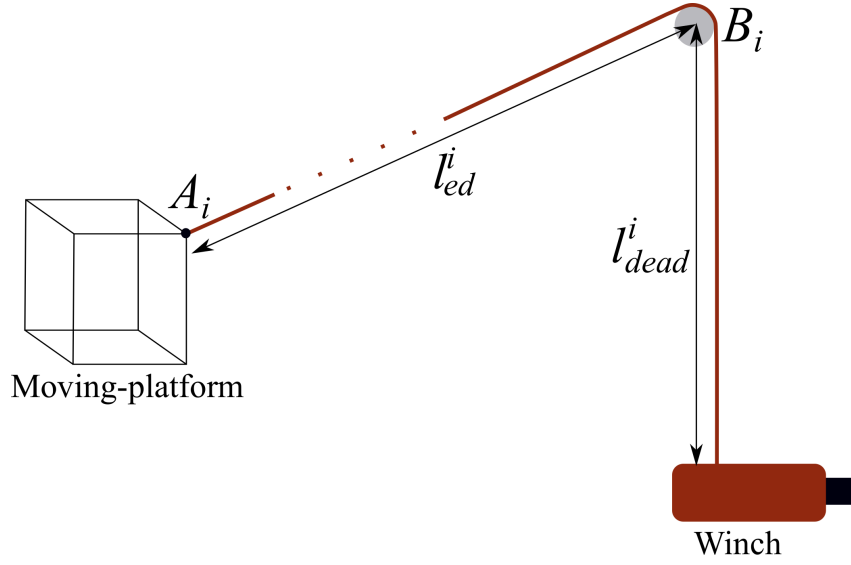


Figure II.8 – Cable parametrization while considering dead length

The CDPR elasto-dynamic model takes the form :

$$\mathbf{M} \ddot{\mathbf{x}}_{ed} + \mathbf{C} \dot{\mathbf{x}}_{ed} = \mathbf{W}_{ed} (\boldsymbol{\tau} + \delta\boldsymbol{\tau}_{ed}) + \mathbf{w}_{ex}, \quad (\text{II.41})$$

where  $\mathbf{W}_{ed} = \mathbf{W}(\mathbf{x}_{ed})$  is the CDPR wrench matrix expressed at the end-effector pose  $\mathbf{x}_{ed}$ . Once the pose  $\mathbf{x}_{ed}$  and the cable tension vector  $\boldsymbol{\tau}_{ed}$  are calculated, the cable elongation vector  $\delta\mathbf{l}_{ed}$  of the elasto-dynamic CDPR model can be determined. Details about the elasto-dynamic model resolution are presented in Appendix C.2.

The measured joint coordinates of the actuators depict neither the vibratory effects nor the cable elongations. The use of the elasto-dynamic model for closed-loop control should be useful to compensate the unwanted effects that cannot be measured by the encoders. The proposed pre-compensation methodology will be discussed in Chapter IV.

## II.5 Summary of the chapter

This chapter presented the dynamic modeling of a CDPR with  $n$  cables and  $m$  DOF, which is fundamental for trajectory tracking. Some CDPR stiffness modeling were discussed. A new non-linear cable tension model for CDPRs was proposed to deal with axial cable vibrations. This non-linear cable tension model expresses the relationship between cable tension and the resulted elongation. It is valid for

---

fast time-varying cable tensions with large strains. An elasto-dynamic model of CDPRs was proposed. It anticipates the full dynamic behavior of the mechanism. Accordingly, one contribution of this chapter deals with a simulation model of CDPRs, including the vibratory effects, cable elongations and their interaction with the whole system. Despite the elasto-static model takes into account cables elasticity, a weakness of this model lies in the absence of the dynamic effects due to the interaction of the cables with the whole system. The elasto-dynamic model aims to remedy this weakness and it depicts the oscillatory behavior of the moving-platform when the latter follows a prescribed trajectory.

Verifying the validity and identifiability of such predictive models is mandatory for control purposes. Accordingly, the next chapter is about the static and dynamic sensitivity analysis of CDPRs in order to end up with a robust control scheme.



# III

---

## Robustness analysis of CDPR

### Contents

---

III.1 Introduction ·····	71
III.2 Error sources affecting CDPR accuracy ·····	72
III.3 Sensitivity analysis of CDPR accuracy to modeling ·····	77
III.4 Uncertainty analysis of CDPR to parameters ·····	89
III.5 Summary of the chapter ·····	105

---

### III.1 Introduction

To deal with a robust control model for CDPR, robustness analysis should be performed through a sensitivity analysis and an uncertainty analysis. While sensitivity analysis is done to make decisions on the choice of CDPR model with respect to the target application, uncertainty analysis of the chosen model is performed to highlight crucial parameters that should be the focus of attention. The input parameters used to describe the robot model for the control loop are uncertain, *i.e.*, only known within certain probability distribution of variable. To overcome the effects of uncertainties, uncertainty analysis should be done to determine the design hypothesis allowing the CDPR to be robust to changes in system parameters or disturbances while performing prescribed tasks. On these grounds, the objectives of this chapter are :

- Sensitivity analysis of CDPR accuracy to modeling type.
- Uncertainty analysis of CDPR accuracy.

## III.2 Error sources affecting CDPR accuracy

CDPR accuracy can be degraded due to error sources coming either from modeling or uncertainties on input parameters. It should be noted that not all properties affect every CDPR prototype in the same way. Many physical properties determine how much influence an uncertain parameter has on the CDPR response. However, some generalizations can be made, and some predefined assessments help recognize which parameters have the highest effect on the CDPR accuracy.

### III.2.1 Modeling

The choice of CDPR model for control purposes is not obvious. It depends strongly on the CDPR configuration and the target task. Different are the levels of CDPR modeling for control purposes. They can be classified with respect to the level of cable stiffness modeling where we consider either the axial stiffness, either the sag-introduced stiffness or both of them (Sec. II.3.1). Note that linear and non-linear cable tension models were proposed for non-sagging cables (Sec. II.3.2). Besides, the prediction of CDPR accuracy is not the same when using the rigid (Sec. II.2), elasto-static (Sec. II.3) or the elasto-dynamic (Sec. II.4) models as a reference model for CDPR control.

### III.2.2 Parameters

It is not obvious to investigate all error sources to the same level of detail. The error modeling includes all the error sources which have been covered in literature [ZDWK14, KZW06] and some additional ones which are expected to be equally significant. For the uncertainty analysis, geometrical and mechanical error sources are considered to investigate their effect onto the static deflection of the moving-platform under an external load.

#### III.2.2.1 Geometrical parameters

The geometrical errors can be divided into base frame geometrical errors and moving-platform geometrical errors and mainly due to manufacturing errors.

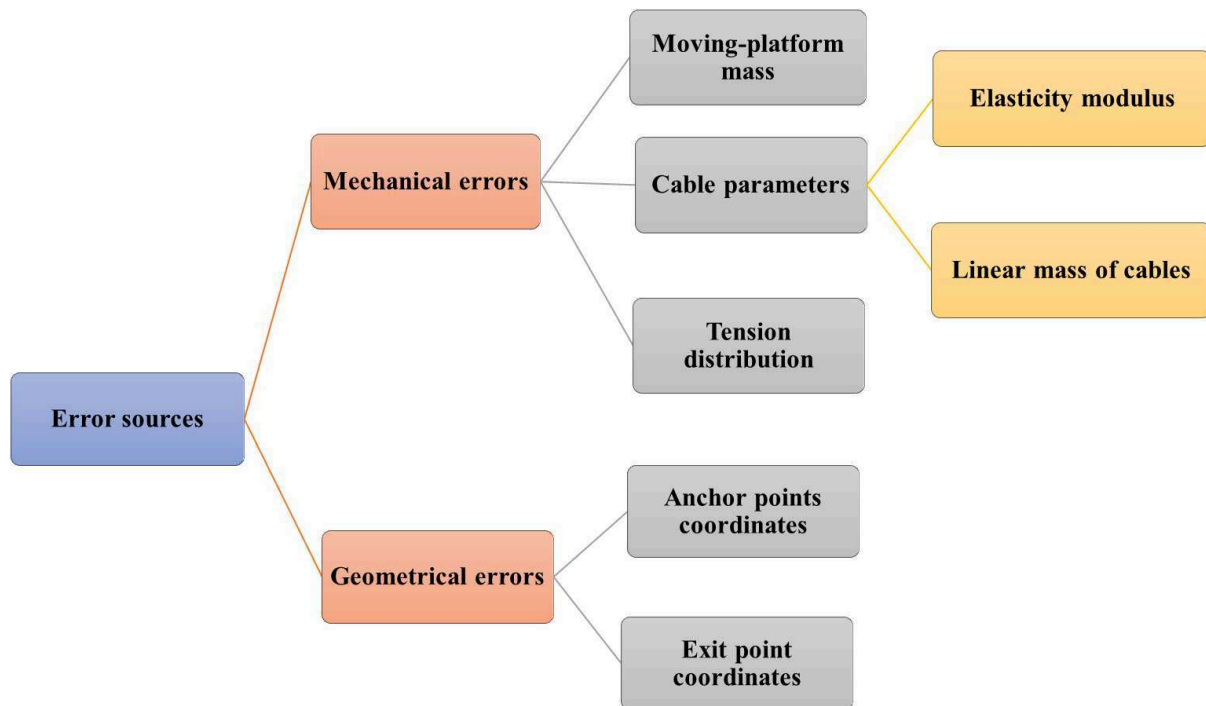


Figure III.1 – Error sources affecting CDPR accuracy

#### III.2.2.1.1 Base frame geometrical errors

The base frame geometrical errors are described by vectors  $\delta\mathbf{b}_i$ , the variation in vector  $\mathbf{b}_i$ ,  $i=[1..n]$ . As the point  $B_i$  is considered as part of its corresponding pulley, it is influenced by the elasticity of the pulley mounting and its assembly tolerance.  $\mathbf{b}_i$  is particularly influenced by pulleys tolerances and reconfigurability impact.

#### III.2.2.1.2 Moving-platform geometrical errors

The moving-platform geometrical errors are described by vectors  $\delta\mathbf{a}_i$ , the variation in vector  $\mathbf{a}_i$ ,  $i=[1..n]$ , and  $\delta\mathbf{g}$ , the uncertainty vector of the gravity center position  $G$  of the moving-platform. This latter is often supposed to coincide with its geometrical center  $P$ . This hypothesis means that the moments generated by an inaccurate knowledge of the gravity center position or by its potential displacement are neglected. This is never perfectly realized since the exact position of the mass center is often uncertain. The Cartesian coordinate vector of the geometric center  $P$  does not change in frame  $\mathcal{F}_p$ , but strongly depends on the real coordinates of exit points  $A_i$  that are related to uncertainties in mechanical welding of the hooks and in moving-platform assembly.

### III.2.2.2 Mechanical parameters

The mechanical errors of the CDPR are described by the uncertainty in the moving-platform mass ( $\delta m_{ee}$ ) and the uncertainty on the cables mechanical parameters ( $\delta \rho$  and  $\delta E$ ). Besides, uncertainties in the cables tension  $\delta \boldsymbol{\tau}$  affect the error model. As a result,  $(3 + n)$  mechanical error sources are taken into account.

#### III.2.2.2.1 End-effector mass

As the moving-platform is a mechanically welded structure, there may be some differences between the moving-platform mass and inertia matrix given by the CAD software and the real ones. The moving-platform mass and inertia may also vary in operation which requires the involvement of these changes while modeling. In this manuscript, moving-platform mass uncertainty  $\delta m_{ee}$  is about  $\pm 10\%$  the nominal mass.

#### III.2.2.2.2 Cables parameters

##### III.2.2.2.2.1 Linear mass

The uncertainty of this parameter can be calculated from the measurement procedure as :

$$\delta \rho = \frac{m_c \delta l + l \delta m_c}{l^2}, \quad (\text{III.1})$$

where  $m_c$  is the measured cable mass for a cable length  $l$ .  $\delta l$  and  $\delta m_c$  are respectively the measurement errors of the cable length and mass.

##### III.2.2.2.2.2 Modulus of elasticity

The error modeling of the modulus of elasticity of cables is based on experimental data. The identification method of the modulus of elasticity of a steel wire cable is specified in section (A.1.1). The elasticity modulus or Young's modulus is the ratio of stress along an axis to strain along that axis within a specified load range and strain rate range. It amounts to an elastic material stiffness. The modulus of elasticity of a wire cable does not depend solely on the properties of the wire material, but on the wires layout and the load history too.

A 4 mm diameter steel cable consisting of 18 strands twisted around a steel core used for the CAROCA prototype is taken as an illustrative example. Each strand of this cable is made up of 7 steel wires (Fig. A.2). The breaking force of

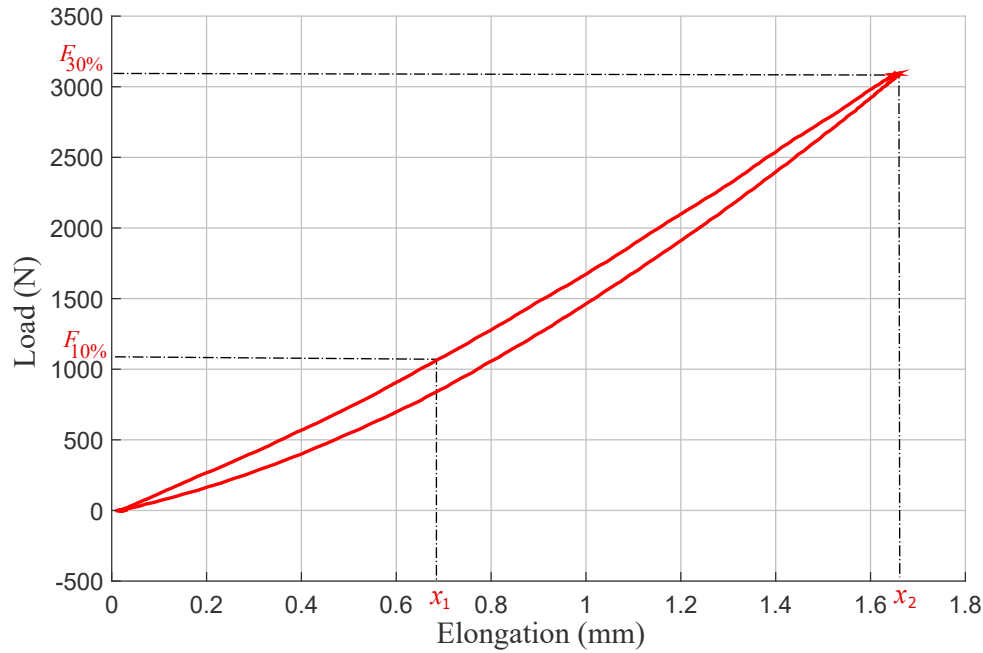


Figure III.2 – Load-elongation diagram of a steel wire cable measured in steady state conditions at the rate of 0.05 mm/s

this cable is equal to 10.29 kN. Based on experimental data presented in Fig. III.2, Table III.1 presents the modulus of elasticity of a steel wire cable for different operating margins, when the cable is in loading or unloading phase. This modulus is calculated as follows :

$$E_{p-q} = l_c \frac{F_{q\%} - F_{p\%}}{S(x_q - x_p)}, \quad (\text{III.2})$$

where  $S$  is the metallic cross-sectional area, i.e. the value obtained from the sum of the metallic cross-sectional areas of the individual wires in the rope based on their nominal diameters.  $x_p$  and  $x_q$  are the elongations at forces equivalent to  $p\%$  and  $q\%$  ( $F_{p\%}$  and  $F_{q\%}$ ), respectively, of the nominal breaking force of the cable measured during the loading path (Fig. A.3).  $l_c$  is the measured initial cable length.

Table III.1 – Modulus of elasticity while loading or unloading phase

$E_{p-q}$ (GPa)	$E_{1-5}$	$E_{5-10}$	$E_{5-20}$	$E_{5-30}$	$E_{10-15}$	$E_{10-20}$	$E_{10-30}$	$E_{20-30}$
Loading	72.5	83.2	92.7	97.2	94.8	98.3	102.2	104.9
Unloading	59.1	82.3	96.2	106.5	100.1	105.1	115	126.8

For a given range of loads (Tab. (III.1)), the uncertainty on the modulus of elasticity depends only on the corresponding elongations and tensions measurements.

In this case, the absolute uncertainty associated with applied force and resulting elongation measurements from the test bench outputs is estimated to be  $\pm 1$  N and  $\pm 0.03$  mm, respectively ; so, an uncertainty of  $\pm 2$  GPa can be applied to the calculation of the modulus of elasticity.

According to the International Standard ISO 12076, the modulus of elasticity of a steel wire cable is  $E_{10-30}$ . However, the CDPR cables do not work always between  $F_{10\%}$  and  $F_{30\%}$  in real life and the cables can be in loading or unloading phase. The mechanical behavior of cables depends on moving-platform dynamics, which affects the variations in cable elongations and tensions. From Table (III.1), it is apparent that the elasticity moduli of cables change with the operating point changes.

For the same applied force, the modulus of elasticity for loaded and unloaded cables are not the same. While the range of the moving-platform loading is unknown, a large range of uncertainties on the modulus of elasticity should be defined as a function of the cable tensions.

### III.2.2.2.3 Tension distribution

Two cases of uncertainties of force determination can be defined depending on the control scheme :

- The first case is when the control scheme gives a tension set-point to the actuators resulting from the force distribution algorithm. If there is no feedback about the tension measurements, the range of uncertainty is relatively high because of the difference between cable tensions and motor set-point coming from tension distribution algorithms. Generally, the effort of compensation does not consider dry and viscous friction in cable drum and pulleys. This non-compensation leads to errors and delay [DWS90] that degrade the CDPR control performance. That leads to a large range of uncertainties in tensions.
- The second case is when the tensions are measured and used in the feedback controller. If measurement signals are very noisy, amplitude peaks of the correction signal may lead to a failure of the force distribution. Such a failure may also occur due to variations in the moving-platform and pulleys parameters.

Here, the deviation is defined based on the measurement tool precision.

Cable tension uncertainty is a function of cable parameter uncertainties, mainly the uncertainty on the modulus of elasticity. There is no need to add tension uncertainties to the analysis as the variation of tensions is translated by a variation of the modulus of elasticity.

### III.3 Sensitivity analysis of CDPR accuracy to modeling

Sensitivity analysis while considering the sag-introduced stiffness has been already done [KZW06]. It is obvious that the consideration of sag has an important impact on the CDPR modeling. However, this work interests in the influence of the cables elasticity and the effects generated by the cable elongations. For this fact, we work under the assumptions that cables keep linear shape along a trajectory and their stiffness is equivalent to stiffness related to the elasticity effects. Here, the assumption of a negligible sag is validated along the trajectory mapped by the moving-platform, either when the sag to span ratio of the cable remains lower than 1/20 [Sta91], or by a simple performance criteria ensuring that the effect of gravity on a cable can be neglected [OPND<sup>+</sup>09].

#### III.3.1 Linear and non-linear cable tension models

To check the sensitivity of the CDPR to cables modeling, a comparison between the CDPR responses while using the linear and the non-linear tension formulation of cables is made. For this fact, the cable tension  $\tau_i$  appearing in Eq. (II.24) is replaced by either the linear tension expression (Eq. (II.28)) or the non-linear one (Eq. (II.31)). This section aims to compare the dynamic responses of three prototypes with different configuration and size, while using linear or non-linear cable tension formulations. For this purpose, a smooth helical trajectory is defined to be followed by the end-effector.

The nominal lengths of the cables are calculated while solving the ideal inverse kinematics model expressed by Eq. (II.5) without considering cable mass and elasticity. These cable lengths are then used to determine the velocities at the pulleys entrances  $V_i$ ,  $i = [1..n]$ , that allow the end-effector to follow the desired trajec-

tory using Eq. (II.29). MATLAB® routine ode45 is then employed for numerical integration to calculate the resulted tensions and elongations while solving the system of non-linear equations respecting the Fundamental Principle of Dynamics (Eq. (II.13)).

### III.3.1.1 Illustrative example

This section aims to present numerical results associated to the dynamic behavior of the 3-DOF CDPR, where three long cables make the end-effector move. The position vector of the exit points in the global frame are :

$\mathbf{b}_1 = [0, 50, 50]^T$  m,  $\mathbf{b}_2 = [0, -50, 50]^T$  m and  $\mathbf{b}_3 = [86.60, 0, 50]^T$  m. The mass of the end-effector is  $m_{ee} = 300$  kg.

An example of a circular helical trajectory from static equilibrium to steady state is proposed to evaluate the difference between the linear and non-linear tension formulations. The end-effector of the CDPR under study is moved from point  $P_1$  of Cartesian coordinate vector  $\mathbf{p}_1 = [28.86, 0, 5]^T$  m to point  $P_2$  of Cartesian coordinate vector  $\mathbf{p}_2 = [28.86, 0, 20]^T$  m tracking a circular helix, which is defined by the following Cartesian equations (Fig. IV.5(b)) :

$$x(t) = R \cos(t_\alpha) + \beta_0, \quad (\text{III.3a})$$

$$y(t) = R \sin(t_\alpha) + \beta_1, \quad (\text{III.3b})$$

$$z(t) = p_t t_\alpha + \beta_2, \quad (\text{III.3c})$$

where

$$t_\alpha = a_5 \left( \frac{t}{t_{sim}} \right)^5 + a_4 \left( \frac{t}{t_{sim}} \right)^4 + a_3 \left( \frac{t}{t_{sim}} \right)^3 + a_2 \left( \frac{t}{t_{sim}} \right)^2 + a_1 \left( \frac{t}{t_{sim}} \right) + a_0. \quad (\text{III.4})$$

The coefficients of the five-order polynomial  $t_\alpha$  are chosen in such a way that the Cartesian velocities are null at the beginning and at the end of the simulation

(Fig. III.3(b)).  $R$  is the radius of the helix,  $p_t$  is its pitch,  $\beta_0$ ,  $\beta_1$  and  $\beta_2$  are constants. The resulting Cartesian velocities of the end-effector are expressed as follows :

$$\dot{x}(t) = -R\dot{t}_\alpha \sin(t_\alpha), \quad (\text{III.5a})$$

$$\dot{y}(t) = R\dot{t}_\alpha \cos(t_\alpha), \quad (\text{III.5b})$$

$$\dot{z}(t) = p_t \dot{t}_\alpha. \quad (\text{III.5c})$$

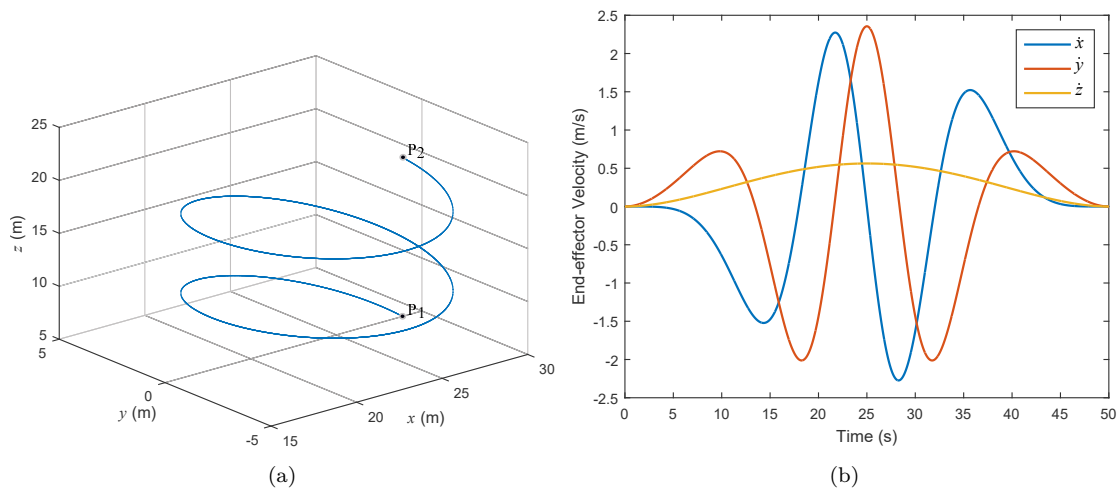


Figure III.3 – Circular helical trajectory : (a) Trajectory and (b) velocities of the end-effector

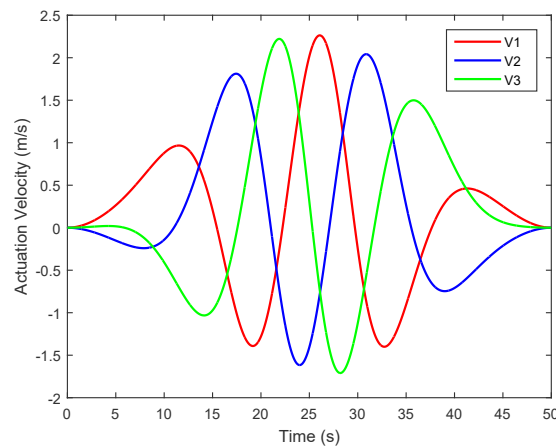


Figure III.4 – Cable linear velocity profiles

For this case study, the chosen parameters are :  $a_5 = 36\pi$ ,  $a_4 = -90\pi$ ,  $a_3 = 60\pi$ ,  $a_2 = a_1 = a_0 = 0$ ,  $p = 0.5$  m,  $\beta_0 = 23.86$  m,  $\beta_1 = 0$  m,  $\beta_2 = 5$  m,  $R = 5$  m and  $t_{sim} = 50$  s. The initial cables lengths are  $l_{1,0} = l_{2,0} = l_{3,0} = 73.2$  m. The simulation starts from the static equilibrium defined with the following initial conditions :  $T_{1,0} = T_{2,0} = T_{3,0} = 1594.1$  N,  $\delta\dot{l}_{1,0} = \delta\dot{l}_{2,0} = \delta\dot{l}_{3,0} = 0$  m/s and  $\delta\ddot{l}_{1,0} = \delta\ddot{l}_{2,0} = \delta\ddot{l}_{3,0} = 0$  m/s<sup>2</sup>.

The cross sectional area of cables is  $S = 7.1675 \times 10^{-6}$  m<sup>2</sup> and the quasi-static equivalent modulus of elasticity is  $E = 102.2$  GPa.

Figure III.4 illustrates the cable linear velocities as a function of time for the end-effector to follow the desired trajectory shown in Fig. III.3(a). The time histories of the tension, the elongation and the strain (defined as  $s_i = \frac{\delta l_i(t)}{l_i(t)}$ ) of each cable when the end-effector moves from point  $P_1$  to point  $P_2$  following the circular helical trajectory are plotted in Fig. III.5.

The comparison between the simulation results obtained with the linear tension (Dash-dot lines) and the non-linear tension formulation (continuous lines) is made. In both cases, the cable tensions remain positive which is a necessary condition for CDPR control. It can also be noticed that the generated trajectory has sufficient smoothness properties to avoid the excitation of the mechanical resonances of the end-effector suspended on the global cables stiffness. The loading frequency is only defined by the time variation of the cable linear velocity (Fig. III.4).

These simulation results show that the difference in terms of cable elongation response can reach up to 2.4 mm at 27.5 s for the first cable, representing 14 % of the global instantaneous elongation. The difference in terms of strain achieves 0.003 %, representing 12 % of the global instantaneous strain in cable 1. The maximum difference is about 2.9 mm for the second cable at 39 s. Note that the cable tensions are the same whichever tension formulation is used. Tension curves are superimposed (Figures III.5(a), III.5(d) and III.5(g)). The non-linear tension formulation reveals a softening behavior when strains become large. In this particular example of large-dimensions CDPR, the consequences on the evaluation of the end-effector position tracking error can be quite important as depicted in Fig. III.6. The positioning error, which is the difference between the desired position of the end-effector and the real one, is assessed along each axis of the base frame. The end-effector trajectory

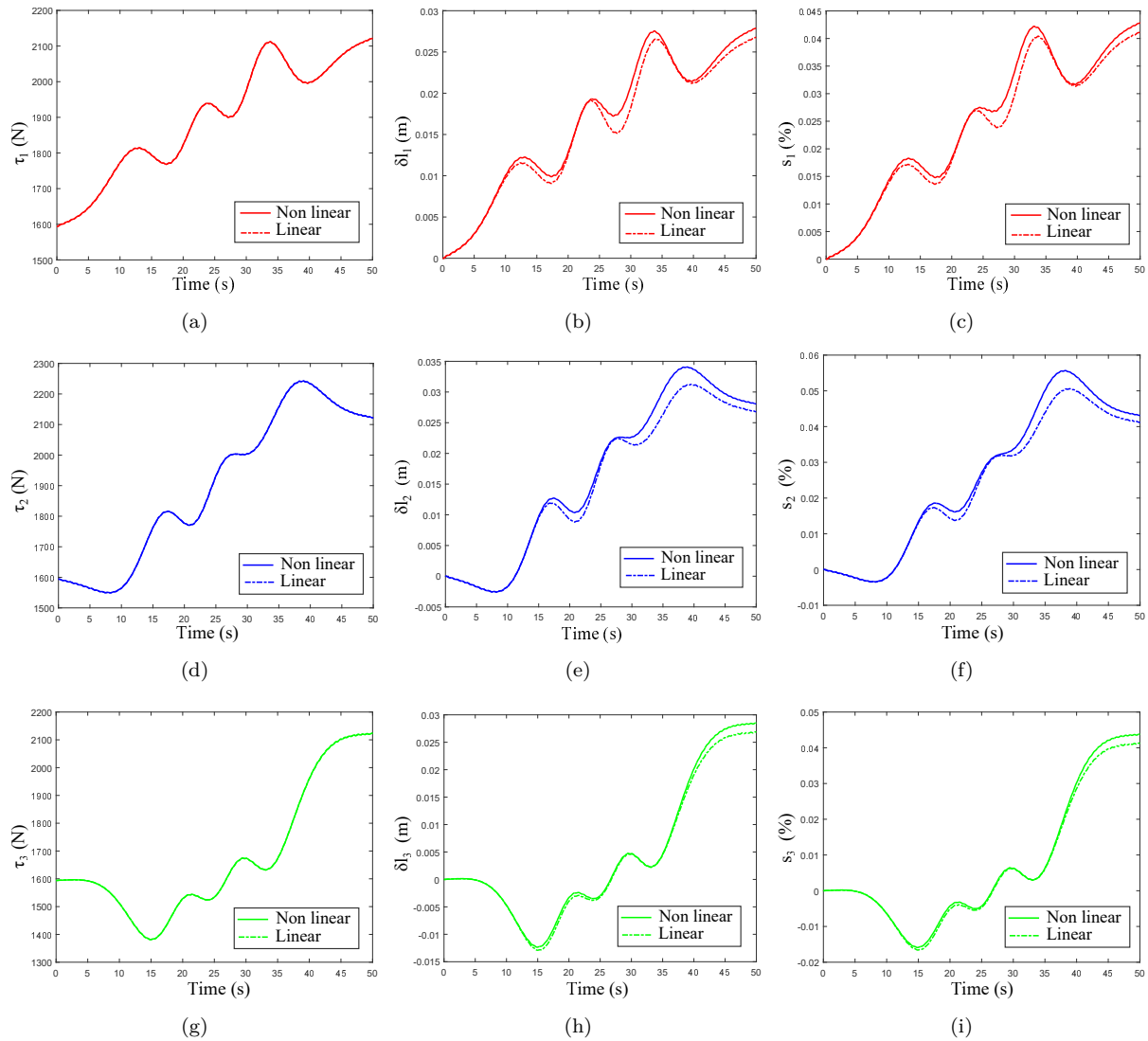


Figure III.5 – Comparison between linear and non-linear tension formulations : Tension, elongation and strain for three cables. Time history of (a)  $\tau_1$ , (b)  $\delta l_1$ , (c)  $s_1$ , (d)  $\tau_2$ , (e)  $\delta l_2$ , (f)  $s_2$ , (g)  $\tau_3$ , (h)  $\delta l_3$ , and (i)  $s_3$

can differ up to 1.5 mm along the  $x$ -axis, 1.4 mm along the  $y$ -axis and 2.9 mm along the  $z$ -axis depending on the formulation. Even if the end-effector position tracking errors are relatively small compared to the overall size of the robot in this particular example, this represents a maximum relative difference of 22 % in the computation of the end-effector tracking errors. This emphasizes the value of the proposed approach for some applications with large dimensions, which improve the tracking accuracy by a model-based compensation [WCG14]. The relevance of the proposed method formulation should be also verified for a CDPR with smaller

dimensions. For this purpose, a comparison between the dynamic responses of two existing CDPRs with different sizes is presented thereafter.

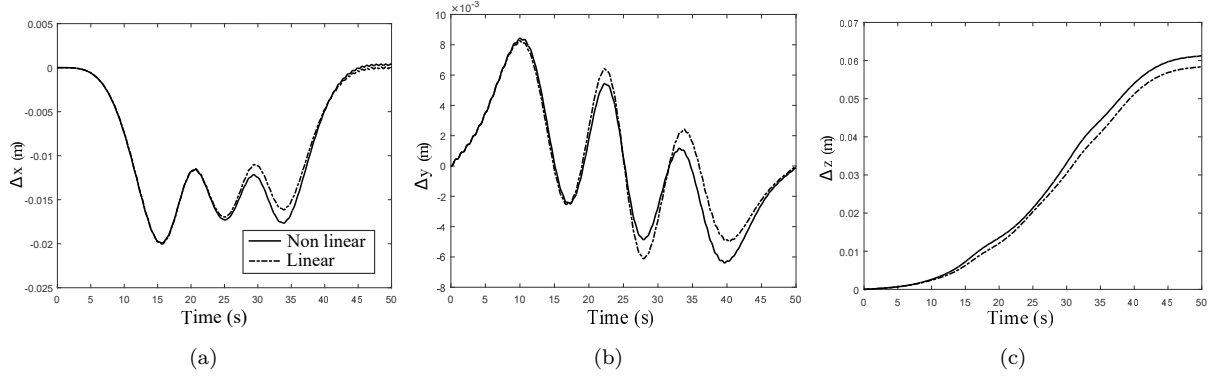


Figure III.6 – Comparison between linear and non-linear tension formulations : Positioning error of the end-effector along (a)  $x$ -axis, (b)  $y$ -axis and (c)  $z$ -axis

### III.3.1.2 Semi-industrial examples

The previous example aims to highlight the difference between linear and non linear cable tension formulations. For a better understanding of the effect of the cable tension model onto the moving-platform pose estimation, two semi-industrial CDPR prototypes are considered in this section :

The 6-DOF FAST robot [Hui15, LTS<sup>+</sup>13] composed of 6 cables (App. B.2) and the CAROCA prototype developed at IRT Jules Verne [GCGG16] in a configuration such that it contains 3 cables and performs 3-DOF translational motions (App. B.1.2). Both CDPRs are described in Tab. (B.4). This latter presents the height, width, the unstrained cables length when the end-effector is in a home position, the end-effector mass and the maximum cable tension.

#### • CAROCA

The CAROCA end-effector, described in App. B.1.2, follows an helical trajectory whose parameters are :  $a_5 = 3.6\pi$ ,  $a_4 = -9\pi$ ,  $a_3 = 6\pi$ ,  $a_2 = a_1 = a_0 = 0$ ,  $p_t = 0.2$  m,  $\beta_0 = 0$  m,  $\beta_1 = 0$  m,  $\beta_2 = 0.1$  m,  $R = 1$  m and  $t_{sim} = 4$  s. For purpose of visibility, only the second cable behavior is plotted (Fig. III.8).

The tension, elongation and strain profiles for cable 2 obtained with both the linear and non-linear cable tension models, when the end-effector tracks the helical trajectory going from point  $P_1$  of Cartesian coordinate vector  $\mathbf{p}_1 = [1, 0, 1]^T$  m

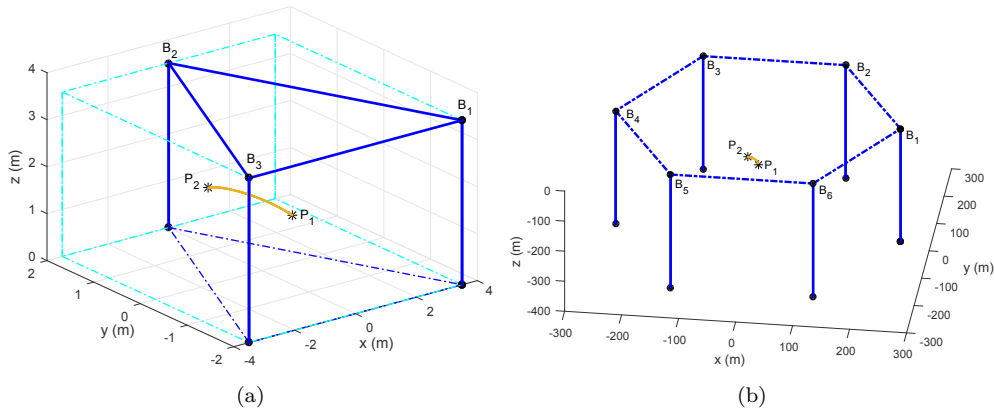


Figure III.7 – Schematics of the (a) CAROCA and (b) FAST CDRP

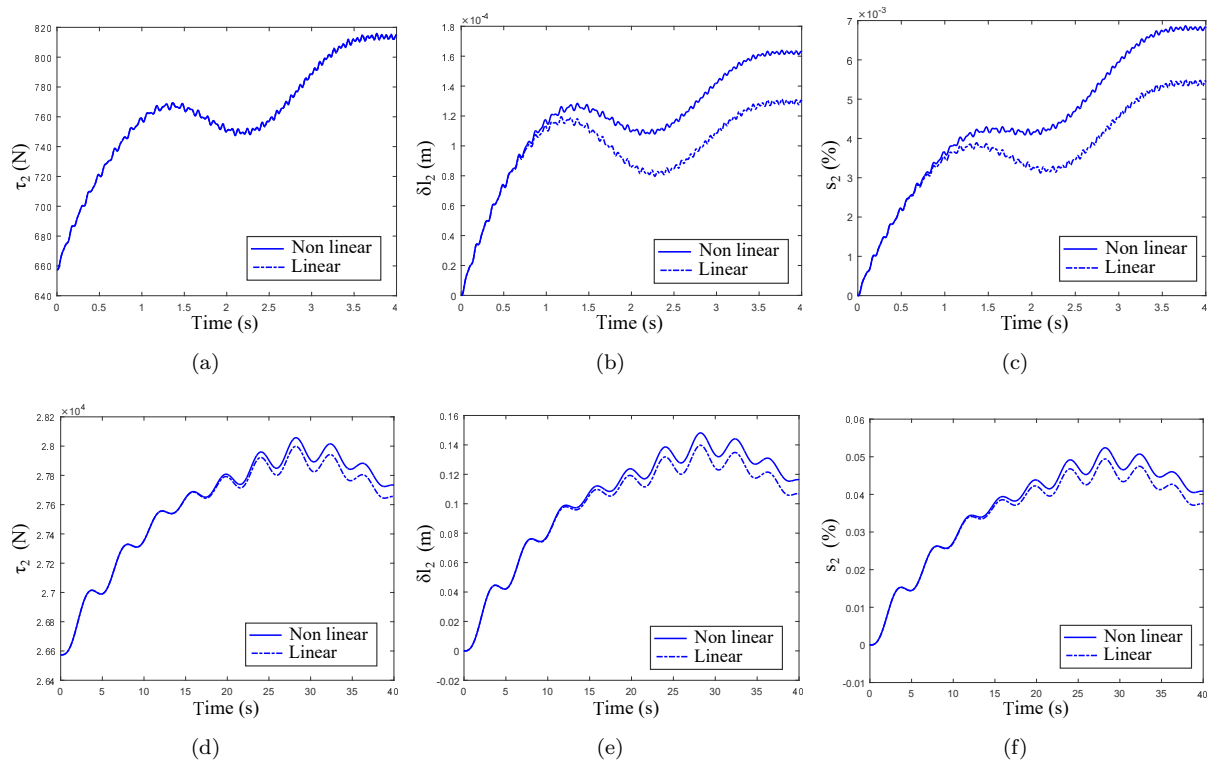


Figure III.8 – Comparison between linear and non-linear tension formulations with respect to CDRP overall size. Time history of (a)  $\tau_2$  : CAROCA, (b)  $\delta l_2$  : CAROCA, (c)  $s_2$  : CAROCA (d)  $\tau_2$  : FAST, (e)  $\delta l_2$  : FAST and (f)  $s_2$  : FAST

to point  $P_2$  of Cartesian coordinate vector  $\mathbf{p}_2 = [-0.4, 1, 1.37]^T$  m, are plotted in Fig. III.8.

These simulation results show that the maximum difference in terms of strain is about 0.0014 %.The difference in terms of cable elongation reaches up to 0.034 mm

for the second cable, representing 25.27 % of the global elongation at 4 s. As shown in Fig. III.9, there is a small difference between the positioning error of the end-effector calculated while considering a linear cable tension model and the one estimated by considering a non-linear cable tension model. This difference is about 0.06 mm and amounts to 6.26 % of the global positioning error of the end-effector. Note that it is difficult to validate those theoretical results experimentally due to the small variations in positioning errors that cannot be measured accurately with an absolute measuring position system such as a laser tracker.

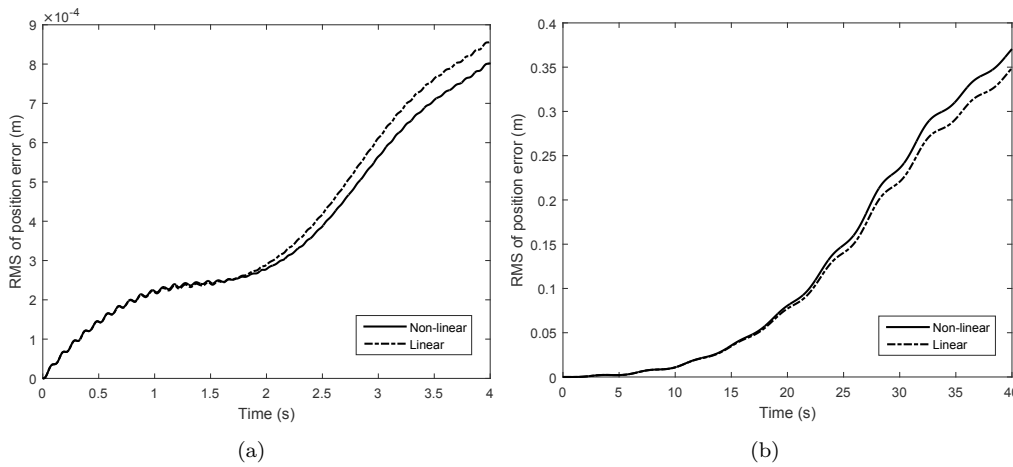


Figure III.9 – Positioning errors of the CDPR end-effector calculated with a linear and a non-linear cable tension model, respectively : (a) CAROCA (b) FAST

### • FAST

Figure III.7(b) represents a schematic of the 6-DOF FAST CDPR [KZW06]. Its end-effector moves along a helical path from point  $P_1$  of Cartesian coordinate vector  $\mathbf{p}_1 = [0, 0, -150]^T$  m to point  $P_2$  of Cartesian coordinate vector  $\mathbf{p}_2 = [-19.64, 14.27, -138.7]^T$  m within  $t_{sim} = 40$  s. The trajectory parameters  $a_0, a_1, a_2, a_3, a_4$  and  $a_5$  are the same as those used to define the trajectory followed by CAROCA *i.e.*  $p_t = 6$  m,  $R = 15$  m,  $\beta_0 = -15$  m,  $\beta_1 = 0$  m and  $\beta_2 = -150$  m.

Figure III.8 represents the time history of the tension, the elongation and the strain profiles for the second cable of the FAST robot by considering a linear and non-linear cable-tension models, respectively. The simulation results show that the difference between the elongations assessed with linear or non-linear cable tension formulations is equal to 8.7 mm at 38 s, which amounts to 7.2 % of the global

instantaneous cable elongation. This difference is due to variation in cable stiffness and leads to a sudden cable tension change (about 71.35 N). The maximum difference in terms of cable strain is about 0.0031 %. Finally, as shown in Fig. III.9, the difference in terms of end-effector positioning error is up to 21.52 mm at 40 s.

As a conclusion, for very large CDPRs such as the FAST robot, the cable tension model that is considered to estimate the pose error of the end-effector do affect the results. Although the variations in pose error estimation obtained from one cable tension model to the other one remain small with respect to the CDPR size, the non-linear cable tension had better be considered to improve the end-effector trajectory tracking.

### III.3.2 Sensitivity of CDPR dynamic behavior to the modeling type

This section aims to check the effects of the choice of the CDPR model onto its dynamic and oscillatory response. This is done through comparing the rigid (Sec. II.2), elasto-static (Sec. II.3) and elasto-dynamic (Sec. II.4) models of CDPR. Here, the nominal values of the input parameters are considered.

An example of a straight line trajectory is proposed to evaluate the difference between the CDPR models. The end-effector of the CDPR under study is moved from point  $P_1$  of Cartesian coordinate vector  $\mathbf{p}_1 = [0, 0, 0.5]^T$  m to point  $P_2$  of Cartesian coordinate vector  $\mathbf{p}_2 = [0, 0, 1.2]^T$  m tracking a vertical straight line. This trajectory is defined by Eq. (III.3) with the following parameters :  $a_5 = 18\pi$ ,  $a_4 = -45\pi$ ,  $a_3 = 30\pi$ ,  $a_2 = a_1 = a_0 = 0$ ,  $p_t = 0.15$  m,  $\beta_0 = \beta_1 = \beta_2 = 0$  m,  $R = 0$  m and  $t_{sim} = 5$  s.

Only the half of this trajectory is simulated as mentions Fig III.10. In this simulation, the quasi-static equivalent modulus of elasticity is used  $E = 102.2$  GPa. As this modulus is identified while respecting the norm ISO 12076, the cross sectional area  $S$  should be assimilated to  $A_c$  and not as a whole,  $S = 7.1675 \times 10^{-6} m^2$ , with  $S = A_c \neq S_c$ . MATLAB<sup>®</sup> routine ode45 is employed for numerical integration to calculate the resulted tensions and elongations while solving Eq. (II.41) respecting

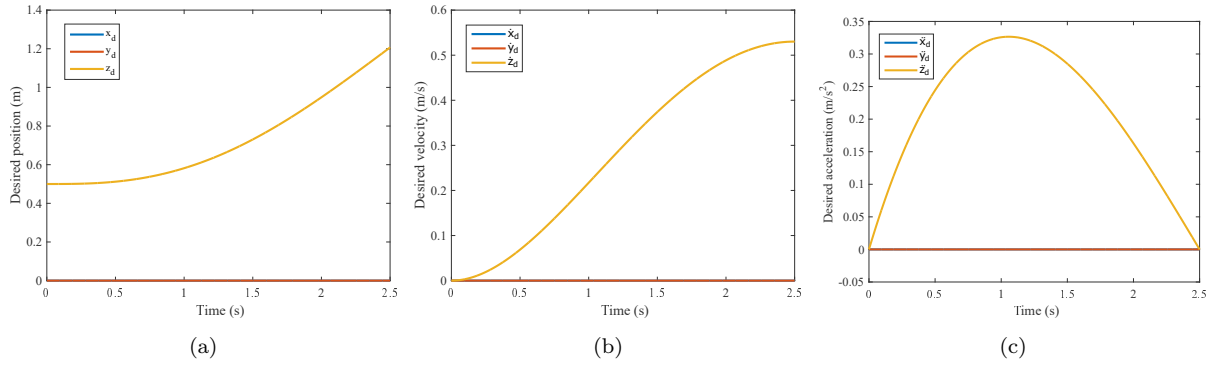


Figure III.10 – (a) Desired position (b) velocity and (c) acceleration of the moving-platform

the Fundamental Principle of Dynamics.

The time histories of the tensions  $\tau_1$  and  $\tau_3$  and the elongations  $\delta l_1$  and  $\delta l_3$  of cables 1 and 3 when the end-effector moves from point  $P_1$  to point  $P_2$  following the straight line trajectory are plotted in Fig. III.11. Same results are obtained for other cables.

The comparison between the simulation results obtained with the rigid model (blue lines), elasto-static model (green dashed lines) and elasto-dynamic model (red lines) is made. In this example, the consequences on the evaluation of the end-effector position tracking can be quite important as depicted in Fig. III.12(a). The deviation of the end-effector position along z-axis  $\delta z$  with respect to the desired one, which is the difference between the desired position of the end-effector and the one generated by the used model, is plotted in Fig. III.12. The deviations along x-axis and y-axis are not plotted as they are null. Fig. III.12(b) plots a zoom in of Fig. III.12(a) to show how the elasto-dynamic response is with respect to the elasto-static one.

At the static equilibrium, a difference between the elasto-static and elasto-dynamic models in terms of cable tensions and elongations is depicted. The first and third cable tensions for the elasto-static model are equal to the tensions generated by the force distribution algorithm, i.e they are equal to 398.01 N and 423.19 N, which correspond to the cable elongations 0.69 mm and 0.73 mm, respectively. In what concern the elasto-dynamic model, the static equilibrium tensions are equal to 391.23 N and 429.37 N, which correspond to 0.68 mm and 0.75 mm, respectively.

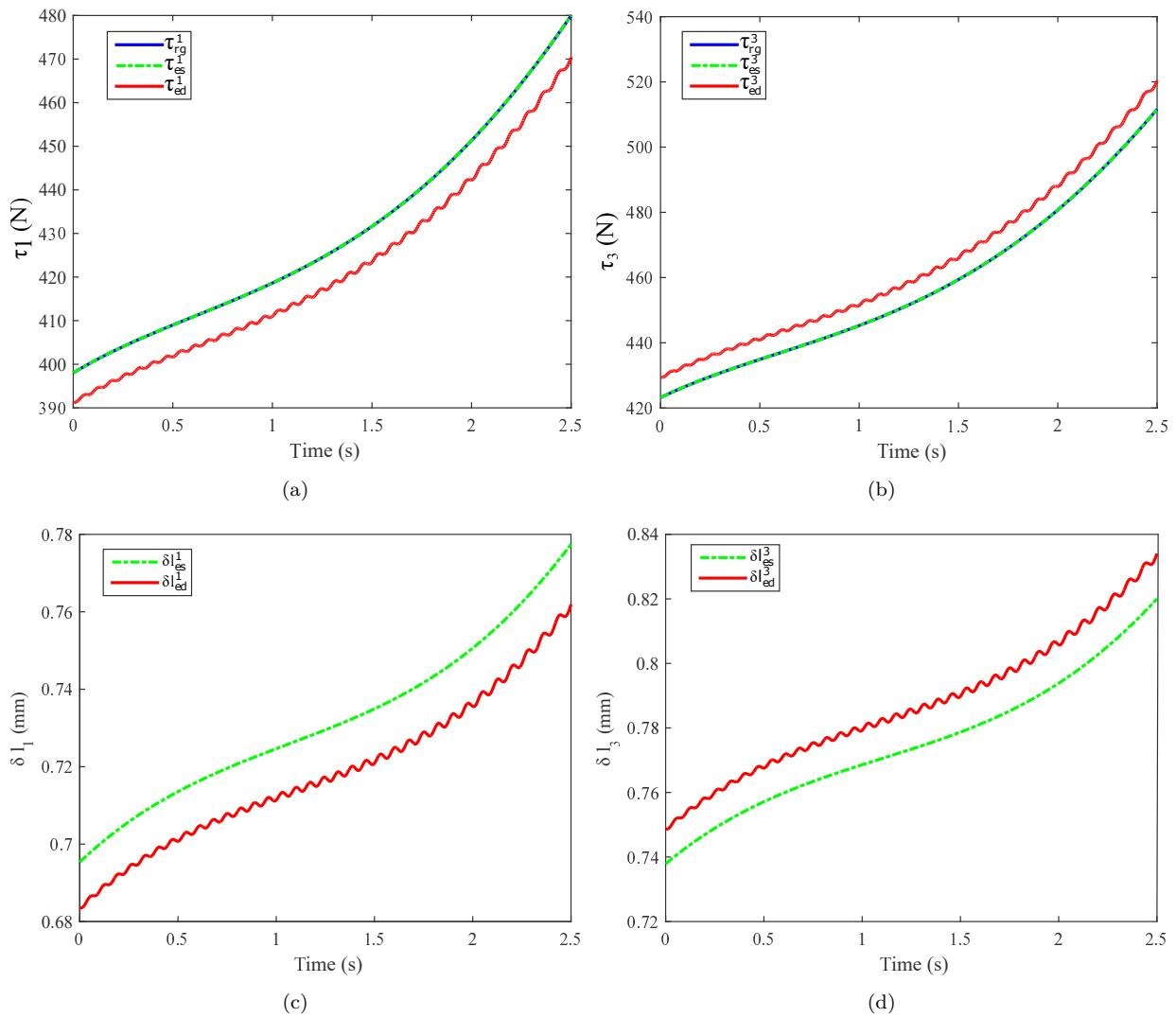


Figure III.11 – Comparison between the cable responses while using different CDPR models : Time history of (a)  $\tau_1$ , (b)  $\tau_3$ , (c)  $\delta l_1$  and (d)  $\delta l_3$

This depicts that for this example, the first cable of the elasto-static model is more tensed than the first cable of the elasto-dynamic model, and then more elongated. It is the opposite case for the third cable, where the third cable of the elasto-dynamic model is more elongated than the third cable of the elasto-static model. Despite this difference, both elasto-static and elasto-dynamic models generate the same static equilibrium for the moving-platform. The deviation with respect to the desired position of the moving-platform along z-axis is equal to 1.2 mm at the start time for both models.

When the moving-platform starts its trajectory, the order of cables tensing

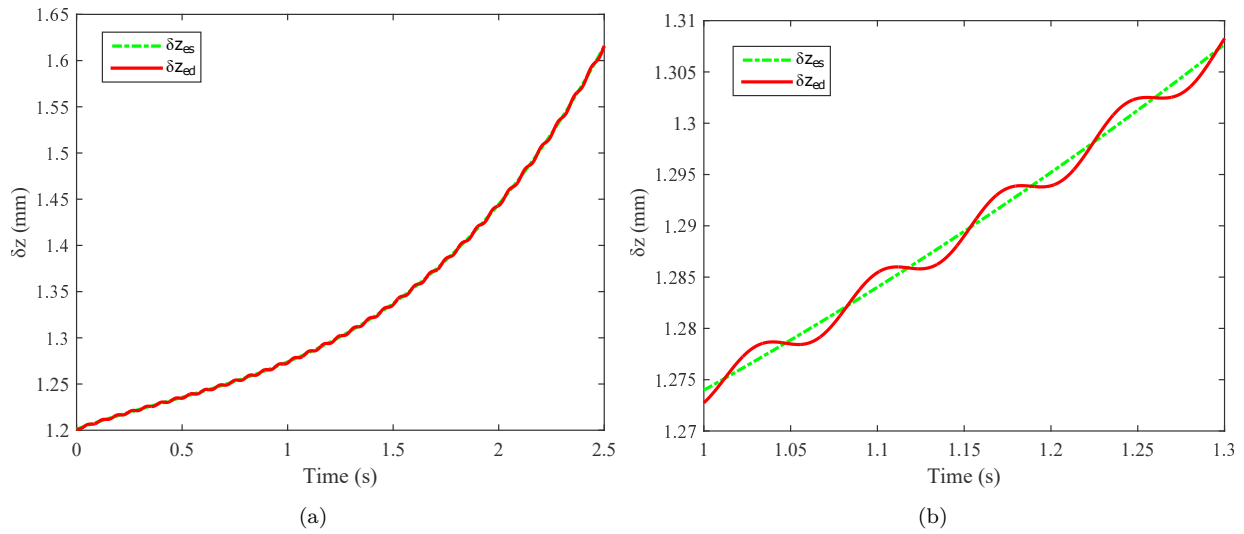


Figure III.12 – Comparison between the different dynamic CDPR models : Time history of (a) the deviation  $\delta z$  of the end-effector position along z-axis and (f) Zoom in  $\delta z$

and elongating stays the same. As one can see, the rigid and elasto-static provide smooth curves of cable tensions. This is due to the non consideration of the cables interaction with the whole system. The elasto-static model of CDPR deviates with respect to the rigid model to establish the static equilibrium at each iteration when cables elongations occur. When cables are no longer isolated in the CDPR model, the oscillatory behavior of the moving-platform becomes visible in the elasto-dynamic model. The moving-platform of the elasto-dynamic model oscillate around the dynamic equilibrium, provided by the elasto-static model, with the fundamental natural frequency of the CDPR, which is around 16 Hz. Despite that the elasto-static model integrates the elasticity of cables, a weakness of this model is that it neglects the dynamic effects due to cables interaction with the whole system. The elasto-dynamic model tries to remedy this weakness and it depicts the oscillatory behavior of CDPR while the moving-platform tracks a trajectory. The elasto-dynamic model of CDPR may be useful for control purposes as it predicts not only the cable elongations but also their dynamic interaction with the moving-platform.

## III.4 Uncertainty analysis of CDPR to parameters

As the uncertainty analysis focuses on determining how uncertain the CDPR response is if the input parameters are uncertain, this analysis is done in Sec. III.4.1, while considering CDPR with fast-varying cable lengths. Experimental data coming from the identification of cables (See App. A) are used to better analyze the effect of uncertainties on the CDPR dynamic response. As the static behavior of the CDPR is dominated by the stiffness, an uncertainty analysis considering the whole stiffness of the CDPR is done in Sec. III.4.2.

### III.4.1 Dynamic uncertainty analysis

#### III.4.1.1 Dynamic stiffening

A smooth and continuous motion as in section (III.3.1) limits the oscillations of the moving-platform. Therefore, a trapezoidal-velocity trajectory of the moving-platform is chosen to analyze the influence of the cable modulus of elasticity on the CDPR dynamic behavior. The lack of smoothness of the trajectory is chosen here to excite the end-effector on its fundamental rigid-body mode frequencies [YCD15]. The shape of the cable linear velocities at the pulley entrance is defined such as the motion is uniformly accelerated until the linear cable velocities achieve the limit value  $V_{max}$  (Fig. III.13(a)). Linear cable accelerations are defined by the coefficients  $a_1$ ,  $a_2$  and  $a_3$  expressed in  $m/s^2$ .

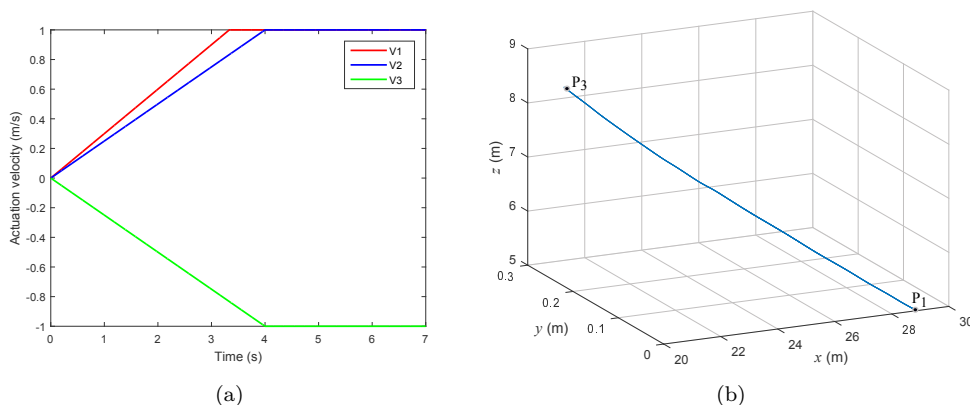


Figure III.13 – Trapezoidal-velocity trajectory : (a) Trapezoidal actuation velocities (b) Trajectory of the end-effector

This section aims to present numerical results associated to the dynamic behavior of the 3-DOF CDPR, where three long cables make the end-effector move.

The position vector of the exit points in the global frame are :  $\mathbf{b}_1 = [0, 50, 50]^T$  m,  $\mathbf{b}_2 = [0, -50, 50]^T$  m and  $\mathbf{b}_3 = [86.60, 0, 50]^T$  m. The mass of the end-effector is  $m_{ee} = 300$  kg.

For the example under study, the coefficients of the cable trapezoidal-velocity profiles are  $a_1 = 0.3$  m/s<sup>2</sup>,  $a_2 = 0.25$  m/s<sup>2</sup>,  $a_3 = -0.25$  m/s<sup>2</sup> and  $V_{max} = 1$  m/s. As a result, the manipulator tracks a straight line from point  $P_1$  of Cartesian coordinate vector  $\mathbf{p}_1 = [28.86, 0, 5]^T$  m to point  $P_3$  of Cartesian coordinate vector  $\mathbf{p}_3 = [20.30, 0.23, 8.5]^T$  m in 7 s (Fig. III.13(b)).

To better visualize the effect of the dynamic stiffness on the dynamic and oscillatory motions of the CDPR, the natural frequencies of the cable manipulator are determined by solving the generalized eigenvalue problem associated with the apparent stiffness of the CDPR [DM09]. Let  $f_1$  denote the first natural frequency,  $f_2$  the second natural frequency and  $f_3$  the third natural frequency. Both the numerical example and the CAROCA prototype are analyzed to check the effect of the frequency dependency of the dynamic stiffness with respect to the CDPR dimensions.

As mentioned in Appendix (A.1.2), DMA allows us to identify the cable's modulus of elasticity under forced oscillatory motions in the frequency range of the intended application. The time histories plotted in Fig. III.14 show a resulting forced elongation at a frequency between 1 and 2 Hz, which correspond to the frequency of the fundamental rigid-body mode of the end-effector suspended on the global cable stiffness. Based on the experimental data presented in Tab. A.1, the corresponding value of the dynamic modulus of elasticity is about 30% higher than the value identified in quasi-static.  $E' = 134.8$  GPa  $\pm$  3.1 GPa at 2 Hz instead of  $E = 102$  GPa  $\pm$  2.2 GPa in quasi-static.

Figure (III.14) shows the tension, the elongation and the strain of the first cable when the value identified in quasi-static at  $E = 102$  GPa (continuous line) or in dynamic at  $E' = 134.8$  GPa at 2 Hz (dashed lines) is used. These curves are computed for the non-linear tension formulation without damping. Since the value of the modulus of elasticity is different, a difference in terms of the oscillation frequency appears in the cable responses. The oscillation frequency increases due to

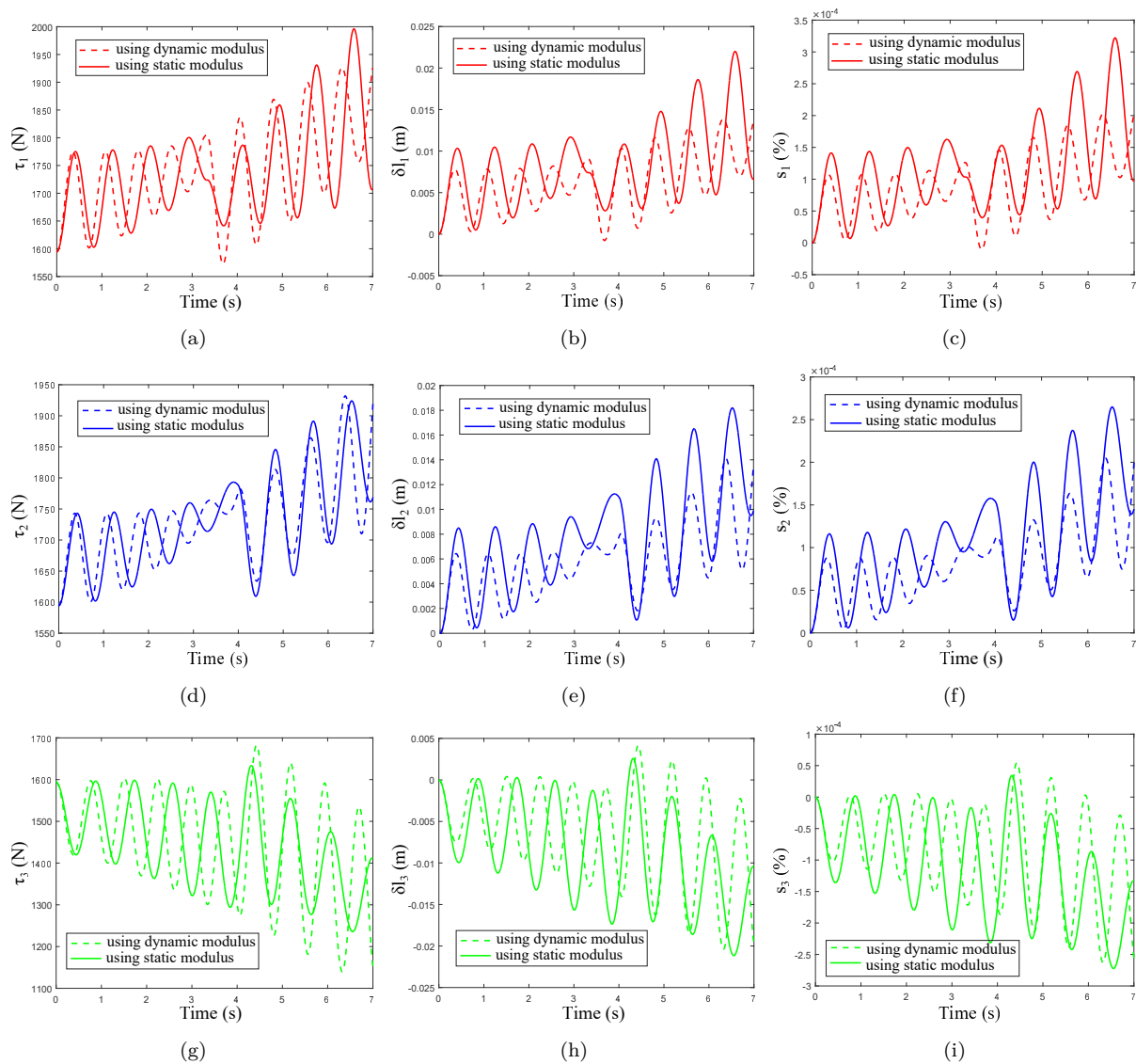


Figure III.14 – Comparison between cables responses while using static or dynamic modulus : Time history of (a)  $\tau_1$ , (b)  $\delta l_1$ , (c)  $s_1$ , (d)  $\tau_2$ , (e)  $\delta l_2$ , (f)  $s_2$ , (g)  $\tau_3$ , (h)  $\delta l_3$  and (j)  $s_3$

the dynamic stiffening phenomena. This dynamic cable stiffening leads to reduce the elongation amplitude over the trajectory. The differences on the end-effector position tracking error are significant both on the shape of the curves and on their level (Fig. III.15). The end-effector trajectory can differ up to 8 mm along the  $x$ -axis, 4.5 mm along the  $y$ -axis and 9 mm along the  $z$ -axis depending on the chosen stiffness. The magnitude of the end-effector positioning errors is significant. Even if these values are relatively small compared to the overall dimensions of the CDPR under study, this represents a maximum relative difference of 24 % in the compu-

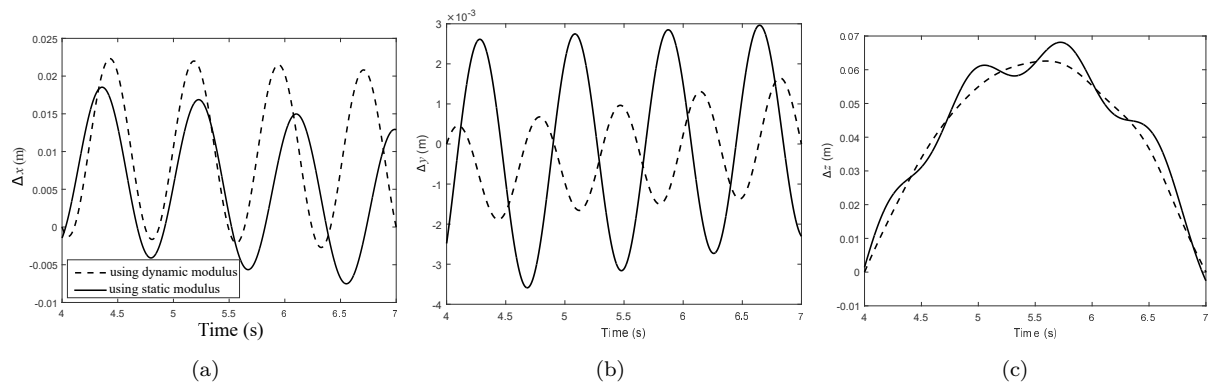


Figure III.15 – Comparison between the CDPR responses while using static or dynamic modulus : Time history of positioning error along (a)  $x$ -axis, (b)  $y$ -axis and (c)  $z$ -axis

tation of the end-effector tracking errors.

Figure III.16 represents the time variation of the three natural frequencies for different cable stiffnesses. The fundamental natural frequency when the dynamic stiffness is considered is around 1.9 Hz. However, when the quasi-static stiffness is considered, the fundamental natural frequency of the CDPR is around 1.67 Hz. As the dynamic modulus of elasticity is higher than the quasi-static one, a difference in terms of the oscillation frequency appears in the cable responses. The increase of the oscillation frequency comes from the dynamic stiffening phenomenon, which leads to a reduction in the cable elongation magnitude along the trajectory. It is noteworthy that the dynamic modulus of elasticity tends to increase the natural frequencies.

The CAROCA prototype is also analyzed to check whether the dynamic stiffness has an effect onto the natural frequencies of a smaller CDPR. The coefficients of the considered cable trapezoidal-velocity profile are  $a_1 = a_2 = a_3 = 0.2 \text{ m/s}^2$  and  $V_{max} = 0.5 \text{ m/s}$ . The end-effector of the CDPR moves from point  $P_1$  of Cartesian coordinate vector  $\mathbf{p}_1 = [1, 0, 0.1]^T \text{ m}$  to point  $P_3$  of Cartesian coordinate vector  $\mathbf{p}_3 = [0.74, -0.4, 2.6]^T \text{ m}$  within 4 s.

From Fig. III.17, a resulting forced elongation is observed at a frequency between 10 and 11 Hz, which corresponds to the frequency of the fundamental rigid-body mode of the end-effector suspended onto the global cable stiffness. Based on the experimental data given in Table A.1, the corresponding value of the dy-

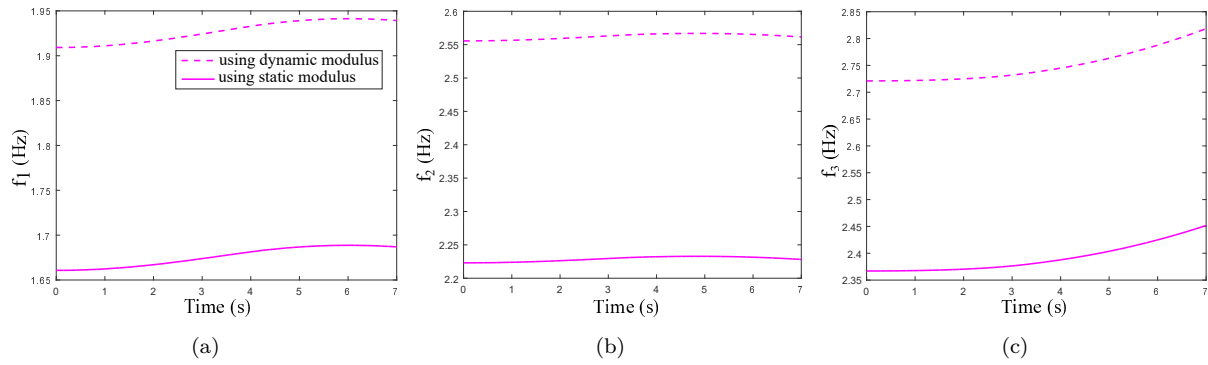


Figure III.16 – Comparison between the CDPR natural frequencies while using static or dynamic modulus (2 Hz) : Time history of natural frequencies (a)  $f_1$ , (b)  $f_2$  and (c)  $f_3$

dynamic modulus of elasticity is  $E' = 130.1 \text{ GPa} \pm 3.0 \text{ GPa}$  at 10 Hz instead of  $E = 102 \text{ GPa} \pm 2.2 \text{ GPa}$  in quasi-static.

The end-effector trajectory can differ up to 1.26 mm along the  $z$ -axis, 0.1 mm along the  $x$ -axis and 0.05 mm along the  $y$ -axis depending on the chosen stiffness. This represents a maximum relative difference of 16.2 % in terms of end-effector tracking errors. The frequency dependency of the dynamic stiffness has the same effects onto the CAROCA as the previous example. Therefore, one can claim that the dynamic and oscillatory responses of the end-effector and cables depend strongly on the dynamic stiffness no matter the size of the CDPR.

### III.4.1.2 Axial cable damping

To show the influence of axial cable damping on the CDPR dynamic behavior, the results of the simulations with the non-linear tension formulation without (continuous line) and with (pointed line) damping are plotted in Figures III.18 and III.19. As the oscillation frequency of the CDPR under study is between 1 and 2 Hz, the corresponding dynamic parameters are selected in Table A.1. At 2 Hz, the cables damping coefficient is  $c = 2.08 \times 10^9 \text{ N.m}^{-1}.\text{s}$  and its corresponding dynamic modulus of elasticity is  $E' = 134.8 \text{ GPa}$ . Using these dynamic parameters, the time histories of cable tension, elongation and strain are presented in Fig. III.18. These curves show that the cable response is obviously highly sensitive to cable damping. The oscillations of the damped model decay during the transient phases between 0 to 3.4 s and between 3.4 to 8 s whereas the conservative

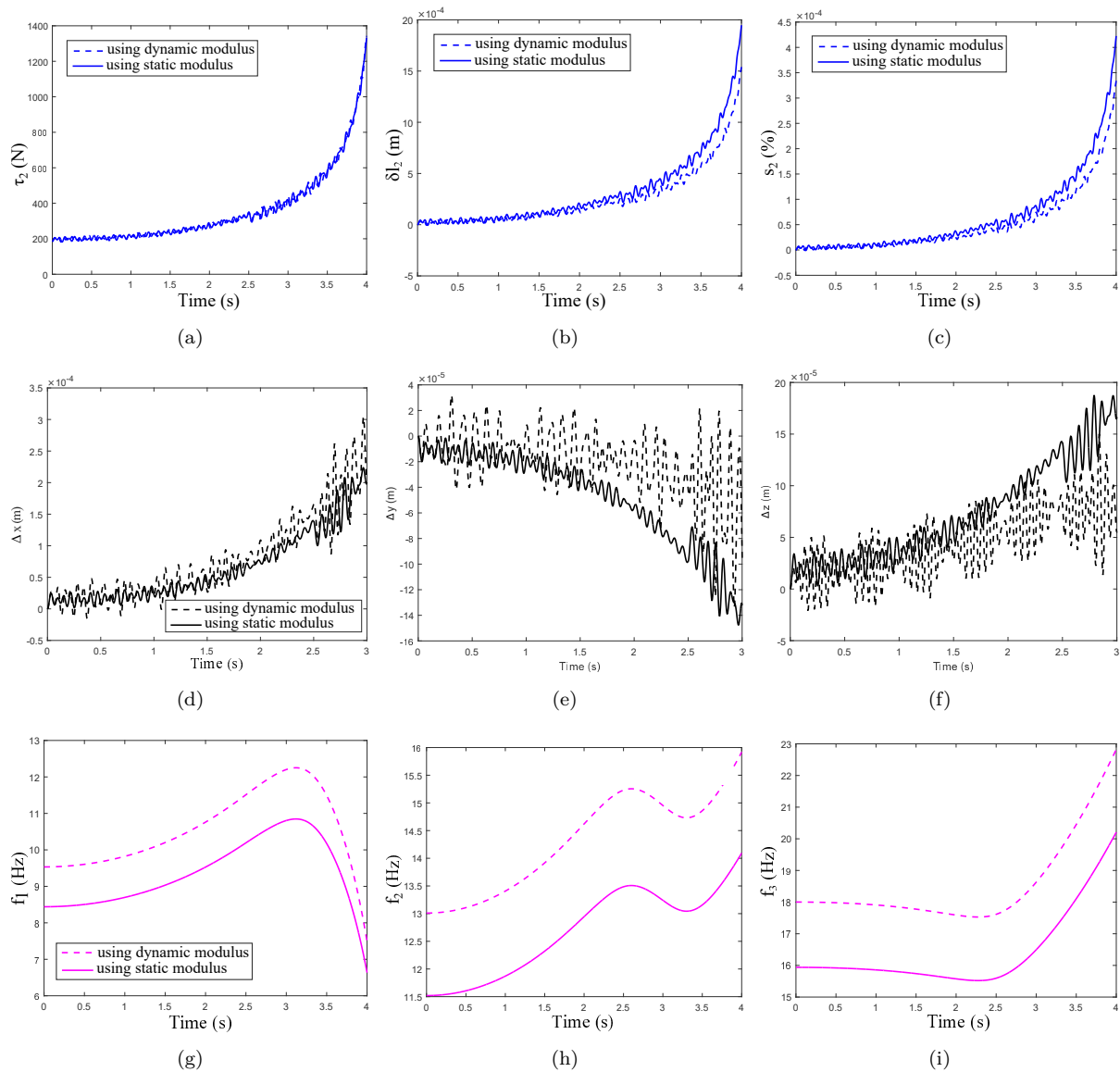


Figure III.17 – Comparison between dynamic responses of the CAROCA while using quasi-static or dynamic modulus (10 Hz) : Time history of (a)  $\tau_2$ , (b)  $\delta l_2$ , (c)  $s_2$ , Positioning error (d) along x-axis, (e) along y-axis, (f) along z-axis, natural frequencies (g)  $f_1$ , (h)  $f_2$  and (i)  $f_3$

model exhibits no energy loss as expected. The influence of the damping is also significant on the evaluation of the end-effector position tracking error (Fig. III.19).

The contribution of these simulations is to show how the cable modulus of elasticity substantially affects the dynamic behavior of CDPR. The results stress

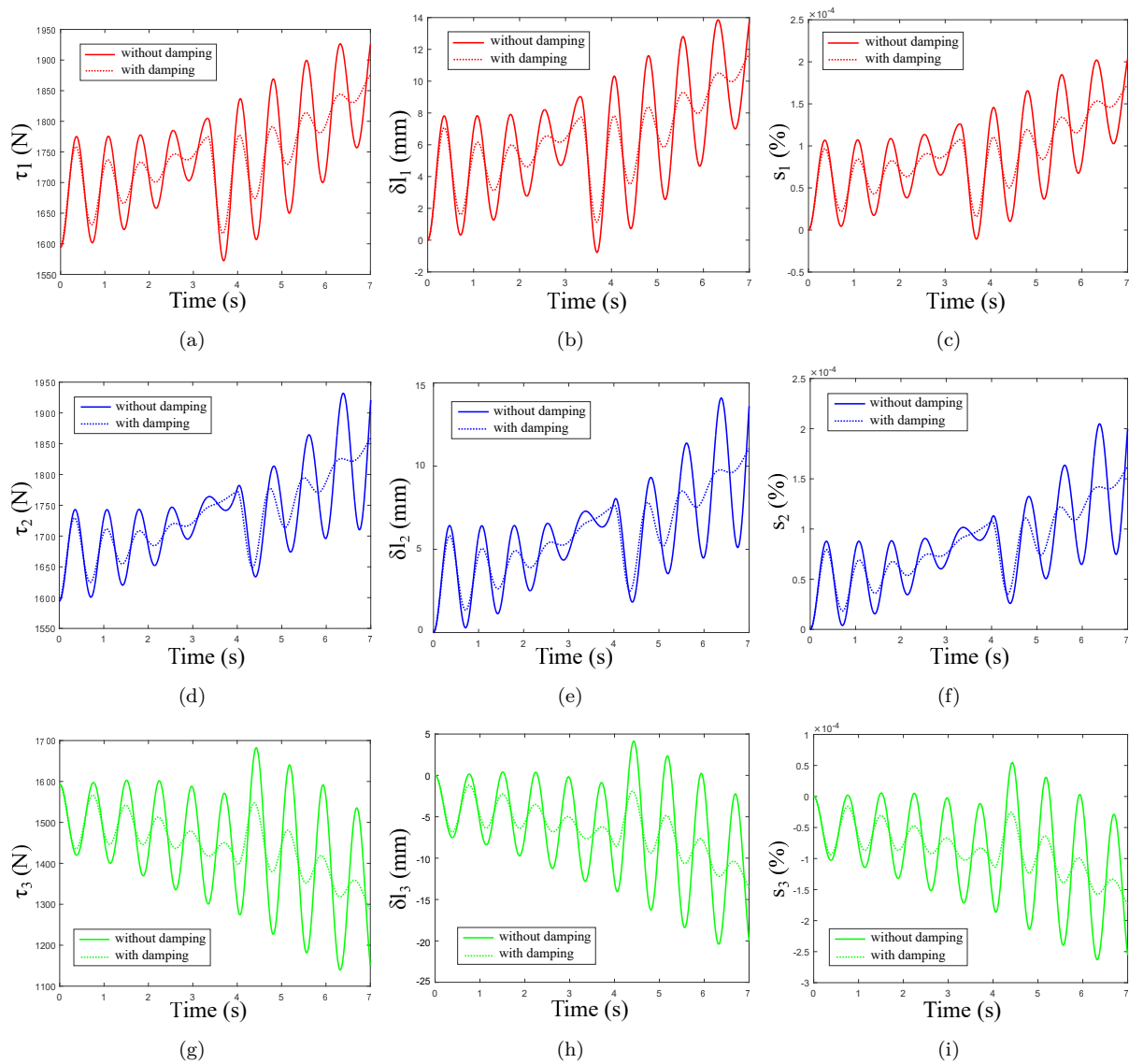


Figure III.18 – Comparison between cables responses with and without damping : Time history of (a)  $\tau_1$ , (b)  $\delta l_1$ , (c)  $s_1$ , (d)  $\tau_2$ , (e)  $\delta l_2$ , (f)  $s_2$ , (g)  $\tau_3$ , (h)  $\delta l_3$  and (j)  $s_3$

the importance of choosing the appropriate method of identification in relation to the frequency range of the CDPR response.

### III.4.2 Static uncertainty analysis

The static behavior of the CDPR is dominated by its overall stiffness. If the compliant displacement of the moving-platform under the external load is small, the uncertainty analysis of the CDPR can be done through linearized static Car-

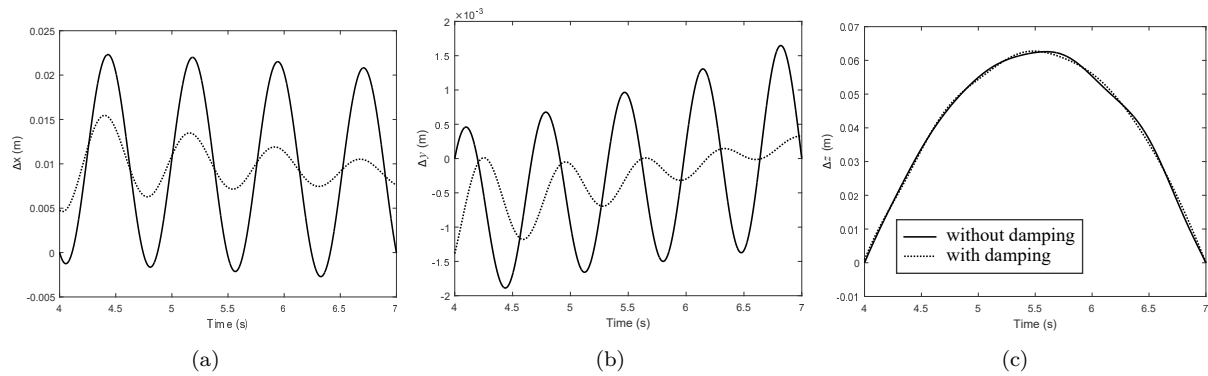


Figure III.19 – Comparison the CDPR responses while using tension model with or without damping : Time history of positioning error along (a)  $x$ -axis, (b)  $y$ -axis and (c)  $z$ -axis

tesian stiffness matrix [Car11]. As in statics it is the stiffness which dominates the static behavior of the CDPR, the static uncertainty analysis in this manuscript considers both sag-introduces stiffness and large compliant displacements. For this fact, the elasto-static model of CDPR while considering elasto-sagging cables is used. As our model is non-linear and complex, the calculation of uncertainty matrix is not evident. For this fact, a new uncertainty index is defined, which is the static deflection of the moving-platform.

### III.4.2.1 Static deflection

The static stiffness of CDPR can be analyzed through the static deflection of its moving-platform [BCC18]. If the compliant displacement of the moving-platform under the external load is small, the static deflection of the moving-platform can be calculated by its static Cartesian stiffness matrix [Car11]. However, once the cable mass is considered, the sag-introduced stiffness should be taken into account. Here, the small compliant displacement assumption is no longer valid, mainly for heavy or/and long cables with light mobile platform. Consequently, the static deflection can not be calculated through the Cartesian stiffness matrix. In this manuscript, the IESM and DESM are used to define and calculate the static deflection of the moving-platform under an external load.

This problem is solved by deriving the static deflection of the CDPR obtained by the subtraction of the poses calculated with and without an external payload. For a desired pose of the moving-platform, the IESM gives a set of unstrained cable

lengths  $\mathbf{l}_{us}$ . This set is used by the DESM to calculate first, the pose of the moving-platform under its own weight. Then, the pose of the moving-platform is calculated when an external load (mass addition) is applied. Note that the positioning and angular static deflection of the moving-platform should be treated separately in order to avoid the homogenization problem [NG14]. Therefore, the positioning and angular static deflection of the moving-platform,  $\mathbf{dp}$  and  $\mathbf{do}^*$  respectively, are expressed as :

$$\mathbf{dp}_{j,k} = \mathbf{p}_{j,k} - \mathbf{p}_{j,1}, \quad (\text{III.6a})$$

$$\mathbf{do}_{j,k}^* = \mathbf{o}_{j,k}^* - \mathbf{o}_{j,1}^*, \quad (\text{III.6b})$$

where

- $\mathbf{p}_{j,1}$  is the position of the moving-platform considering only its own weight for the  $j^{\text{th}}$  pose configuration,
- $\mathbf{p}_{j,k}$  is the position of the moving-platform for the set of the  $j^{\text{th}}$  pose and  $k^{\text{th}}$  load configuration,
- $\mathbf{o}_{j,1}^*$  is the orientation of the moving-platform with respect to  $x$ -axis,  $y$ -axis and  $z$ -axis, considering only its own weight for the  $j^{\text{th}}$  pose configuration,
- $\mathbf{o}_{j,k}^*$  is the orientation of the moving-platform with respect to  $x$ -axis,  $y$ -axis and  $z$ -axis, for the set of the  $j^{\text{th}}$  pose and  $k^{\text{th}}$  load configuration.

### III.4.2.2 Uncertainty range of parameters

The influence of uncertainties on CDPR parameters is analyzed through the evaluation of the static deflection of the moving platform as it corresponds to the CDPR stiffness. The experience to make is to apply an external load on the moving-platform by adding an additional mass. As an illustrative example, a suspended configuration of the reconfigurable CAROCA prototype (See App. B.1.1) with 8 cables and 6 DOF is studied. The Cartesian coordinates of  $A_i$  ( $B_i$ , resp.) expressed in  $\mathcal{F}_p$  (in  $\mathcal{F}_b$ , resp.) of the considered prototype are given in Tab. (B.1). The nominal mass of the moving-platform and the additional mass are equal to 180 kg and 50 kg, respectively. The moving-platform is supposed to be placed in a symmetric position (0 m, 0 m, 1.75 m), see Fig. B.2(a).

Table III.2 shows the nominal value, the range of uncertainty and the analysis step of each uncertain parameter. Based on the knowledge of the tension set-point<sup>1</sup>, two levels of uncertainties are defined.

- **Level 1** : The tension set-point is unknown. A large range of uncertainty on the modulus of elasticity is defined. It is to be determined based on the tension variation on the cables and its correspondence in the experimental hysteresis loop shown in the Fig. A.4.
- **Level 2** : The tension set-point is known. Here, we consider only the measurement uncertainties.

**Table III.2** – Nominal values, uncertainty ranges and discretization step of uncertain parameters

Parameter	Nominal value	Step	Range of uncertainty	
			Level 1	Level 2
$E$ (GPa)	102	0.05	[- 18 2]	$\pm 2$
$m_{ee}$ (kg)	180	0.05	$\pm 18$	
$\rho$ (kg/m)	0.1015	$3 \cdot 10^{-5}$	$\pm 0.01015$	
$\mathbf{a}_i$ (m)	$\mathbf{a}_i$	0.0006	$\pm 0.015$	
$\mathbf{b}_i$ (m)	$\mathbf{b}_i$	0.0012	$\pm 0.03$	

As one can see, the uncertainty on the exit points coordinates is two times the uncertainty on the anchor point coordinates. The reason lies in the fact that the exit point coordinates depend not only on assembly but also on the uncertainty on the gravity center coordinates. Since the moving-platform is a mechanically welded structure, an error range of 10 % is defined. The linear mass  $\rho$  of CAROCA cables is equal to 0.1015 kg/m leading to an uncertainty of  $\pm 0.01015$  kg/m.

In what concern the modulus of elasticity, it is defined with respect to the tension set-point. If this set-point is known (level 2), we consider only the measurement uncertainty. If not, a larger range of uncertainty is defined. It is to be determined based on the tension variation on the cables and its correspondence in the experimental hysteresis. The additional mass corresponds to a variation in cable tensions from 574 N to 730 N, which corresponds to a modulus of elasticity of 84.64 GPa, which leads to an error of 18 GPa. The nominal modulus of elasticity  $E = 102$  GPa

1. A tension set-point is a tension distribution that balances the wrench applied on the platform, that the tension controllers attempt to maintain.

is determined with respect to ISO norm 12076.

Due to the non-linearities of the elasto-static model, explicit uncertainty matrix and coefficients [ZDWK14, MKLP15] cannot be computed. Therefore, the uncertainty of the elasto-static model of the CDPR to geometrical and mechanical errors is evaluated statistically. Here, MATLAB® has been coupled with modeFRONTIER®, a process integration and optimization software platform [Est14] for the analysis. The analysis process is viewed as a stochastic estimation problem in which the level of uncertainty in the design parameters and quantities of interest is characterized probabilistically, and updated through successive iterations as new information becomes available. The RMS (Root Mean Square) of the static deflection of CAROCA moving-platform is studied. All the uncertain parameters of the elasto-static CAROCA model are defined with uniformly distributed deviations.

### III.4.2.3 Uncertainty analysis with unknown tension set-point

Figure III.20(a) displays the distribution fitting of the static deflection RMS. It shows that the RMS distribution follows a quasi-uniform law whose mean  $\mu_1$  is equal to 1.34 mm. The RMS of the static deflection of the moving-platform is bounded between a minimum value  $\text{RMS}_{min}$  equal to 1.12 mm and a maximum value  $\text{RMS}_{max}$  equal to 1.63 mm; a variation of 0.51 mm under all uncertainties, which presents 38 % of the nominal value of the static deflection.

Figure III.20(b) depicts the RMS of the moving-platform static deflection as a function of variations in  $E$  and  $\rho$  simultaneously, whose values vary respectively from 0.09135 to 0.11165 kg/m and from 84.2 to 120.2 GPa. The static deflection is very sensitive to cables mechanical behavior. The RMS varies from 0.42 mm to 0.67 mm due to the uncertainties of these two parameters only. As a matter of fact, the higher the cable modulus of elasticity, the smaller the RMS of the moving-platform static deflection. Conversely, the smaller the linear mass of the cable, the smaller the RMS of the moving-platform static deflection. Accordingly, the higher the sag-introduced stiffness, the higher the moving-platform static deflection. Besides, the higher the axial stiffness of the cable, the lower the moving-platform static deflection.

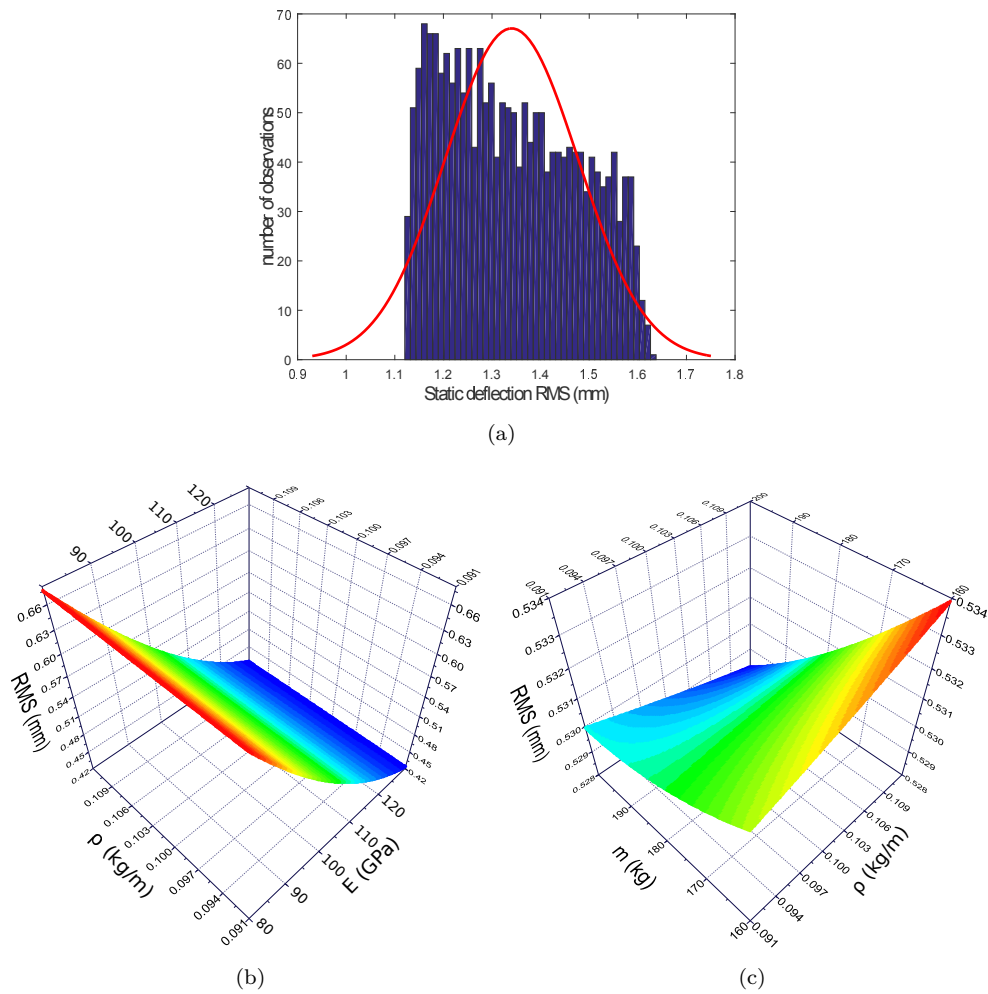


Figure III.20 – (a) Distribution of the RMS of the moving-platform static deflection, Evolution of the RMS under a simultaneous variations of (b)  $E$  and  $\rho$  (c)  $m$  and  $\rho$

Figure III.20(c) illustrates the RMS of the moving-platform static deflection as a function of variations in  $\rho$  and  $m$ , whose value varies from 162 kg to 198 kg. The RMS varies from 0.52 mm to 0.53 mm due to the uncertainties of these two parameters only. The moving-platform mass affects the mechanical behavior of cables : the heavier the moving-platform, the larger the axial stiffness, the smaller the moving-platform static deflection. Therefore, a fine identification of  $m$  and  $\rho$  is very important to establish a good CDPR model. Comparing to the results plotted in Fig. III.20(b), it is clear that  $E$  affects the RMS of the moving-platform static deflection more than  $m$  and  $\rho$ .

For the analyzed pose of the moving-platform, it is shown that the uncertainty on the elasticity modulus affects the most the static deflection of the moving-platform and then the static stiffness of the CDPR. Next, an analysis is made in the CAROCA workspace to check the effect of cables elasticity into the static deflection for different poses of the moving-platform.

#### III.4.2.3.1 Analysis of the elasticity modulus over the workspace

Figure III.21 presents the variation of the static deflection norm in the sub-workspace of the CAROCA prototype defined with  $-1.5 < x < 1.5$  m,  $-1.5 < y < 1.5$  m and  $z = 1$  m. Here, only the uncertainty on the modulus of elasticity is considered, so it varies from 84.90 GPa to 120.2 GPa. A sliced presentation of the static deflection variation is adopted to be able to visualize it for a given modulus of elasticity. The volume slices are spaced by 4 GPa.

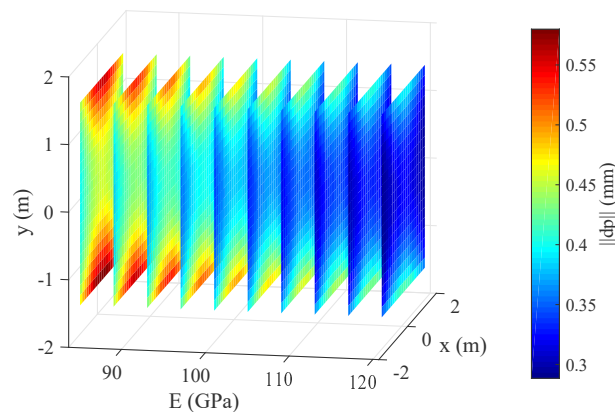


Figure III.21 – Variation of the static deflection norm considering uncertainty on the modulus of elasticity over the sub-workspace ( $-1.5 < x < 1.5$  m,  $-1.5 < y < 1.5$  m and  $z = 1$  m)

The static deflection is very sensitive to the cables elasticity. It varies from 0.28 mm to 0.58 mm in the defined sub-workspace, a variation of 0.3 mm. When the modulus of elasticity is at its higher bound, the static deflection varies from 0.28 mm to 0.41 mm, a variation of 0.13 mm presenting 43 % of the whole variation. When the modulus of elasticity is at its lower bound, the static deflection varies from 0.40 mm to 0.58 mm, a variation of 0.18 mm presenting 60 % of the whole variation. Also, for the same plane (xy) the effect of the modulus of elasticity

decreases with the increase of its value. Accordingly, the smaller the modulus of elasticity, the higher its influence on the static deflection.

#### III.4.2.4 Uncertainty analysis with known tension set-point

In this section, the cable tension set-points during moving-platform operation are supposed to be known. so, the modulus of elasticity can be calculated around the operating point and the confidence interval is reduced to  $\pm 2$  GPa. The uncertainty range and the discretization step are provided in Tab. III.2 for the second level.

Figure III.22(a) displays the distribution fitting of the moving-platform static deflection RMS. It shows that the RMS distribution follows a normal law whose mean  $\mu_2$  is equal to 1.32 mm and its standard deviation  $\sigma_2$  is equal to 0.01 mm. This deviation is relatively small with respect to the CAROCA prototype size. The RMS of the static deflection of the moving-platform is bounded between a minimum value  $RMS_{min}$  equal to 1.28 mm and a maximum value  $RMS_{max}$  equal to 1.39 mm ; a variation of 0.11 mm under all uncertainties. The modulus of elasticity affects the static compliant of the moving-platform, which imposes to always consider  $E$  error while designing a CDPR model.

The bar charts plotted in Fig. III.22(b) and Fig. III.22(c) present, respectively, the effects of the uncertainties in  $\mathbf{a}_i$  and  $\mathbf{b}_i$ ,  $i=[1..8]$ , to the static deflection of the CAROCA for symmetric (0 m, 0 m, 1.75 m) and non-symmetric (3.2 m, 1.7 m, 3 m) robot configurations (Fig. B.2(a) and Fig. B.2(b), respectively).

These effects are determined based on  $t$ -student index  $st$  of each uncertain parameter. This index is a statistical tool that can estimate the relationships between outputs and uncertain inputs. The t-Student test compares the difference between the means of two samples of designs taken randomly in the design space :

- $M_+$  is the mean of the  $n_+$  values for an objective  $S$  in the upper part of domain of the input variable,
- $M_-$  is the mean of the  $n_-$  values for an objective  $S$  in the lower part of domain of the input variable.

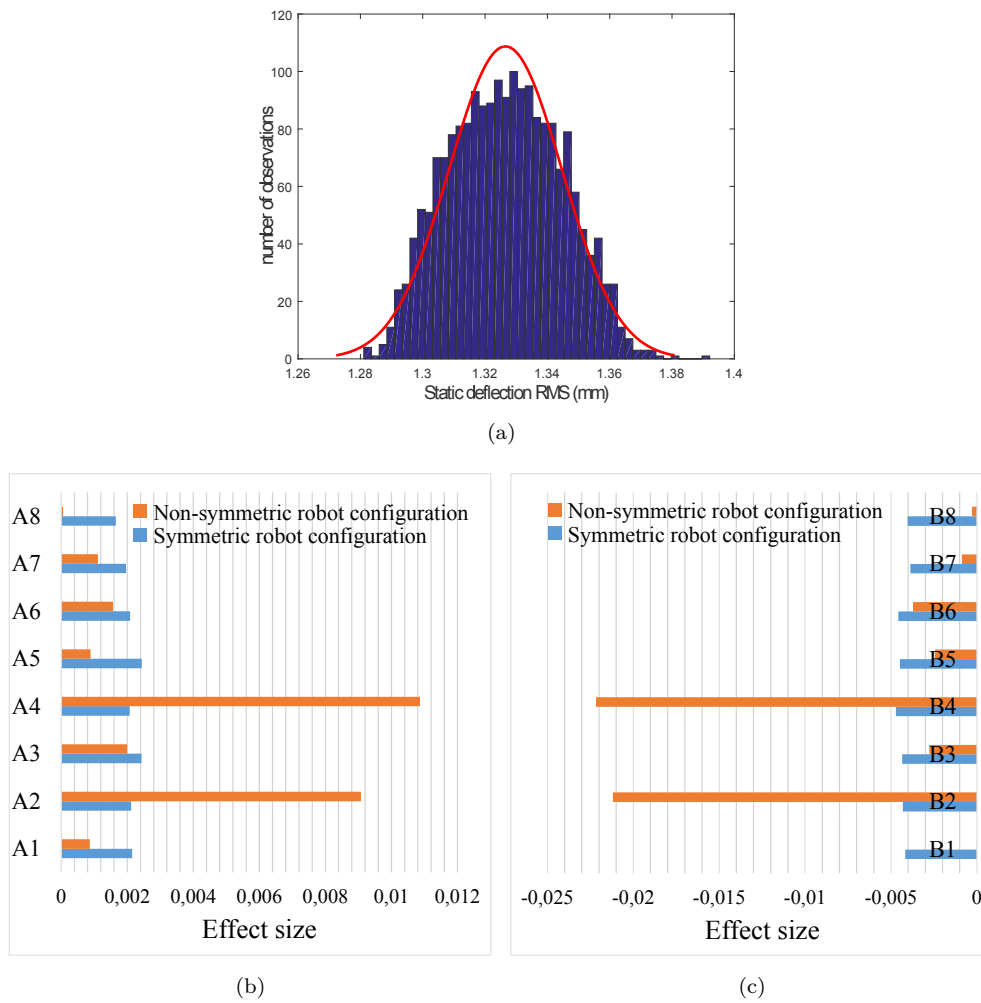


Figure III.22 – (a) Distribution of the RMS of the moving-platform static deflection (b) Effect of uncertainties in  $\mathbf{a}_i$  (c) Effect of uncertainties in  $\mathbf{b}_i$

The  $t$ -Student [Est14] is defined as :

$$st = \frac{|M_- - M_+|}{\sqrt{\frac{V_g^2}{n_-} + \frac{V_g^2}{n_+}}}, \quad (\text{III.7})$$

where  $V_g$  is the general variance.

When the moving-platform is in a symmetric configuration, all attachment points have nearly the same effect amplitudes. However, when it is located close to points  $B_2$  and  $B_4$ , the effect size of their uncertainties becomes high. Moreover, the effects of the corresponding mobile points ( $A_2$  and  $A_4$ ) increase. It means that the closer the moving-platform to a given point, the higher the effect of the variations

in the Cartesian coordinates of the corresponding exit point of the moving-platform onto its static deflection. That can be explained by the fact that when some cables are longer than others and become slack for a non-symmetric position, the sag effect increases. Consequently, a good identification of geometrical parameters is highly required. In order to minimize these uncertainties, a good calibration leads to a better error model.

#### III.4.2.4.1 Analysis of the natural frequency over the workspace

Multidimensional stiffness can make the appropriate analysis complicated, essentially when both rotational and transitional stiffness elements are considered in the same stiffness matrix. An easier way to analyze the CDPR stiffness is the analysis of its natural frequencies. Here, the natural frequencies are calculated with respect to the linearized stiffness matrix around a set-point [KZW06], which deals with elastic cables with non-negligible mass. The first, second and third natural frequencies of the moving-platform are noted  $f_1$ ,  $f_2$  and  $f_3$ , respectively. They are shown in Fig. III.23 over the sub-workspace of the CAROCA prototype defined as  $-1.5 < x < 1.5$  m,  $-1.5 < y < 1.5$  m and  $z = 1$  m, when the rotations are neglected and the nominal values of the input parameters are considered.

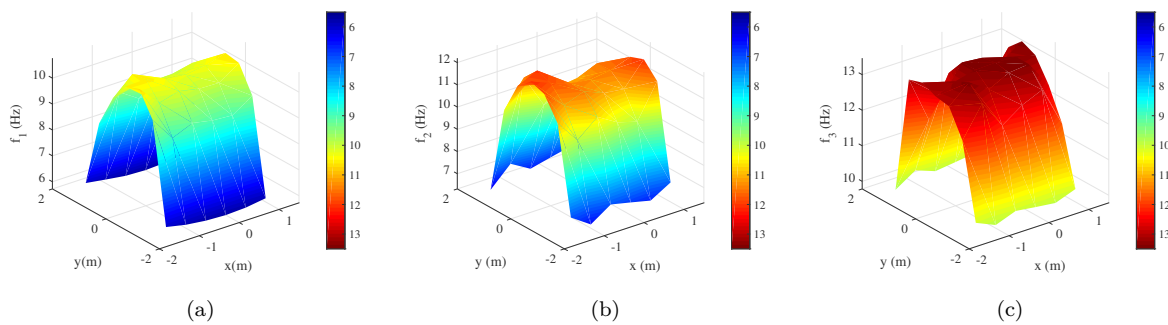


Figure III.23 – Variation in the end-effector natural frequencies  $f_1$ ,  $f_2$  and  $f_3$  over a sub-workspace ( $-1.5 < x < 1.5$  m,  $-1.5 < y < 1.5$  m and  $z = 1$  m)

As mentions Fig. III.23, the natural frequency increases when the moving-platform is closer to the workspace center and it decreases when it is closer to the workspace edges. Thus, the CDPR is more stiff when its moving-platform is in the workspace center, leading to lower static deflection. It should be noticed that the stiffness of the CDPR depends strongly on the moving-platform position.

## III.5 Summary of the chapter

This section dealt with the sensitivity analysis of the CDPR to its modeling, particularly to the level of cables modeling. Once identified experimentally, the cable dynamic parameters were integrated into the non-linear cable tension formulation, which allowed us to study the dynamic behavior of a three DOF CDPR while considering both linear and non-linear cable tension formulations. The comparison between the dynamic responses of the two semi-industrial CDPRs of different sizes shows that substantial differences between the proposed non-linear approach and the classical linear one are more meaningful for large-size CDPRs. Accordingly, the first contribution of this chapter deals with a good choice of the cable tension model with regard to the CDPR size and dynamics.

A sensitivity analysis of CDPR to its level of modeling was also performed through a comparison between the rigid, elasto-static and elasto-dynamic models of CDPR while the linear model of cable tension is adopted. The choice of CDPR model should be made based on the control scheme used and the task. When using the elasto-static static model for high dynamics articular correction, the controller will not see the oscillatory effects due to interactions of the cables with the complete system. As the encoder feedback is not influenced by vibrations, the elasto-dynamic model can help predict the unseen oscillations.

An uncertainty analysis of the static and dynamic responses of CDPRs to uncertainties on the model parameters was made in this chapter. It appears that the effect of the elasticity and the dynamic stiffening of cables is the highest onto the dynamic and oscillatory motions of the moving-platform. This emphasizes the importance of the integration of the cables hysteresis into error modeling, which requires an upstream identification of the cable elasticity parameters in relation to the frequency range of the CDPR response. It appears that the effect of geometrical errors onto the static deflection of the moving-platform is significant too. However, geometrical effects are negligible with respect to the elasticity contributions on the moving-platform static deflection variation. They can be identified using some calibration [dSTDC14, JS03] or self-calibration [MPV, BJB<sup>+</sup>09] techniques, allowing us to fix them at a nominal value. This finding supports the idea to adjust each cable model and parameters to the CDPR dynamic model for a good trajectory

tracking.

With respect to the uncertainty analysis, the uncertain parameters can be sorted to be identified as shown in Fig. III.24. Here, the static deflection of the moving-platform to error sources was evaluated in terms of test of student  $st$ . If  $st_{critical} < st$ , where  $st_{critical}$  is the critical  $t$ -student, the uncertain parameter has a significant effect on the static deflection. The critical parameters are listed below from the most influential to the least influential starting from the modulus of elasticity on the top priority, the geometrical parameters, arriving to mass parameters.

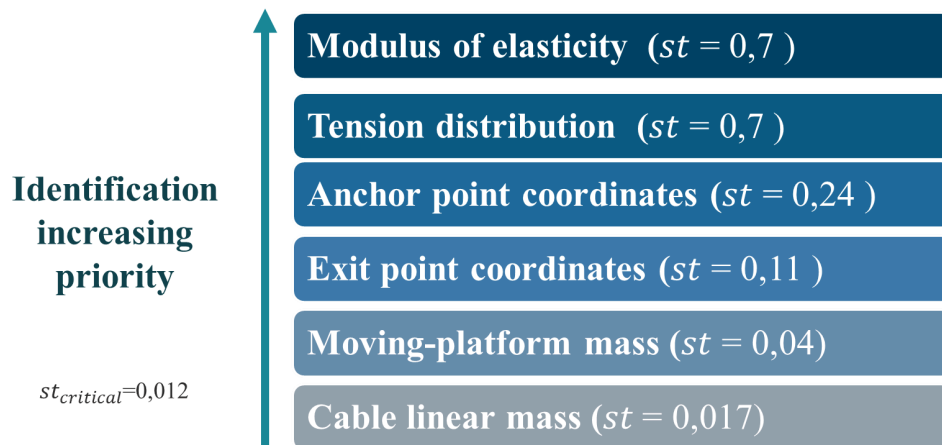


Figure III.24 – Increasing priority of identification of uncertain parameters

These conclusions are established based on the analysis of some CDPRs and they are valid for every CDPR whatever is its overall size. It is still important to compensate for all the CDPR error sources through a good control. This uses a priori knowledge of the robot dynamics to improve the trajectory tracking by generating an additional feed-forward reference. As a consequence, next chapter presents two complementary control strategies. The first one deals with the feed-forward model-based control allowing to compensate not only the elasticity, but the oscillatory effects too. The second control strategy manifests in the integration of the input-shaping into the proposed model-based control.

# IV

---

## CDPR control for accuracy improvement

### Contents

---

IV.1 Introduction ·····	107
IV.2 Feed-forward model-based control ·····	108
IV.3 Input-shaping for feed-forward control ·····	139
IV.4 Summary of the chapter ·····	150

---

### IV.1 Introduction

The main objective of this thesis is to improve the trajectory tracking of the end-effector and to reduce its vibrations due to the CDPR overall elasticity. For this purpose, this chapter proposes two complementary control strategies dealing with the stiffness analysis presented in Chapter II while considering the results on sensitivity and uncertainty analysis of CDPRs obtained in Chapter III. These control strategies manifest in :

- Elasto-dynamic model-based control.
- Input-shaping for model-based control.

The elasto-dynamic model-based control is the coupling of a PID feedback controller with a model-based feed-forward torque control scheme for CDPR. The feed-forward controller is based on the elasto-dynamic model of CDPR (Sec. II.4), which compensates the joint errors due to the dynamic and oscillatory behavior of the CDPR. The predicted errors are corrected "off-line" to generate a pre-compensated input signal, which remedies the deflection of the end-effector due

to cable elasticity and its vibrations due to the dynamic interactions. The proposed control strategy based on the elasto-dynamic model leads to a feed-forward controller for moving-platform oscillatory motion compensation in addition to the conventional rigid body feedback. The integration of cable tension distribution is part of this control strategy in order to guarantee positive cable tensions along the trajectory.

The second contribution of this chapter deals with the integration of input-shaping filters to the previously proposed model-based feed-forward control. These filters are integrated upstream of the pre-compensation block in order to increase the CDPR performances by the improvement of residual vibrations attenuation. Input-shaping filters consist in convolving the desired command signal with a sequence of impulses. The resulting convolution is used as a new reference control signal.

Experimentations are performed to validate the two feed-forward control strategies and check their performances on the CDPR positioning accuracy and trajectory tracking.

## IV.2 Feed-forward model-based control

The feed-forward model-based control uses a priori knowledge of the CDPR dynamics to improve the end-effector trajectory tracking by generating a pre-compensated control input. The pre-compensation unit is seen as an off-line compensation of the actuated joint displacement in such way that after execution the end-effector follows the desired position trajectory with a better accuracy.

The feed-forward model-based control scheme is shown in Fig. IV.1. It is composed of a feed-forward block in which the inverse kinematic model is determined based on a CDPR reference model (Red block in Fig. IV.1). This latter is a predictive model of the dynamic behavior of the mechanism. Its input is the torque set-point  $\zeta_{rg} \in \mathbb{R}^n$  generated by the inverse rigid dynamic model, and its output is the reference winch angular displacement  $\mathbf{q}_{ref} \in \mathbb{R}^n$  and velocity  $\dot{\mathbf{q}}_{ref} \in \mathbb{R}^n$ ;  $n$  being the number of actuators. These reference vectors pre-compensate the joint errors estimated by the used reference model.

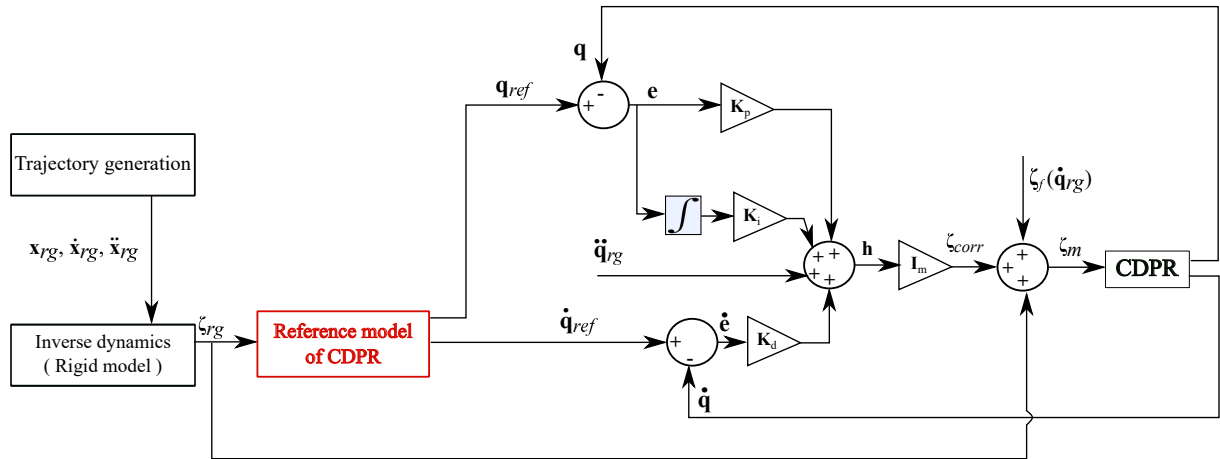


Figure IV.1 – Feed-forward model-based PID control

$\zeta_{rg}$  is calculated using the inverse rigid model of CDPR, which depends on the desired moving-platform pose  $\mathbf{x}_{rg}$  and acceleration  $\ddot{\mathbf{x}}_{rg}$ . The angular displacement vector  $\mathbf{q}_{rg}$ , velocity vector  $\dot{\mathbf{q}}_{rg}$  and acceleration vector  $\ddot{\mathbf{q}}_{rg}$  of joints are calculated based on the rigid model of CDPR depending on the desired motion of the end-effector (pose  $\mathbf{x}_{rg}$ , velocity  $\dot{\mathbf{x}}_{rg}$  and acceleration  $\ddot{\mathbf{x}}_{rg}$ ).

Considering the dynamic model of the motors described in Eq. (II.16), the set-point is assigned to the motors :

$$\zeta_m = \zeta_{corr} + \zeta_f(\dot{\mathbf{q}}_{rg}) + \zeta_{rg}, \quad (\text{IV.1})$$

where  $\zeta_m$  corresponds to the torque set-point applied to the motor and  $\zeta_f(\dot{\mathbf{q}}_{rg})$  is the joint friction torque vector (Eq. (II.17)).  $\zeta_{corr} = \mathbf{I}_m \mathbf{h}(t)$  corresponds to the torque of correction, where  $\mathbf{I}_m$  is a diagonal matrix containing the winch moment of inertia.  $\mathbf{h}(t)$  is defined by :

$$\mathbf{h}(t) = \ddot{\mathbf{q}}_{rg} + \mathbf{K}_p (\mathbf{q}_{ref} - \mathbf{q}) + \mathbf{K}_d (\dot{\mathbf{q}}_{ref} - \dot{\mathbf{q}}) + \mathbf{K}_i \int_{t_i}^{t_i^+} (\mathbf{q}_{ref} - \mathbf{q}) dt, \quad (\text{IV.2})$$

where  $\mathbf{K}_p \in \mathbb{R}^{n \times n}$  is the proportional gain matrix,  $\mathbf{K}_d \in \mathbb{R}^{n \times n}$  is the derivative gain matrix,  $\mathbf{K}_i \in \mathbb{R}^{n \times n}$  is the integrator gain matrix.  $\ddot{\mathbf{q}}_{rg}$ ,  $\dot{\mathbf{q}}_{ref}$ ,  $\mathbf{q}_{ref}$  represent the desired angular acceleration coming from the rigid model, the desired angular velocity and the desired angular displacement of the motors coming from the chosen reference model, respectively.  $\dot{\mathbf{q}}$  and  $\mathbf{q}$  represent the measured angular velocity and the measured angular displacement of motors, respectively.

Through the identification between Eq. (II.16) and Eq. (IV.1) describing the

dynamic model of the motors, we obtain :

$$\ddot{\mathbf{q}} = \ddot{\mathbf{q}}_{rg} + \mathbf{K}_p (\mathbf{q}_{ref} - \mathbf{q}) + \mathbf{K}_d (\dot{\mathbf{q}}_{ref} - \dot{\mathbf{q}}) + \mathbf{K}_i \int_{t_i}^{t_i^+} (\mathbf{q}_{ref} - \mathbf{q}) dt. \quad (\text{IV.3})$$

If the difference between measured and desired joint angular positions and velocities is null, the end-effector will track exactly the desired trajectory and  $\ddot{\mathbf{q}} = \ddot{\mathbf{q}}_{rg}$ .

The closed-loop dynamics corresponds to the following tracking error equation :

$$\ddot{\mathbf{e}} + \mathbf{K}_p \mathbf{e} + \mathbf{K}_d \dot{\mathbf{e}} + \mathbf{K}_i \int_{t_i}^{t_i^+} \mathbf{e} dt = \mathbf{0}. \quad (\text{IV.4a})$$

$$\mathbf{e} = \mathbf{q}_{ref} - \mathbf{q}. \quad (\text{IV.4b})$$

$\mathbf{e}$  being the tracking error, which is the difference between  $\mathbf{q}_{ref}$  and  $\mathbf{q}$ .

The feed-back control is a real-time operation. By calculating off-line an appropriate trajectory pre-compensation, the effects of the oscillatory dynamics are compensated. However, this may lead to non-robustness of the control with respect to model uncertainties and a delay between the reference and the real CDPR behavior may occur. To handle this issue, the off-line feed-forward part should respect the findings of Chapter III to deal with robust model for control. This leads to the attenuation of errors coming from modeling and parameters uncertainties as shown for different industrial robots [ODB<sup>+</sup>12, VS02].

## IV.2.1 Discrete-time control of CDPR

The equivalence between a CDPR and its control unit is described in Fig. IV.2. It is composed of 3 units : (i) Actuation systems, (ii) Feedback controller and (iii) Feed-forward controller.

Each unit of the equivalent control scheme is characterized by its own discretization time. Let  $\Delta t_a$  be the sampling time of the actuation model, which is a function of the feed-back controller frequency.  $\Delta t_b$  is the sampling time of the feed-forward unit. It is chosen greater or equal to  $\Delta t_a$  to avoid delays and divergence.

### IV.2.1.1 Actuation system

This model presents the actuators of the CDPR. Its input is the motor torque vector  $\zeta_m$  and its output is the measured angular coordinates  $\mathbf{q}$  and velocities  $\dot{\mathbf{q}}$  of the actuators. This measurement is obtained at each time  $t = \beta \Delta t_a$ .

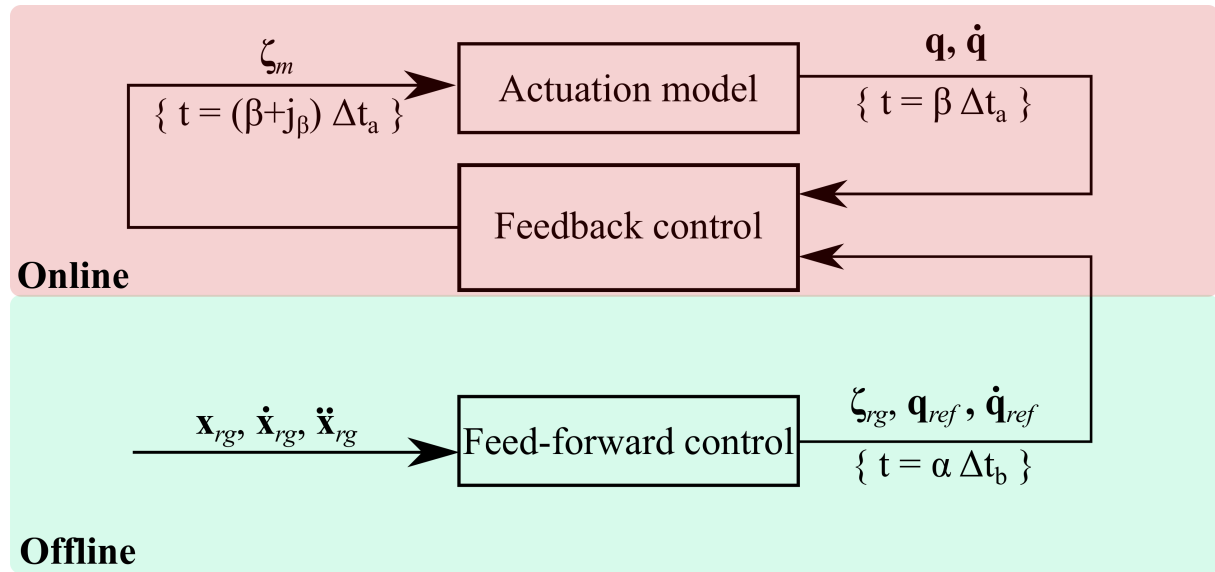


Figure IV.2 – Equivalent control scheme : Discrete-time control

### IV.2.1.2 Feedback control loop

This control loop permits the application of the control law mentioned in Eq. (IV.1). The feedback control loop has a sampling time  $\Delta t_a$ . At each time  $t = \beta \Delta t_a$ , the loop calculates a new value for  $\zeta_m$ , which is sent to the actuation model at time  $t = (\beta + j_\beta) \Delta t_a$ ,  $\beta \in \mathbb{N}^+$ , at which a new measurement of  $\mathbf{q}$  and  $\dot{\mathbf{q}}$  is made.  $j_\beta \in \mathbb{N}^+$  presents the delay between the generation of the control set-point by the feed-back controller and the reception of the encoder information. The value of  $\zeta_m$  is kept constant in the time interval  $[(\beta + j_\beta) \Delta t_a \quad (\beta + j_\beta + 1) \Delta t_a]$ .

### IV.2.1.3 Feed-forward control loop

This control loop aims to generate the modified trajectory. The input of this loop is the desired motion of the moving-platform, which manifests in the desired pose  $\mathbf{x}_{rg}$ , velocity  $\dot{\mathbf{x}}_{rg}$  and acceleration  $\ddot{\mathbf{x}}_{rg}$  of the moving platform. The output is the reference angular displacement  $\mathbf{q}_{ref}$  and velocity  $\dot{\mathbf{q}}_{ref}$ . The sampling time of the feed-forward control loop is  $\Delta t_b$ .

At each time  $\alpha \Delta t_b$ , a set of torques  $\zeta_{rg}$  is calculated, coming from a cable tension distribution algorithm, with respect to the desired motion of the moving-platform (pose  $\mathbf{x}$ , velocity  $\dot{\mathbf{x}}$  and acceleration  $\ddot{\mathbf{x}}$ ). The pre-compensation of the trajectory is obtained by generating the joint angular displacement  $\mathbf{q}_{ref}$  and velocity  $\dot{\mathbf{q}}_{ref}$  with respect to the chosen reference model of the CDPR.  $\zeta_{rg}$  and  $\mathbf{q}_{ref}$  are sent to the

feedback control loop at each time  $\alpha\Delta t_b$ ,  $\alpha \in \mathbb{N}^+$ . These vectors are kept constant in the time interval  $[\alpha\Delta t_b \quad (\alpha + 1)\Delta t_b]$ .

## IV.2.2 Pre-compensation

The reference angular displacement of joints is obtained by using a reference model of CDPR. Therefore, the kinematic constraints are implicitly considered depending on the chosen model. The reference model of the proposed control strategy manifests in an off-line pre-compensation of the desired trajectory.

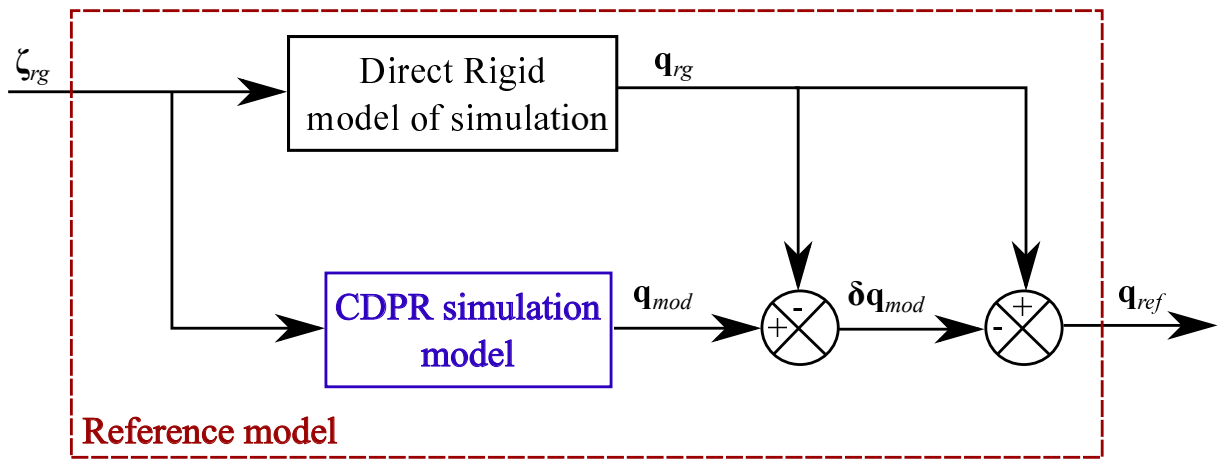


Figure IV.3 – Model-based pre-compensation

The off-line pre-compensation strategy is applied to eliminate the trajectory tracking errors due to the robot compliance. This strategy is based on the anticipation of the joint errors and correcting them by modifying the reference actuated joint position  $\mathbf{q}_{ref}$  as follows :

$$\mathbf{q}_{ref}^j = \mathbf{q}_{rg} - \delta \mathbf{q}_{mod}^j, \quad (\text{IV.5a})$$

$$\delta \mathbf{q}_{mod}^j = \mathbf{q}_{mod}^j - \mathbf{q}_{rg}, \quad (\text{IV.5b})$$

where  $j$  refers to the reference model control. It can be either "rg", "es" or "ed" to mention the *rigid*, *elasto-static* and *elasto-dynamic* models, resp.  $\delta \mathbf{q}_{mod}^j \in \mathbb{R}^n$  is a vector of angular displacements errors, leading to trajectory tracking errors. This vector is calculated by using a CDPR model of simulation depending on the sources of errors that are considered. It anticipates the correction of the actuated joint angles  $\mathbf{q}_{mod}^j$  with respect to the displacement vector  $\mathbf{q}_{rg}$ , which is calculated

through the rigid model of CDPR and corresponds to the unstrained cable length. The subtraction of  $\delta\mathbf{q}_{mod}^j$  from  $\mathbf{q}_{rg}$  generates a new reference input signal  $\mathbf{q}_{ref}^j$  allowing the end-effector to track more accurately the desired trajectory.

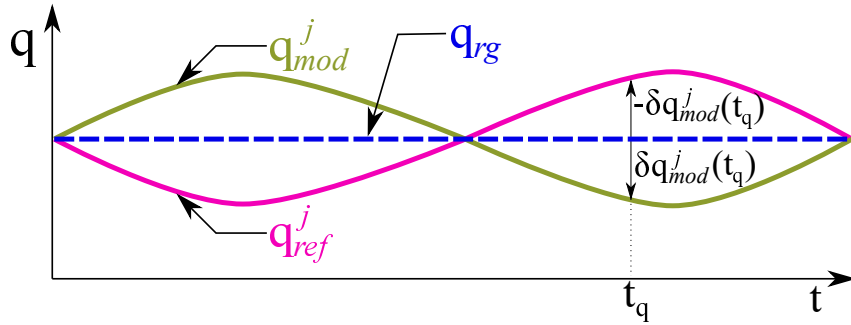


Figure IV.4 – Pre-compensation : illustrative example

Fig. IV.4 presents an illustrative example of the proposed pre-compensation in the articular space. When the rigid joint angles  $\mathbf{q}_{rg}$  are constant and the anticipated actuated joint angles  $\mathbf{q}_{mod}^j$  oscillate around  $\mathbf{q}_{rg}$ , the control input signal  $\mathbf{q}_{ref}^j$  is the "mirror image" of  $\mathbf{q}_{mod}^j$  with respect to  $\mathbf{q}_{rg}$ .

It is noteworthy that  $\delta\mathbf{q}_{mod}^j$  depends on the CDPR reference model used to calculate the vector  $\mathbf{q}_{ref}^j$ . To the best of our knowledge, two CDPR models have been used in the literature for the feed-forward model-based control of CDPRs with non-sagging cables : (i) rigid model (see Sec. II.2) and (ii) elasto-static model (see Sec. II.3) [BLS<sup>+</sup>13, Ars13b]. As a consequence, one contribution of this chapter deals with the use of the (iii) elasto-dynamic model (Sec. II.4) of CDPRs for feed-forward control.

### IV.2.2.1 Rigid pre-compensation

When using the rigid model of simulation, the reference signal  $\mathbf{q}_{ref}$  anticipates neither the cable elongation nor the oscillatory motions of the moving-platform. So, the rigid reference signal  $\mathbf{q}_{ref}^{rg}$  is expressed as :

$$\mathbf{q}_{ref}^{rg} = \mathbf{q}_{rg}. \quad (\text{IV.6})$$

The PID feedback controller uses the motor encoders response  $\mathbf{q}$ , which is related to the unstrained cable length  $\mathbf{l}_{rg}$ . This latter corresponds to the winch angular displacement  $\mathbf{q}_{rg}$ . It should be noted that the cable elongations and moving-platform

oscillatory motions are not considered here, and as a consequence, cannot be rejected.

### IV.2.2.2 Elasto-static pre-compensation

The CDPR elasto-static model integrates a feed-forward cable elongation compensation [BLS<sup>+</sup>13]. Here, at each sampling time  $t = \alpha\Delta t_b$ , each cable of the CDPR is isolated and its elongation is determined with respect to the discretized end-effector pose. Knowing the force applied on each cable, we estimate its elongation based on the chosen cable tension model. This is done while considering both axial and sag-introduced stiffness or while neglecting sag through linear or non-linear cable tension model (Section II.3).

When  $\mathbf{q}_{ref}^{rg}$  is used as a reference signal in the feedback control scheme, the moving-platform displacement  $\delta\mathbf{x}_{es}$  is obtained from cable elongation vector  $\delta\mathbf{l}_{es}$ . To compensate for the cable elongation effects,  $\delta\mathbf{l}_{es}$  is converted into winch displacement  $\delta\mathbf{q}_{mod}^{es}$ , which estimates the joint error with respect to the rigid angular position  $\mathbf{q}_{rg}$ . Thus, the elasto-static reference angular displacement  $\mathbf{q}_{ref}^{es}$  becomes :

$$\mathbf{q}_{ref}^{es} = \mathbf{q}_{rg} - \delta\mathbf{q}_{mod}^{es}. \quad (\text{IV.7})$$

As the CDPR cable tensions are always positive,  $\delta\mathbf{l}_{es} > 0$  corresponding to  $\delta\mathbf{q}_{mod}^{es} < 0$ . The reference signal  $\mathbf{q}_{ref}^{es}$  corresponds to a fake position of the moving-platform for the cable elongation compensation. Here, under the effect of cable elongations, the reference moving-platform pose is estimated to achieve the desired pose. Although the elasto-static reference model takes into account the cable elongations, the non-compensation for the moving-platform pose errors due to the cable interaction with the whole system and elasto-dynamic behavior is not considered.

### IV.2.2.3 Elasto-dynamic pre-compensation

The CDPR elasto-dynamic model of simulation takes into account the oscillatory and dynamic behavior of the moving-platform due to cable elongations. Here, the cables are no-longer isolated and are affected by the moving-platform dynamic behavior.

Once the moving-platform pose  $\mathbf{x}_{ed}$  is calculated through the direct elasto-dynamic model employing MATLAB<sup>®</sup> routine ode45, the cable elongation vector

$\delta \mathbf{l}_{ed}$  can be determined. This latter is converted into  $\delta \mathbf{q}_{mod}^{ed}$ , which corrects the angular position vector  $\mathbf{q}_{rg}$ . The elasto-dynamic reference angular displacement  $\mathbf{q}_{ref}^{ed}$  becomes :

$$\mathbf{q}_{ref}^{ed} = \mathbf{q}_{rg} - \delta \mathbf{q}_{mod}^{ed}. \quad (\text{IV.8})$$

The proposed control strategy based on the elasto-dynamic model leads to a feed-forward controller for moving-platform oscillatory motion compensation in addition to the conventional rigid body feedback while considering the measurements from motor encoders.

### IV.2.3 Controller tuning

Whatever the used reference model for control, the controller tuning methodology remains the same. Applying the Laplace transform to the tracking error differential Eq. (IV.4a), and assuming zero initial conditions, we obtain for each drive :

$$e(s)(s^3 + K_p s + K_d s^2 + K_i) = 0. \quad (\text{IV.9})$$

While assigning :

$$K_p = (2v + 1)\Upsilon_n^2, \quad (\text{IV.10a})$$

$$K_d = (2v + 1)\Upsilon_n, \quad (\text{IV.10b})$$

$$K_i = v_n^3, \quad (\text{IV.10c})$$

Eq. (IV.9) can be expressed as follows :

$$e(s)(s + \Upsilon_n)(s^2 + 2v\Upsilon_n s + \Upsilon_n^2) = 0. \quad (\text{IV.11})$$

This differential equation expresses the dynamic behavior of the closed-loop tracking error in response to a perturbation. This corresponds to a first-order system followed by a second-order system. Since the parameters  $v$  and  $\Upsilon_n$  are strictly positive real numbers, the system is always stable.

To obtain the fastest answer without oscillation,  $v = 1$  is chosen. Thus, a third order system with a triple real pole is obtained. In this case, the PID gains become :

$$K_p = 3\Upsilon_n^2, \quad (\text{IV.12a})$$

$$K_d = 3\Upsilon_n, \quad (\text{IV.12b})$$

$$K_i = \Upsilon_n^3, \quad (\text{IV.12c})$$

It is therefore the choice of  $\Upsilon_n$  that will determine the value of the coefficients

Note that  $K_p$ ,  $K_d$  and  $K_i$  are all a function of  $\Upsilon_n$ . A simple and effective method is to select  $\Upsilon_n$  twice the breaking pulse  $\Upsilon_c$  of the motors, which is expressed as :

$$\Upsilon_c = \frac{k_t k_e}{\varpi I_m}, \quad (\text{IV.13})$$

where  $\varpi$  is the resistance of the motor armature,  $k_e$  is the counter-electromotive force coefficient and  $k_t$  represents the electromagnetic torque coefficient of the motor. These parameters are available in the user manual of winches.

## IV.2.4 Numerical results

A spatial CDPR with three cables and three translational-DOF is considered. This CDPR is composed of a point-mass end-effector, which is connected to three massless but elastic linear cables. A suspended configuration of the CREATOR prototype (Fig. IV.5(a)), being developed at LS2N, is chosen such that the cables are tensed along a prescribed trajectory. This configuration is taken as an illustrative example. However, the proposed model-based feed-forward control can be applied not only to suspended CDPRs but also to fully-constrained ones.

The Cartesian coordinate vectors of the cable exit points expressed in the global frame  $\mathcal{F}_b$  are described in Tab. B.5. The end-effector mass  $m_{ee}$  is equal to 1 kg. The identified polyethylene cables presented in App.A.2 are used for the simulations. Their modulus of elasticity is equal to 70 GPa and their volumetric density is equal 0.901 g/cm<sup>3</sup>. Here, the hysteresis effects are not taken into consideration as the tension set-point is known.

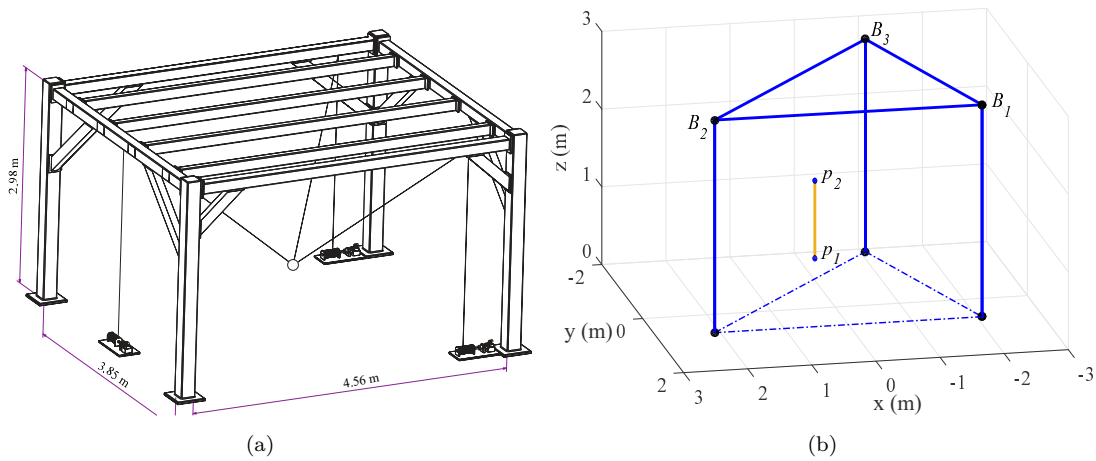


Figure IV.5 – (a) CREATOR prototype CAD diagram (b) End-effector desired path in  $\mathcal{F}_b$

Table IV.1 – Characteristics of the CREATOR actuators

Parameter (Unit)	Value
$I_{motor}$ (kg.m <sup>2</sup> )	42.5e-6
$I_{reducer}$ (kg.m <sup>2</sup> )	6.5e-6
$r$	8
$I_m$ (kg.m <sup>2</sup> )	0.0031
$k_e$ (Vrms.s/rad)	0.48
$\varpi$ (ohm)	12.8

To determine the coefficients  $K_p$ ,  $K_d$  and  $K_i$  of the PID controller, the parameters presented in the motor<sup>1</sup> and reducer<sup>2</sup> catalogs are used and they are presented in Tab. IV.1.  $I_{motor}$  is the inertia of the motor with brakes in its entry.  $I_{reducer}$  is the inertia of the reducer.  $r$  is the transmission ratio of the reducer.  $I_m$  is the total inertia of the motor seen at its exit and is calculated as follows :

$$I_m = r^2(I_{motor} + I_{reducer}). \quad (IV.14)$$

These parameters lead to the PID controller coefficients displayed in Tab. IV.2.

Table IV.2 –  $K_p$ ,  $K_d$  and  $K_i$  gains of the PID controller

$K_p$	$K_d$	$K_i$
1125.8	58.12	7269.60

1. Parker™ SMB/SME Brushless servo motor series. Ref : SMEA 60601- 489IZ64S54.  
<http://www.parkermotion.com/dmxreadyv2/faqsmanager/faqsmanager.asp?category=75&question=1391>

2. Parker™ Economical Planetary Gearheads - PE. Ref : PE3-008-10M040/063/09/20.  
<http://ph.parker.com/us/17607/en/standard-precision-inline-planetary-gearboxes-pe-series>

It is noteworthy that for accuracy purposes, the cable dead length between the drum and the pulley is considered while calculating the cable elongation.

#### IV.2.4.1 Trajectory generation

Before running trajectory tracking, a pre-compensation of the end-effector static deflection is performed when adopting the control of the CDPR based on its elasto-static and the elasto-dynamic models, respectively. It is to compensate the static deflection due to the end-effector weight by correcting the joint angular displacement leading to trajectory tracking error.

A linear path along the vertical axis with a 5-th degree polynomial motion profile is considered. It goes from the initial pose  $\mathbf{p}_1 = [x_1, y_1, z_1]^T$  to the final pose  $\mathbf{p}_2 = [x_2, y_2, z_2]^T$ , 1 m high along  $z$ -axis, during  $t_f = 3$  s. A pause equal to  $t_f$  at the final pose is considered. The effects of the end-effector residual oscillations are easily detected during the steady-state phase. Therefore, the end-effector trajectory is parametrized as follows :

$$\mathbf{p}(t) = \mathbf{p}_1 + \alpha(t) (\mathbf{p}_2 - \mathbf{p}_1); \quad t \in [0 \ t_f], \quad (\text{IV.15a})$$

$$\mathbf{p}(t) = \mathbf{p}_2; \quad t > t_f. \quad (\text{IV.15b})$$

The fifth degree polynomial for the linear path is expressed as :

$$\alpha(t) = \beta_5 t^5 + \beta_4 t^4 + \beta_3 t^3 + \beta_2 t^2 + \beta_1 t + \beta_0, \quad (\text{IV.16})$$

where  $\beta_5 = \frac{6}{t_f^5}$ ,  $\beta_4 = \frac{-15}{t_f^4}$ ,  $\beta_3 = \frac{10}{t_f^3}$ ,  $\beta_2 = 0$ ,  $\beta_1 = 0$  and  $\beta_0 = 0$ . These values are chosen such that the velocity and acceleration of the end-effector are null at the beginning and the end of the trajectory as shown in Figs. IV.6(b) and IV.6(c).

#### IV.2.4.2 Trajectory tracking

The end-effector trajectory error  $\delta\mathbf{p}$  is defined as the difference between its desired position  $\mathbf{p}_{rg}$  and its real one  $\mathbf{p}$ . This latter should be normally determined

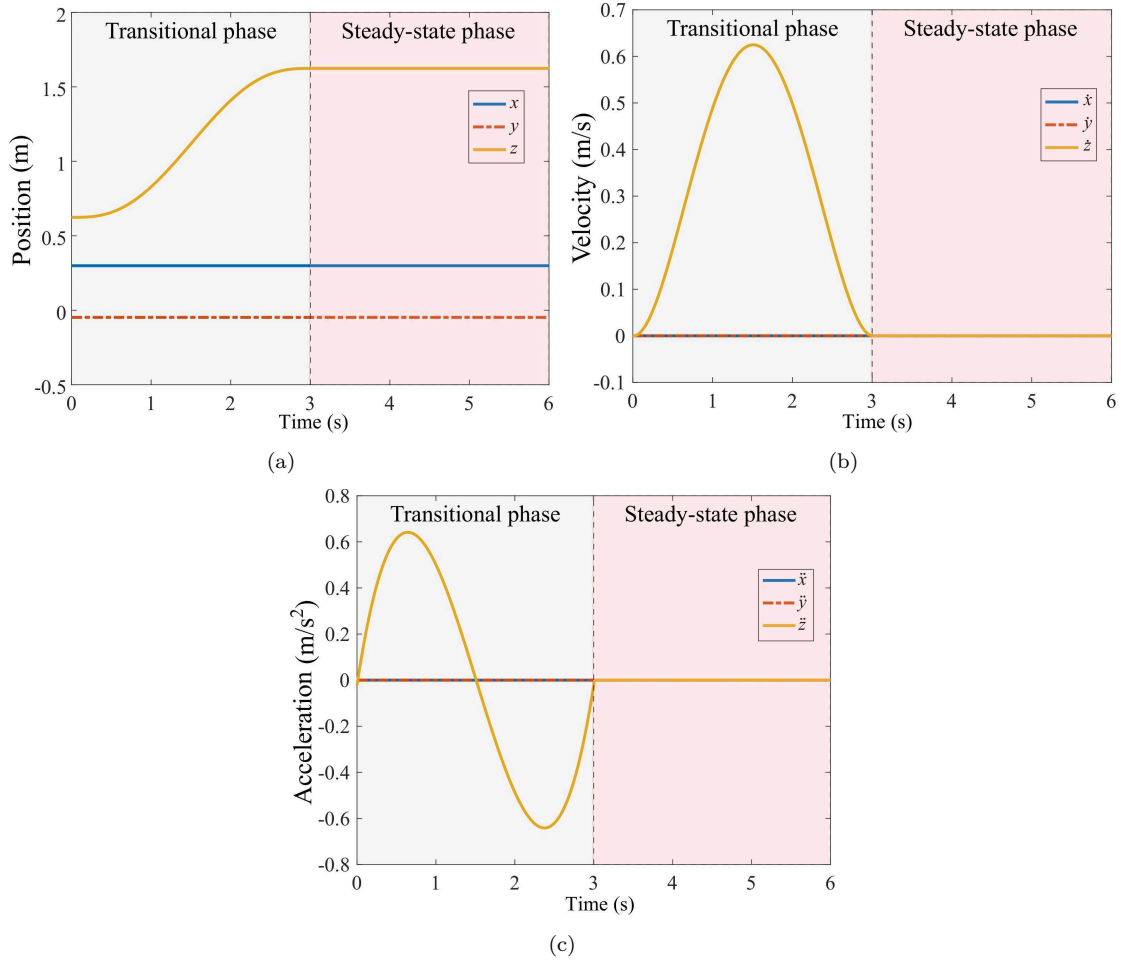


Figure IV.6 – Desired (a) Position (b) Velocity and (c) Acceleration profiles of the end-effector

experimentally. To assess the performances of different control laws, a good CDPР predictive model should be used to estimate the end-effector real position. The CDPР elasto-dynamic model is the closest one to the real CDPР with non sagging cables. Therefore, it is used to predict the real behavior of the CDPР. The input of this model is  $\zeta_m$ , which leads to the Cartesian coordinate vector  $\mathbf{p}_{ed}^m$  of the end-effector position. The trajectory error is defined as  $\delta\mathbf{p}(t) = \mathbf{p}_{ed}^m(t) - \mathbf{p}_{rg}(t)$ .

To analyze the relevance of the proposed control strategy, the three control schemes under study were simulated through Matlab-Simulink<sup>®</sup>.

The sampling times  $\Delta t_a$  and  $\Delta t_b$  are supposed to be equal in the simulations, i.e.,  $\Delta t_a = \Delta t_b = 1$  ms.

Figure IV.7(b) shows the norm  $\|\delta\mathbf{p}\|$  of the end-effector trajectory tracking er-

ror when the proposed model-based feed-forward control law is applied. The three CDPR models are successively used to generate the reference signal. Figure IV.7(a) illustrates the end-effector trajectory tracking error  $\delta z$  along the  $z$ -axis, which is the main one as the CDPR under study is assembled in a suspended configuration and its end-effector tracks a vertical trajectory. The red (green, blue, resp.) curve depicts the end-effector trajectory tracking error when the elasto-dynamic (elasto-static, rigid, resp.) model is used as a reference model.

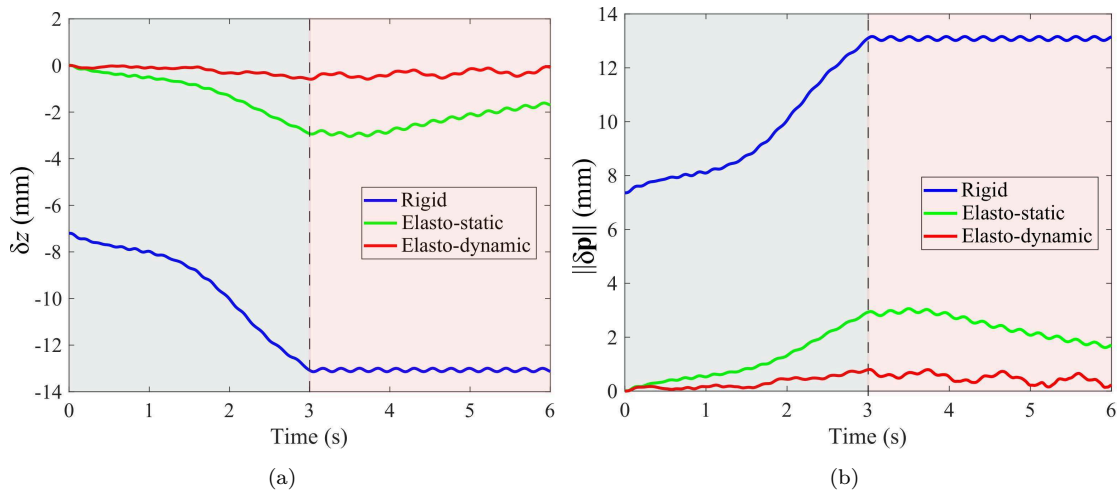


Figure IV.7 – (a) Position error of the end-effector along the  $z$ -axis (b) 2-norm of the end-effector Cartesian trajectory tracking error vector

The CDPR end-effector should oscillate around a final pose during the steady state phase. We can notice in Fig. IV.10 that the simulated responses obtained through the elasto-static and elasto-dynamic controls lead to varying position error of the end-effector. This is due to PID effects as the input  $\mathbf{e}$  of the PID controller is never null.

#### IV.2.4.2.1 Transitional phase

As shown in Fig. IV.8, the position error norm  $\|\delta \mathbf{p}\|$  while using the rigid model as a reference for the feed-forward at time  $t = 3$  s is equal to 13.14 mm. This value is equal to 2.18 mm when the elasto-static model is used as a reference for the feed-forward, which represents a relative difference of 83 % with respect to the rigid

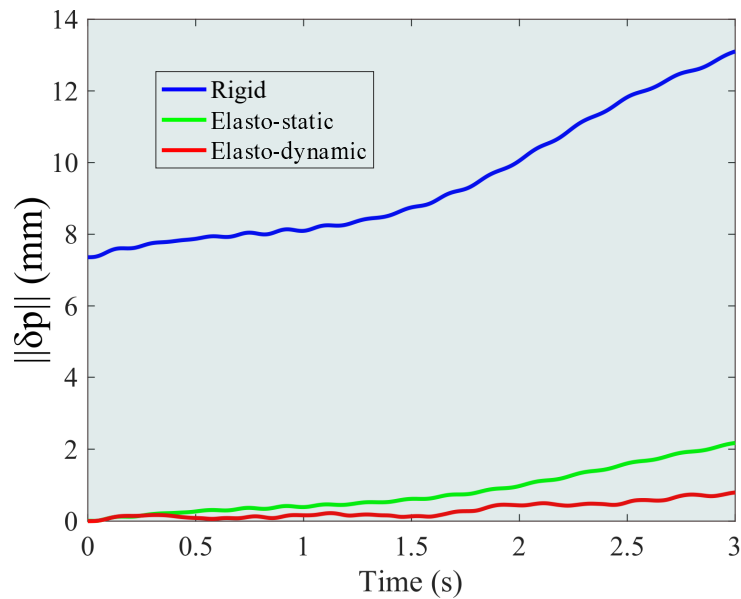


Figure IV.8 – Position error norm during the transitional phase

control<sup>3</sup>. The position error norm  $\|\delta\mathbf{p}\|$  while using the elasto-dynamic model as a reference for the feed-forward at time  $t = 3$  s is equal to 0.58 mm, which represents a relative difference of 95 % with respect to the rigid control.

This shows a good improvement of the moving-platform positioning accuracy at the end of the trajectory through the elasto-dynamic compensation comparing to classical feed-forwards. The trajectory tracking error is also reduced significantly with the CDPR elasto-dynamic control<sup>4</sup> compared to the classical feed-forward model-based control schemes. This is due to the fact that the elasto-dynamic control compensates not only the static errors due to cable elongations but also the oscillatory behavior of the moving-platform.

#### IV.2.4.2.2 Steady-state phase

To define the performance indexes of control laws with respect to residual vibration reduction, an illustrative example of an oscillatory time function  $f$  is given in Fig. IV.9. It firstly illustrates the definition of the first and the fifth Peak-to-Peak amplitudes of the time response. The corresponding function damping can also be described by the decrement of residual vibrations. Here, this decrement is defined as the ratio between the first and the fifth Peak-to-Peak amplitudes.

3. "rigid control" refers to "rigid model-based control of CDPR"

4. "elasto-dynamic control" refers to "elasto-dynamic model-based control of CDPR"

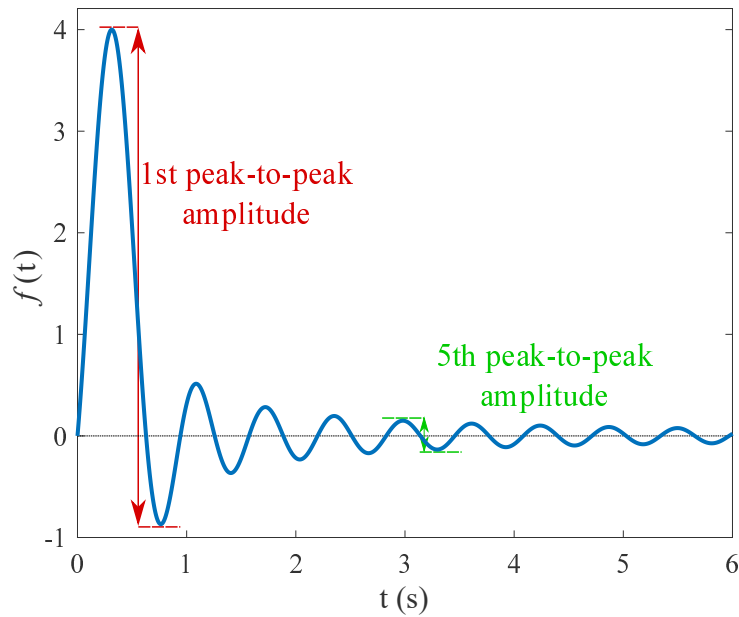


Figure IV.9 – Illustrative example : Peak-to-Peak amplitudes

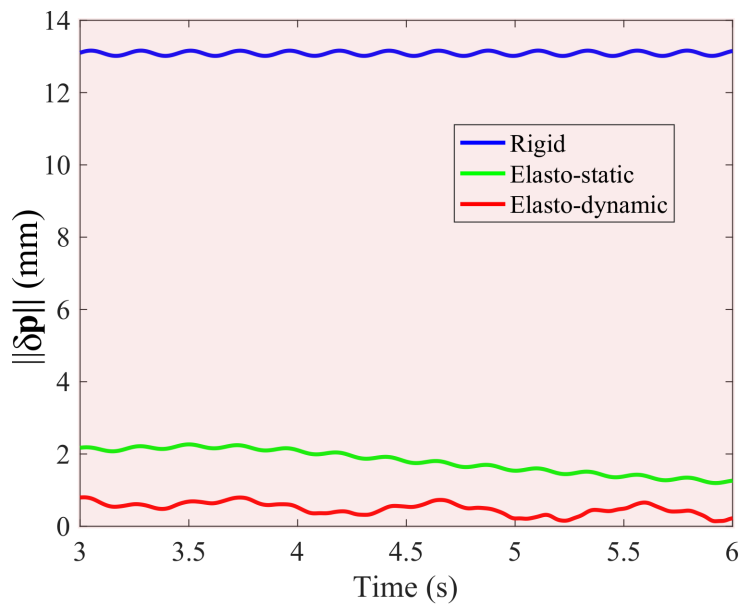


Figure IV.10 – Position error norm during the steady-state phase

As shown in Fig. IV.10, at time  $t = 3$  s, the end-effector achieves its final position and then oscillates.

Figure IV.11 shows the first and fifth Peak-to-Peak amplitudes of the residual vibrations of the end-effector during the steady state phase while using the rigid, elasto-static and elasto-dynamic feed-forwards.

When the rigid model is used as a reference for the feed-forward, the first Peak-

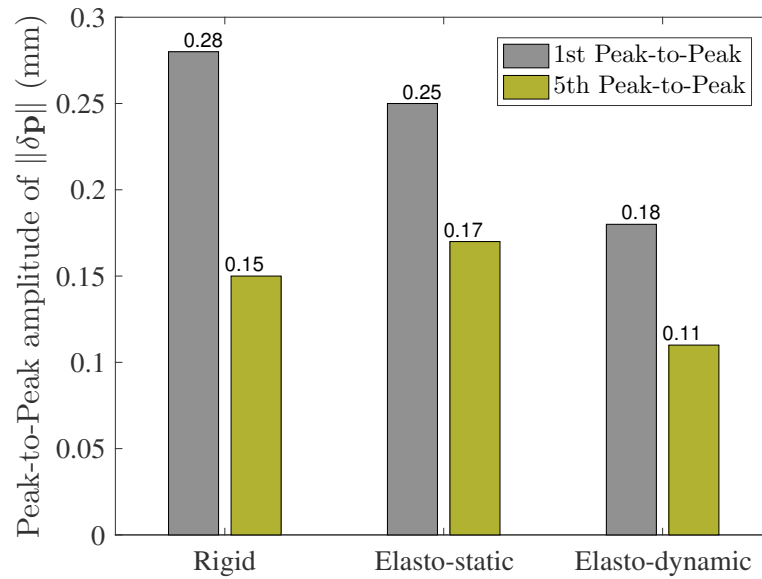


Figure IV.11 – Histogram of the first and fifth Peak-to-Peak amplitude of  $\|\delta\mathbf{p}\|$  during the steady-state phase

to-Peak amplitude of residual vibrations is equal to 0.28 mm. This value is equal to 0.25 mm when the elasto-static model is used as a reference for the feed-forward, which represents a relative difference of 10 % with respect to the rigid control. When the elasto-dynamic model is used as a reference for the feed-forward, the first Peak-to-Peak amplitude of residual vibrations is equal to 0.18 mm, which represents a relative improvement of 35 % with respect to the rigid control.

The fifth Peak-to-Peak amplitude of residual vibrations is equal to 0.15 mm when the rigid model is used as a reference for the feed-forward. This value is equal to 0.17 mm when the elasto-static model is used as a reference for the feed-forward. The fifth Peak-to-Peak amplitude of residual vibrations is equal to 0.11 mm when the elasto-dynamic model is used as a reference for the feed-forward, which represents a relative improvement of 26 % with respect to the rigid control. The advantage of the elasto-dynamic control stays the best with respect to the classical feed-forwards for the fifth Peak-to-Peak.

It is clear that the elasto-dynamic control leads to better attenuation of residual vibrations of the moving-platform than the conventional elasto-static and rigid controls.

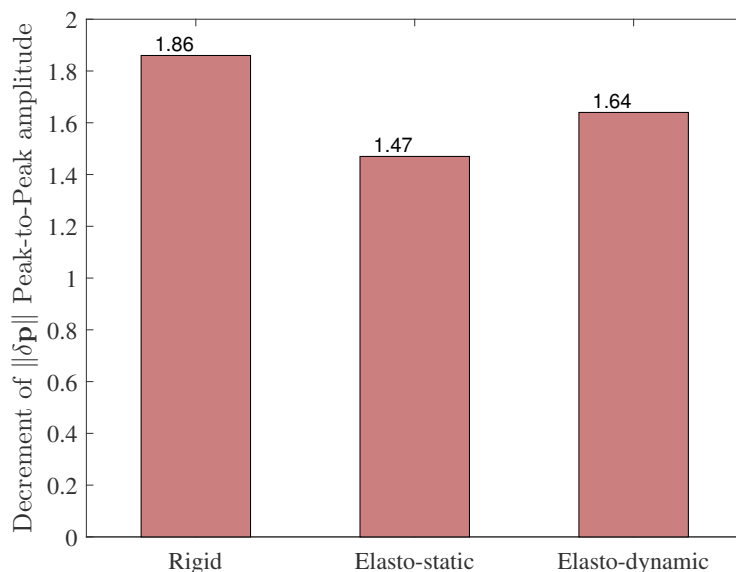


Figure IV.12 – Histogram of Decrement of the Peak-to-Peak amplitudes of  $\|\delta\mathbf{p}\|$  during the steady-state phase

Figure IV.12 shows the decrement of the Peak-to-Peak amplitudes of  $\|\delta\mathbf{p}\|$  during the steady-state phase. This decrement is equal to 1.64 (1.47, 1.86, resp.) when the elasto-dynamic (elasto-static, rigid, resp.) model is used as a reference for the feed-forward. The decrement of the Peak-to-Peak amplitudes of  $\|\delta\mathbf{p}\|$  during the steady-state phase is quasi identical for the different control schemes as the cable damping is the same in the different reference models used and the PID gains of the feedback controller are also the same.

These interesting results are supported in [BCC19] by the analysis of the proposed model-based control scheme, when the end-effector tracks a circular helical trajectory.

## IV.2.5 Experimental results

The objective of the experiments is to check the relevance of the elasto-dynamic feed-forward control with respect to the classical rigid and elasto-static ones. In this section, the variation of the pose error of the end-effector along a trajectory is experimentally studied on the CREATOR prototype arranged with three cables and a point-mass end-effector (see App. B.3). The end-effector is requested to track

the linear path defined in Section IV.2.4.1. The transitional phase allows us to depict the trajectory tracking of the end-effector. The steady-state phase is useful to analyze the residual vibrations.

For experimentations, the CREATOR prototype is set up to match with the robot configuration used in numerical simulations. The test bench is prepared under the assumption that cables are elastic and keep linear shape along a trajectory. The end-effector and pulleys are considered as points. To provide this configuration, some precautions are taken into account on the test bench to provide the particular configuration of the CREATOR prototype. The experimental test bench is described in Section IV.2.5.1.

### IV.2.5.1 Test bench

The equivalent architecture of the CREATOR prototype is described in Fig. IV.13.

- The CREATOR prototype is actuated by three Parker™ motors with reducers connected to 3D printed winches. The motors characteristics are given in Tab. IV.1. Each motor is connected to a Parker™ motor drive, which communicates with the dSpace™ controller through bi-directional real-time links.

The friction torques of the actuators are identified with respect to the static friction model [KD04] by incrementing the joint angular velocity, as shown in Fig. IV.14. The first move of the actuator corresponds to the dry friction torque  $\zeta_d$ . As we do not have an accurate measurement of the motor torques, we suppose that the viscous friction torque is zero. Here, the dry friction value is  $\zeta_d = 0.14$  N.m.

- The winch is 3D printed and it is mounted to the reducer axis. Its pitch is equal to 2 mm and its radius is equal to 50 mm.
- 3D printed pieces are used as pulleys of the CREATOR prototype (See Fig. IV.15). They were designed in such a way that their exit amount to a point. The entrance of the pulley is conical and their exit is a hole of 3 mm of diameter.

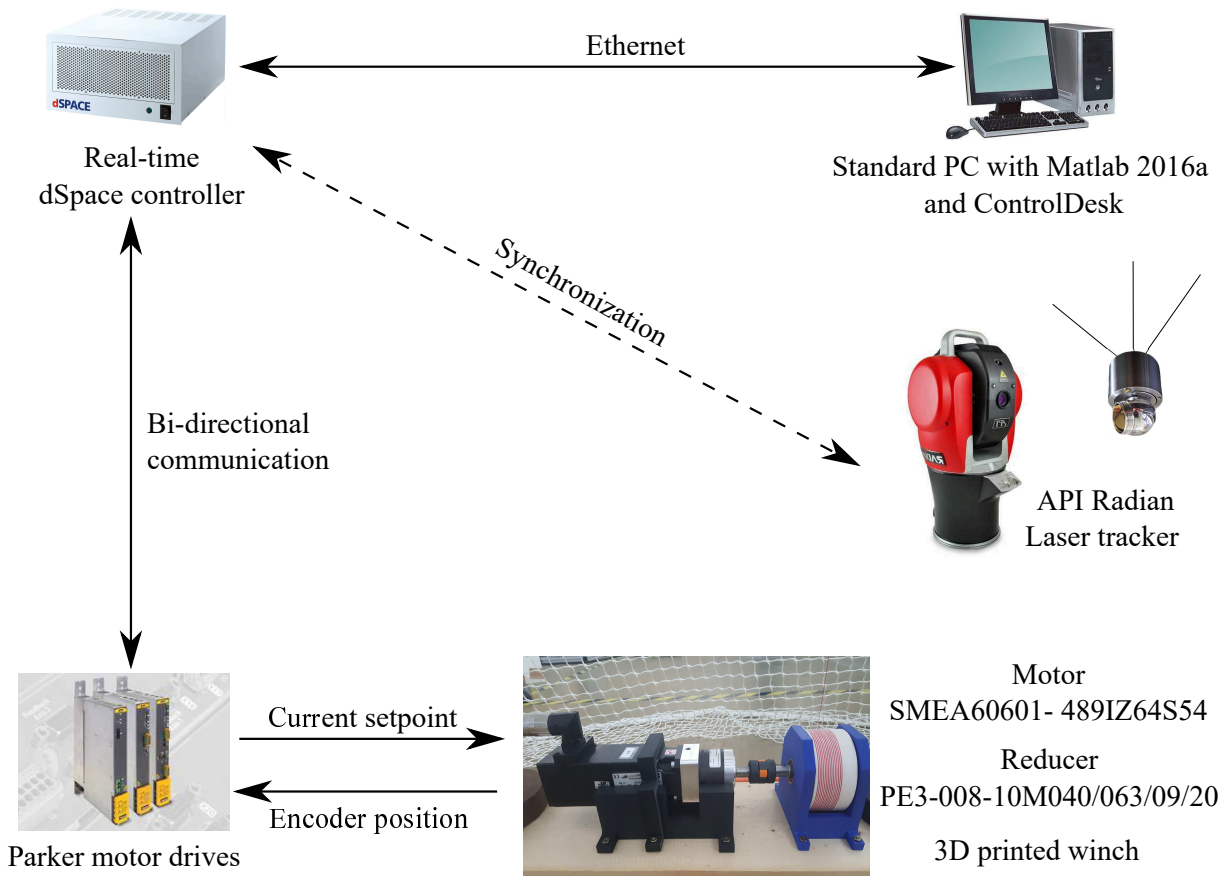


Figure IV.13 – Equivalent architecture of the CREATOR prototype

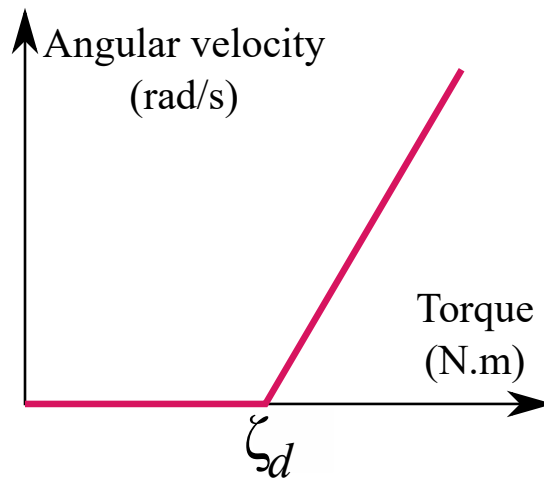


Figure IV.14 – Determination of the static friction

Grease is added inside the pulley to reduce friction between the cable and the pulley.

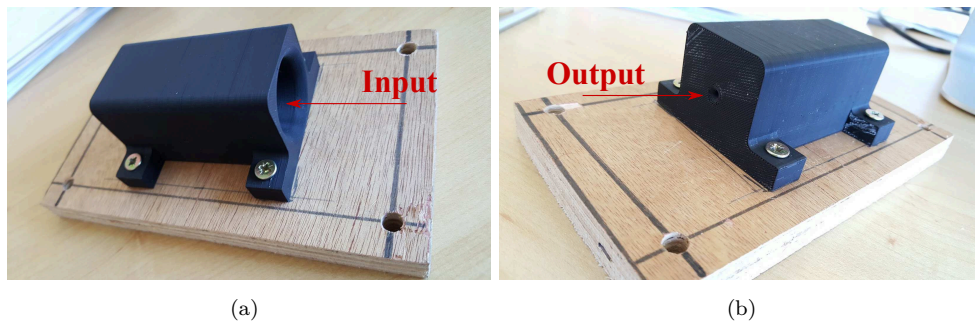


Figure IV.15 – 3D-printed pulleys used for the CREATOR prototype

- As the sensitivity analysis in Chapter III highlighted the high effect of the cables elasticity onto the dynamic and oscillatory motions of the moving-platform, the CREATOR cables were experimentally upstream identified (See Appendix A.2). These cables are made up of eight threads of polyethylene fiber with a diameter of 0.5 mm.

The following trajectory tracking experiments will confirm a good identification of the modulus of elasticity. This is shown through the measurement of a natural frequency  $\approx 3.5$  Hz, which corresponds to the calculated natural frequency (3.67 Hz) while using the identified modulus of elasticity. As mentioned in [BCCD17], the absolute uncertainties in the applied force and resulting elongation measurements from the test bench outputs are estimated to be  $\pm 1$  N and  $\pm 0.03$  mm, respectively. The resulting modulus of elasticity of the cable is equal to  $70 \pm 1.51$  GPa.

- The end-effector was designed such that it is close to a point-mass. It is a steel machined cylinder with a hole that crosses vertically and a conical hole on its top surface (Fig. IV.17). This makes the cables to intersect at the same point. The magnetic support of the laser tracker target is connected to end-effector at its bottom part. The laser tracker target is then connected to this magnetic support, Fig. IV.16. The acquired information from the laser tracker is obtained with respect to the target center. An offset with respect to the end-effector gravity center is considered to get the appropriate trajectory tracking measurements.

The total mass of the end-effector used for the control gathers its own mass

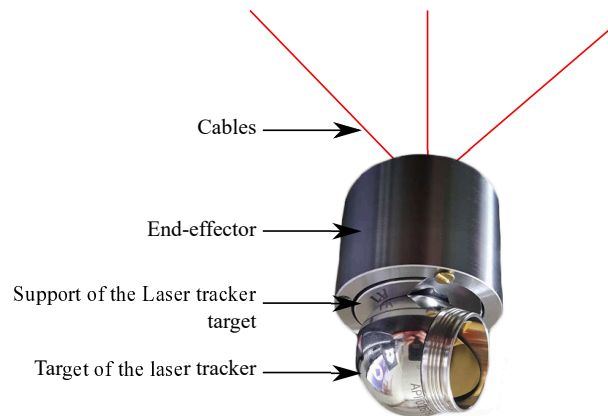


Figure IV.16 – End-effector and laser tracker target

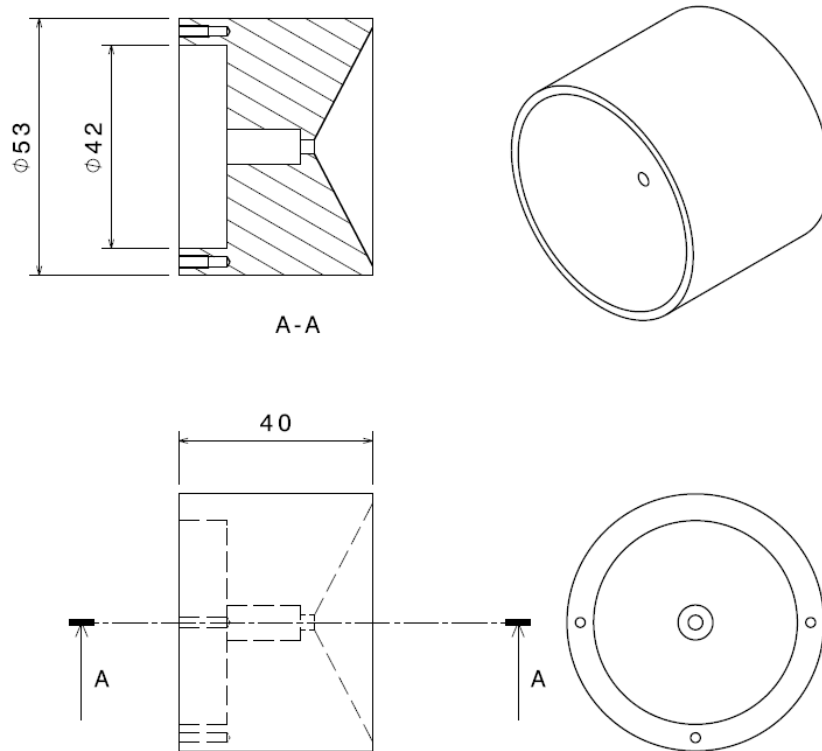


Figure IV.17 – CAD modeling and manufacturing drawings of the end-effector

plus the mass of the laser tracker target and its magnetic support. The total mass of the end-effector is equal to 0.780 kg.

— The command of the CREATOR prototype is implemented in a host PC

through a software interface generated by ControlDesk<sup>®</sup> 5. This latter enables the real-time simulation of the control schemes, created with Matlab-Simulink<sup>®</sup>, in the dSpace<sup>™</sup> control unit. The control sampling times  $\Delta t_a$  and  $\Delta t_b$  are considered equal :  $\Delta t_a = \Delta t_b = 1$  ms.

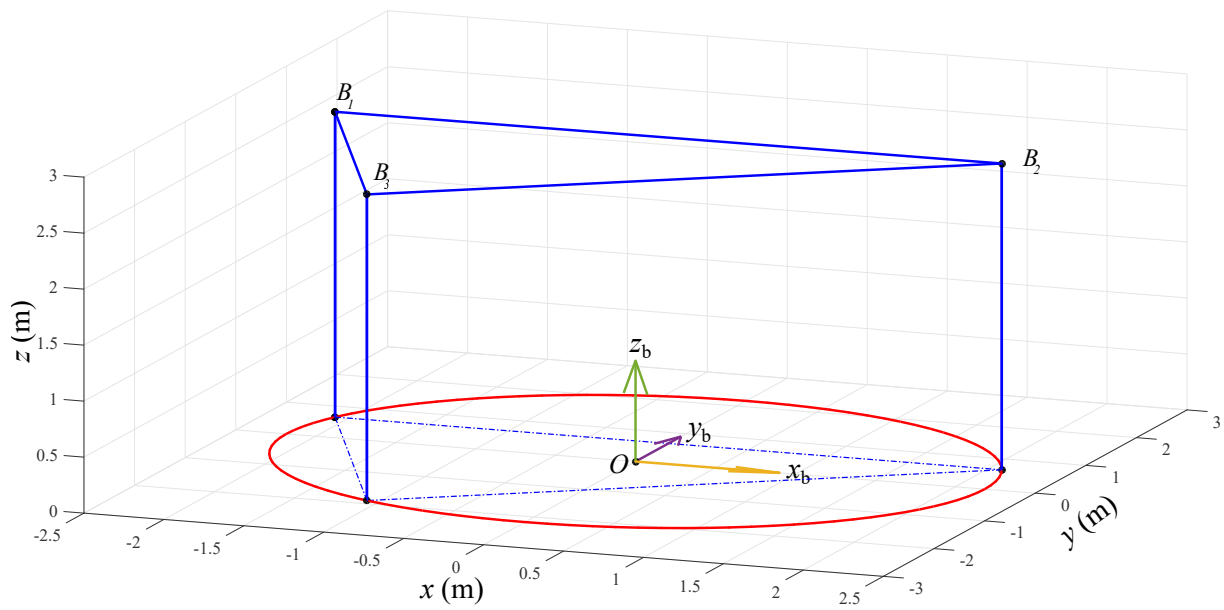


Figure IV.18 – Base frame  $\mathcal{F}_b$  of the CREATOR prototype

- An API Radian laser tracker is used to define the base frame  $\mathcal{F}_b = \{O, x_b, y_b, z_b\}$ . A circle plane passing through points  $B_1$ ,  $B_2$  and  $B_3$  is created and is projected on the floor to create the base frame, whose origin is the circle center as shown in Fig. IV.18. All the measurements are expressed in that frame.

Moreover, the laser tracker is used to measure the pose of the end-effector along the tracked trajectory in the global base frame  $\mathcal{F}_b$ . The static measurement accuracy of the used laser tracker is  $\pm 10 \mu\text{m}$ . The measurement start signal is synchronized with the control signal through the dSpace controller.

5. ControlDesk is the dSPACE experiment software for seamless electronic control unit development. It performs all the necessary tasks and gives a single working environment, from the start of experimentation right to the end.

### IV.2.5.2 Experimental setup

The experimental setup of the trajectory tracking of the CREATOR prototype is shown in Sec. IV.2.5.1. Experimental procedure, made for the verification of numerical results, is as following :

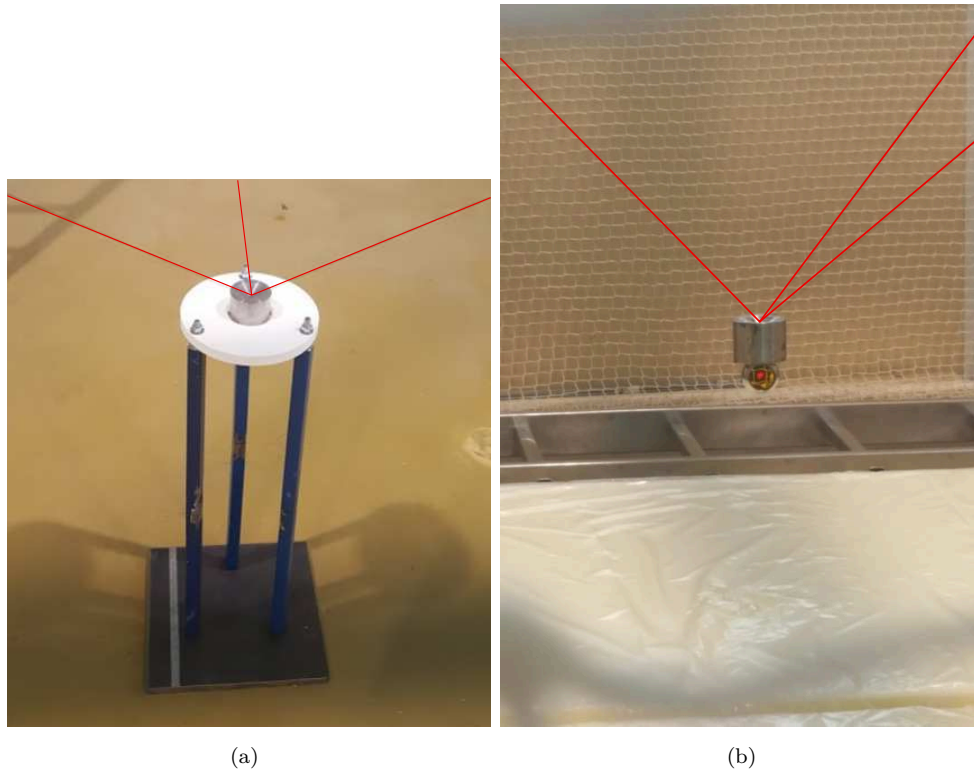


**Figure IV.19** – Experimental setup : (a) Non-suspended, (b) Suspended initial pose of the end-effector

- A support for the end-effector, shown in Fig. IV.19(a), is placed on its desired initial position. The base plate of this support is 3D printed and is connected to a steel block through steel square tubes. This base is a negative form of the end-effector. The support is useful to define the relationship between actuated angles and the corresponding unstrained cable lengths. Besides, it provides the same initial pose for the end-effector for the different experiments.

As shown in Fig. IV.19(a), the end-effector is first located on the support. In this way, it is in the non-suspended initial pose and it undergoes neither the external effects nor its stiffness. The non-suspended absolute position of the end-effector is measured.

- Modify cable lengths to get a minimize cables tension the maximum possible while keeping cables without sag. Then, lock the motors.
- The support is removed and the end-effector becomes suspended under the effect of its own weight subjected to cable elasticity (Fig. IV.19(b)). Then, the suspended position of the end-effector is measured.
- A command is generated through ControlDesk® in combination with Matlab-Simulink®. It makes the end-effector move along a straight line, the same trajectory as the numerical example described in Sec. IV.2.4.1.
- When the elasto-static or elasto-dynamic models are used as references for the control, a compensation of the static deflection is performed before starting the trajectory. This is done through smooth angular displacements of joints corresponding to the correction of the static deflection.

### IV.2.5.3 Static analysis

The ideal initial position of the end-effector corresponds to the initial rigid position  $\mathbf{p}_{rg}(t = 0^- s)$ . This latter is measured when the end-effector is located on the support in the absence of the stiffness effect ;

$$\mathbf{p}_{rg}(t = 0^- s) = [0.299, -0.047, 0.623] \text{ m.}$$

Three tests are performed to check the positioning repeatability. This is done by suspending the end-effector and measuring its elasto-static position and the corresponding static deflection. The suspended position  $\mathbf{p}_{es}(t = 0^- s)$  of the end-effector is measured when the support is removed and the end-effector is suspended under the effect of its own weight. Table IV.3 displays the static deflection  $\|\mathbf{dp}\|$  with respect to the same non-suspended rigid position  $\mathbf{p}_{rg}(t = 0^- s)$  for different tests.

The end-effector presents a different static deflection for each test. This depends on the initial tensions on the cables when the end-effector is in its ideal initial position. The absence of tension sensors make it hard to start the experiments with

**Table IV.3** – Experimental data : Static deflection of the end-effector before compensation

Experience	Static deflection $\ \mathbf{d}\mathbf{p}\ $ (mm)
Test 1	9.00
Test 2	6.32
Test 3	8.30

zero cable tensions without sag, leading to different static deflections.

The position repeatability is not good enough that for each test we obtain a different position for the end-effector. Indeed, the trajectory does not start with the same position for the different tests. Comparing the control laws by comparing the absolute trajectory errors will not project the true improvement of the accuracy as the different trajectories do not start with the same static error.

For this fact, we propose to define a new reference  $\mathbf{p}^*$  to be used for the determination of the trajectory error.  $\mathbf{p}^*$  is defined as described in Sec. IV.2.4.1 starting from the compensated position, where  $\mathbf{p}^*(t = 0\text{ s}) = \mathbf{p}_{es}(t = 0^+\text{ s})$ . This allows to compensate the static error for the different tests at the start time of the trajectory. This static error should be seen at the end of the trajectory.

#### IV.2.5.4 Trajectory tracking

The trajectory error  $\delta\mathbf{p}$  is defined as the difference between the measured trajectory  $\mathbf{p}$  and the reference one  $\mathbf{p}^*$  :  $\delta\mathbf{p}(t) = \mathbf{p}(t) - \mathbf{p}^*(t)$ . Figure IV.21(b) shows the norm of the end-effector trajectory tracking error  $\|\delta\mathbf{p}\|$  when the proposed feed-forward control law is applied while using successively the three CDPR models to generate the reference signal. Figure IV.21(a) illustrates the end-effector trajectory tracking error along the  $z$ -axis  $\delta z$ , which is the main one as the CDPR under study is assembled in a suspended configuration and the trajectory is vertical. The red (gree, blue, resp.) curve depicts the end-effector trajectory tracking error when the elasto-dynamic (elasto-static, rigid, resp.) model is used as a reference.

Figure IV.20 shows the set-point of current  $\mathbf{i}_m = [i_m^1, i_m^2, i_m^3]^T$  sent to the actuators, which is an image of torque set-point  $\zeta_m$ . It is noteworthy that the elasto-dynamic current set-point takes into account the oscillatory behavior on the contrary to classical feed-forwards.

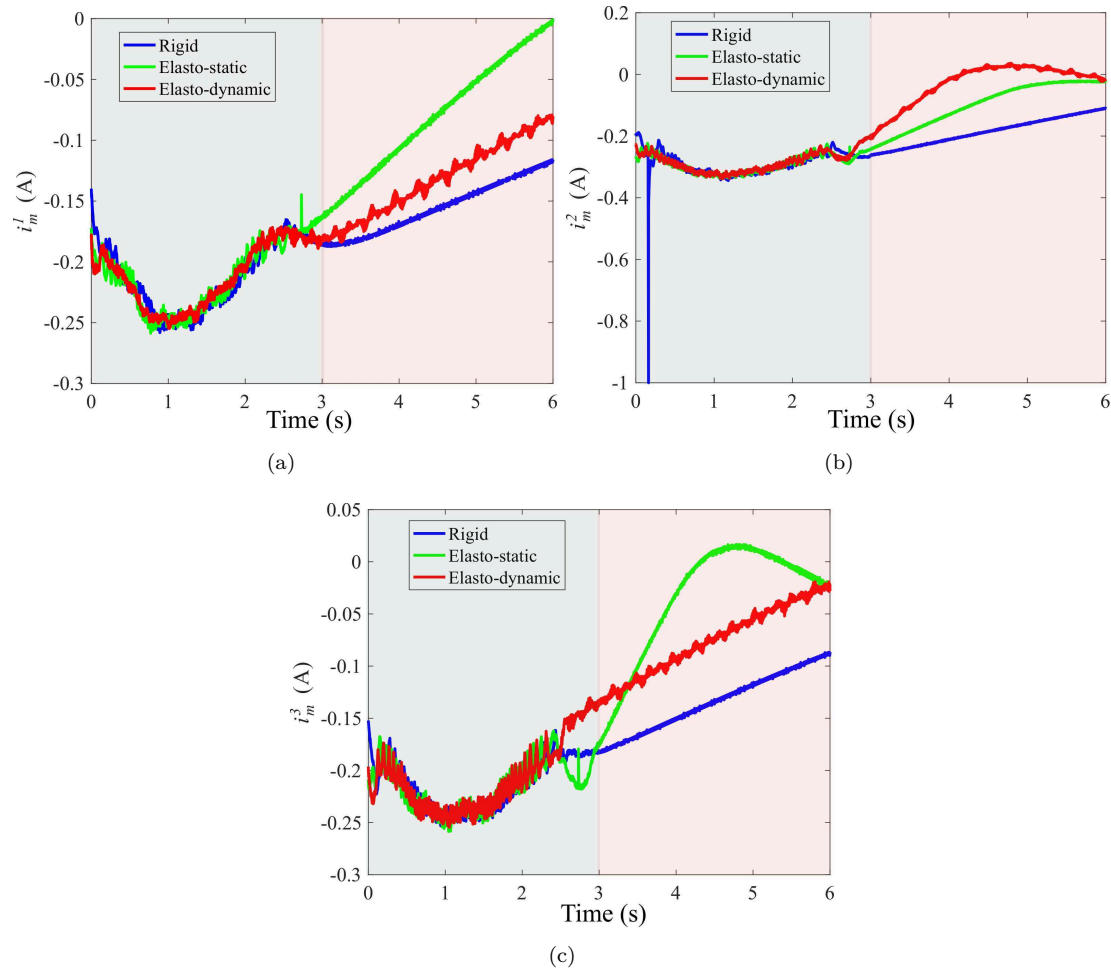


Figure IV.20 – Experimental results : Current set-points (a)  $i_m^1$ , (b)  $i_m^2$  and (c)  $i_m^3$

As one can see, the set-point of current is not constant during the steady-state phase. This reflects the integrator effect of the PID controller as its input is never zero. In addition, the torques  $\zeta_{rg}$  and  $\zeta_f$  do not compensate totally the gravity and friction effects as they are obtained by identification, which is influenced by uncertainties.

While applying  $\mathbf{i}_m$ , the resulting trajectory error of the end-effector is plotted in Fig. IV.21. The first thing worth noting in these plots is that the end-effector oscillations are of a frequency of 3.5 Hz, which is close to the calculated first natural frequency  $f_1 = 3.67$  Hz. A good identification of the modulus of elasticity, respecting the uncertainty analysis conclusions, is confirmed.

From Figs. IV.20 and IV.21, the delay  $j_\beta$  can be determined. When the rigid model of the CDPR is used, a current discontinuity at time 2.53 s is depicted. This leads to a discontinuity in  $\|\delta\mathbf{p}\|$  at time 2.68 s, which corresponds to  $j_\beta^{rg} = 0.15$  s. When the elasto-static model of the CDPR is used, a current discontinuity at time 2.73 s is depicted. This leads to a discontinuity in  $\|\delta\mathbf{p}\|$  at time 2.87 s, which corresponds to  $j_\beta^{es} = 0.14$  s. When the elasto-dynamic model of the CDPR is used, a current discontinuity at time 2.57 s is depicted. This leads to a discontinuity in  $\|\delta\mathbf{p}\|$  at time 2.70 s, which corresponds to  $j_\beta^{ed} = 0.13$  s.

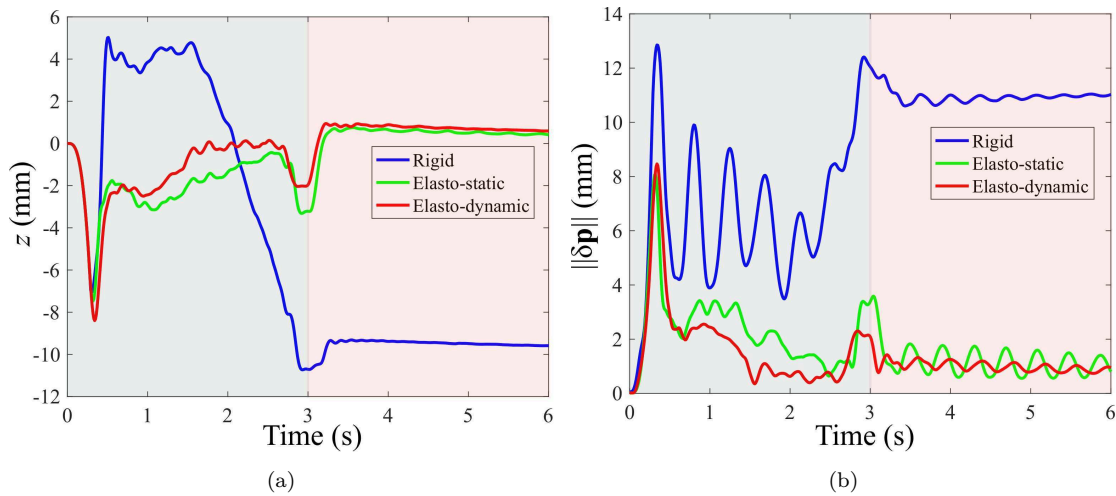


Figure IV.21 – Experimental results : (a) Position error along z-axis of the end-effector (b) Position error norm

#### IV.2.5.4.1 Transitional phase

At time  $t = 0$  s, the trajectory error is set to be zero. In fact, the static error is reported artificially to the end of the trajectory as the real trajectory of the end-effector is compared to the modified rigid one  $\mathbf{p}^*$ .

As shown in Fig. IV.22, the trajectory tracking error norm  $\|\delta\mathbf{p}\|$  while using the rigid model as a reference for the feed-forward at time  $t = 3$  s is equal to 12.05 mm. This value is equal to 3.45 mm when the elasto-static model is used as a reference for the feed-forward, which represents a relative difference of 71 % with respect to the rigid control. The position error norm  $\|\delta\mathbf{p}\|$  while using the elasto-dynamic model as a reference for the feed-forward at time  $t = 3$  s is equal to 2.01 mm, which represents a relative improvement of 83 % with respect to the rigid control.

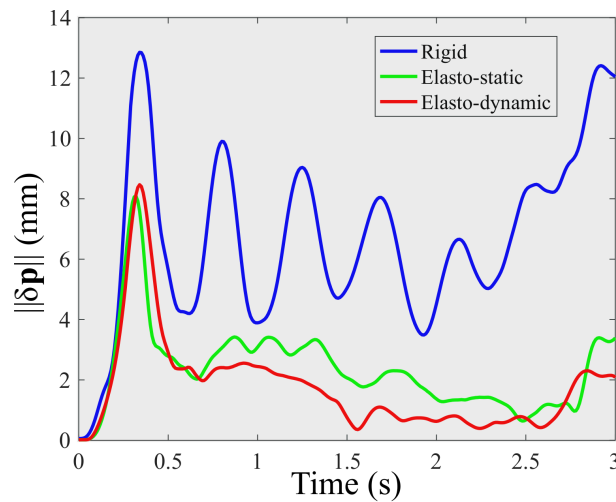


Figure IV.22 – Experimental results : Trajectory tracking error norm during the transitional phase

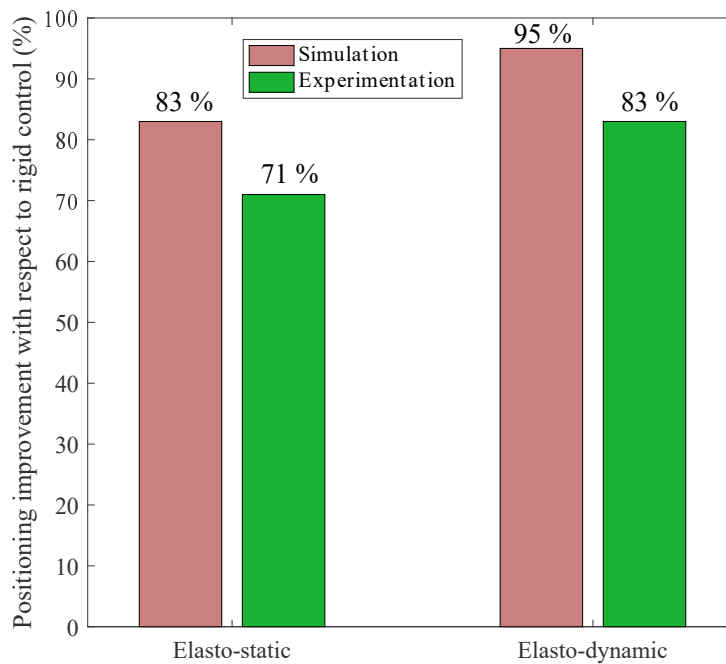


Figure IV.23 – Experimental results : Positioning improvement with respect to rigid control at time  $t = 3$  s.

Fig. IV.23 shows that experimental results present the same tendency as simulations. This confirms a better improvement of the moving-platform positioning errors through the elasto-dynamic compensation comparing to classical feed-forwards. This is due to the correction of static errors through the compensation of cable elongations and the compensation of the oscillatory effects of the moving-platform.

#### IV.2.5.4.2 Steady-state phase

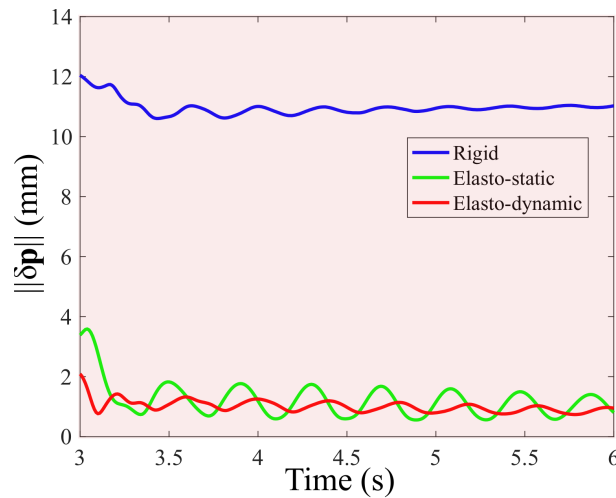


Figure IV.24 – Experimental results : Position error norm during the steady-state phase

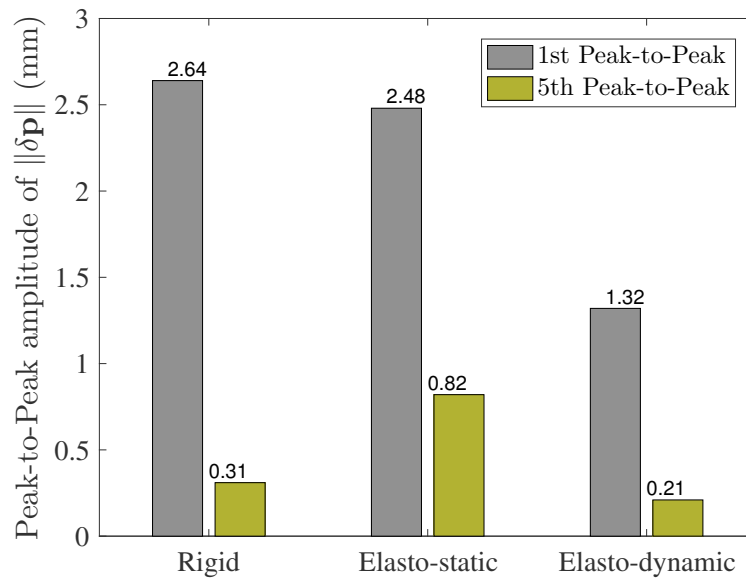


Figure IV.25 – Experimental results : Histogram of the first and fifth Peak-to-Peak amplitudes of  $\|\delta\mathbf{p}\|$  during the steady-state phase

As shown in Fig. IV.24, at time  $t = 3$  s, the end-effector achieves its final position and then oscillates. Fig. IV.25 depicts that when the rigid control is used, the first Peak-to-Peak amplitude of residual vibrations is equal to 2.64 mm. This value is equal to 2.48 mm when the elasto-static model is used as a reference for the

feed-forward, which represents a relative difference of 6 % with respect to the rigid control. When the elasto-dynamic model is used as a reference for the feed-forward, the first Peak-to-Peak amplitude of residual vibrations is equal to 1.32 mm, which represents a relative improvement of 50 % with respect to the rigid control.

The fifth Peak-to-Peak amplitude of residual vibrations is equal to 0.31 mm when the rigid model is used as a reference for the feed-forward. This value is equal to 0.82 mm when the elasto-static model is used as a reference for the feed-forward. The fifth Peak-to-Peak amplitude of residual vibrations is equal to 0.21 mm when the elasto-dynamic control is used, which represents a relative improvement of 32 % with respect to the rigid control.

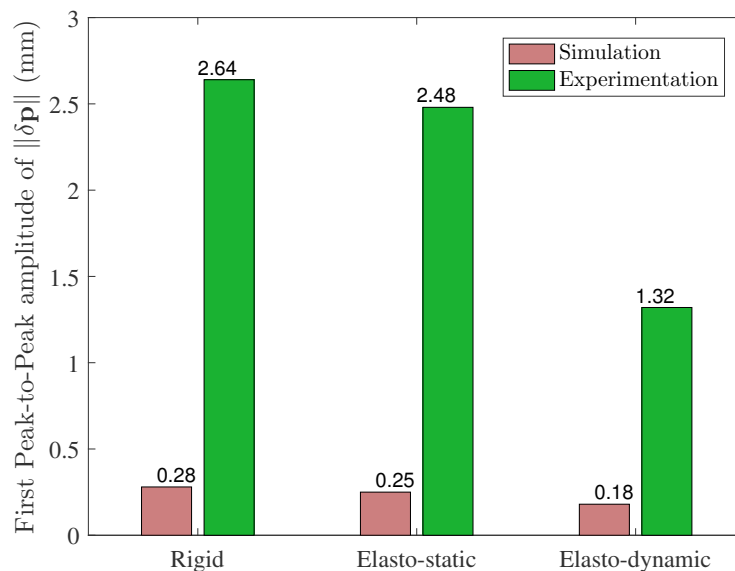


Figure IV.26 – First Peak-to-Peak amplitudes of  $\|\delta\mathbf{p}\|$  : Comparison of numerical and experimental results

Note that the experimental first Peak-to-Peak amplitude of residual vibrations is  $\approx 10$  times higher than the numerical one as shown in Fig. IV.26. This is due to the oscillatory behavior of the end-effector, which is a non-perfect point-mass that may swing out along the trajectory.

Figure IV.27 shows the decrement of the Peak-to-Peak amplitudes of  $\|\delta\mathbf{p}\|$  during the steady-state phase. This decrement is equal to 6.28 (2.94, 8.51, resp.) when

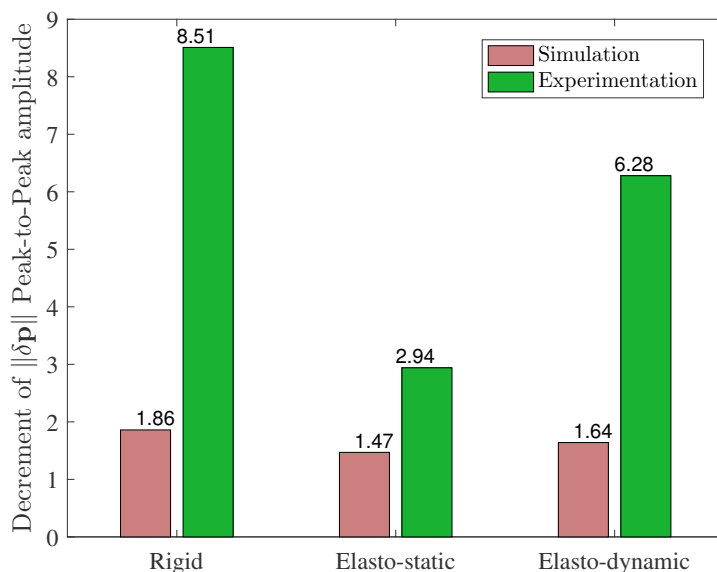


Figure IV.27 – Experimental results : Decrement of the Peak-to-Peak amplitudes of  $\|\delta\mathbf{p}\|$  during the steady-state phase

the elasto-dynamic (elasto-static, rigid, resp.) model is used as a reference for the feed-forward. The decrement of the Peak-to-Peak amplitudes of  $\|\delta\mathbf{p}\|$  obtained through experiments presents the same tendency than the numerical one. However, this experimental decrement is lower than the simulated ones. This means that some damping effects were not taken into consideration in simulations. A part of the damping may occur in the pulley system as the different control laws take into account neither the pulley friction nor the cable sliding into the pulley grooves. Furthermore, the winch friction torques are not well identified as the drums are 3D printed, leading to uncertainties. However, there is a clear improvement of trajectory tracking and vibration attenuation.

The different experimental results confirm the numerical ones stating that the elasto-dynamic control leads to better attenuation of residual vibrations of the moving-platform than the conventional elasto-static and rigid controls. Numerical results mention that elasto-dynamic control leads to an improvement of 35 % for the first Peak-to-Peak amplitude and an improvement of 26 % for the fifth one with respect to the rigid control. Accordingly, experimentations confirm this improvement as shown in Fig. IV.28. In fact, elasto-dynamic control leads to an

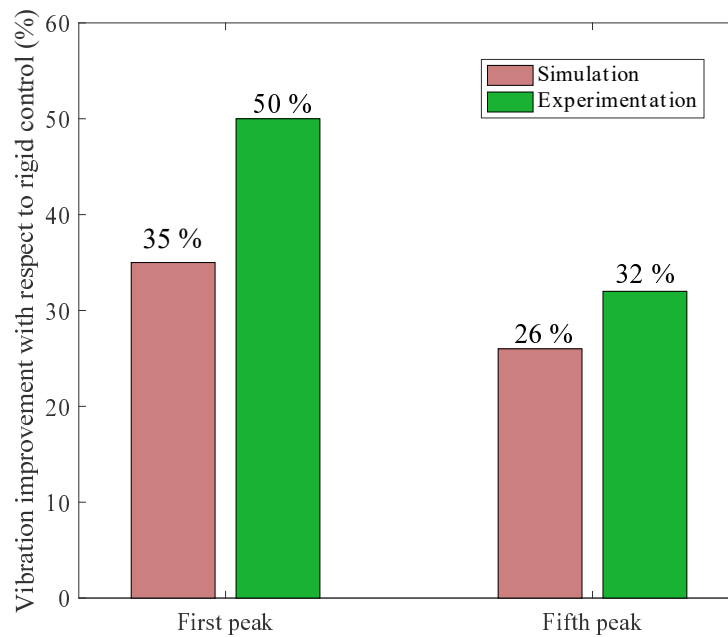


Figure IV.28 – Vibration improvement of the elasto-dynamic control with respect to rigid control during the steady-state phase

improvement of 50 % for the first Peak-to-Peak amplitude and an improvement of 32 % for the fifth one with respect to the rigid control. This confirms a good ability of residual vibrations attenuation through the elasto-dynamic control.

Next section presents a frequency dependent control strategy, which deals with the input-shaping for the feed-forward control. The following section aims to verify if it is worth to establishing an elasto-dynamic model for feed-forward model-based control or it is worth to use a the simple integration of input-shaping filters to redesign the original control signals for better positioning accuracy and disturbance rejection.

### IV.3 Input-shaping for feed-forward control

When the input of the controlled robot is an impulse, it leads to vibrations. When a second impulse is applied, the vibrations induced by the first impulse can be canceled if the relative phase is well chosen. Input-shaping control is based on this logic. Input shaping is a technique used to eliminate inertia excited vibrations in dynamic systems. It attenuates the residual vibrations by creating a modified control signal, which is self-canceling. The convolution of the original in-

put signal and a sequence of impulses forms the shaped input signal, which permits to suppress unwanted vibrations [SS02]. In addition to the process of convolution, input-shaping can be completed by time-delay blocks, depending on the natural frequency of the robot.

Here, the original input signal is the desired motion (pose  $\mathbf{x}_{rg}$ , velocity  $\dot{\mathbf{x}}_{rg}$ , acceleration  $\ddot{\mathbf{x}}_{rg}$ ) of the moving-platform. Based on the natural frequencies of the system, the sequence of impulses, or mathematically the time-domain impulse response of the input-shaping filter, to be convolved with the original input signal are generated to create a modified input motion (pose  $\mathbf{x}_{rg}^{sh}$ , velocity  $\dot{\mathbf{x}}_{rg}^{sh}$ , acceleration  $\ddot{\mathbf{x}}_{rg}^{sh}$ ) of the moving-platform.

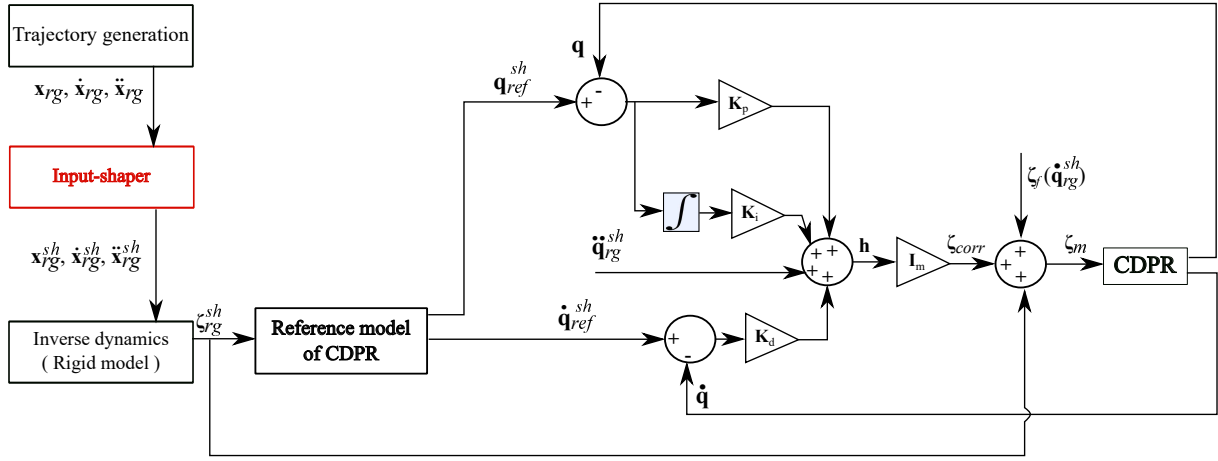


Figure IV.29 – Block diagram for closed-loop input-shaping control scheme

Figure IV.29 presents the main idea of the proposed closed-loop input-shaping control for CDPRs. The input-shaping filter convolves the reference input with a sequence of impulses having appropriate magnitudes  $D_i$ , and time location  $t_i$ ,  $i = [1..k]$ ,  $k$  being the number of impulses. Let's note that :

$$\mathbf{q}_{ref}^{sh} = \mathbf{q}_{ref}(\mathbf{x}_{rg}^{sh}), \quad (IV.17a)$$

$$\dot{\mathbf{q}}_{ref}^{sh} = \mathbf{q}_{ref}(\mathbf{x}_{rg}^{sh}, \dot{\mathbf{x}}_{rg}^{sh}), \quad (IV.17b)$$

$$\zeta_{rg}^{sh} = \zeta_{rg}(\mathbf{x}_{rg}^{sh}, \dot{\mathbf{x}}_{rg}^{sh}, \ddot{\mathbf{x}}_{rg}^{sh}). \quad (IV.17c)$$

The shaped vector of the actuator displacement  $\mathbf{q}_{ref}^{sh}$  and the shaped vector of the actuator angular velocity  $\dot{\mathbf{q}}_{ref}^{sh}$  become the reference of the feedback controller,

which generates a correction torque  $\zeta_{corr}$ . The applied closed-loop command for motors is expressed as follows :

$$\zeta_m = \mathbf{I}_m \mathbf{h}(t) + \zeta_f(\dot{\mathbf{q}}_{rg}^{sh}) + \zeta_{rg}^{sh}, \quad (\text{IV.18})$$

where  $\zeta_m$  corresponds to the torque command applied to the motor,  $\zeta_{corr} = \mathbf{I}_m \mathbf{h}$  corresponds to the torque of correction and  $\mathbf{h}(t)$  is defined by :

$$\mathbf{h}(t) = \ddot{\mathbf{q}}_{rg}^{sh} + \mathbf{K}_p (\mathbf{q}_{ref}^{sh} - \mathbf{q}) + \mathbf{K}_d (\dot{\mathbf{q}}_{ref}^{sh} - \dot{\mathbf{q}}) + \mathbf{K}_i \int_{t_i}^{t_i^+} (\mathbf{q}_{ref}^{sh} - \mathbf{q}) dt, \quad (\text{IV.19})$$

where  $\ddot{\mathbf{q}}_{rg}^{sh}$ ,  $\dot{\mathbf{q}}_{ref}^{sh}$ ,  $\mathbf{q}_{ref}^{sh}$  represent the desired angular acceleration coming from the rigid model, the desired angular velocity and the desired angular displacement of the motors generated by the shaped input signal, respectively.  $\dot{\mathbf{q}}$  and  $\mathbf{q}$  represent the measured angular velocity and the measured angular displacement of motors, respectively.

The closed-loop command corresponds to the following tracking error equation :

$$\ddot{\mathbf{e}} + \mathbf{K}_p \mathbf{e} + \mathbf{K}_d \dot{\mathbf{e}} + \mathbf{K}_i \int_{t_i}^{t_i^+} \mathbf{e} dt = 0. \quad (\text{IV.20})$$

$\mathbf{e}$  being the tracking error, which is the difference between  $\mathbf{q}_{ref}^{sh}$  and  $\mathbf{q}$ .

The time-domain sequence of impulses of the input-shaping filter is generally expressed as :

$$s(t) = \sum_1^k D_i \delta(t - t_i), \quad (\text{IV.21})$$

where  $k$  is the number of impulses,  $D_i$  and  $t_i$  are the magnitude and the time location of the  $i$ th impulse, respectively.

The unwanted residual vibrations resulting from a sequence of impulses can be expressed as a function of the estimated natural frequency  $\Omega$  and the damping ratio  $\Gamma$ , as follows :

$$V(\Omega, \Gamma) = e^{\Gamma \Omega t_k} \sqrt{C(\Omega, \Gamma)^2 + S(\Omega, \Gamma)^2}, \quad (\text{IV.22})$$

where

$$C(\Omega, \Gamma) = \sum_{i=1}^k D_i e^{\Gamma \Omega t_i} \cos(\Omega_d t_i) \quad (\text{IV.23a})$$

$$S(\Omega, \Gamma) = \sum_{i=1}^k D_i e^{\Gamma \Omega t_i} \sin(\Omega_d t_i) \quad (\text{IV.23b})$$

The damped frequency is expressed as following :

$$\Omega_d = \Omega\sqrt{1 - \Gamma^2}. \quad (\text{IV.24})$$

Eq. (IV.22) gives tips on the vibrations generated by a sequence of impulses. When this equation is null, the impulse amplitudes  $D_i$  and their time locations  $t_i$ ,  $i = [1..k]$ , inducing zero residual vibration can be calculated. As Eq. (IV.23a) and Eq. (IV.23b) are squared in Eq. (IV.22), this latter is equal to zero when both Eq. (IV.23a) and Eq. (IV.23b) are null independently.

Some constraints should be taken into account for the time-delay impulses to avoid having zero or an infinity of solutions. The first restriction permits avoiding all zero-valued impulses. Therefore, it makes the shaped command results in the same final set point as the original command. This restriction manifests in the fact that the sum of the impulse amplitudes has to be equal to one :

$$\sum_{i=1}^k D_i = 1. \quad (\text{IV.25})$$

Satisfying only Eq. (IV.25) may lead to very large positive values of impulses and some negative ones. However, a bounded solution is required. This can be done by restricting the impulse amplitudes to finite values or to strictly positive values :

$$D_i > 0, \quad i = [1..k] \quad (\text{IV.26})$$

The first impulse of the input-shaping filter must be set at time zero, to reduce the time delay introduced by the input modification process :

$$t_1 = 0. \quad (\text{IV.27})$$

Consequently, the problem to be solved is to find a time-domain sequence of impulses  $s(t)$ , whose first impulse is defined at time  $t = 0$ . This sequence should make Eq. (IV.22) true and satisfy Eq. (IV.25) and Eq. (IV.26).

### IV.3.1 Single mode Input-shaping control

Single mode Input-shaping filters are easy to implement. Numerous single mode input-shaping methods have been proposed in the last decades. The Zero-Vibration (ZV) and the Zero-Vibration-Derivative (ZVD) input-shaping filters are the most common input-shapers in the literature [VYS08].

### IV.3.1.1 Zero-Vibration input-shaper

Zero-Vibration input-shaper manifests in the convolution of the original input signal with a sequence of two impulses. The response to second impulse suppresses the vibrations resulting from the first impulse. This two-impulse sequence is determined while satisfying Eq. (IV.25) and Eq. (IV.26) and vanishing Eq. (IV.22) and Eq. (IV.23). The impulses are separated by the half of the robot's natural period. Hence, the ZV input-shaping filter is expressed by the following matrix form [MNA16] :

$$\mathbf{ZV} = \begin{bmatrix} \mathbf{D}_i \\ \mathbf{t}_i \end{bmatrix} = \begin{bmatrix} \frac{1}{1+K} & \frac{K}{1+K} \\ 0 & \frac{t_d^i}{2} \end{bmatrix}, \quad (\text{IV.28})$$

where  $D_i$  and  $t_i$  are the  $i$ th impulse amplitude and impulse time vectors, respectively.  $t_d^i = \frac{2\pi}{\Omega_d^i}$  is the damped period of the system corresponding to the  $i$ th natural frequency  $\Omega_d^i$ . The constant  $K$  is expressed as following :

$$K = e^{\frac{-\Gamma\pi}{\sqrt{1-\Gamma^2}}}. \quad (\text{IV.29})$$

### IV.3.1.2 Zero-Vibration-Derivative input-shaper

In addition to the satisfaction of ZV-shaper conditions, a ZVD-shaper should satisfy a zero derivative of Eq. (IV.22). The ZVD input-shaping filter consists in the convolution of the original input signal with a sequence of three impulses separated by half the period of the robot's vibration [SS90]. It is expressed in a matrix form as follows :

$$\mathbf{ZVD} = \begin{bmatrix} \mathbf{D}_i \\ \mathbf{t}_i \end{bmatrix} = \begin{bmatrix} \frac{1}{1+2K+K^2} & \frac{2K}{1+2K+K^2} & \frac{K^2}{1+2K+K^2} \\ 0 & \frac{t_d^i}{2} & t_d^i \end{bmatrix}, \quad (\text{IV.30})$$

where  $K$  is expressed by Eq. (IV.29).

### IV.3.1.3 Robustness to modeling errors

The difference between  $\Omega$  (a variable), which is the actual value of the undamped natural frequency of the system, and  $\Omega_m$  (a constant), which is the "mode-

led" value of the undamped natural frequency  $\Omega$ , was pointed in [Kan11]. The latter proves that vibration approaches zero when  $\Omega$  tends to  $\Omega_m$ . This research work shows that for a vibratory system, a modeling frequency is chosen such that  $\frac{d C(\Omega, \Gamma)}{d \Omega} = \frac{d S(\Omega, \Gamma)}{d \Omega} = 0$  at the modeling frequency  $\Omega = \Omega_m$ .

Figure IV.30 displays the sensitivity curves for ZV and ZVD shapers. It shows the amplitude of residual vibrations as a function of the normalized frequency  $\Omega/\Omega_m$ . This allows us to compare the performance of the robust and non-robust approaches. Here, the modeling frequency  $\Omega_m$  is set to  $2\pi$  rad/s and the damping ratio  $\Gamma$  to zero. The percentage vibration is the ratio between the amplitude of vibrations when using input shaping and the amplitude of residual vibrations when shaping is not used.

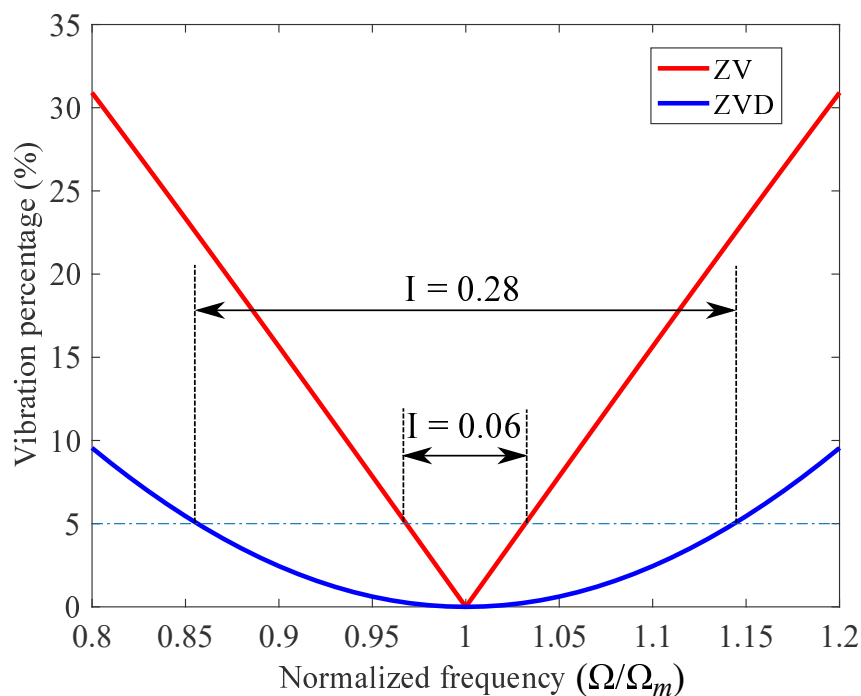


Figure IV.30 – Sensitivity curves of ZV and ZVD input-shapers

The sensitivity curve of the ZV-shaper shows that the higher the modeling errors, the faster the residual vibration increase when using a ZV-shaper. Besides, the vibrations generated when using a ZVD shaper remain at a lower level. The robustness can be measured quantitatively by measuring the width of the curve at some

low level of vibrations. This non-dimensional robustness measurement is called the shaper insensitivity  $I$ . The 5 % insensitivity has been labeled in Fig. IV.30.

For the ZV shaper, the 5 % insensitivity  $I$  is equal to 0.06 before the residual exceeds 5 % of the unshaped vibration. The ZVD shaper presents an insensitivity  $I = 0.28$ . By comparing the 5 % insensitivities shown in Fig. IV.30, it can be concluded that the ZVD shaper is significantly more robust to modeling errors than the ZV shaper.

### IV.3.2 Multi-mode input-shaping control

For CDPRs, there are two or more natural modes to be addressed by the input-shaping process. A simple way to obtain a two-mode shaper is to convolve two single-mode shapers together [SCS97]. When describing a two-mode shaper, the constraints used to eliminate each mode will be stated explicitly. For example, if ZV constraints are used for the first mode and ZVD is used for the second mode, then the result will be a ZV-ZVD shaper. In real systems, the residual vibrations can never be null because of the modeling errors and disturbances. The integration of the input-shaping filter leads to oscillation attenuation, but not to cancellation even if a multi-mode shaper is used.

### IV.3.3 Experimental results

Experimentations are addressed here to check the effect of the integration of input-shaping filters into the closed-loop control scheme. In this section, the rigid model of simulation is used to establish the reference signal. The suspended configuration of the CREATOR prototype described in App. B.3 is studied. The gains  $K_p$ ,  $K_d$  and  $K_i$  of the PID controller are given in Tab. IV.2.

#### IV.3.3.1 Trajectory generation

A non-smooth velocity trajectory is chosen to stimulate the natural modes of the CDPR. The motion is uniformly accelerated until the end-effector achieves a desired position along  $x$ -axis,  $y$ -axis and  $z$ -axis. The accelerations of the end-effector along  $x$ -axis,  $y$ -axis and  $z$ -axis are defined by a bang-bang profile (Fig. IV.31(c)). The nominal trajectory of the moving-platform is a vertical straight line from point  $P_1$  of Cartesian coordinate vector  $\mathbf{p}_1$  to point  $P_2$  of Cartesian coordinate vector  $\mathbf{p}_2$  during

$t_f = 3$  s. Therefore, the trajectory followed by the end-effector is parametrized as follows :

$$\mathbf{p}(t) = \beta_1 t^2 + \beta_2 t + \beta_3, \quad t \in [0, \frac{t_f}{2}], \quad (\text{IV.31a})$$

$$\mathbf{p}(t) = \beta_4 (t - t_f)^2 + \beta_5 (t - t_f) + \beta_6, \quad t \in [\frac{t_f}{2}, t_f], \quad (\text{IV.31b})$$

$$\mathbf{p}(t) = \mathbf{p}_2, \quad t > t_f, \quad (\text{IV.31c})$$

where

$$\beta_1 = \beta_4 = \frac{2(\mathbf{p}_1 - \mathbf{p}_2)}{t_f^2}, \quad (\text{IV.32a})$$

$$\beta_3 = \mathbf{p}_1, \quad (\text{IV.32b})$$

$$\beta_6 = \mathbf{p}_2, \quad (\text{IV.32c})$$

$$\beta_2 = \beta_5 = \mathbf{0}, \quad (\text{IV.32d})$$

The manipulator tracks a straight line (Fig IV.31(a)) from point  $P_1$  of Cartesian coordinate vector  $\mathbf{p}_1 = [0.29, -0.047, 0.62]^T$  m to point  $P_2$  of Cartesian coordinate vector  $\mathbf{p}_2 = [0.29, -0.047, 1.62]^T$  m. The nominal velocity (Fig. IV.31(b)) and acceleration (Fig. IV.31(c)) profiles of the moving-platform are the time derivatives of the nominal trajectory.

### IV.3.3.2 Input-shaping

Figure IV.32 shows the determinant of the global stiffness matrix of the CREATOR prototype along the trajectory represented in Fig. IV.31(a). This index is used to evaluate the CDPR natural modes because it contains all the dynamic information of the robot. It is clear that the stiffness of the robot varies a little bit around the initial value defined at the start point. Here, the assumption of low variations in CDPR natural frequencies is valid. Those natural frequencies are calculated around the initial pose of the end-effector. It was verified in Section IV.2.5.4 that the identified natural frequencies correspond to those determined by solving

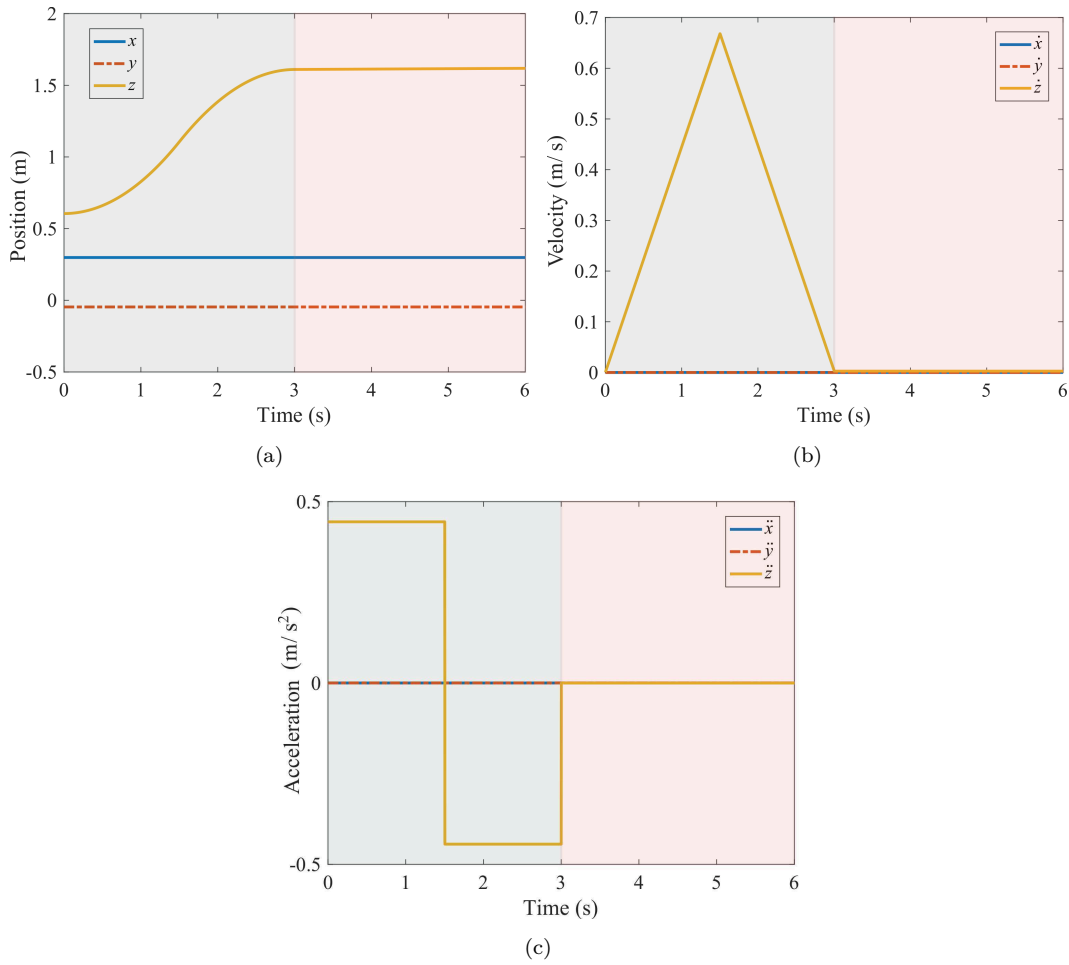


Figure IV.31 – Nominal (a) position (b) velocity (c) acceleration profiles of the moving-platform

the generalized eigenvalue problem associated with the apparent stiffness of the CDPR [DM09].

The first two modes correspond to the natural frequencies  $f_1 = 3.67$  Hz and  $f_2 = 6.34$  Hz, which correspond to impulse times 0.27 s and 0.15 s. For the first mode,  $f_1 = 3.67$  Hz, the ZV and ZVD input-shapers are defined by Eq. (IV.33) and Eq. (IV.34), respectively :

$$\mathbf{ZV}_{3.67 \text{ Hz}} = \begin{bmatrix} 0.5000 & 0.5000 \\ 0 & 0.1360 \end{bmatrix}, \quad (\text{IV.33})$$

$$\mathbf{ZVD}_{3.67 \text{ Hz}} = \begin{bmatrix} 0.2500 & 0.5000 & 0.2500 \\ 0 & 0.1360 & 0.2720 \end{bmatrix}. \quad (\text{IV.34})$$

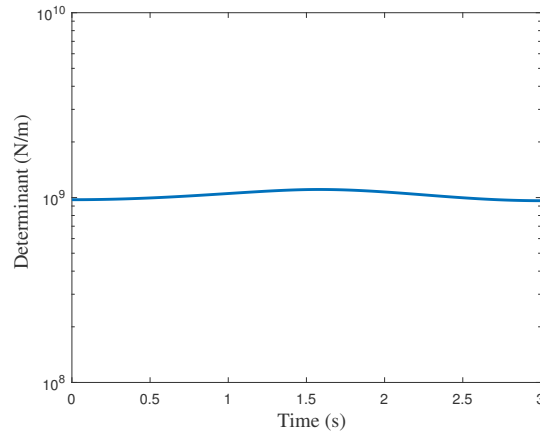


Figure IV.32 – Determinant of the global stiffness matrix along the nominal trajectory of the moving-platform

For the second mode,  $f_2 = 6.34$  Hz, the ZV and ZVD input-shapers are presented by Eq. (IV.35) and Eq. (IV.36), respectively :

$$\mathbf{ZV}_{6.34 \text{ Hz}} = \begin{bmatrix} 0.5000 & 0.5000 \\ 0 & 0.0788 \end{bmatrix}, \quad (\text{IV.35})$$

$$\mathbf{ZVD}_{6.34 \text{ Hz}} = \begin{bmatrix} 0.2500 & 0.5000 & 0.2500 \\ 0 & 0.0788 & 0.1576 \end{bmatrix}. \quad (\text{IV.36})$$

The convolution of the ZV-shapers given in Eq. (IV.33) and Eq. (IV.35) generates a ZV-ZV input-shaping filter described by the following matrix form :

$$\mathbf{ZV} - \mathbf{ZV} = \begin{bmatrix} 0.2500 & 0.2500 & 0.2500 & 0.2500 \\ 0 & 0.0788 & 0.1360 & 0.2148 \end{bmatrix}. \quad (\text{IV.37})$$

The convolution of the ZVD-shapers given in Eq. (IV.34) and Eq. (IV.36) generates a ZVD-ZVD input-shaping filter described by the following matrix form :

$$\mathbf{ZVD-ZVD} = \begin{bmatrix} 0.0625 & 0.1250 & 0.0625 & 0.1250 & 0.2500 & 0.1250 & 0.0625 & 0.1250 & 0.0625 \\ 0 & 0.0788 & 0.1576 & 0.1360 & 0.2148 & 0.2936 & 0.2720 & 0.3508 & 0.4296 \end{bmatrix}. \quad (\text{IV.38})$$

Figure IV.33 plots the velocity error  $\delta\dot{z}$  of the moving-platform along z-axis, which is defined as the difference between the nominal velocity of the moving-platform and the measured one. The black (red, blue, green, cyan, resp.) curve depicts  $\delta\dot{z}$  when the unshaped (ZV-shaped, ZVD-shaped, ZV-ZV-shaped, ZVD-ZVD-shaped, resp.) motion is used as a reference. To compare the different input-shaping filters, we focus on the oscillations generated by discontinuities. Accordingly, a zoom is made at time range  $t \in [3 \ 5]$  s, as the moving-platform is supposed

to become motionless at time  $t = 3$  s and then residual vibrations appear. From Fig. IV.33, it appears that the ZVD-ZVD shaper is the fastest one in terms of residual vibration attenuation.

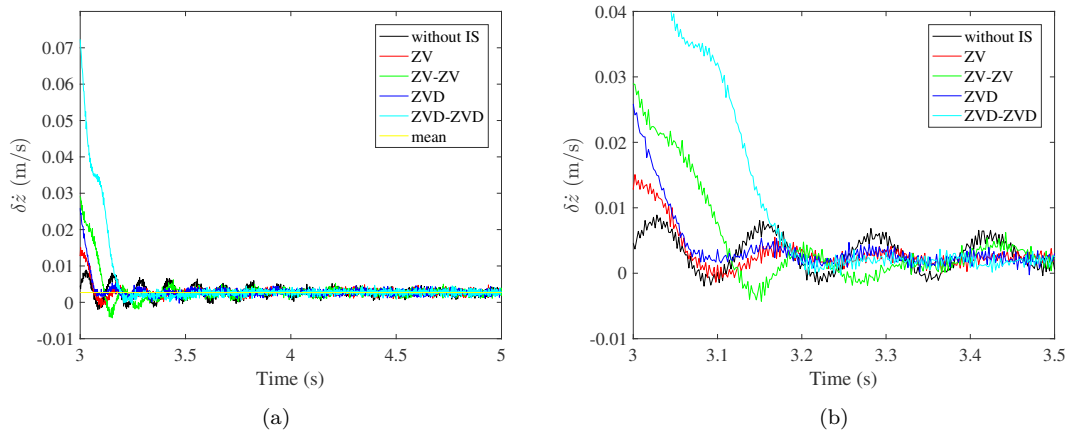


Figure IV.33 – (a) Moving-platform Velocity error with and without input-shaping (b) Zoom on the moving-platform velocity error with and without input-shaping

To better compare the performances of the different input-shapers, Fig. IV.34 represents a bar chart showing the first Peak-to-Peak amplitude of  $\delta\dot{z}$ . This period starts when the  $\delta\dot{z}$  curve intersects with the line presenting the mean value of oscillations. When no input-shaper is used, the Peak-to-Peak amplitude of  $\delta\dot{z}$  is equal to 0.0097 m/s. It is equal to 0.0061 m/s, 0.0045 m/s, 0.0056 m/s and to 0.0028 m/s when the ZV, ZVD, ZV-ZV and the ZVD-ZVD shapers are used, respectively. These results confirm that the ZVD and the ZVD-ZVD shaper lead to the most stable behavior of the end-effector.

On the contrary to the ZV-shaper, the ZVD-shaper is robust to modeling errors. The convolution of two one-mode robust shapers results in a two-mode robust shaper treating two natural modes of the robot under study. That explains the fact that the ZVD-ZVD filter leads to better oscillation attenuations. The two-mode ZVD-ZVD input-shaping filter leads to the most robust control scheme and the best one in terms of vibration rejection. Nevertheless, this robustness incurs in a time penalty so that the non-robust ZV-shapers are faster (Fig. IV.33) than the robust ZVD-shapers.

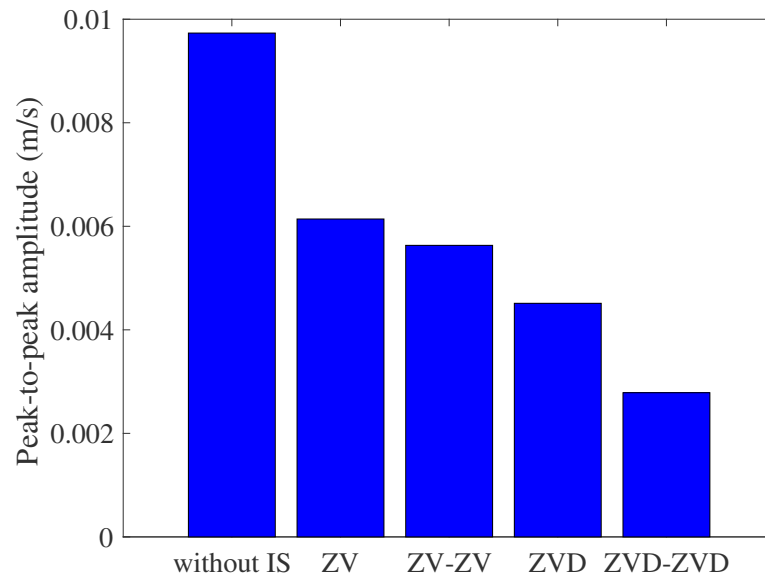


Figure IV.34 – Bar chart of the first period Peak-to-Peak amplitude of  $\delta\dot{z}$

## IV.4 Summary of the chapter

This chapter proposed a model-based feed-forward control strategy for CDPRs. The elasto-dynamic model of CDPRs was proposed to anticipate the full dynamic behavior of the mechanism including the vibratory effects, cable elongations and their interaction with the whole system to compensate them. The integration of tension calculation makes the proposed control scheme valid for every configuration of CDPRs. The comparison between the trajectory tracking errors obtained when using the proposed elasto-dynamic model or the classical rigid and elasto-static ones as control references shows meaningful differences. These differences reveal that the proposed control strategy guarantees a better trajectory tracking when adopting the proposed elasto-dynamic model to generate the reference control signal for CDPRs. Experimental results confirm that this accuracy improvement in terms of trajectory error norm achieves  $\approx 83\%$  with respect to the rigid control. Additionally, the robustness and the disturbance rejection of the proposed control strategy was confirmed for the non-redundant and suspended CREATOR prototype.

A second contribution of this chapter is to propose a frequency-dependent method to attenuate the unwanted vibrations of the CDPR. This method manifests in

the integration of input-shaping filters to the proposed model-based feed-forward control. In other words, in addition to the improvement of accuracy through model-based control, the proposed control scheme tries to cancel residual vibrations due to inertia and flexibility thanks to input-shaping filters. Two classes of input-shapers were proposed : single-mode and multi-mode input-shapers. These filters re-design the input signal to make it self-canceling of residual vibrations. The comparison between the velocity errors obtained through experimentations when using unshaped input signal or shaped ones as control references shows meaningful differences. Accuracy improvement with respect to the unshaped control in terms of Peak-to-Peak amplitude of velocity error achieves 53 % while using the ZVD input-shaper and 72 % while using the ZVD-ZVD input-shaper. However, this percentage is equal to 36 % while using the ZV input-shaper and 42 % while using the ZV-ZV input-shaper. This confirms vibration rejection by robust input-shapers [SCS97].

Experimental results confirm that the integration of input-shaping filters into the model-based feed-forward control scheme, when adopting the rigid model of CDPR as a reference, is useful to attenuate residual vibrations and increase the trajectory tracking of a non-redundant CDPR. Further experiments should be performed to confirm or not this statement while using elasto-static or elasto-dynamic models to pre-compensate cable stiffness.



# V

---

## Conclusions and Future Work

### Contents

---

V.1 Conclusions ·····	153
V.2 Future Work ·····	156

---

### V.1 Conclusions

Being a special type of parallel robots, Cable-Driven Parallel Robots (CDPRs) are characterized by their large workspace. Thanks to their low inertia, CDPRs can reach high velocities and accelerations in large workspaces. However, vibrations may occur and pose stabilization and/or trajectory tracking of the end-effector can be degraded due to the compliance of cables. To deal with this problem, this thesis focused on the improvement of static and dynamic accuracy of CDPRs. It proposed two complementary control strategies valid for any CDPR configuration (suspended, fully-constrained, redundant, non-redundant).

The first control method lies in the coupling of a model-based feed-forward control scheme for CDPR with a PID feedback controller. Here, an **elasto-dynamic model** of the CDPR was expressed in order to compensate the oscillatory motions of its moving-platform due to cable elongations and its dynamic behavior.

The second control method uses **input-shaping** filters into the proposed model-based feed-forward control in order to cancel the oscillatory motions the moving-platform. Thus, the input signal is modified for the CDPR to self-cancel residual vibrations.

The integration of cable tension distribution algorithms into these control schemes make them deal with the different CDPR configurations and guarantee positive cable tensions along the trajectory.

The integration of cable tension calculation or tension distribution algorithms into these control schemes make them deal with the different CDPR configurations and to guarantee positive cable tensions along the trajectory.

The parameters used in the proposed CDPR control models are subjected to uncertainties. The mathematical models do not perfectly reflect the robot behavior because of uncertainties such as the assembly and manufacturing inaccuracies of geometrical components. Moreover, these models are influenced by non-geometrical origin uncertainties. A robustness analysis was performed through sensitivity and uncertainty analysis to lead to a robust model-based control of CDPRs. As a result, an appropriate CDPR model was defined as a function of the targeted application and the main sources of CDPR moving-platform pose errors were identified.

The main contributions of this thesis are listed as following :

### V.1.1 Contribution on CDPR dynamic modeling

In **Chapter II**, the dynamic modeling of CDPRs was introduced. Different dynamic models of CDPRs used for feed-forward control were reviewed and the **elasto-dynamic model** was presented. As the choice of cable models is a primary task for CDPR modeling, the different levels of cable stiffness used for dynamic modeling were also discussed in Section II.3. Usually, the dynamic stiffness analysis of CDPRs is made under the assumption that dynamic loads induce only small elongations of the cables. The cable tension is usually considered proportional to the variations in the cable length for a constant stiffness coefficient. Therefore, such a model is not valid when cables are subjected to high strains due to large dynamic oscillations or quick cable-length variations. As a consequence, a new **non-linear cable tension model** was proposed in Section II.3.2 to express the dynamic and oscillatory motions of CDPRs with cables subjected to fast varying lengths. This formulation revealed a softening behavior when strains become large.

## V.1.2 Robustness analysis

**Chapter III** listed the different mechanical and geometrical error sources and investigated their effects onto the trajectory tracking accuracy.

**Sensitivity analysis** was performed through a comparison between the conventional dynamic models and the proposed elasto-dynamic model of CDPR. A weakness of the conventional models used for model-based control is that they neglect the dynamic effects due to cable interactions with the whole system. The elasto-dynamic model tries to remedy this weakness by anticipating the oscillatory behavior of CDPR while the moving-platform tracks a trajectory. Such a model is useful for control purposes as it predicts not only the cable elongations but also their dynamic interaction with the moving-platform.

Moreover, sensitivity analysis of CDPR accuracy to cable tension modeling was made through a comparison between the CDPR responses while using the linear and the non-linear tension formulation of cables. This analysis mentioned that the cable tension model does affect the trajectory errors for CDPRs with large overall size, such as the FAST robot. It was demonstrated that variations in trajectory tracking errors obtained from one cable tension model to the other one remains small with respect to the CDPR size.

**Uncertainty analysis** was performed to test the robustness of CDPR model to variations in parameters into a known range. It is useful for the reduction of uncertainty, through the identification of model inputs that cause significant uncertainty and should therefore be the focus of attention. The critical parameters were then listed from the most influential to the least. It appeared from this analysis that the effect of the modulus of elasticity of cables is the highest onto the dynamic and oscillatory motions of the moving-platform. For this purpose, the experimental method named **Dynamic Mechanical Analysis** (DMA) was proposed to identify carefully the dynamic elastic and damping moduli of some cables to better compensate the stiffness effects leading to pose errors and trajectory tracking degradation.

### V.1.3 Control for CDPR accuracy improvement

Chapter IV dealt with the implementation of two complementary feed-forward model-based control strategies, which aim to improve the end-effector trajectory tracking and reduce vibrations due to overall elasticity.

Section IV.2 dealt with the introduction of the proposed **elasto-dynamic feed-forward control** and the establishment of the corresponding control laws. To check the effectiveness of this control, a numerical comparison of the end-effector trajectory tracking with respect to the classical feed-forward control schemes was made. Moreover, experimentations were performed on the CREATOR prototype located at LS2N, Nantes, France; a CDPR with three cables and three Degree-Of-Freedom. The experimental tests confirmed the numerical results, revealing that the elasto-dynamic control scheme leads to better moving-platform trajectory tracking.

In addition, Section IV.3 deals with the integration of **input-shaping** filters into the proposed model-based feed-forward control. These filters are integrated upstream of the pre-compensation block in order to increase the CDPR performances by the improvement of residual vibrations attenuation. Experimental tests are made on the CREATOR prototype to verify the ability of the control scheme to vanish residual vibrations of the manipulator. Experimentations were made on the CREATOR prototype to verify the ability of the proposed control scheme integrating input-shapers to vanish residual vibrations of the manipulator. These tests were made while adopting the rigid model of CDPR for the feed-forward. The comparison between the velocity errors obtained through experimentations when using unshaped input signal or shaped ones as control references showed meaningful differences. Accordingly, accuracy improvement in terms of Peak-to-Peak amplitude of velocity error with respect to the unshaped control can achieve up to 72 % while using the ZVD-ZVD input-shaper. This confirmed the vibration rejection by robust input-shapers integrated into feed-forward control schemes for non-redundant suspended CDPR.

## V.2 Future Work

This thesis focused on the improvement of the dynamic accuracy of CDPRs. A significant feature of this research work is the introduction of the oscillatory

and dynamic behavior of the end-effector due to cable elongations into the feed-forward control and its implementation in real applications. The integration of input-shapers into the proposed feed-forward model-based control schemes is also an important contribution of this thesis. Both control methods were taking into account the conclusions drawn from the robustness analysis of CDPRs.

Basing on the above conclusions, some future works are proposed thereafter :

Feed-forward model-based control schemes with and without input-shaping were validated experimentally for a suspended and non-redundant CDPR. Further experiments should be performed to check the results obtained with other CDPR configurations (fully-constrained, redundant). Besides, experimental results confirmed that the integration of input-shaping filters into the model-based feed-forward control scheme when adopting the rigid model of CDPR as a reference is useful to attenuate residual vibrations and increase the trajectory tracking of a non-redundant CDPR. This statement should be verified as well while using elasto-static or elasto-dynamic models to pre-compensate cable elasticity.

Several parameters, such as the positions of the cable exit points on the drums, were taken into account to establish the relationship between the uncoiled cable lengths by the winches and the angular coordinates of the actuators. For better repeatability of the proposed control schemes, the cable tensions should be measured to estimate the elongations contained in the winches to compensate the static offset more accurately.

The above conclusions are presented and verified experimentally for CDPR prototypes where cable elasticity arises. Future research work should focus on the cable dynamic sagging modeling, which may be more relevant for other CDPR configurations. Such a case will occur when cable sagging becomes more influential than cable elasticity. The interaction between cables and pulleys and cable sliding into the pulley grooves should be studied and taken into consideration for a better accuracy of the model. The integration of all these information and their coupling into the proposed feed-forward control laws leads to non-linearities and high time-consumption. A good real-time model of cable elongation while considering its

overall stiffness may be promising for the improvement of control performances.

The proposed control strategies consider the CDPR parameters unchangeable. This assumption is valid when infinitesimal variations occur. In order to compensate for the uncertainties and variations in the parameters of dynamic models, an adaptive control should be implemented [LGCH13, BKT15, JFGK15]. This control makes it possible to estimate the moving-platform mass, its load, its gravity center position with respect to its center of reference, its moments of inertia, the dry and viscous friction coefficients as well as the inertia of winches. The on-line adjustment of these parameters may considerably reduce trajectory tracking errors.

As discussed previously, trajectory tracking errors are mainly due to cable elasticity, which is compensated in the control laws presented in this thesis. This reveals the importance of integrating cable hysteresis effect into the error modeling to enhance the cable mechanical behavior model. This is important especially when cable tensions are not measured. Integrating this model into adaptive control should further improve the overall CDPR performance.

In order to improve the performances of multi-mode input-shaping control schemes, an on-line estimation of CDPR natural frequencies, with respect to CDPR geometry, cable tensions and the end-effector trajectory, will allow the user to tune input-shaping filters as a function of those estimated natural along a prescribed trajectory of the moving-platform and to reduce the moving-platform pose stabilization time.

Last but not least, future research work should focus on the consideration of environmental factors such as wind, humidity,... which may degrade CDPR performance through cable wear for example.

# List of Publications

- BAKLOUTI Sana, COURTEILLE Eric, CARO Stéphane and al. *Dynamic and Oscillatory Motions of Cable-Driven Parallel Robots Based on a Nonlinear Cable Tension Model*. Journal of Mechanisms and Robotics, 2017, vol. 9, no 6, p. 061014.
- BAKLOUTI Sana, CARO Stéphane and COURTEILLE Eric. *Sensitivity Analysis of the Elasto-Geometrical Model of Cable-Driven Parallel Robots*. In : Cable-Driven Parallel Robots. Springer, Cham, 2018. p. 37-49.
- BAKLOUTI Sana, CARO Stéphane and COURTEILLE Eric. *Elasto-Dynamic Model-Based Control of Non-Redundant Cable-Driven Parallel Robots*. In : ROMANSY 22-Robot Design, Dynamics and Control. Springer, Cham, 2019. p. 238-246.
- BAKLOUTI Sana, COURTEILLE Eric, LEMOINE Philippe and CARO Stéphane. *Vibration Reduction of Cable-Driven Parallel Robots through Elasto-dynamic Model-Based Control*. Journal of Mechanism and Machine Theory, submitted in December 2018.



# A

---

## Cable identification : Modulus of elasticity

### Contents

---

A.1 Steel Cable ·····	161
A.2 Polyethylene Cable ·····	167

---

The identification of the mechanical parameters of the cable remains a practical issue. A procedure to identify experimentally the quasi-static and dynamic modulus of cable elasticity is presented. Dynamic Mechanical Analysis (DMA) is used to study the effect of loading frequency on the elastic and damping mechanical properties of cables.

For this purpose, Tema Concept cyclic loading test bench is used to identify the quasi-static and dynamic modulus of elasticity of cables. The loading frequency of this machine can achieve 10 Hz at the rate of 1 mm/s. To get higher frequencies, the displacement rate should be reduced. The maximal charge of this test bench is about 250 kN.

## A.1 Steel Cable

### A.1.1 Modulus of elasticity

An identification method of the modulus of elasticity of a steel wire cable is specified in the International Standard ISO 12076. The elasticity modulus or Young's modulus is defined as the ratio of stress along an axis to strain along that axis within a specified load range and strain rate range. It amounts to an elastic material stiffness. The modulus of elasticity of a wire cable does not depend solely on the properties of the wire material, but on the wires layout and the load history too.

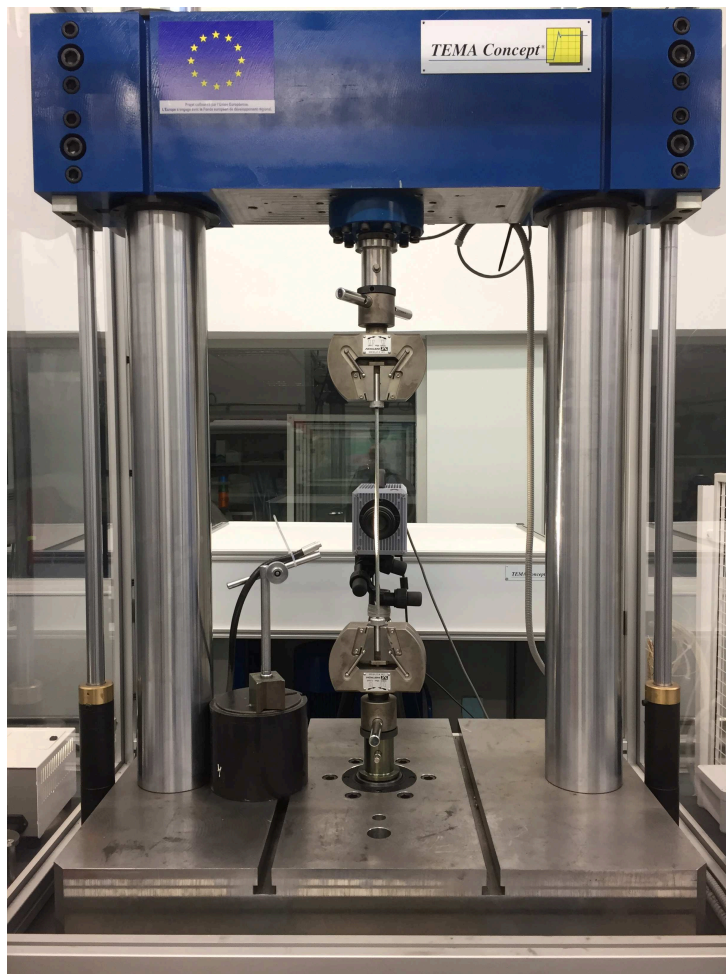


Figure A.1 – Tema Concept cyclic loading test bench

The determination of the modulus of elasticity of a steel wire cable is described in the International Standard ISO 12076.

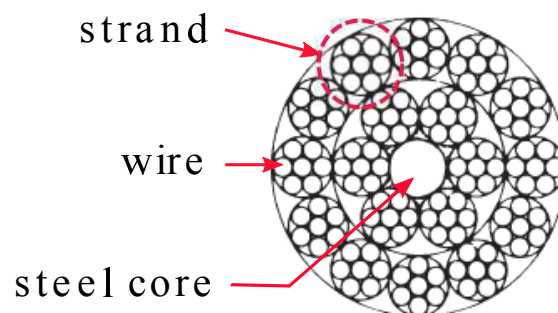


Figure A.2 – Cross section of a rotation-resistant steel wire cable; Carl Stahl Technocables Ref 1692

A steel cable consisting of 18 strands twisted around a steel core used for the CAROCA prototype is taken as an illustrative example for the identification. Each strand of this cable is made up of 7 steel wires (Fig. A.2). The breaking force of this cable is 10.29 kN. Force controlled cycles from 0 to 3087 N (30% of the breaking force as specified in the International Standard ISO 12076) were applied 50 times at the rate of 0.05 mm/s. The free length of cable between the grips of the tensile machine (Tema Concept cyclic loading test bench, see Fig. A.1) is 350 mm (15 times higher than the nominal cable diameter). A wire cable should always be loaded and relieved multiple times for identifying the modulus of elasticity. A relative steady state is reached when repeated extension readings are consistent at both ends of the force range.

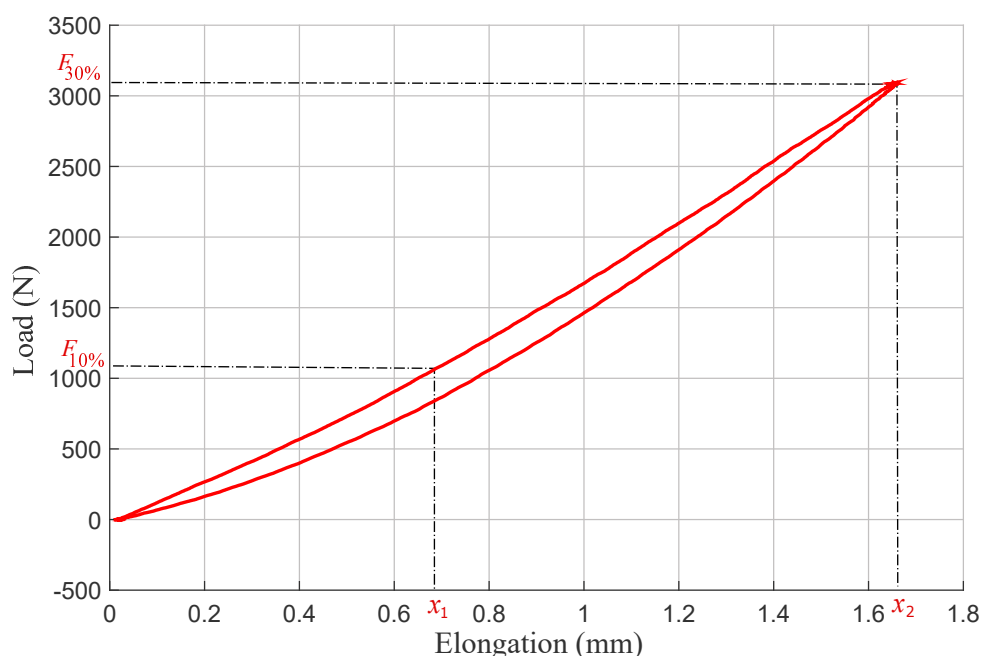


Figure A.3 – Load-elongation diagram of a steel wire cable measured in steady state conditions at the rate of 0.05 mm/s

Figure A.3 shows the load-elongation diagram of a rotation-resistant steel wire cable of 4 mm diameter obtained after 50 cycles. It depicts that the unloading path does not correspond to the loading path. The area in the center of the hysteresis loop is the energy dissipated due to internal friction in the cable. Figure A.3 depicts a non-linear correlation in the lower area between load and cable elongation. The load-elongation diagram only gets linear when all the wires in each strand and all the strands in the cable share the load together.

According to the International Standard ISO 12076, the modulus of elasticity of a steel wire cable has to be calculated using the tests reading as follows :

$$E_{10-30} = l_c \frac{F_{30\%} - F_{10\%}}{A_c(x_{30} - x_{10})}, \quad (\text{A.1})$$

where  $A_c$  is the metallic cross-sectional area, i.e. the value obtained from the sum of the metallic cross-sectional areas of the individual wires in the rope based on their nominal diameters.  $x_{10}$  and  $x_{30}$  are the elongations at forces equivalent to 10% and 30% ( $F_{10\%}$  and  $F_{30\%}$ ), respectively, of the nominal breaking force of the cable (10.29 kN) measured during the loading path (Fig. A.3).  $l_c$  is the measured initial cable length.

It is noteworthy that this value differs from the one classically calculated using the cross-sectional area of the cable as a whole, *i.e.*  $S_c = \pi \left(\frac{\phi_c}{2}\right)^2$ .  $\phi_c$  being the apparent diameter of the cable. In that case the modulus of elasticity is equal to  $58.2 \pm 1.3$  GPa. This value differs from the one obtained following the International Standard ISO 12076. The consequences will be limited in the presented application if the definition of the cross-sectional area is the same in the identification procedure of the cable behavior. However, vagueness in data exchange may lead to major modeling errors.

## A.1.2 Dynamic modulus of elasticity

The DMA supplies a sinusoidal load to be applied to the cable used for the CAROCA prototype, which generates a sinusoidal elongation. By measuring both the amplitude of the resulting elongation and the lag between the force and the elongation, the modulus of elasticity and also the damping of the cable can be identified. One advantage of DMA is that we can obtain a dynamic modulus for different frequencies of the sine wave applied, allowing us to sweep across the frequency range of the intended application. Six tests were performed on the cable at frequencies  $f$  of 0.1, 1, 2, 5, 10, and 20 Hz (Fig. A.4). A preload was applied to the cable before the sinusoidal force controlled waves, at 1500 N corresponding to an operating point in the linear area of the load-elongation diagram.

The DMA allows us to calculate from the cable response to the sine wave a dynamic modulus  $E^*$ , which is a complex value. The real part of the dynamic modulus  $E'$  represents the ability of the cable to return energy and can be assimilated to the elastic modulus. The imaginary part  $E''$  provides the capacity of the

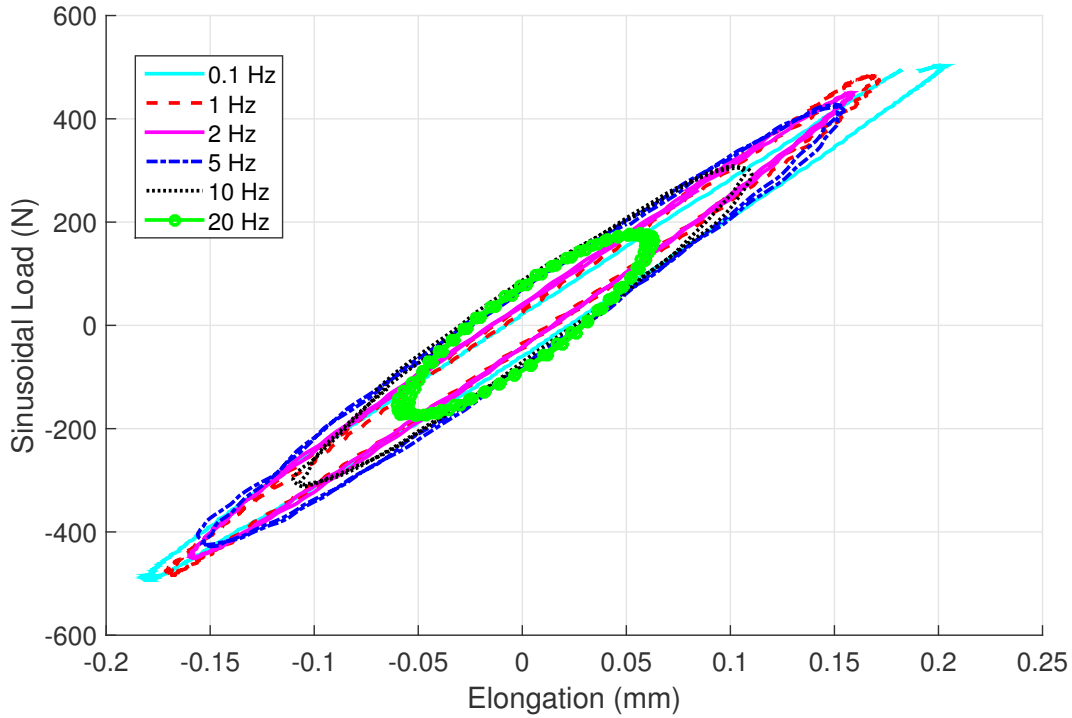


Figure A.4 – Hysteresis loops for a 4 mm steel wire cable preloaded at 1500 N with force controlled sine waves applied at 0.1, 1, 2, 5, 10, and 20 Hz

cable to dissipate energy. The applied sinusoidal force and resulting elongation are used to calculate the absolute value of the dynamic modulus  $|E^*|$ , *i.e.* the ratio of the maximum amplitude of the applied idealized stress  $\sigma_{max}$  to the maximum amplitude of the resulting strain  $\epsilon_{max}$ , as well as the phase angle  $\varphi$  between the force and elongation. In this paper, the definition of the strain assumes an idealized stress-strain response with a constant metallic cross-sectional area of the individual wires in the cable, based on their nominal diameters. The corresponding elastic,  $E'$ , and loss,  $E''$ , moduli are obtained from the dynamic modulus and phase angle as  $E' = |E^*|.cos\varphi$  and  $E'' = |E^*|.sin\varphi$  [Had95]. The intrinsic damping of the cable can be described by the loss factor [CLP98] :

$$\eta = \frac{E''}{E'} = \tan(\varphi), \quad (\text{A.2})$$

which is the ratio between the imaginary and real parts of the complex modulus.

The dynamic and elastic modulus, the phase angle  $\varphi$  and the loss factor  $\eta$  are given for each DMA test in Table (A.1).

**Table A.1** – Frequency dependency of the modulus of elasticity of the steel wire cable at loading frequencies between 0.1 and 20 Hz

$f$ (Hz)	$\sigma_{max}$ (MPa)	$\epsilon_{max}$	$ E^* $ (GPa)	$E'$ (GPa)	$\varphi$ ( $^\circ$ )	$\eta$	$c$ ( $N.m^{-1}.s$ )
0.1	69.731	$5.7439 \cdot 10^{-4}$	$121.4 \pm 2.8$	$120.5 \pm 2.8$	$6.8 \pm 2.3$	$0.12 \pm 0.04$	$22.8 \cdot 10^9$
1	67.136	$4.8474 \cdot 10^{-4}$	$138.5 \pm 3.3$	$137.3 \pm 3.3$	$7.5 \pm 2.8$	$0.13 \pm 0.05$	$2.87 \cdot 10^9$
2	62.379	$4.5499 \cdot 10^{-4}$	$137.1 \pm 3.3$	$134.8 \pm 3.1$	$11.0 \pm 2.8$	$0.19 \pm 0.05$	$2.08 \cdot 10^9$
5	58.654	$4.3159 \cdot 10^{-4}$	$135.9 \pm 3.1$	$131.0 \pm 3.0$	$14.1 \pm 2.8$	$0.25 \pm 0.05$	$1.04 \cdot 10^9$
10	41.618	$3.0490 \cdot 10^{-4}$	$136.5 \pm 3.2$	$130.1 \pm 3.0$	$17.6 \pm 2.8$	$0.31 \pm 0.05$	$0.65 \cdot 10^9$
20	24.025	$1.7447 \cdot 10^{-4}$	$137.7 \pm 3.3$	$126.2 \pm 2.8$	$23.5 \pm 2.8$	$0.43 \pm 0.05$	$0.44 \cdot 10^9$

We can see that the stiffness and damping are highly dependent on frequency for a given preload, over a representative frequency range of the CDPR behavior [YCD15]. The elastic modulus increases significantly at very low frequencies, from  $120.5 \pm 2.8$  GPa at 0.1 Hz to  $137.3 \pm 3.3$  GPa at 1 Hz (Table (A.1)). This is compared to the quasi-static modulus of elasticity calculated following the International Standard whose value is equal to  $102.2 \pm 2.2$  GPa. The elastic modulus is secondly found to decrease slowly with higher frequency. At higher frequencies, the dynamic modulus is approximately constant, with values within the confidence interval referring to the reliability of the test procedure. Large changes in the phase angle occur over the frequency range. The frequency-dependent loss factor appears consistent with increased hysteresis and thus loading velocity.

The cable damping is modeled by using a linearly viscoelastic definition. Indeed, an equivalent viscous coefficient can be defined as :

$$c = \frac{E' \eta}{2\pi f}, \quad (\text{A.3})$$

$f$  being the loading frequency.

These dynamic characteristics indicate how well the cable works in oscillatory motions around a static equilibrium or along a dynamic trajectory since we can get this value for a range of frequencies. Our results show that the apparent cable stiffness can change significantly under dynamic loading and may lead to large displacements of the CDPR end-effector.



Figure A.5 – Polyethylene Cable used for the CREATOR prototype

## A.2 Polyethylene Cable

The modulus of elasticity of cables is identified experimentally through a cyclic traction test. The cable used in this application consists of textile cable. Force controlled cycles from 0 to 200 N were applied 50 times to 4 cables at the rate of 50 mm/min. The different cables should not be twisted, but run in parallel. The free length of cable between the grips of the tensile machine is 356 mm. Fig. A.6 shows the charge-deformation diagram of the polyethylene cable of 0.5 mm diameter obtained after 50 cycles.

The slope of the yield curve presents the cable stiffness. This slope corresponds to a modulus of elasticity of 70 GPa, which corresponds to a flexible cable resistant to a maximum charge of 250 N. The end-effector mass and trajectory should be chosen the way that the cable tension set stays in the secure range (between 0 and 250 N).

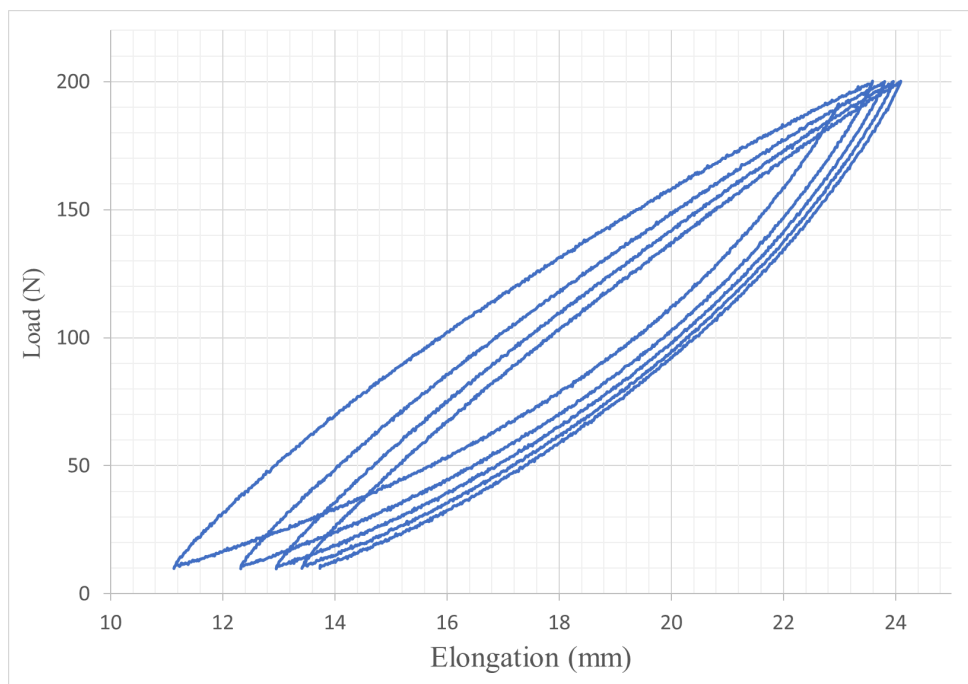


Figure A.6 – Elongation-load diagram of a polyethylene cable

# B

## Example prototypes

### Contents

---

B.1 CAROCA ·····	169
B.2 FAST ·····	170
B.3 CREATOR prototype ·····	171

---

### B.1 CAROCA

The CAROCA prototype developed at IRT Jules Verne [GCGG16] uses a 4 mm diameter steel cable consisting of 18 strands twisted around a steel core, where each strand of this cable is made up of 7 steel wires (Fig. A.2). The experimental identification of this cable is presented in Section (A.1) and experimental data is used for the uncertainty analysis.

#### B.1.1 Redundant configuration

The redundant configuration of the reconfigurable CAROCA prototype (Fig. I.12) presents 8 cables and 6 DOF. The Cartesian coordinates of  $A_i$  ( $B_i$ , resp.) expressed in  $\mathcal{F}_p$  (in  $\mathcal{F}_b$ , resp.) of the considered prototype are given in Tab. B.1.

#### B.1.2 Non-redundant configuration

The non-redundant configuration of the reconfigurable CAROCA prototype presents 3 cables and 3 DOF. The Cartesian coordinates of  $A_i$  ( $B_i$ , resp.) expressed in  $\mathcal{F}_p$  (in  $\mathcal{F}_b$ , resp.) of the considered prototype are given in Tab. B.2.



Figure B.1 – CAROCA prototype, Courtesy of IRT Jules Verne, Nantes

Table B.1 – Redundant CAROCA prototype : Cartesian coordinates of anchor points  $A_i$  (exit points  $B_i$ , resp.) expressed in  $\mathcal{F}_p$  (in  $\mathcal{F}_b$ , resp.)

	x (m)	y (m)	z (m)		x (m)	y (m)	z (m)
$B_1$	-3.5	2	3.5	$A_1$	0.2	0.15	0.125
$B_2$	3.5	2	3.5	$A_2$	-0.2	0.15	-0.125
$B_3$	-3.5	2	3.5	$A_3$	-0.2	-0.15	-0.125
$B_4$	3.5	2	3.5	$A_4$	0.2	-0.15	0.125
$B_5$	-3.5	-2	3.5	$A_5$	-0.2	0.15	0.125
$B_6$	3.5	-2	3.5	$A_6$	0.2	0.15	-0.125
$B_7$	-3.5	-2	3.5	$A_7$	0.2	-0.15	-0.125
$B_8$	3.5	-2	3.5	$A_8$	-0.2	-0.15	0.125

## B.2 FAST

The 6-dof FAST robot [Hui15, LTS<sup>+</sup>13] composed of 6 cables is considered. The Cartesian coordinates of  $A_i$  ( $B_i$ , resp.) expressed in  $\mathcal{F}_p$  (in  $\mathcal{F}_b$ , resp.) of the considered prototype are given in Tab. B.1.

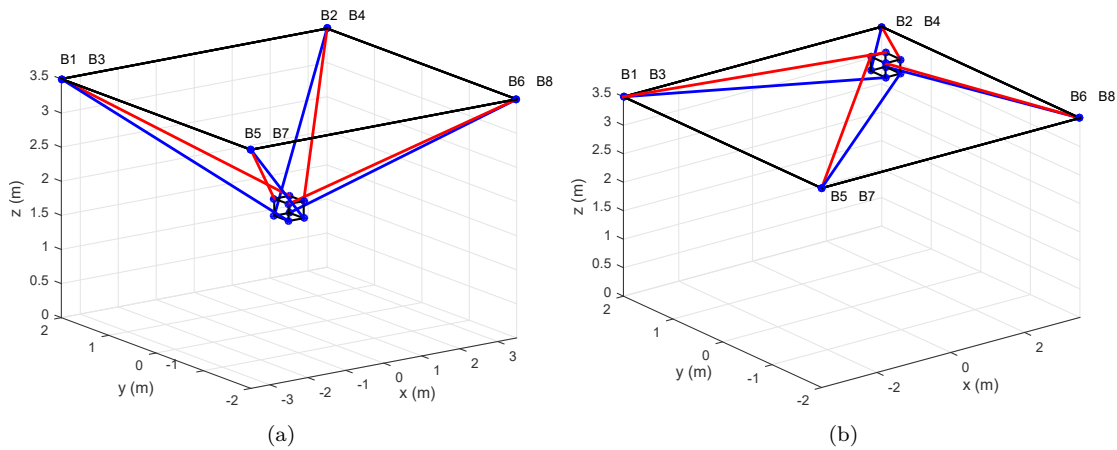


Figure B.2 – CAROCA schematic (a) in a symmetric position (b) in a non-symmetric position

Table B.2 – Non-redundant CAROCA : Cartesian coordinates of anchor points  $A_i$  (exit points  $B_i$ , resp.) expressed in  $\mathcal{F}_p$  (in  $\mathcal{F}_b$ , resp.)

	x (m)	y (m)	z (m)
$B_1$	3.5	-2	3.5
$B_2$	0	2	3.5
$B_3$	-3.5	-2	3.5

Table B.3 – Non-redundant FAST : Cartesian coordinates of anchor points  $A_i$  (exit points  $B_i$ , resp.) expressed in  $\mathcal{F}_p$  (in  $\mathcal{F}_b$ , resp.)

	x (m)	y (m)	z (m)		x (m)	y (m)	z (m)
$B_1$	250	0	0	$A_1$	8	0	0
$B_2$	125	216.50	0	$A_2$	4	7	0
$B_3$	-125	216.50	0	$A_3$	-4	7	0
$B_4$	-250	0	0	$A_4$	-8	0	0
$B_5$	-125	-216.50	0	$A_5$	-4	-7	0
$B_6$	125	-216.50	0	$A_6$	4	-7	0

Both CAROCA prototype and FAST CDPRs are compared in Tab. B.4. This latter presents the height, width, the unstrained cables length when the end-effector is in a home position, the end-effector mass and the maximum cable tension.

## B.3 CREATOR prototype

CREATOR prototype is a CDPR dedicated for pedagogical applications and then to be improved for specific industrial applications.

A suspended configuration of the reconfigurable CREATOR prototype with 3

Table B.4 – Characteristics of CAROCA and FAST CDPRs

	Height (m)	Width (m)	Unloaded cable length (m)	End-effector mass (kg)	Maximal design allowable cable tension (kN)
CAROCA	3.5	7	4.6	100	10
FAST	376	500	284.7	10000	500

cables and 3 DOF is studied. The dimensions of this prototype are about 4.5 m long, 4 m wide and 3 m high. The nominal mass of the moving-platform is equal to 0.650 kg. It is supposed to be a point-mass. The cables used for the CREATOR prototype are composed of 8 threads of polyethylene fiber. Their diameter is equal to 0.5 mm and their modulus of elasticity is equal to 70 GPa as identified experimentally (See Appendix A.2).



Figure B.3 – CREATOR prototype : Courtesy of LS2N, Nantes, France

The Cartesian coordinates of  $B_i$  expressed in  $\mathcal{F}_b$  of the considered prototype are given in Tab. (B.5). They are determined experimentally by means of a RADIANT Laser tracker.

The tracker weighs 9 kg and it is 177 mm  $\times$  177 mm  $\times$  355 mm. The static

Table B.5 – Measured Cartesian coordinates of exit points  $B_i$  in  $\mathcal{F}_b$ 

	x (m)	y (m)	z (m)
$B_1$	-2.085	0.651	2.726
$B_2$	2.085	0.651	2.735
$B_3$	-1.079	-1.898	2.733



Figure B.4 – RADIANT Laser tracker

measurement accuracy of the used laser tracker is  $\pm 10 \mu\text{m}$ . Its range of working is between 0 and 25 m.



# C

## Complement for modeling

### C.1 Euler angles convention

To represent the orientation the orientation of the mobile frame  $\mathcal{F}_p$  with respect to the fixed frame  $\mathcal{F}_b$ , the convention  $X$ - $Y$ - $Z$  of the Euler angles is used. This convention makes it possible to generate the three angles representing the rotations around the three reference axes of the platform. The description of the Euler angles consists of three successive elementary rotations, corresponding to the angles  $\phi$ ,  $\theta$  and  $\psi$  (see Fig. C.1) in the following order :

- a rotation about the  $x$  axis of an angle  $\phi$ , passes from the reference  $(x, y, z)$  to landmark  $(x, u, v)$ .
- a rotation around the axis  $u$  of an angle  $\theta$ , moves from the reference  $(x, u, v)$  to the mark  $(w, u, z_1)$ .
- a rotation around the axis  $z_1$  of an angle  $\psi$ , finally brings the reference  $(w, u, z_1)$  on the reference mark  $(x_1, y_1, z_1)$ .

Finally, the rotation matrix is calculated as  ${}^b\mathbf{R}_p(\phi, \theta, \psi) = \mathbf{R}_x(\phi)\mathbf{R}_y(\theta)\mathbf{R}_z(\psi)$ , where

$$\mathbf{R}_x(\phi) = \begin{bmatrix} 1 & 0 & 0 \\ 0 & c_\phi & -s_\phi \\ 0 & s_\phi & c_\phi \end{bmatrix}, \quad \mathbf{R}_y(\theta) = \begin{bmatrix} c_\theta & 0 & s_\theta \\ 0 & 1 & 0 \\ -s_\theta & 0 & c_\theta \end{bmatrix}, \quad \mathbf{R}_z(\psi) = \begin{bmatrix} c_\psi & -s_\psi & 0 \\ s_\psi & c_\psi & 0 \\ 0 & 0 & 1 \end{bmatrix}. \quad (\text{C.1})$$

Then,

$${}^b\mathbf{R}_p(\phi, \theta, \psi) = \begin{bmatrix} c_\theta c_\psi & -c_\theta s_\psi & s_\theta \\ c_\phi s_\psi + s_\phi s_\theta c_\psi & c_\phi s_\psi - s_\phi s_\theta c_\psi & -s_\phi c_\theta \\ s_\phi s_\psi - c_\phi s_\theta c_\psi & s_\phi c_\psi + c_\phi s_\theta c_\psi & c_\phi c_\theta \end{bmatrix}. \quad (\text{C.2})$$

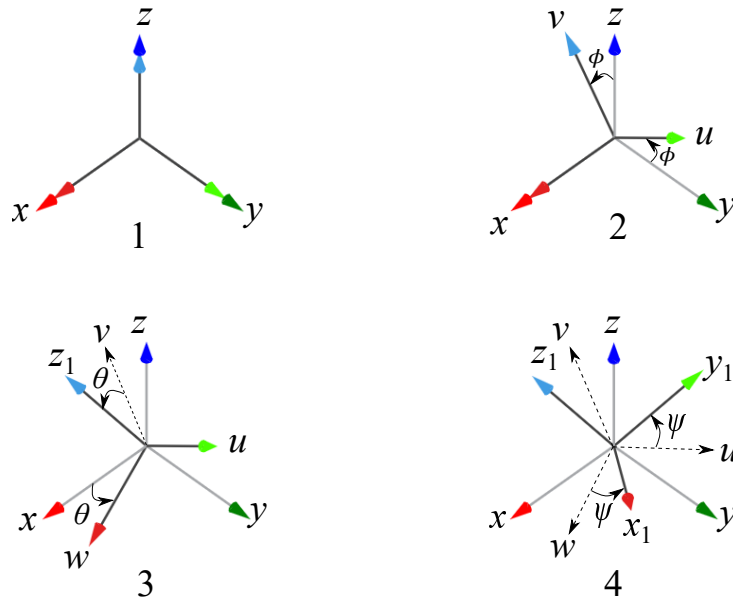


Figure C.1 – Representation of the successive rotations of the Euler X-Y-Z convention

### C.1.1 Angular velocity

The vector  $\boldsymbol{\omega} = [\omega_1 \ \omega_2 \ \omega_3]^T$  describes the end-effector angular velocity in  $\mathcal{F}_b$ . With respect to the Euler angles convention, three successive angular velocities occur :

- $\dot{\phi}$  around  $x$ -axis.
- $\dot{\theta}$  around  $u$ -axis, which is expressed as  $\mathbf{u} = [0 \ c_\phi \ s_\phi]^T$  in  $\mathcal{F}_b$ .
- $\dot{\psi}$  around  $z_1$ -axis, which is expressed as  $\mathbf{z}_1 = [s_\theta \ -c_\theta s_\phi \ c_\theta c_\phi]^T$  in  $\mathcal{F}_b$ .

Accordingly, the angular velocity vector  $\boldsymbol{\omega}$  of the moving-platform can be expressed as following :

$$\boldsymbol{\omega} = \dot{\phi} \begin{bmatrix} 1 \\ 0 \\ 0 \end{bmatrix} + \dot{\theta} \begin{bmatrix} 0 \\ c_\phi \\ s_\phi \end{bmatrix} + \dot{\psi} \begin{bmatrix} s_\theta \\ -c_\theta s_\phi \\ c_\theta c_\phi \end{bmatrix}, \quad (\text{C.3})$$

which permits to rewrite it as :

$$\boldsymbol{\omega} = \begin{bmatrix} \dot{\phi} + \dot{\psi} s_\theta \\ \dot{\theta} c_\phi - \dot{\psi} c_\theta s_\phi \\ \dot{\theta} s_\phi + \dot{\psi} c_\theta c_\phi \end{bmatrix}. \quad (\text{C.4})$$

Therefore, the angular velocity vector  $\boldsymbol{\omega}$  of the moving-platform can be writing in matrix form as following :

$$\boldsymbol{\omega} = \begin{bmatrix} \omega_1 \\ \omega_2 \\ \omega_3 \end{bmatrix} = \mathbf{U}\dot{\boldsymbol{\phi}}, \quad (\text{C.5})$$

where

$$\mathbf{U} = \begin{bmatrix} 1 & 0 & s_\theta \\ 0 & c_\phi & -c_\theta s_\phi \\ 0 & s_\phi & c_\theta c_\phi \end{bmatrix}, \quad \dot{\boldsymbol{\phi}} = \begin{bmatrix} \dot{\phi} \\ \dot{\theta} \\ \dot{\psi} \end{bmatrix}. \quad (\text{C.6})$$

## C.2 Elasto-dynamic model resolution

Figure C.2 presents the resolution method of the CDPR elasto-dynamic model. The applied motor torque  $\boldsymbol{\zeta}_m$  and the cable length vector  $\mathbf{l}_{es}$  considering static deflection are the input. The output is the moving-platform pose estimated by solving the CDPR elasto-dynamic model and integrating two times the MP acceleration. MATLAB<sup>®</sup> routine ode45 is used in this thesis to solve the elasto-dynamic model.

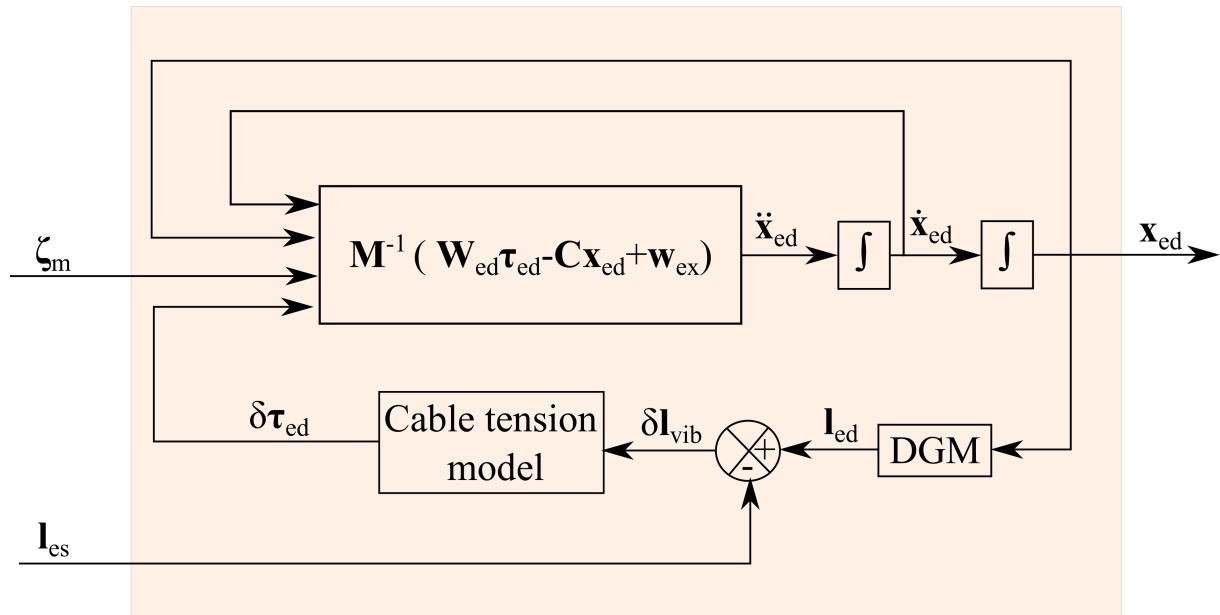


Figure C.2 – Elasto-dynamic model resolution method

The elasto-dynamic cable length vector  $\mathbf{l}_{ed}$  is determined through the DGM presented by Eq. (II.5). The elasto-static cable length vector  $\mathbf{l}_{es}$  is subtracted from

$\mathbf{l}_{ed}$  to obtain  $\delta\mathbf{l}_{vib}$ , where  $\delta l_{vib}^i$  being the  $i$ th cable elongation due to the vibratory effects only. This cable elongation is used to calculate the deviation  $\delta\boldsymbol{\tau}_{ed}$  of the cable tension  $\boldsymbol{\tau}_{ed}$  with respect to  $\boldsymbol{\tau}$ . Let's recall Eq. (II.37) where :

$$\tau_{ed}^i = \tau^i + \delta\tau_{ed}^i. \quad (\text{C.7})$$

The expression of  $\delta\tau_{ed}^i$  is a function of the  $i$ th cable stiffness and depends on the chosen cable tension model either linear or non-linear (See Section II.3.2).

The moving-platform acceleration vector  $\ddot{\mathbf{x}}_{ed}$  is obtained upon multiplication of Eq. (II.13) by the inverse mass matrix  $\mathbf{M}^{-1}$  :

$$\ddot{\mathbf{x}}_{ed} = \mathbf{M}^{-1} (\mathbf{W}_{ed} (\boldsymbol{\tau} + \delta\boldsymbol{\tau}_{ed}) - \mathbf{C} \dot{\mathbf{x}}_{ed} + \mathbf{w}_{ex}), \quad (\text{C.8})$$

while considering the dynamics of actuators :

$$\boldsymbol{\tau} = \boldsymbol{\chi}^{-1} (\boldsymbol{\zeta}_m - \mathbf{I}_m \ddot{\mathbf{q}} - \boldsymbol{\zeta}_d \tanh(c \dot{\mathbf{q}}) + \boldsymbol{\zeta}_v \dot{\mathbf{q}}). \quad (\text{C.9})$$

where

- $\mathbf{I}_m \in \mathbb{R}^{n \times n}$  is a diagonal matrix containing the winch moment of inertia.
- $\boldsymbol{\zeta}_d \in \mathbb{R}^{n \times n}$  : a diagonal matrix containing the dry friction coefficients.
- $\boldsymbol{\zeta}_v \in \mathbb{R}^{n \times n}$  : a diagonal matrix containing the viscous friction coefficients.

## Bibliography

- [AA02] Abdullah B Alp and Sunil K Agrawal. Cable suspended robots : design, planning and control. In IEEE International Conference on Robotics and Automation, 2002. Proceedings. ICRA'02., volume 4, pages 4275–4280. IEEE, 2002. 34
- [ABAV11] Alireza Alikhani, Saeed Behzadipour, Aria Alasty, and S Ali Sadough Vanini. Design of a large-scale cable-driven robot with translational motion. Robotics and Computer-Integrated Manufacturing, 27(2) :357–366, 2011. 17, 23
- [ABVA09] Alireza Alikhani, Saeed Behzadipour, S Ali Sadough Vanini, and Aria Alasty. Workspace analysis of a three dof cable-driven mechanism. Journal of Mechanisms and Robotics, 1(4) :041005, 2009. 35
- [AC15] Ghasem Abbasnejad and Marco Carricato. Direct geometrico-static problem of under-constrained cable-driven parallel robots with cables. IEEE Transactions on Robotics, 31(2) :468–478, 2015. 34
- [ADG<sup>+</sup>09] Sunil K Agrawal, Venketesh N Dubey, John J Gangloff, Elizabeth Brackbill, and Vivek Sangwan. Optimization and design of a cable driven upper arm exoskeleton. In ASME 2009 International Design Engineering Technical Conferences and Computers and Information in Engineering Conference, pages 3–10. American Society of Mechanical Engineers, 2009. 17, 23, 36, 39
- [Alt02] Daniel R Altschuler. The national astronomy and ionosphere center’s (naic) arecibo observatory in puerto rico. In Single-Dish Radio Astronomy : Techniques and Applications, volume 278, pages 1–24, 2002. 30

- [Ars13a] Marc Arsenault. Stiffness analysis of a planar 2-dof cable-suspended mechanism while considering cable mass. In Cable-Driven Parallel Robots, pages 405–421. Springer, 2013. 40
- [Ars13b] Marc Arsenault. Workspace and stiffness analysis of a three-degree-of-freedom spatial cable-suspended parallel mechanism while considering cable mass. Mechanism and Machine Theory, 66 :1–13, 2013. 62, 113
- [AY17] Hamed Jabbari Asl and Jungwon Yoon. Robust trajectory tracking control of cable-driven parallel robots. Nonlinear Dynamics, 89(4) :2769–2784, 2017. 44
- [AYTK10] Wisnu Aribowo, Takahito Yamashita, Kazuhiko Terashima, and Hideo Kitagawa. Input shaping control to suppress sloshing on liquid container transfer using multi-joint robot arm. In IEEE/RSJ International Conference on Intelligent Robots and Systems (IROS), 2010, pages 3489–3494. IEEE, 2010. 45
- [BAD<sup>+</sup>94] Roger Bostelman, James Albus, Nicholas Dagalakis, Adam Jacoff, and John Gross. Applications of the nist robocrane. In Proceedings of the 5th International Symposium on Robotics and Manufacturing, pages 14–18, 1994. 33
- [BCC18] Sana Baklouti, Stéphane Caro, and Eric Courteille. Sensitivity analysis of the elasto-geometrical model of cable-driven parallel robots. In Cable-Driven Parallel Robots, pages 37–49. Springer, 2018. 96
- [BCC19] Sana Baklouti, Stéphane Caro, and Eric Courteille. Elasto-dynamic model-based control of non-redundant cable-driven parallel robots. In ROMANSY 22—Robot Design, Dynamics and Control, pages 238–246. Springer, 2019. 48, 124
- [BCCD17] Sana Baklouti, Eric Courteille, Stéphane Caro, and Mohamed Dkhil. Dynamic and oscillatory motions of cable-driven parallel robots based on a non-linear cable tension model. Journal of Mechanisms and Robotics, 9(6) :061014, 2017. 40, 44, 51, 127
- [Bes16] Raphaël Besson. Villes créatives. déconstruire les illusions technologistes et totémiques. 2016. 38
- [BFV16] Nicole Barry, Erin Fisher, and Joshua Vaughan. Modeling and control of a cable-suspended robot for inspection of vertical structures. In Journal of Physics : Conference Series, volume 744, page 012071. IOP Publishing, 2016. 19, 25, 46, 49
- [BG05] Guillaume Barrette and Clément M Gosselin. Determination of the dynamic workspace of cable-driven planar parallel mechanisms. Journal of Mechanical Design, 127(2) :242–248, 2005. 62
- [BJB<sup>+</sup>09] Per Henrik Borgstrom, Brett L Jordan, Bengt J Borgstrom, Michael J Stealey, Gaurav S Sukhatme, Maxim A Batalin, and William J Kaiser. Nims-pl : A cable-driven robot with self-calibration capabilities. IEEE Transactions on Robotics, 25(5) :1005–1015, 2009. 105
- [BJLP16] Mathieu Babaz, Louis Jezequel, Claude-Henri Lamarque, and Patrick Perrard. Unusual expression of tension of a massless cable with application to the oscillations of a

- 
- mass suspended to a cable with a variable length. Journal of Sound and Vibration, 363 :446–459, 2016. 62, 63, 64
- [BJS<sup>+</sup>09] Per Henrik Borgstrom, Brett L Jordan, Gaurav S Sukhatme, Maxim A Batalin, and William J Kaiser. Rapid computation of optimally safe tension distributions for parallel cable-driven robots. IEEE Transactions on Robotics, 25(6) :1271–1281, 2009. 33, 58
- [BKT15] Reza Babaghasabha, Mohammad A Khosravi, and Hamid D Taghirad. Adaptive robust control of fully-constrained cable driven parallel robots. Mechatronics, 25 :27–36, 2015. 34, 45, 158
- [BLS<sup>+</sup>13] Tobias Bruckmann, Wildan Lalo, Christian Sturm, Dieter Schramm, and Manfred Hiller. Design and realization of a high rack storage and retrieval machine based on wire robot technology. DINAME, 2013. 18, 24, 45, 48, 113, 114
- [cab] Cablebot- parallel cable robotics for improving maintenance and logistics of large-scale products. 35
- [Car11] Giuseppe Carbone. Stiffness analysis and experimental validation of robotic systems. Frontiers of Mechanical Engineering, 6(2) :182–196, 2011. 96
- [CCL15] Ryad Chellal, Loïc Cuvillon, and Edouard Laroche. A kinematic vision-based position control of a 6-dof cable-driven parallel robot. In Cable-Driven Parallel Robots, pages 213–225. Springer, 2015. 43
- [CCYJ13] Xiang Cui, Weihai Chen, Guilin Yang, and Yan Jin. Closed-loop control for a cable-driven parallel manipulator with joint angle feedback. In IEEE/ASME International Conference on Advanced Intelligent Mechatronics (AIM), 2013, pages 625–630. IEEE, 2013. 45
- [CF14] Ryan James Caverly and James Richard Forbes. Dynamic modeling and noncollocated control of a flexible planar cable-driven manipulator. IEEE Transactions on Robotics, 30(6) :1386–1397, 2014. 40
- [CFM15] Ryan James Caverly, James Richard Forbes, and Donya Mohammadshahi. Dynamic modeling and passivity-based control of a single degree of freedom cable-actuated system. IEEE Transactions on Control Systems Technology, 23(3) :898–909, 2015. 40
- [CLC14] Ryad Chellal, Edouard Laroche, and Loic Cuvillon. An  $h_\infty$  methodology for position control of 6-dof cable-driven parallel robots. In European Control Conference (ECC), 2014, pages 358–363. IEEE, 2014. 44
- [CLCG13] Ryad Chellal, Edouard Laroche, Loïc Cuvillon, and Jacques Gangloff. An identification methodology for 6-dof cable-driven parallel robots parameters application to the inca 6d robot. In Cable-Driven Parallel Robots, pages 301–317. Springer, 2013. 43
- [CLP98] Monica Carfagni, Edoardo Lenzi, and Marco Pierini. The loss factor as a measure of mechanical damping. In Proceedings-spie the international society for optical

- engineering, volume 1, pages 580–284. Spie International Society for Optical, 1998. 165
- [CLP18] Jorge Ivan Ayala Cuevas, Édouard Laroche, and Olivier Piccin. Assumed-mode-based dynamic model for cable robots with non-straight cables. In Cable-Driven Parallel Robots, pages 15–25. Springer, 2018. 18, 24, 44
- [CN12] David W Crawford and Edward A Nemeth. Amusement park ride with cable-suspended vehicles, April 3 2012. US Patent 8,147,344. 32, 38
- [Con85] Lawrence L Cone. Skycam-an aerial robotic camera system. Byte, 10(10) :122, 1985. 37
- [COR14] Gianni Castelli, Erika Ottaviano, and Pierluigi Rea. A cartesian cable-suspended robot for improving end-users’ mobility in an urban environment. Robotics and Computer-Integrated Manufacturing, 30(3) :335–343, 2014. 35
- [DA15] Jingli Du and Sunil K Agrawal. Dynamic modeling of cable-driven parallel manipulators with distributed mass flexible cables. Journal of Vibration and Acoustics, 137(2) :021020.1–021020.8, 2015. 62
- [DBDC10] Jingli Du, Hong Bao, Xuechao Duan, and Chuanzhen Cui. Jacobian analysis of a long-span cable-driven manipulator and its application to forward solution. Mechanism and Machine Theory, 45(9) :1227–1238, 2010. 60
- [DDB13] Jingli Du, Wen Ding, and Hong Bao. Cable vibration analysis for large workspace cable-driven parallel manipulators. In Cable-Driven Parallel Robots, pages 437–449. Springer, 2013. 40
- [DGA<sup>+</sup>12] Tej Dallej, Marc Gouttefarde, Nicolas Andreff, Redwan Dahmouche, and Philippe Martinet. Vision-based modeling and control of large-dimension cable-driven parallel robots. In IEEE/RSJ International Conference on Intelligent Robots and Systems (IROS), 2012, pages 1581–1586. IEEE, 2012. 17, 23
- [Dia15] Xiumin Diao. Singularity analysis of fully-constrained cable-driven parallel robots with seven cables. In IEEE International Conference on Mechatronics and Automation (ICMA), 2015, pages 1537–1541. IEEE, 2015. 34
- [DM09] Xiumin Diao and Ou Ma. Vibration analysis of cable-driven parallel manipulators. Multibody system dynamics, 21(4) :347–360, 2009. 44, 62, 90, 147
- [DQZZ09] BY Duan, YY Qiu, FS Zhang, and B Zi. On design and experiment of the feed cable-suspended structure for super antenna. Mechatronics, 19(4) :503–509, 2009. 34, 37, 60
- [dRRK18] Rogier de Rijk, Mitchell Rushton, and Amir Khajepour. Out-of-plane vibration control of a planar cable-driven parallel robot using a multi-axis reaction system. IEEE/ASME Transactions on Mechatronics, 2018. 17, 24, 39
- [dSF02] ART de Silva and Long Woon Fong. Effect of abrasive wear on the tensile strength of steel wire rope. Engineering Failure Analysis, 9(3) :349–358, 2002. 41

- 
- [dSTDC14] Julien Alexandre dit Sandretto, Gilles Trombettoni, David Daney, and Gilles Chabert. Certified calibration of a cable-driven robot using interval contractor programming. In Computational Kinematics, pages 209–217. Springer, 2014. 105
- [DWS90] C Canudas De Wit and V Seront. Robust adaptive friction compensation. In IEEE International Conference on Robotics and Automation, 1990. Proceedings., 1990, pages 1383–1388. IEEE, 1990. 76
- [Est14] Srl Esteco. Modelfrontier 2014 user manual. 2014. 99, 103
- [EUV04] Imme Ebert-Uphoff and Philip A Voglewede. On the connections between cable-driven robots, parallel manipulators and grasping. In IEEE International Conference on Robotics and Automation, 2004. Proceedings. ICRA'04. 2004, volume 5, pages 4521–4526. IEEE, 2004. 58
- [FFT<sup>+</sup>04] Shiqing Fang, Daniel Franitza, Marc Torlo, Frank Bekes, and Manfred Hiller. Motion control of a tendon-based parallel manipulator using optimal tension distribution. IEEE/ASME Transactions On Mechatronics, 9(3) :561–568, 2004. 17, 24, 33, 34, 39
- [GCF18] Harsh Atul Godbole, Ryan James Caverly, and James Richard Forbes. Modelling of flexible cable-driven parallel robots using a rayleigh-ritz approach. In Cable-Driven Parallel Robots, pages 3–14. Springer, 2018. 40
- [GCG<sup>+</sup>14] Lorenzo Gagliardini, Stéphane Caro, Marc Gouttefarde, Philippe Wenger, and Alexis Girin. Optimal design of cable-driven parallel robots for large industrial structures. In IEEE International Conference on Robotics and Automation (ICRA), 2014, pages 5744–5749. IEEE, 2014. 17, 23, 39
- [GCGG15] Lorenzo Gagliardini, Stéphane Caro, Marc Gouttefarde, and Alexis Girin. A re-configuration strategy for reconfigurable cable-driven parallel robots. In IEEE International Conference on Robotics and Automation (ICRA), 2015, pages 1613–1620. IEEE, 2015. 32
- [GCGG16] Lorenzo Gagliardini, Stéphane Caro, Marc Gouttefarde, and Alexis Girin. Discrete reconfiguration planning for cable-driven parallel robots. Mechanism and Machine Theory, 100 :313–337, 2016. 35, 82, 169
- [GCRB12] Marc Gouttefarde, Jean-François Collard, Nicolas Riehl, and Cédric Baradat. Simplified static analysis of large-dimension parallel cable-driven robots. In IEEE International Conference on Robotics and Automation (ICRA), 2012, pages 2299–2305. IEEE, 2012. 62
- [GCRB15] Marc Gouttefarde, Jean-François Collard, Nicolas Riehl, and Cédric Baradat. Geometry selection of a redundantly actuated cable-suspended parallel robot. IEEE Transactions on Robotics, 31(2) :501–510, 2015. 38
- [GCRS15] Rogério Sales Gonçalves, João Carlos Mendes Carvalho, José Francisco Ribeiro, and Vitor Vieira Salim. Cable-driven robot for upper and lower limbs rehabilitation. In Handbook of Research on Advancements in Robotics and Mechatronics, pages 284–315. IGI Global, 2015. 36

- [GG11] Clément Gosselin and Martin Grenier. On the determination of the force distribution in overconstrained cable-driven parallel mechanisms. Meccanica, 46(1) :3–15, 2011. 18, 33, 58
- [GLRB15] Marc Gouttefarde, Johann Lamaury, Christopher Reichert, and Tobias Bruckmann. A versatile tension distribution algorithm for  $n$ -dof parallel robots driven by  $n + 2$  cables. IEEE Transactions on Robotics, 31(6) :1444–1457, 2015. 18, 24
- [Had95] Yehia M Haddad. Viscoelasticity of engineering materials. Chapman & Hall, 2-6 Boundary Row, London, SE 1 8 HN, UK, 1995. 378, 1995. 165
- [HBY<sup>+</sup>16] Sung Wook Hwang, Jeong-Hyeon Bak, Jonghyun Yoon, Jong Hyeon Park, and Jong-Oh Park. Trajectory generation to suppress oscillations in under-constrained cable-driven parallel robots. Journal of Mechanical Science and Technology, 30(12) :5689–5697, 2016. 19, 25, 46, 49
- [HFM<sup>+</sup>05] Manfred Hiller, Shiqing Fang, Sonja Mielczarek, Richard Verhoeven, and Daniel Franitza. Design, analysis and realization of tendon-based parallel manipulators. Mechanism and Machine Theory, 40(4) :429–445, 2005. 33, 34
- [HFN02] Keiko Homma, Osamu Fukuda, and Yoshihiko Nagata. Study of a wire-driven leg rehabilitation system. In IEEE/RSJ International Conference on Intelligent Robots and Systems, 2002., volume 2, pages 1451–1456. IEEE, 2002. 36
- [HK15] Manh-Tuan Ha and Chul-Goo Kang. Wireless-communicated computed-torque control of a scara robot and two-dimensional input shaping for a spherical pendulum. In 12th International Conference on Ubiquitous Robots and Ambient Intelligence (URAI), 2015, pages 58–62. IEEE, 2015. 45
- [Hui15] LI Hui. A giant sagging-cable-driven parallel robot of fast telescope : its tension-feasible workspace of orientation and orientation planning. In Proceedings of the 14th IFToMM World Congress, pages 373–381, 2015. 34, 37, 82, 170
- [HW06] Thomas Heyden and Christoph Woernle. Dynamics and flatness-based control of a kinematically undetermined cable suspension manipulator. Multibody System Dynamics, 16(2) :155, 2006. 34
- [IDH<sup>+</sup>18] Jean-Baptiste Izard, Alexandre Dubor, Pierre-Elie Hervé, Edouard Cabay, David Culla, Mariola Rodriguez, and Mikel Barrado. On the improvements of a cable-driven parallel robot for achieving additive manufacturing for construction. In Cable-Driven Parallel Robots, pages 353–363. Springer, 2018. 7, 17, 23, 38
- [IGB<sup>+</sup>13] Jean-Baptiste Izard, Marc Gouttefarde, Cédric Baradat, David Culla, and Damien Sallé. Integration of a parallel cable-driven robot on an existing building façade. In Cable-driven parallel robots, pages 149–164. Springer, 2013. 38
- [Irv92] H Max Irvine. Cable structures. Number Sirsi) i9780486671277. 1992. 40, 60, 61, 62
- [JFGK15] H Jamshidifar, B Fidan, G Gungor, and A Khajepour. Adaptive vibration control of a flexible cable driven parallel robot. IFAC-PapersOnLine, 48(3) :1302–1307, 2015. 17, 24, 39, 43, 158

- 
- [JKFK18] Hamed Jamshidifar, Saeid Khosravani, Baris Fidan, and Amir Khajepour. Vibration decoupled modeling and robust control of redundant cable-driven parallel robots. IEEE/ASME Transactions on Mechatronics, 23(2) :690–701, 2018. 43
- [JKK99] Jae Won Jeong, Soo Hyun Kim, and Yoon Keun Kwak. Kinematics and workspace analysis of a parallel wire mechanism for measuring a robot pose. Mechanism and Machine Theory, 34(6) :825–841, 1999. 37
- [JKKS98] Jae Won Jeong, Soo Hyun Kim, Yoon Keun Kwak, and Craig C Smith. Development of a parallel wire mechanism for measuring position and orientation of a robot end-effector. Mechatronics, 8(8) :845–861, 1998. 37
- [JS03] SA Joshi and A Surianarayan. Calibration of a 6-dof cable robot using two inclinometers. Performance Metrics for Intelligent Systems, pages 3660–3665, 2003. 105
- [K<sup>+</sup>95] Sadao Kawamura et al. Development of an ultrahigh speed robot falcon using wire drive system. Robotics and Automation, pages 215–220, 1995. 31, 33, 34, 35, 54
- [Kan11] Chul-Goo Kang. On the derivative constraints of input shaping control. Journal of Mechanical Science and Technology, 25(2) :549–554, 2011. 144
- [KD04] Wisama Khalil and Etienne Dombre. Modeling, identification and control of robots. Butterworth-Heinemann, 2004. 56, 125
- [KEUS04] Kris Kozak, Imme Ebert-Uphoff, and William Singhose. Locally linearized dynamic analysis of parallel manipulators and application of input shaping to reduce vibrations. Journal of Mechanical design, 126(1) :156–168, 2004. 45
- [KMP13] Werner Kraus, Philipp Miermeister, and Andreas Pott. Investigation of the influence of elastic cables on the force distribution of a parallel cable-driven robot. In Cable-Driven Parallel Robots, pages 103–115. Springer, 2013. 44
- [KSHA16] Asuka Kobayashi, Hironori Suzuki, Toshiki Hirogaki, and Eiichi Aoyama. Investigation of impact task performed by humanoid robot using input shaping control method. In 14th International Conference on Automation, Robotics and Vision (ICARCV), 2016, pages 1–6. IEEE, 2016. 45
- [KT11] Mohammad A Khosravi and Hamid D Taghirad. Dynamic analysis and control of cable driven robots with elastic cables. Transactions of the Canadian Society for Mechanical Engineering, 35(4) :543–558, 2011. 18, 24, 44
- [KT14] Mohammad A Khosravi and Hamid D Taghirad. Dynamic modeling and control of parallel robots with elastic cables : singular perturbation approach. IEEE Transactions on Robotics, 30(3) :694–704, 2014. 18, 24, 40, 44
- [KT15] Mohammad A Khosravi and Hamid D Taghirad. Dynamic analysis and control of fully-constrained cable robots with elastic cables : variable stiffness formulation. In Cable-Driven Parallel Robots, pages 161–177. Springer, 2015. 44, 62
- [KT16] MA Khosravi and Hamid D Taghirad. Stability analysis and robust pid control of cable driven robots considering elasticity in cables. AUT Journal of Electrical Engineering, 48(2) :113–126, 2016. 18, 24, 44

- [KTH17] SA Khalilpour, HD Taghirad, and H Habibi. Wave-based control of suspended cable-driven parallel manipulators. In 5th International Conference on Control, Instrumentation, and Automation (ICCIA), 2017, pages 173–178. IEEE, 2017. 44
- [KZW06] Kris Kozak, Qian Zhou, and Jinsong Wang. Static analysis of cable-driven manipulators with non-negligible cable mass. IEEE Transactions on Robotics, 22(3) :425–433, 2006. 41, 60, 61, 62, 72, 77, 84, 104
- [Laf04] Pascal Lafourcade. Étude des manipulateurs parallèles à câbles : conception d’une suspension active pour soufflerie. PhD thesis, Toulouse, ENSAE, 2004. 43
- [LB01] Yan Li and Gary M Bone. Are parallel manipulators more energy efficient? In IEEE International Symposium on Computational Intelligence in Robotics and Automation, 2001. Proceedings 2001, pages 41–46. IEEE, 2001. 31
- [LCCG13] Edouard Laroche, Ryad Chellal, Loïc Cuvillon, and Jacques Gangloff. A preliminary study for  $h_\infty$  control of parallel cable-driven manipulators. In Cable-Driven Parallel Robots, pages 353–369. Springer, 2013. 44
- [LCDA<sup>+</sup>04] H Le Coroller, J Dejonghe, C Arpesella, D Vernet, and A Labeyrie. Tests with a carlina-type hypertelescope prototype-i. demonstration of star tracking and fringe acquisition with a balloon-suspended focal camera. Astronomy & Astrophysics, 426(2) :721–728, 2004. 37
- [LG13] Johann Lamaury and Marc Gouttefarde. Control of a large redundantly actuated cable-suspended parallel robot. In IEEE International Conference on Robotics and Automation (ICRA), 2013, pages 4659–4664. IEEE, 2013. 31, 34, 35
- [LGCH13] Johann Lamaury, Marc Gouttefarde, Ahmed Chemori, and Pierre-Elie Hervé. Dual-space adaptive control of redundantly actuated cable-driven parallel robots. In IEEE/RSJ International Conference on Intelligent Robots and Systems (IROS), 2013, pages 4879–4886. IEEE, 2013. 17, 23, 158
- [Li15] Hui Li. On the static stiffness of incompletely restrained cable-driven robot. In Cable-Driven Parallel Robots, pages 55–69. Springer, 2015. 40
- [LL16] Jonqlan Lin and Guan-Ting Liao. Design and oscillation suppression control for cable-suspended robot. In American Control Conference (ACC), 2016, pages 3014–3019. IEEE, 2016. 19, 25, 46, 49
- [LNC07] Casey Lambert, Meyer Nahon, and Dean Chalmers. Implementation of an aerostat positioning system with cable control. IEEE/ASME Transactions on Mechatronics, 12(1) :32–40, 2007. 40
- [LTS<sup>+</sup>13] Zhihua Liu, Xiaoqiang Tang, Zhufeng Shao, Liping Wang, and Lewei Tang. Research on longitudinal vibration characteristic of the six-cable-driven parallel manipulator in fast. Advances in Mechanical Engineering, 2013. 82, 170
- [LZM<sup>+</sup>09] Bing Li, Xuping Zhang, James K Mills, William L Cleghorn, and Liyang Xie. Vibration suppression of a 3-prr flexible parallel manipulator using input shaping. In

- 
- International Conference on Mechatronics and Automation, 2009. ICMA 2009., pages 3539–3544. IEEE, 2009. 45
- [MBHS08] Lars Mikelsons, Tobias Bruckmann, Manfred Hiller, and Dieter Schramm. A real-time capable force calculation algorithm for redundant tendon-based parallel manipulators. In IEEE International Conference on Robotics and Automation, 2008. ICRA 2008., pages 3869–3874. IEEE, 2008. 58
- [MD10] Jean-pierre Merlet and David Daney. A portable, modular parallel wire crane for rescue operations. In 2010 IEEE International Conference on Robotics and Automation (ICRA), pages 2834–2839. IEEE, 2010. 36
- [Mer06] Jean-Pierre Merlet. Parallel robots, volume 128. Springer Science & Business Media, 2006. 29
- [Mer08] Jean-Pierre Merlet. Kinematics of the wire-driven parallel robot marionet using linear actuators. In IEEE International Conference on Robotics and Automation, 2008. ICRA 2008., pages 3857–3862. IEEE, 2008. 32, 36
- [Mer09] Jean-Pierre Merlet. Interval analysis for certified numerical solution of problems in robotics. International Journal of Applied Mathematics and Computer Science, 19(3) :399–412, 2009. 42
- [Mer12] Jean-Pierre Merlet. The kinematics of the redundant  $n-1$  wire driven parallel robot. In IEEE International Conference on Robotics and Automation (ICRA), 2012, pages 2313–2318. IEEE, 2012. 33
- [Mer14] Jean-Pierre Merlet. The influence of discrete-time control on the kinematico-static behavior of cable-driven parallel robot with elastic cables. In Advances in Robot Kinematics, pages 113–121. Springer, 2014. 17, 23
- [Mer17] Jean-Pierre Merlet. Simulation of discrete-time controlled cable-driven parallel robots on a trajectory. IEEE Transactions on Robotics, 2017. 44
- [Mer18] Jean-Pierre Merlet. Direct kinematics of cdpr with extra cable orientation sensors : the 2 and 3 cables case with perfect measurement and ideal or elastic cables. In Cable-Driven Parallel Robots, pages 180–191. Springer, 2018. 17, 23
- [MKLP15] Philipp Miermeister, Werner Kraus, Tian Lan, and Andreas Pott. An elastic cable model for cable-driven parallel robots including hysteresis effects. In Cable-Driven Parallel Robots, pages 17–28. Springer, 2015. 41, 99
- [MLB<sup>+</sup>16] Philipp Miermeister, Maria Lächele, Rainer Boss, Carlo Masone, Christian Schenk, Joachim Tesch, Michael Kerger, Harald Teufel, Andreas Pott, and Heinrich H Bülthoff. The cablerobot simulator large scale motion platform based on cable robot technology. In IEEE/RSJ International Conference on Intelligent Robots and Systems (IROS), 2016, pages 3024–3029. IEEE, 2016. 17, 23
- [MNA16] Ziyad Masoud, Mohammad Nazzal, and Khaled Alhazza. Multimode input shaping control of flexible robotic manipulators using frequency-modulation. Jordan Journal of Mechanical & Industrial Engineering, 10(3), 2016. 143

- [MP10] Philipp Miermeister and Andreas Pott. Modelling and real-time dynamic simulation of the cable-driven parallel robot ipanema. In New Trends in Mechanism Science, pages 353–360. Springer, 2010. 19, 25, 41
- [MPV] Philipp Miermeister, Andreas Pott, and Alexander Verl. Auto-calibration method for overconstrained cable-driven parallel robots. In 7th German Conference on Robotics ; Proceedings of ROBOTIK 2012. 105
- [MV17] Forrest Montgomery and Joshua Vaughan. Suppression of cable suspended parallel manipulator vibration utilizing input shaping. In IEEE Conference on Control Technology and Applications (CCTA), 2017, pages 1480–1485. IEEE, 2017. 19, 25, 46, 49
- [NG14] Dinh Quan Nguyen and Marc Gouttefarde. Stiffness matrix of 6-dof cable-driven parallel robots and its homogenization. In Advances in Robot Kinematics, pages 181–191. Springer, 2014. 97
- [NGP+14] Dinh Quan Nguyen, Marc Gouttefarde, Francois Pierrot, et al. On the analysis of large-dimension reconfigurable suspended cable-driven parallel robots. In IEEE International Conference on Robotics and Automation (ICRA), 2014, pages 5728–5735. IEEE, 2014. 17, 23
- [Not15] Leila Notash. Analytical methods for solution sets of interval wrench. In ASME International Design Engineering Technical Conferences and Engineering Conference in Computers and Information, 2015, pages V05CT08A057–V05CT08A057. American Society of Mechanical Engineers, 2015. 42
- [Not16] Leila Notash. On the solution set for positive wire tension with uncertainty in wire-actuated parallel manipulators. Journal of Mechanisms and Robotics, 8(4) :044506, 2016. 42
- [OA05] So-Ryeok Oh and Sunil Kumar Agrawal. Cable suspended planar robots with redundant cables : Controllers with positive tensions. IEEE Transactions on Robotics, 21(3) :457–465, 2005. 43
- [OC10] Erika Ottaviano and Gianni Castelli. A study on the effects of cable mass and elasticity in cable-based parallel manipulators. In ROMANSY 18 Robot Design, Dynamics and Control, pages 149–156. Springer, 2010. 41
- [ODB+12] Adel Olabi, Mohamed Damak, Richard Bearee, Olivier Gibaru, and Stephane Leleu. Improving the accuracy of industrial robots by offline compensation of joints errors. In Industrial Technology (ICIT), 2012 IEEE International Conference on, pages 492–497. IEEE, 2012. 110
- [ÖKO16] Julian Öltjen, Jens Koblarski, and Tobias Ortmaier. On the reduction of vibration of parallel robots using flatness-based control and adaptive input shaping. In IEEE International Conference on Advanced Intelligent Mechatronics (AIM), 2016, pages 695–702. IEEE, 2016. 45
- [OPND+09] Martin J-D Otis, Simon Perreault, Thien-Ly Nguyen-Dang, Patrice Lambert, Marc Gouttefarde, Denis Laurendeau, and Clément Gosselin. Determination and mana-

- gement of cable interferences between two 6-dof foot platforms in a cable-driven locomotion interface. IEEE Transactions on Systems, Man, and Cybernetics-Part A : Systems and Humans, 39(3) :528–544, 2009. 63, 77
- [PBM09] Andreas Pott, Tobias Bruckmann, and Lars Mikelsons. Closed-form force distribution for parallel wire robots. In Computational Kinematics, pages 25–34. Springer, 2009. 33, 58
- [PCPL06] Juyi Park, Pyung-Hun Chang, Hyung-Soon Park, and Eunjeong Lee. Design of learning input shaping technique for residual vibration suppression in an industrial robot. IEEE/ASME Transactions on Mechatronics, 11(1) :55–65, 2006. 45
- [PKP13] Jaehwan Park, Ohung Kwon, and Jong Hyeon Park. Anti-sway trajectory generation of incompletely restrained wire-suspended system. Journal of Mechanical Science and Technology, 27(10) :3171–3176, 2013. 19, 25, 46, 49
- [PMV10] Andreas Pott, Christian Meyer, and Alexander Verl. Large-scale assembly of solar power plants with parallel cable robots. In 41st International Symposium on Robotics (ISR) and 6th German Conference on Robotics (ROBOTIK), 2010, pages 1–6. VDE, 2010. 7, 34, 35, 36
- [Pot12] Andreas Pott. Influence of pulley kinematics on cable-driven parallel robots. In Latest Advances in Robot Kinematics, pages 197–204. Springer, 2012. 19, 25, 41
- [Pot14] Andreas Pott. An improved force distribution algorithm for over-constrained cable-driven parallel robots. In Computational Kinematics, pages 139–146. Springer, 2014. 18, 24, 33, 58
- [Pot18a] Andreas Pott. Cable-Driven Parallel Robots : Theory and Application, volume 120. Springer, 2018. 7, 36
- [Pot18b] Andreas Pott. Classification and Architecture, pages 15–43. Springer International Publishing, Cham, 2018. 7, 32, 33, 39
- [PRF90] François Pierrot, C Reynaud, and Alain Fournier. Delta : a simple and efficient parallel robot. Robotica, 8(2) :105–109, 1990. 29
- [Pyl] Pylos. 38
- [RABG07] Giulio Rosati, Mattia Andreolli, Andrea Biondi, and Paolo Gallina. Performance of cable suspended robots for upper limb rehabilitation. In IEEE 10th International Conference on Rehabilitation Robotics, 2007. ICORR 2007., pages 385–392. IEEE, 2007. 36
- [RB93] Jim Rodnunsky and Trou Bayliss. Aerial cableway and method for filming subjects in motion, July 6 1993. US Patent 5,224,426. 37
- [RGK<sup>+</sup>09] Nicolas Riehl, Marc Gouttefarde, Sébastien Krut, Cédric Baradat, and François Pierrot. Effects of non-negligible cable mass on the static behavior of large workspace cable-driven parallel mechanisms. In IEEE International Conference on Robotics and Automation, 2009. ICRA'09., pages 2193–2198. IEEE, 2009. 59, 62

- [RGM07] Giulio Rosati, Paolo Gallina, and Stefano Masiero. Design, implementation and clinical tests of a wire-based robot for neurorehabilitation. IEEE Transactions on Neural Systems and Rehabilitation Engineering, 15(4) :560–569, 2007. 36
- [RGPB10] Nicolas Riehl, Marc Gouttefarde, François Pierrot, and Cédric Baradat. On the static workspace of large dimension cable-suspended robots with non negligible cable mass. In ASME 2010 International Design Engineering Technical Conferences and Computers and Information in Engineering Conference, pages 261–270. American Society of Mechanical Engineers, 2010. 41
- [RHK15] Levi Rupert, Phillip Hyatt, and Marc D Killpack. Comparing model predictive control and input shaping for improved response of low-impedance robots. In IEEE-RAS 15th International Conference on Humanoid Robots (Humanoids), 2015, pages 256–263. IEEE, 2015. 45
- [RLMGC18a] Tahir Rasheed, Philip Long, David Marquez-Gamez, and Stéphane Caro. Kinematic modeling and twist feasibility of mobile cable-driven parallel robots. In The 16th International Symposium on Advances in Robot Kinematics, 2018. 31
- [RLMGC18b] Tahir Rasheed, Philip Long, David Marquez-Gamez, and Stéphane Caro. Tension distribution algorithm for planar mobile cable-driven parallel robots. In Cable-Driven Parallel Robots, pages 268–279. Springer, 2018. 18, 24, 35
- [RR06] Thomas J Rudolph and Allen V Reicks. Viscoelastic indentation and resistance to motion of conveyor belts using a generalized maxwell model of the backing material. Rubber chemistry and technology, 79(2) :307–319, 2006. 64
- [SB04] Dragoljub Surdilovic and Rolf Bernhardt. String-man : a new wire robot for gait rehabilitation. In IEEE International Conference on Robotics and Automation, 2004. Proceedings. ICRA'04, 2004, volume 2, pages 2031–2036. IEEE, 2004. 32, 36
- [Sch17] Valentin Lorenz Schmidt. Modeling techniques and reliable real-time implementation of kinematics for cable-driven parallel robots using polymer fiber cables. Stuttgart : Fraunhofer Verlag, 2017. 41
- [SCS97] W Singhose, E Crain, and W Seering. Convolved and simultaneous two-mode input shapers. IEEE Proceedings-Control Theory and Applications, 144(6) :515–520, 1997. 145, 151
- [SL<sup>+</sup>91] Jean-Jacques E Slotine, Weiping Li, et al. Applied nonlinear control, volume 199. Prentice hall Englewood Cliffs, NJ, 1991. 45
- [SP17] Valentin Schmidt and Andreas Pott. Increase of position accuracy for cable-driven parallel robots using a model for elongation of plastic fiber ropes. In New Trends in Mechanism and Machine Science, pages 335–343. Springer, 2017. 41
- [SP18] Valentin Schmidt and Andreas Pott. Bending cycles and cable properties of polymer fiber cables for fully constrained cable-driven parallel robots. In Cable-Driven Parallel Robots, pages 85–94. Springer, 2018. 41

- 
- [SS90] Neil C Singer and Warren P Seering. Preshaping command inputs to reduce system vibration. Journal of Dynamic Systems, Measurement, and Control, 112(1) :76–82, 1990. 143
- [SS02] Tarunraj Singh and William Singhose. Input shaping/time delay control of maneuvering flexible structures. In American Control Conference, 2002. Proceedings of the 2002, volume 3, pages 1717–1731. IEEE, 2002. 140
- [SSVO09] B Siciliano, L Sciavicco, L Villani, and G Oriolo. Robotics–modelling, planning and control. advanced textbooks in control and signal processing series, 2009. 55
- [Sta91] Uwe Starossek. Dynamic stiffness matrix of sagging cable. Journal of engineering mechanics, 117(12) :2815–2828, 1991. 63, 77
- [TSPE15] Philipp Tempel, Fabian Schnelle, Andreas Pott, and Peter Eberhard. Design and programming for cable-driven parallel robots in the german pavilion at the expo 2015. Machines, 3(3) :223–241, 2015. 7, 32, 38, 39
- [TVHT99] Satoshi Tadokoro, Richard Verhoeven, Manfred Hiller, and Toshi Takamori. A portable parallel manipulator for search and rescue at large-scale urban earthquakes and an identification algorithm for the installation in unstructured environments. In IEEE/RSJ International Conference on Intelligent Robots and Systems, 1999. IROS'99. Proceedings. 1999, volume 2, pages 1222–1227. IEEE, 1999. 36
- [VAT10] Alaleh Vafaei, Mohammad M Aref, and Hamid D Taghirad. Integrated controller for an over-constrained cable driven parallel manipulator : Kntu cdrpm. In IEEE International Conference on Robotics and Automation (ICRA), 2010, pages 650–655. IEEE, 2010. 43
- [VP15] La Duc Viet and Youngjin Park. A cable-passive damper system for sway and skew motion control of a crane spreader. Shock and Vibration, 2015, 2015. 17, 23, 39
- [VS02] Walter Verdonck and Jan Swevers. Improving the dynamic accuracy of industrial robots by trajectory pre-compensation. In Robotics and Automation, 2002. Proceedings. ICRA'02. IEEE International Conference on, volume 4, pages 3423–3428. IEEE, 2002. 110
- [VvdWH12] Kevin HJ Voss, Volkert van der Wijk, and Just L Herder. Investigation of a cable-driven parallel mechanism for interaction with a variety of surfaces, applied to the cleaning of free-form buildings. In Latest Advances in Robot Kinematics, pages 261–268. Springer, 2012. 33
- [VW04] Wolfram Vogel and Karl-Heinz Wehking. Neuartige maschinenelemente in der fordertechnik und logistik : Hochfeste, laufende faserseile. Logistics Journal : nicht-referierte Veroffentlichungen, 2004(Okttober), 2004. 42
- [VYS08] Joshua Vaughan, Aika Yano, and William Singhose. Comparison of robust input shapers. Journal of Sound and Vibration, 315(4-5) :797–815, 2008. 142
- [WCG14] Xavier Weber, Loic Cuvillon, and Jacques Gangloff. Active vibration canceling of a cable-driven parallel robot using reaction wheels. In IEEE/RSJ International

- Conference on Intelligent Robots and Systems, 2014, pages 1724–1729. IEEE, 2014. 17, 23, 39, 81
- [WCG15] Xavier Weber, Loic Cuvillon, and Jacques Gangloff. Active vibration canceling of a cable-driven parallel robot in modal space. In IEEE International Conference on Robotics and Automation (ICRA), 2015, pages 1599–1604. IEEE, 2015. 40
- [XCCJ10] Lin Xu, Yi Cao, Jin Chen, and Shuai Jiang. Design and workspace optimization of a 6/6 cable-suspended parallel robot. In International Conference on Computer Application and System Modeling (ICCASM), 2010, volume 10, pages V10–610. IEEE, 2010. 17, 23, 33, 34, 39
- [YCD14] Han Yuan, Eric Courteille, and Dominique Deblaise. Elastodynamic analysis of cable-driven parallel manipulators considering dynamic stiffness of sagging cables. In IEEE International Conference on Robotics and Automation (ICRA), 2014, pages 4055–4060. IEEE, 2014. 60
- [YCD15] Han Yuan, Eric Courteille, and Dominique Deblaise. Static and dynamic stiffness analyses of cable-driven parallel robots with non-negligible cable mass and elasticity. Mechanism and Machine Theory, 85 :64–81, 2015. 40, 60, 89, 166
- [YCD16] Han Yuan, Eric Courteille, and Dominique Deblaise. Force distribution with pose-dependent force boundaries for redundantly actuated cable-driven parallel robots. Journal of Mechanisms and Robotics, 8(4) :041004, 2016. 18, 24, 33, 42
- [YCGH17] Han Yuan, Eric Courteille, Marc Gouttefarde, and Pierre-Elie Hervé. Vibration analysis of cable-driven parallel robots based on the dynamic stiffness matrix method. Journal of Sound and Vibration, 394 :527–544, 2017. 17, 23
- [YHB<sup>+</sup>16] Jonghyun Yoon, Sung Wook Hwang, Jeong-Hyeon Bak, Jong Hyeon Park, and Sung Young Ko. Multi-mode input shaping for vibration suppression of over-constrained cable-driven parallel robots with cable stiffness. In 7th International Conference on Mechanical and Aerospace Engineering (ICMAE), 2016, pages 363–367. IEEE, 2016. 19, 25, 46, 49
- [YLK09] Kun Yu, Leng-Feng Lee, and Venkat N Krovi. Simultaneous trajectory tracking and stiffness control of cable actuated parallel manipulator. In ASME 2009 International Design Engineering Technical Conferences and Computers and Information in Engineering Conference, pages 55–63. American Society of Mechanical Engineers, 2009. 43
- [YLZ13] Rui Yao, Hui Li, and Xinyu Zhang. A modeling method of the cable driven parallel manipulator for fast. In Cable-Driven Parallel Robots, pages 423–436. Springer, 2013. 40
- [YTWH10] Rui Yao, Xiaoqiang Tang, Jinsong Wang, and Peng Huang. Dimensional optimization design of the four-cable-driven parallel manipulator in fast. IEEE/ASME Transactions On Mechatronics, 15(6) :932–941, 2010. 17, 23, 39
- [YYM01] Noritaka Yanai, Motoji Yamamoto, and Akira Mohri. Inverse dynamics analysis and trajectory generation of incompletely restrained wire-suspended mechanisms. In

- 
- IEEE International Conference on Robotics and Automation, 2001. Proceedings 2001 ICRA., volume 4, pages 3489–3494. IEEE, 2001. 49
- [YZXW16] Jiang Yi, Qiuguo Zhu, Rong Xiong, and Jun Wu. Vibration suppression based on input shaping for biped walking. In IEEE-RAS 16th International Conference on Humanoid Robots (Humanoids), 2016, pages 236–241. IEEE, 2016. 45
- [ZCTT16] Yu Zhao, Wenjie Chen, Te Tang, and Masayoshi Tomizuka. Zero time delay input shaping for smooth settling of industrial robots. In IEEE International Conference on Automation Science and Engineering (CASE), 2016, pages 620–625. IEEE, 2016. 45
- [ZDDB08] Bin Zi, BY Duan, JL Du, and Hong Bao. Dynamic modeling and active control of a cable-suspended parallel robot. Mechatronics, 18(1) :1–12, 2008. 17, 24, 39, 60
- [ZDWK14] Bin Zi, Huafeng Ding, Xia Wu, and Andres Kecskemethy. Error modeling and sensitivity analysis of a hybrid-driven based cable parallel manipulator. Precision Engineering, 38(1) :197–211, 2014. 72, 99
- [ZGQ03] DK Zhang, SR Ge, and YH Qiang. Research on the fatigue and fracture behavior due to the fretting wear of steel wire in hoisting rope. Wear, 255(7-12) :1233–1237, 2003. 41
- [ZSC17] Bingyuan Zhang, Weiwei Shang, and Shuang Cong. Dynamic control with tension compensation of a 3-dof cable-driven parallel manipulator. In Cybernetics and Intelligent Systems (CIS) and IEEE Conference on Robotics, Automation and Mechatronics (RAM), 2017, pages 508–513. IEEE, 2017. 45







## AVIS DU JURY SUR LA REPRODUCTION DE LA THESE SOUTENUE

**Titre de la thèse:**

Vibration analysis and reduction of Cable-Driven Parallel Robots

**Nom Prénom de l'auteur : BAKLOUTI SANA**

**Membres du jury :**

- Monsieur CARO Stéphane
- Monsieur RAGNEAU ERIC
- Monsieur COURTEILLE Eric
- Monsieur GOUTTEFARDE Marc
- Monsieur LAROCHE Edouard
- Madame PIET-LAHANIER Héléne
- Monsieur MERLET Jean-Pierre

Président du jury : *M. MERLET Jean-Pierre*

Date de la soutenance : 11 Décembre 2018

Reproduction de la these soutenue

- Thèse pouvant être reproduite en l'état  
 Thèse pouvant être reproduite après corrections suggérées

Fait à Rennes, le 11 Décembre 2018

Signature du président de jury

Le Directeur,

*M'hamed DRISSI*  
M'hamed DRISSI







**Titre :** Analyse et réduction des vibrations des Robots Parallèles à Câbles

**Mots clés :** Robot parallèle à câbles, Robustesse, Modélisation élasto-dynamique, Commande référencée modèle, Input-shaping.

**Résumé :** Cette thèse vise à améliorer le positionnement statique et la précision de suivi de trajectoire des Robots Parallèles à Câbles (RPC) tout en prenant en compte leur élasticité globale. A cet effet, deux stratégies de commandes complémentaires valables pour toute configuration de RPC sont proposées.

Tout d'abord, une analyse de robustesse est réalisée pour aboutir à une commande robuste des RPC référencée modèle. Un modèle de RPC approprié est défini en fonction de l'application visée et les principales sources d'erreurs de pose de la plate-forme mobile sont identifiées.

Une première méthode de commande est proposée sur la base des résultats de l'analyse de robustesse. Cette première méthode réside dans le couplage d'une commande référencée modèle d'un contrôleur PID.

Dans le cadre de cette thèse, un modèle élasto-dynamique de RPC est exprimé afin de compenser le comportement oscillatoire de sa plate-forme mobile dû à l'élongation des câbles et de son comportement dynamique.

La deuxième méthode de commande utilise des filtres "input-shaping" dans la commande référencée modèle proposée afin d'annuler les mouvements oscillatoires de la plate-forme mobile. Ainsi, le signal d'entrée est modifié pour que le RPC annule automatiquement les vibrations résiduelles.

Les résultats théoriques obtenus sont validés expérimentalement à l'aide d'un prototype de RPC non redondant en actionnement et en configuration suspendue. Les résultats expérimentaux montrent la pertinence des stratégies de commande proposées en termes d'amélioration de la précision de suivi de trajectoire et de réduction des vibrations.

**Title:** Vibration Analysis and Reduction of Cable-Driven Parallel Robots

**Keywords:** Cable-Driven Parallel Robot, Non-linear tension model, Elasto-dynamic model, Robustness analysis, Model-based control, Input-shaping.

**Abstract:** This thesis aims at improving the static positioning and trajectory tracking accuracy of Cable-Driven Parallel Robots (CDPRs) while considering their overall elasticity. Accordingly, two complementary control strategies that are valid for any CDPR configuration are proposed.

First, a robustness analysis is performed to lead to a robust model-based control of CDPRs. As a result, an appropriate CDPR model is defined as a function of the targeted application and the main sources of CDPR moving-platforms pose errors are identified.

A first control method is determined based on the results of the robustness analysis. This first method lies in the coupling of a model-based feed-forward control scheme for CDPR with a PID feedback controller.

Here, an elasto-dynamic model of the CDPR is expressed to compensate the oscillatory motions of its moving-platform due to cable elongations and its dynamic behavior.

The second control method uses input-shaping filters into the proposed model-based feed-forward control in order to cancel the oscillatory motions the moving-platform. Thus, the input signal is modified for the CDPR to self-cancel residual vibrations.

Experimental validations are performed while using suspended and non-redundant CDPR prototype. The proposed feed-forward model-based control schemes are implemented, and their effectiveness is discussed. Results show the relevance of the proposed control strategies in terms of trajectory tracking accuracy improvement and vibration reduction.